

Molecular Doping of Organic Semiconductors: Role of Steric Hindrance

Somaiyeh Charoughchi

A Thesis
In the Department of
Chemistry and Biochemistry

Presented in Partial Fulfillment of the Requirements
For the Degree of
Doctor of Philosophy (Chemistry and Biochemistry) at
Concordia University
Montréal, Québec, Canada

September 2024

©Somaiyeh Charoughchi, 2024

CONCORDIA UNIVERSITY
SCHOOL OF GRADUATE STUDIES

This is to certify that the thesis prepared
By: Somaiyeh Charoughchi

Entitled: Molecular Doping of Organic Semiconductors: Role of Steric Hindrance

and submitted in partial fulfillment of the requirements for the degree of

Doctor of Philosophy (Chemistry and Biochemistry)

complies with the regulations of the University and meets the accepted standards with respect to originality and quality.

Signed by the final examining committee:

_____ Chair
Dr. Rafik Naccache

_____ External Examiner
Dr. Dima Perepichka

_____ Examiner
Dr. Ayşe Turak

_____ Examiner
Dr. Valter Zazubovits

_____ Examiner
Dr. Christine DeWolf

_____ Thesis Co-Supervisor
Dr. Pat Forgione

_____ Thesis Supervisor
Dr. Ingo Salzmann

Approved by _____
Dr. Louis Cuccia, Graduate Program Director

October, 2024 _____
Dr. Pascale Sicotte, Dean of the Faculty of Arts and Sciences

Abstract

Molecular Doping of Organic Semiconductors: Role of Steric Hindrance

Somaiyeh Charoughchi
Concordia University, 2024

The p-doping of organic semiconductors, that is, conjugated organic molecules (COMs) and polymers (COPs), is generally done using strong molecular acceptors as dopants. In principle, high doping efficiency can be achieved with dopants of high electron affinity (EA) to promote integer electron transfer between COP/COM and the p-dopant. Common dopants of high EA (> 5 eV) are, however, often unstable, show low solubility in common solvents with most COPs/COMs, and tend to diffuse through the organic semiconductor owing to low molecular weight. Furthermore, their planarity can promote the formation of ground-state charge transfer complexes (CPXs) with the COPs/COMs, which is detrimental to doping efficiency due to fractional instead of integer charge transfer. To address this issue, this thesis focuses on a new strategy towards more efficient molecular p-dopants: The optimization of EA to promote integer electron transfer is therein augmented by a novel strategy to inhibit CPX formation, which relies on directed dopant design exploiting steric hindrance. First, to identify promising alternative dopants with high EA, we systematically compared the interplay between molecular EA and steric shielding of the core resulting from the peripheral substitution of analogues molecules with cyclohexadiene and cyclopropane cores. To this end, we performed a simple analysis based on Hammett parameters followed by density functional theory (DFT) calculations on a library of modified doping agents. Second, based on the outcome of the DFT pre-characterization we focused on cyclopropane core-based dopants and synthesized and characterized 2',2''-(cyclopropane-1,2,3-triylidene)tris(2-(perfluorophenyl)-acetonitrile) (PFP3CN3-CP) as one of the most promising species. PFP3CN3-CP has pendant functional groups that sterically shield its central core while still maintaining a comparably high EA. By using various spectroscopy and electrical characterization we demonstrate for the prototypical COP, poly(3-hexylthiophene) (P3HT), that, indeed, CPX formation can be inhibited by exploiting steric hindrance brought by PFP3CN3-CP. It outperforms a planar dopant with similar EA, showing tenfold higher conductivity and superior stability in aging experiments. Overall, this thesis introduces a novel strategy for improving p-doping efficiency in organic semiconductors by incorporating steric hindrance to prevent CPX formation. It advances the development of more efficient p-dopants, contributing valuable knowledge to the field.

Acknowledgements

I would like to express my deepest gratitude to my supervisor, Dr. Ingo Salzmann, for his support, guidance, and invaluable supervision throughout my entire PhD journey. His expertise, encouragement, and constructive feedback have been instrumental in shaping the direction of this thesis. I am fortunate to have had Dr. Salzmann as my supervisor.

I would equally like to extend my appreciation to my co-supervisor, Dr. Pat Forgione, for their invaluable guidance, support, and collaborative spirit throughout my PhD journey. Working with Dr. Forgione has been a truly enriching experience, and their expertise has significantly contributed to the success of my work.

My work on this thesis was enabled through funds from the Concordia International Tuition Award of Excellence, and a research bursary from my supervisor which was paid from funds provided by the Natural Sciences and Engineering Research Council (NSERC), Le Fonds de Recherche du Québec, Nature et Technologies (FRQNT), and the New Frontiers in Research Fund (NFRF).

I extend my appreciation to my committee members Dr. Christine DeWolf and Dr. Valter Zazubovits for their invaluable feedback and suggestions during our meetings over the years, as well as to Dr. Louis Cuccia and my colleagues Melissa Berteau-Rainville, Hannes Hase, Jiang Tian Liu, Mohammad S. Askari, and Shubham Bhagat who have contributed to this work in so many ways. Their insights and assistance have enriched the quality of this thesis.

Part of the research described in this thesis was performed at the Canadian Light Source, a national research facility of the University of Saskatchewan, which is supported by the Canada Foundation for Innovation (CFI), NSERC, the National Research Council (NRC), the Canadian Institutes of Health Research (CIHR), the Government of Saskatchewan, and the University of Saskatchewan; I thank Dr. Beatriz Diaz Moreno and Dr. Chang-Yong Kim for experimental support at the Brockhouse Diffraction Sector Beamlines (BXDS-IVU and -WLE). I would also like to extend my heartfelt gratitude to CSICOMP Nuclear magnetic resonance (NMR) facility manager and specialist Dr. Darcy Burns and Dr. Jack Sheng at the University of Toronto for their invaluable assistance in measuring the NMR spectra of our samples. The availability of instruments and their support have significantly contributed to the accuracy and reliability of the results presented in this thesis. Likewise, I would like to thank Dr. Constantin Yannopoulos for his assistance with the primary NMR measurements and valuable insights. Additionally, I would like to acknowledge Dr. Nooshin Movahed for providing training and access to the Atomic Force Microscopy (AFM) facility. Further, I would like to thank Dr. Laszlo Kalman and Dr. Valter Zazubovits for granting constant access to the use of the Ultravi-

olet/Visible/Near Infrared Spectroscopy (UV/VIS/NIR) instrument in their lab.

I owe an immeasurable debt of gratitude to my parents. Their support, encouragement, and sacrifices have been the bedrock of my academic journey. Their belief in my abilities and their constant encouragement propelled me through the challenges of pursuing my PhD journey. They have been a source of inspiration, offering unconditional love and understanding during the highs and lows of my studies. Their sacrifices, both big and small, have played a crucial role in my success, and I am grateful for the values of hard work and perseverance they instilled in me. I am blessed to have such wonderful parents. Thank you for being my pillar of strength throughout this journey.

Hannes Hase and Melissa Berteau-Rainville have been invaluable sources of assistance, always ready to lend a helping hand and share their insights. The journey of completing this thesis has been made smoother by the continuous encouragement and guidance provided by them.

Last but not least, I wanna thank me for believing in me, for doing all this hard work, for never quitting, for always being a giver and trying to give more than I receive, and for just being me at all times.

Contribution of Authors

Chapter 3 is, except for a thesis-related foreword, based on a submitted manuscript by equal contribution of myself and Melissa Berteau-Rainville (MBR) as co-first authors, and Dr. Emanuele Orgiu, and Dr. Ingo Salzmann (ISA) as senior authors. While all authors reviewed the final manuscript and approved the contents, the original draft was written and conceptualized by myself, Melissa Berteau-Rainville, and in-depth revisions were done with ISA. MBR conducted all the DFT calculations for this paper. I compiled and analyzed all the data from those calculations. The final data analysis was conducted together with MBR.

Chapter 4 is, except for a thesis-related foreword, based on a published manuscript by myself as the first author, Jiang Tian Liu (JTL), Melissa Berteau-Rainville, Hannes Hase (HH), Mohammad S. Askari (MSA), Shubham Bhagat (SBH), Dr. Pat Forgione (PF), and Dr. Ingo Salzmann. While all authors reviewed the final manuscript and approved of the contents, the original draft was written by myself and in-depth revisions were done together with MBR, HH, and IS. I (SCH) conducted the primary synthesis trials and prepared the samples for experiments, including cyclic voltammetry, AFM, UV-vis, FTIR, GIXRD, and conductivity measurements. I also performed FTIR, UV-vis, GIXRD, and cyclic voltammetry experiments, as well as analyzed and interpreted all experimental data. HH was involved in conducting primary UV-vis and FTIR measurements on the doped films (P3HT:PFP3CN3-CP at different dopant ratios). Additionally, he measured the conductivity of these doped films. SBH conducted AFM measurements on P3HT:PFP3CN3-CP doped films. JTL successfully synthesized our novel dopant (PFP3CN3-CP) and conducted NMR and mass spectrometry analyses. MBR conducted all the DFT calculations for this paper. MSA prepared the modified synthesis procedure based on the patent and his trial-and-error experiences during the synthesis. PF conceptualized the chemical synthesis and supervised JTL and me during its realization.

Chapter 5 is, except for a thesis-related foreword, based on an ongoing study targeting an upcoming manuscript prepared by myself, Melissa Berteau-Rainville (MBR), Dr. Mihails Arhangel'skis (MA), and Dr. Ingo Salzmann. MBR led the density functional theory calculations, MA conducted the modeling of the molecular orientation based on the unit cell dimensions determined by powder X-ray diffraction at the Canadian Light Source.

Table of Contents

List of Figures	x
List of Tables	xvii
List of Associated Works	xx
1 Fundamentals of a Doping Organic Semiconductors	1
1.1 Conjugated Molecules and organic semiconductors	1
1.2 Organic <i>versus</i> Inorganic Semiconductors	5
1.3 Organic Semiconductor Doping Mechanisms	7
1.4 Common p-Dopants (Cyclohexadiene and Cyclopropane Core-Based Dopants)	10
1.5 Statement of the Problem	13
1.5.1 Electron affinity	13
1.5.2 Doping efficiency (inhibiting the CPX formation)	14
1.5.3 Diffusibility	14
1.5.4 Processibility	14
1.6 Thesis Objectives/ Research Goal	15
1.7 Thesis Organization	16
2 Experimental Methods	17
2.1 Optical Absorption Spectroscopy (UV-vis/NIR)	17
2.1.1 Setup fundamentals	17
2.1.2 Inert atmosphere sample holder and cuvette	19
2.1.3 Sample spectra acquisition and treatment	19
2.2 Fourier-Transform Infrared Spectroscopy	20
2.2.1 Setup and fundamentals	21
2.2.2 Data acquisition and treatment	22
2.3 Cyclic Voltammetry (CV)	23
2.3.1 Setup fundamentals	24
2.3.2 Data acquisition and treatment	25
2.4 Electrical Characterization (thin-film conductivity)	26
2.4.1 Setup fundamentals	26
2.4.2 Data acquisition and treatment	27
2.5 Atomic Force Microscopy (AFM)	28

2.5.1	Setup fundamentals	29
2.5.2	Data acquisition and treatment	30
2.6	Grazing-Incidence X-Ray Diffraction	30
2.6.1	Setup and fundamentals	30
2.6.2	Data Treatment	33
3	Design Strategies for Optimized Molecular p-Dopants: Decoupling Electronic and Geometric Effects	34
3.1	Introduction	35
3.2	Methods	38
3.3	Results and discussion	41
3.3.1	Choice of molecules	41
3.3.2	Hammett indices predict electron affinities	42
3.3.3	Relation between atomic charge on the core and electron affinity	44
3.3.4	Cyano vibrational modes	46
3.3.5	Comparison of molecular factors and selected molecules of interest	49
3.4	Conclusion	54
4	Sterically-Hindered Molecular p-Dopants Promote Integer Charge Transfer in Organic Semiconductors	56
4.1	Introduction	57
4.2	Methods	58
4.2.1	Materials	58
4.2.2	Sample preparation	59
4.2.3	Column Chromatography	59
4.2.4	Mass Spectra	59
4.2.5	NMR	60
4.2.6	Cyclic Voltammetry	60
4.2.7	UV-vis/NIR and FTIR Spectroscopy	60
4.2.8	Conductivity	60
4.2.9	GIXRD Experiments	61
4.2.10	AFM	61
4.2.11	DFT calculations	61
4.3	Results and discussion	61
4.4	Conclusion	68
5	Reversible Dimerization of <i>PFP3CN3-CP</i>	69
5.1	Introduction	69
5.2	Methods	71
5.2.1	Materials	71
5.2.2	Sample preparation	71
5.2.3	NMR	71
5.2.4	DFT calculations	72
5.2.5	PXRD	72
5.3	Results and discussion	72

5.4 Conclusion	75
6 Conclusion	77
Bibliography	80
A Supporting Information of chapter 3	96
A.1 Predicted EAs	96
A.2 Geometrical considerations	97
A.3 Molecular descriptors	100
A.4 Hammett indices predict electron affinities	102
A.5 Relation between atomic charge on the core and electron affinity	105
A.6 Cyano vibrational modes	108
A.7 Comparison of molecular factors	114
B Supporting Information of chapter 4	116
B.1 Chemical structures	117
B.2 DFT calculations	118
B.3 Synthesis of PFP3CN3-CP	125
B.4 Cyclic voltammetry	129
B.5 Supporting UV-vis/NIR absorption data	131
B.6 Aging experiments	134
B.7 Supporting conductivity data	135
B.8 Grazing-Incidence X-Ray Diffraction (GIXRD) data	136
B.9 Atomic Force Microscopy (AFM) data	139
C List of Abbreviations	140

List of Figures

1.1	Schematic energy level diagram of σ - and π -bonds forming from atomic orbitals between the carbon atoms in ethene (i.e. the two $2sp^2$ -orbitals forming σ -bonds with the hydrogen atoms are omitted). Figure adapted from [1] A. Köhler and H. Bässler, <i>Electronic Processes in Organic Semiconductors: An Introduction</i> . Weinheim: Wiley-VCH, 2015. Copyright 2015 Wiley-VCH Verlag GmbH & Co. KGaA.	3
1.2	Chemical structures of some conjugated polymers (CPs) and conjugated organic molecules (COMs).	5
1.3	p-type and n-type doping of the organic semiconductor. Figure has adapted from [2] L. M. Cowen, J. Atoyo, M. J. Carnie, D. Baran, and B. C. Schroeder, "Review—organic materials for thermoelectric energy generation," <i>ECS Journal of Solid State Science and Technology</i> , vol. 6, no. 3, p. N3080, Jan 2017. Published 2017 by ECS under CC BY 4.0.	8
1.4	a) ICT upon integer charge transfer from the HOMO (H) of the OSC to the LUMO (L) of the p-dopant (DOP) leads to ionized molecules. b) Alternative model assuming the hybridization of the frontier molecular orbitals of the OSC and the p-dopant in a supramolecular ground-state charge transfer complex (CPX); β denotes the resonance integral. c) Complexes within the OSC matrix: within the OSC matrix, complexes exhibit low-lying unoccupied states in the OSC gap, which are being occupied according to the Fermi–Dirac distribution ($f(E)$); shaded/white boxes denote HOMO/LUMO levels. The figure has adapted from [3] H. Mendez, G. Heimel, A. Opitz, K. Sauer, P. Barkowski, M. Oehzelt, J. Soeda, T. Okamoto, J. Takeya, J.-B. Arlin, J.-Y. Balandier, Y. Geerts, N. Koch, and I. Salzmann, "Doping of Organic Semiconductors: Impact of Dopant Strength and Electronic Coupling," <i>Angewandte Chemie International Edition</i> , vol. 52, no. 30, pp. 7751–7755, Jul. 2013. Copyright 2013 WILEY-VCH Verlag GmbH Co. KGaA, Weinheim	9
1.5	Chemical structure of TCNQ- based p-dopants discussed in this work . a) $FX - TCNQ$; where X shows the substitution of 1, 2, or 4 hydrogen atoms by fluorine atoms. b) $F6 - TCNNQ$. c) $HAT - CN$	11
1.6	Schematic structure of a CP-core based molecular dopant as suggested in Ref. [4]	11
1.7	Chemical structures of CP-based p-dopants discussed in this thesis	13

2.1	A typical double-beam configuration of optical absorbance; the simplified figure is missing filters, additional monochromator gratings, and variable slits.	18
2.2	A spectroscopy sample holder for measurements in an inert atmosphere is used in this thesis. The figure adapted from: Hase, H. (2023). Integer and fractional charge transfer in the doping of poly- and oligothiophenes (Unpublished doctoral dissertation). Concordia University. (Figure 3.2, p. 24).	19
2.3	The standard configuration for a Fourier-transform infrared spectrometer in transmission mode utilizing a Michelson interferometer. The figure missing details such as filters, aperture control, and mirrors.	21
2.4	Schematic of a typical three electrode electrochemical set-up. Current flows between CE and WE whilst E is controlled between WE and RE. The figure has been edited and adapted from: Colburn, A. W., Levey, K. J., O'Hare, D., Macpherson, J. V. (2021). Lifting the lid on the potentiostat: a beginner's guide to understanding electrochemical circuitry and practical operation. <i>Phys. Chem. Chem. Phys.</i> , 23, 8100. https://doi.org/10.1039/D1CP00661D . [Creative Commons Attribution 3.0 Unported License]	25
2.5	Visualization sample dimensions in thin-film conductivity measurements. These dimensions include the film thickness t , channel length L , and channel width w . (a) Offers a side view into the channel between electrodes. (b) Provides a top view onto the substrate, with connections to the source-measure unit illustrated (no thin film depicted for clarity). At the interdigitated regions of the three fingers of each electrode, five electrically parallel channels are formed, with their widths summing up to w . The figure has been adapted from: Hase, H. (2023). Integer and fractional charge transfer in the doping of poly- and oligothiophenes (Unpublished doctoral dissertation). Concordia University. (Figure 3.9, p. 40)	27
2.6	Schematic depiction of an atomic force microscopy (AFM). The figure has been edited and adapted from: Walker, Jack; Jamal, Umer; Mohammadpour, Mahdi; Theodossiades, Stephanos; Bewsher, Stephen R.; Offner, Guenter; Bansal, Hemant; Leighton, Michael; Braunstingl, Michael; Flesch, Heinz-Georg. (2021). "Asperity level characterization of abrasive wear using atomic force microscopy." <i>Proceedings of the Royal Society A</i> , 477(2021), 20210103. DOI: http://doi.org/10.1098/rspa.2021.0103	29
2.7	Visualization of the Bragg equation; depicted are the incoming and outgoing wavevectors \mathbf{k}_i and \mathbf{k}_o respectively, their angle θ with the lattice plane, the lattice plane distance d , the lattice normal \mathbf{n}_{lat} , and the scattering vector \mathbf{q}	31

3.1	Chemical structure of some p-dopants discussed in this work. a) F_x -TCNQ; where X indicates the substitution of 1, 2, 3 or 4 hydrogen atoms by fluorine atoms. b) F_6 -TCNNQ. c) HAT-CN. d) $(CN)_6$ -CP. e) $(CO_2CH_3)_3(CN)_3$ -CP, and its higher EA analogues, $(CO_2CH_3)_2(CN)_4$ -CP, and $(CO_2CH_2CH_3)(CN)_5$ -CP, where X shows the substitution of 1, 2 or 3 cyano groups by either 1 $CO_2CH_2CH_3$ group, 2 CO_2CH_3 groups, or 3 CO_2CH_3 groups respectively. f) $(F_5-Ph)_3(CN)_3$ -CP, and its higher EA analogue $(F_4CN-Ph)_3(CN)_3$ -CP, where X represents either a fluorine atom or a cyano group.	37
3.2	Substitution pattern nomenclature. a) Pattern (1): four substituents (R) directly on a CHD core. b) Pattern (2): same as a) but through phenyl groups. c) Pattern (3): three substituents directly on a CP core. d) Pattern (4): same as c) but through phenyl groups. e) Pattern (5): 8 substituents directly on a CHD core. f) Pattern (6): six substituents directly on a CP core. g) Pattern (7): same as f) but through phenyl groups.	42
3.3	Relationship between the Hammett index and EAs for the molecules listed in Tables 3.1 and 3.2. a) EA_1 and EA_2 of CHD-based molecules, for substitution patterns (1), (2), and (5); trend quality is particularly poor for EA_1 of patterns (1) and (5) (black squares). b) EA_1 and EA_2 of CP molecules, for patterns (3), (4), (6), and (7). The lines have been added as guides to the eye to highlight the general behavior discussed in the text.	43
3.4	Relationship between atomic charges and EAs. The sum of partial atomic charges on the core atoms in neutral molecules against their EA_1 is shown in a) while the sum of partial atomic charges on the core atoms in radical anionic molecules against their EA_2 is shown in b), in both cases for substitution patterns (2), (3), (4), (6), and (7). Data points for patterns (4) and (7) segregate on individual lines which have been identified directly on the Figure (this cannot be done for patterns (3) and (6) since they are mixed). The relationship for patterns (1) and (5) is poor because of geometric distortions, see Figure A.9.	45
3.5	Cyano vibration shifts across the three different charge states of the molecules (neutral, radical anionic and dianionic). a) Shifts of the highest wavenumber cyano vibrational mode as a function of the molecular charge for a selection of electron acceptors. b) Standard deviation of the linear fits for CHD-based (patterns (1) and (2)) and CP-based molecules (patterns (3) and (4)) plotted against the fit curvature ratio (see text); $(SO_2CN)_4$ -TCNQ was excluded from the plot because the ratio is extremely high (622%) due to coupling between the backbone cyano and (SO_2CN) vibrations. c) Relationship between EA_1 and cyano vibration shifts between the radical anionic and neutral molecules for molecules with a CP core (patterns (3) and (4)). d) Relationship between EA_1 and cyano vibration shifts between the radical anionic and neutral molecules for molecules with a CHD core (pattern (2)).	47

3.6	Impact of molecular factors on EAs. a) Role of through-phenyl-substitution on the EA_1 and EA_2 of molecules with a CP core. Note that to supplement the comparison $(CF_3)_6-CP$ and $(PhCF_3)_6-CP$ were added despite not being part of patterns (3) or (4). b) Role of the core type on EA_1 and EA_2 for molecules with a phenyl group. The dashed line represents the identity line, i.e. where the points would lie if molecules with the same substituents but different cores had identical EAs.	50
4.1	Chemical structures of p-dopants discussed in this work; additional structures are depicted in Figure B.1.	62
4.2	Isosurface plots of the exposed and shielded LUMOs of $(CN)_6-CP$ (left) and $PFP3CN3-CP$ (right), respectively; the average twisting angle of the PFP rings is 36.1°	63
4.3	UV-vis/NIR absorption spectra of dropcast P3HT films doped with increasing molar ratios of $PFP3CN3-CP$. Data obtained under identical conditions as in (a). P1 and P2 indicate optical transitions assigned to the positive polaron in P3HT. [5–8] Stars mark transitions assigned to the $PFP3CN3-CP$ radical anions ($PFP3CN3-CP^{\cdot-}$; see Refs. [3, 5] and Figure B.12, respectively). Transitions of neutral $PFP3CN3-CP$ are assigned by supporting DFT calculations (Figure B.7).	65
4.4	Conductivity of P3HT films doped with F_4-TCNQ , F_2-TCNQ , and $PFP3CN3-CP$ versus the molar doping ratio (%); F_4-TCNQ and F_2-TCNQ data taken from our own previous study [5] and obtained under identical conditions as the $PFP3CN3-CP$ data.	67
5.1	The σ and π radical dimerization modes for $TMCN3-CP$ and $DMCN4-CP$ respectively; $R=CO_2Me$. The figure has been edited and adapted from: Hasan, F., Gillen, J. H., Jayaweera, A. T., McDearmon Jr., W. D., Winter, A. H., Bejger, C. M. (2023).[9] The σ dimerization mode forms through a single covalent bond.	70
5.2	^{19}F NMR spectrum of $PFP3CN3-CP$ in acetonitrile (dilute (3 g/l) and concentrated (30 g/l)) and toluene (concentrated (30 g/l)). The star signs relate to monomers, and the circle signs rise from dimers in high concentrations.	73
5.3	Three different possible dimer conformations for $PFP3CN3-CP$ based on our DFT calculations, and their corresponding schematics; $R=PFP$. The average PFP ring rotation angle and the dihedral angles between CN and the core are $(41^\circ, 9^\circ)$, $(47^\circ, 1.9^\circ)$, and $(45^\circ, 1.3^\circ)$ respectively for (a), (b), and (c) in the gas phase.	74
5.4	Powder X-ray Diffraction (PXRD) pattern of $PFP3CN3-CP$ showing the intensity (in arbitrary units) as a function of the scattering vector q_z (corresponding to specific d-spacings)	75

A.1	Experimental against computational EA_1 for selected molecules. The slope (0.97) and intercept (1.13) of the linear fit have been used to calculate $EA_1^{pred.}$ in the main text.	96
A.2	Example conformations of $(Ph)_8\text{-CHD}$	97
A.3	Example of a) boat and b) chair conformations for neutral $(SO_2F)_4\text{-TCNQ}$ molecule.	98
A.4	Conformations of $(PhSO_2CF_3)_4\text{-TCNQ}$. Panel a) is the lowest energy conformation.	99
A.5	Impact of the Hammett index on a) EA_1 and b) EA_2 of molecules following substitution patterns (1) and (5).	102
A.6	Impact of the Hammett index on a) EA_1 and b) EA_2 of molecules following substitution pattern (2).	102
A.7	Impact of the Hammett index on a) EA_1 and b) EA_2 of molecules following substitution patterns (3) and (6).	103
A.8	Impact of the Hammett index on a) EA_1 and b) EA_2 of molecules following substitution patterns (4) and (7).	103
A.9	Impact of the partial atomic charges of core atoms on EAs of molecules following substitution patterns (1) and (5). a) Impact of the charge in neutral molecules on EA_1 . b) Impact of the charge in radical anionic atoms on EA_2	105
A.10	Impact of the partial atomic charges of core atoms on EAs of molecules following substitution patterns (3) and (6). a) Impact of the charge in neutral molecules on EA_1 . b) Impact of the charge in radical anionic atoms on EA_2	105
A.11	Impact of the partial atomic charges of core atoms on EAs of molecules following substitution patterns (2). a) Impact of the charge in neutral molecules on EA_1 . b) Impact of the charge in radical anionic atoms on EA_2	106
A.12	Impact of the partial atomic charges of core atoms on EAs of molecules following substitution patterns (4) and (7). a) Impact of the charge in neutral molecules on EA_1 . b) Impact of the charge in radical anionic atoms on EA_2	106
A.13	Standard deviation of the linear fits against their coefficient of determination R^2 , to quantify how much this non-linearity leads to an error in the correspondence between cyano vibration wavenumber and the molecular charge when assuming a linear fit.	113
A.14	Impact of phenyl groups on the EAs of molecules with a CHD core. a) For EA_1 , no clear trend is visible due to core bending of the neutral molecules when the substituents are attached directly to the CHD core. b) For EA_2 , a trend emerges as discussed in the main text, due to the fact that much of the physical reorganization of the CHD cores has already occurred during their first ionization.	114
A.15	Impact of the core on the EAs of molecules without phenyl groups; patterns (1), (5), (3), and (6).	115

B.1	Chemical structures in addition to those shown in Figure 4.11 of the main text.	117
B.2	a) $LUMO_{\text{neutral}} - EA$ b) $HOMO_{\text{charged}} - EA$ c) $LUMO_{\text{neutral}} - HOMO_{\text{charged}}$ d) EA e) Band gap for $TMCN3 - CP$, $PFP3CN3 - CP$, $(CN)_6 - CP$, $TCNQ$, $FTCNQ$, $F_2 - TCNQ$, and $F_4 - TCNQ$ molecules f) Level position of $(CN)_6 - CP$, all as a function of ω . Charged refers to the radical anion.	120
B.3	Computational versus experimental electron affinity at different ω values for $PFP3CN3 - CP$, $(CN)_6 - CP$, $TCNQ$, $FTCNQ$, $F_2 - TCNQ$, $F_4 - TCNQ$ a) with and b) without $TMCN3 - CP$ included in the fit.	121
B.4	Difference of computational and experimental electron affinity (EA) for $TMCN3 - CP$, $PFP3CN3 - CP$, $(CN)_6 - CP$, $TCNQ$, $FTCNQ$, $F_2 - TCNQ$, $F_4 - TCNQ$ molecules as a function of ω	122
B.5	Spread of the error as a function of ω for $PFP3CN3 - CP$, $(CN)_6 - CP$, $TCNQ$, $FTCNQ$, $F_2 - TCNQ$, and $F_4 - TCNQ$ molecules: (a) With $TMCN3 - CP$ (b) Without $TMCN3 - CP$	123
B.6	Schematic of the ring twisting angle, which is defined as the angle between the vector normal to the plane of the PFP ring and the vector normal to the plane of the CP core; values for neutral molecules given in Table B.2.	124
B.7	DFT calculated UV-vis/NIR spectra of neutral $F_2 - TCNQ$ (left) and $PFP3CN3 - CP$ (right). Spectra were calculated using 25 singlet and 25 triplet excited states and were obtained using the default broadening in the software package Gaussian [10] (which assumes a Gaussian peak shape with $\sigma = 0.4$ eV).	125
B.8	High resolution mass spectra (HRMS) of $PFP3CN3 - CP$	127
B.9	^{19}F NMR spectrum of $PFP3CN3 - CP$	128
B.10	Fourier-transform infrared spectroscopy of a dropcast $PFP3CN3 - CP$ film; peak assignment of the highlighted vibrations (based on DFT calculations): 2218 (w) cm^{-1} and 2203 (w) cm^{-1} : cyano stretch, 1813 (m) cm^{-1} symmet- ric cyclopropane ring stretch, 1654 (m) cm^{-1} : PFP ring stretch, 1524 (vs) cm^{-1} and 1502 (vs) cm^{-1} : pentafluoro phenyl ring twist, 997 (s) cm^{-1} : cy- clopropane ring vibration.	129
B.11	Cyclic voltammograms of $F_4 - TCNQ$ and $F_2 - TCNQ$ in 0.1 M $n\text{-Bu}_4\text{NPF}_6$ acetonitrile solution using 50 mV/s scan rate referenced to ferrocene, and of $PFP3CN3 - CP$ in 0.1 M $n\text{-Bu}_4\text{NPF}_6$ dichloromethane solution using 100 mV/s scan rate; $E_{\text{pa},i}$ and $E_{\text{pc},i}$ depict the anodic and cathodic peak potentials.	130
B.12	Evolution of absorbance spectra of $PFP3CN3 - CP$ (0.8 g/L) upon increas- ing titration (T1 . . . T10) with KI (0.35 g/L) in acetonitrile solution. Tran- sitions assigned to the $PFP3CN3 - CP$ radical anion are highlighted in red, those of the neutral species in blue. Transitions assigned to the neutral $PFP3CN3 - CP$ are at 2.59 , 2.77 , and 3.95 eV, those of the dopant radical anion $PFP3CN3 - CP^{\cdot-}$ arise at 1.93 , 2.13 eV and at 3.71 eV.	131

B.13 UV-vis/NIR absorbance spectra of P3HT films doped with increasing molar ratios of and <i>PFP3CN3-CP</i> , spin-coated from common solution. Spectra are normalized to common thickness as individually determined by AFM; the results fully agree with the findings for dropcast films reported in the main text (Figure 4.3b).	132
B.14 UV-vis/NIR absorbance spectra of dropcast pure <i>PFP3CN3-CP</i> , pure h10T, and h10T films blended with <i>F₂-TCNQ</i> and <i>PFP3CN3-CP</i> at a molar ratio of 67%. For <i>F₂-TCNQ</i> , the characteristic transitions of the CPX are observed, while no sub-gap features are found for <i>PFP3CN3-CP</i> , indicating suppressed CPX formation for the latter.	133
B.17 GIXRD reciprocal space maps of dropcast films of pure P3HT (a) and films doped with <i>PFP3CN3-CP</i> at increasing dopant molar ratios of 1%, 2%, 5%, 9%, and 17% (b-f). q_z , q_{xy} are the out-of-plane and in-plane components of the scattering vector q , respectively; colors correspond to intensities on a logarithmic scale. (100), (200), and (300) indicate the lamellar spacing of the P3HT chains, while (020) stems from their $\pi-\pi$ backbone stacking.	137
B.18 GIXRD intensities radially integrated along constant values of the scattering vector $q = q = \sqrt{q_{xy}^2 + q_z^2}$ of the data shown in Figure B.17; data is shown in the range around (a) the peak corresponding to the (100) P3HT lamellar stacking and (b) that corresponding to the (020) $\pi-\pi$ stacking distance of P3HT; positions of the pristine P3HT film are marked by vertical lines. The <i>PFP3CN3-CP</i> percentages are mentioned in the figure.	138

List of Tables

3.1	Substituents and molecular nomenclature employed for molecules with the same number of cyano groups and substituents (Figures 3.2a-d). The first two columns refer to the substituents used and their Hammett index, calculated from values found in Ref. [11], except when specified otherwise. The four other columns contain the names of the molecules either with a CHD or CP core, both when substituents are connected directly to the core (substitution patterns (1) and (3)) or through phenyl groups (substitution patterns (2) and (4)). Note that we did not include the two molecules from Ref. [12] in this table, as molecules with a very analogous substituent ((CO ₂ CH ₃) ₃ (CN) ₃ -CP) are already listed. N/A indicates molecules that have not been studied – the three phenyl-containing substituents (<i>Ph</i> , <i>F₅-Ph</i> , <i>F₄CN-Ph</i>) were not considered on a bridging phenyl group, as discussed in the Methodology, and the two monoatomic substituents (<i>F</i> , <i>H</i>) are provided as reference, because <i>TCNQ</i> and <i>F₄-TCNQ</i> are experimentally well studied dopants.	40
3.2	Substituents and molecular nomenclature employed for molecules with only substituents and no cyano groups (Figures 3.2e-g). The table follows the same idea as Table 3.1 but all molecules follow patterns (5), (6) or (7). The Hammett indices of the last six substituents (<i>PhF</i> to <i>PhOH</i>) are the same as if connected directly to the core (Table 3.1); N/A indicates molecules that have not been studied due to the excessive number of possible configurations as discussed in Figure A.2.	43
3.3	Selected molecules of interest for the discussion of EAs and steric shielding. Relevant experimentally-characterized species were added for comparison; $EA_1^{pred.}$ values were calculated as described in the Methodology section, all energies are given in eV. The color scale reflects the $EA_1^{pred.}$ values with a minimum of 4.14 eV (B) in red, the range of “strong” molecular p-dopants starting around the $EA_1^{pred.}$ value of <i>F₄-TCNQ</i> (N) (5.30 eV) in yellow, and the highest derived value of 7.51 eV (I) in green.	52
4.1	Comparison of DFT-calculated <i>EA</i> values (EA_{calc}) with experimental (EA_{exp}) and predicted experimental values (EA_{pred}).	63

A.1	Molecular descriptors of patterns (1) and (5). EA_1 and EA_2 are provided in eV, AIM represents the sum of partial atomic charges on core atoms calculated from the quantum theory of atoms in molecules for neutral ($AIM_{(0,1)}$) and radical anionic ($AIM_{(-1,2)}$) molecules, the charge is given in fraction of the elementary charge e	100
A.2	Molecular descriptors of pattern (2). Content follows Table A.1.	100
A.3	Molecular descriptors of patterns (3) and (6). Content follows Table A.1.	101
A.4	Molecular descriptors patterns (4) and (7). Content follows Table A.1.	101
A.5	Linear fit parameter (slope, intercept, and R^2 values) of the EAs against the Hammett index. Patterns (1) and (5) are CHDs without phenyl, patterns (3) and (6) are CPs without phenyl, patterns (4) and (7) are CPs with phenyl, pattern (2) is CHDs with phenyl. The standard errors of the parameters are reported as \pm values.	104
A.6	Linear fit parameters (slope, intercept, and R^2 values) of the EAs against the sum of partial atomic charges of core atoms. Patterns (1) and (5) are CHDs without phenyl, patterns (3) and (6) are CPs without phenyl, patterns (4) and (7) are CPs with phenyl, pattern (2) is CHDs with phenyl. The standard errors of the parameters are reported as \pm	107
A.7	Highest-energy cyano vibrational mode of molecules following substitution patterns (1) and (5). Energy is given in wavenumber (cm^{-1}). Where applicable, the vibration that belongs to isolated cyano groups and not to cyano groups on substituents were selected. (0,1) represents neutral molecules, (-1,2) represents radical anionic molecules, and (-2,1) represents dianionic molecules. The energies of the cyano vibrations were scaled according to the precomputed vibrational scaling factors from the Computational Chemistry Comparison and Benchmark Database (CCCBDB) corresponding to our model chemistry. [13] N/A indicates molecules that have no cyano groups.	108
A.8	Highest-energy cyano vibrational mode of molecules following substitution pattern (2). Content follows Table A.7.	109
A.9	Highest-energy cyano vibrational mode of molecules following substitution pattern (3) and (6). Content follows Table A.7.	109
A.10	Highest-energy cyano vibrational mode of molecules following substitution pattern (4) and (7). Content follows Table A.7.	110
A.11	Results of first and second order fits to the position of CN vibrations against the molecular charge for patterns (1) and (5). The number in parentheses identifies the order of the fit to which parameters belong. N/A indicates molecules that have no cyano groups.	111
A.12	Results of first and second order fits to the position of CN vibrations against the molecular charge for pattern (2). Content follows Table A.11.	111
A.13	Results of first and second order fits to the position of CN vibrations against the molecular charge for patterns (3) and (6). Content follows Table A.11.	112

A.14	Results of first and second order fits to the position of CN vibrations against the molecular charge for patterns (4) and (7). Content follows Table A.11.	112
A.15	Linear fit parameters (intercept, slope, and R^2 values) of the EAs of molecules with phenyl groups against those of molecules without. Slopes smaller than 1 indicate that the connection of substituents via a phenyl group decreases their electronic impact, while the intercept reflects the impact of the phenyl itself.	114
A.16	Linear fit parameters (intercept, slope, and R^2 values) of the EAs of molecules with a CHD core (patterns (1), (2) and (5)) against those with a CP core ((3), (4), (6) and (7)).	115
B.1	Linear fit parameters of computational versus experimental electron affinities (as plotted in Figure B.3) with different ω values	122
B.2	The DFT calculated Highest Occupied Molecular Orbital (HOMO) energies, the Lowest Unoccupied Molecular Orbital (LUMO) energies, total energy of neutral and charged molecules (radical anion), EA_{calc} and EA_{pred} (see main text), and the average ring-twisting angles for neutral molecules ($^\circ$).	125
B.3	Reduction potentials from cyclic voltammetry experiments and the derived LUMO energies of $F_4\text{-TCNQ}$, $F_2\text{-TCNQ}$ and $PFP3CN3\text{-CP}$	130

List of Associated Works

[14] **Doping-Related Broadening of the Density of States Governs Integer-Charge Transfer in P3HT**

H. Hase, M. Berteau-Rainville, S. Charoughchi, E. Orgiu, and I. Salzmann
Applied Physics Letters, vol. 118, no. 20, p. 203301, May 2021.

I was involved in cyclic voltammetry measurements on poly(3-hexylthiophene-2,5-diyl), tetrafluorotetracyanoquinodimethane (F4TCNQ) and its derivatives (F2TCNQ, FTCNQ, TCNQ).

[5] **Critical Dopant Concentrations Govern Integer and Fractional Charge-Transfer Phases in Doped P3HT**

H. Hase, M. Berteau-Rainville, S. Charoughchi, W. Bodlos, E. Orgiu, and I. Salzmann
Journal of Physics: Materials, vol. 6, no. 1, p. 014004, Jan. 2023.

I was involved in cyclic voltammetry measurements on poly(3-hexylthiophene-2,5-diyl), tetrafluorotetracyanoquinodimethane (F4TCNQ) and its derivatives (F2TCNQ, FTCNQ, TCNQ).

[15] **Sterically-Hindered Molecular p-Dopants Promote Integer Charge Transfer in Organic Semiconductors**

S. Charoughchi, J. T. Liu, M. Berteau-Rainville, H. Hase, M. S. Askari, S. Bhagat, P. Forgione, and I. Salzmann
Angewandte Chemie International Edition, vol. 62, no. 31, p. e202304964, Aug. 2023.

It is chapter 4.

Design Strategies for Optimized Molecular p-Dopants: Decoupling Electronic and Geometric Effects

M. Berteau-Rainville, S. Charoughchi, E. Orgiu, and I. Salzmann

MBR and SC contributed equally. This manuscript is submitted in *Physical Review Materials*. It is chapter 3.

Reversible Dimerization of the PFP3CN3-CP

S. Charoughchi, M. Berteau-Rainville, M. Arhangelskis, and . Salzmann

This manuscript is in progress. It is chapter 5.

Chapter 1

Fundamentals of a Doping Organic Semiconductors

In this chapter, first, an introduction to the fundamentals of conjugated molecular orbitals is provided in section 1.1. The following section 1.2 provides the comparison of organic and inorganic semiconductors. The next section 1.3 covers the fundamentals of the two known p-doping mechanisms, that is, integer charge transfer (ICT) and ground state charge complex formation (CPX). Moving forward, section 1.4 presents some common p-dopants in literature that are most prominently addressed throughout this thesis, and also introduces the background and previous work on cyclopropane-based p-dopants. Section 1.5 ventures into a discussion of open questions and potential issues in the doping mechanism, addressing challenges that may arise. Subsequently, Section 1.6 outlines the objectives underlying the thesis and delineates strategies to overcome challenges. Lastly, Section 1.7, outlines the structure of the subsequent chapters, offering guidance to the reader's journey through the thesis.

1.1 Conjugated Molecules and organic semiconductors

Organic semiconductors (OSC) are materials formed by small conjugated organic molecules (COMs) or conjugated polymers (COPs); mainly formed by carbon and hydrogen atoms, with some heteroatoms such as sulfur, oxygen, and nitrogen included, that exhibit a delocalized π -electron system due to carbon sp^2 -hybridization. In a semiconductor, the highest occupied electron energy (HOMO) level is separated from the lowest unoccupied energy (LUMO) level by an energy gap, referred to as fundamental gap of the OSC. For OSCs, it has typical values of 2-3 eV (i.e., it lies in the visible region), which is thus (at least) twice as wide as that of inorganic semiconductors (ISC) such as Si (1.1 eV). This entails the absorption and emission of light within the visible spectral range, along with a level of conductivity adequate for operating traditional semiconductor devices such as light-emitting diodes (LEDs), solar cells, and field-effect transistors (FETs). It is important to note that while they possess semiconducting properties, the "semiconducting" nature varies significantly between inorganic and organic materials.

[1]

In carbon's ground state, its atomic configuration consists of $1s^2 2s^2 2p_x^1 2p_y^1$. In this arrangement, carbon can only form two covalent bonds. However, by rearranging its electrons so that one of the $2s$ electrons occupies the vacant $2p_z$ orbital, carbon can form four covalent bonds. [1] The energy gained from establishing these four bonds surpasses the energy required to transition an electron from the $2s$ orbital to the $2p_z$ orbital. When other atoms, such as hydrogen or another carbon, approach as binding partners, external forces come into play to offset the energy gap between the $2s$ and $2p$ orbitals, effectively making them equal in energy, or degenerate. Consequently, new hybrid orbitals formed by interference between the $2s$ with one, two, or three $2p$ orbitals; leading to sp , sp^2 , and sp^3 , respectively. The origin of hybridization can be understood by considering the four atomic orbitals centered on a nucleus as waves that interfere destructively and constructively in different regions, resulting in the formation of four new shapes.[1, 16]

In OSCs generally, each carbon atom possesses three sp^2 hybrid orbitals arranged in a plane and one $2p_z$ orbital perpendicular to this plane. While the sp^2 orbitals result in three σ -bonds, the electron in the $2p_z$ orbital of one carbon atom pairs with the electron in the $2p_z$ orbital of the other atom, and as a consequence, the electrons exhibit spatial probability density both above and below the molecular axis, giving rise to a molecular orbital known as a π -orbital. This shared pair of electrons corresponds to a π -bond. [1]

To comprehend the energy distribution of molecular orbitals, the interaction among various atomic orbitals can be analyzed. The $1s$ orbitals, situated near the core, generate a bonding (σ) and an antibonding (σ^*) orbital with minimal energy splitting (Figure 1.1). The interaction of the $2sp^2$ hybrid orbitals produces strong bonding (σ) and antibonding (σ^*) orbitals, characterized by significant charge overlap between the nuclei. However, the interaction of the $2p_z$ orbitals occurs at a distance from the nuclei, resulting in a weaker splitting between the bonding (π) and antibonding (π^*) orbitals. [1]

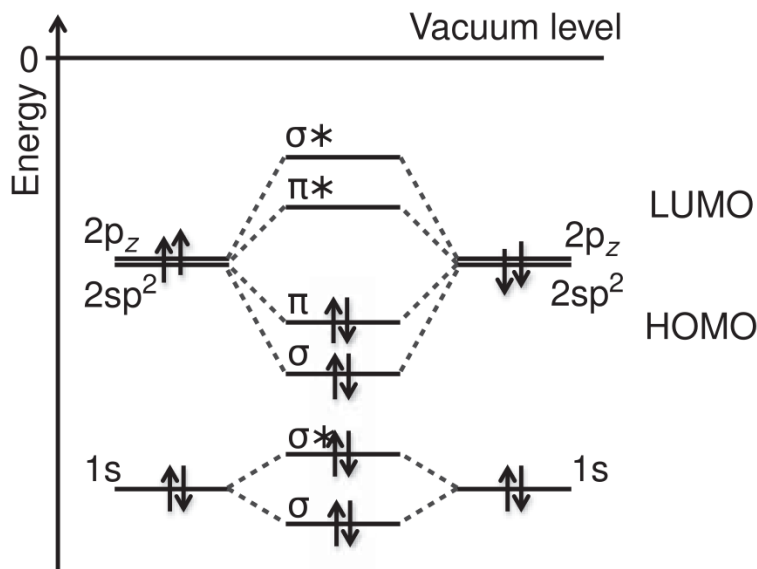


Figure 1.1: Schematic energy level diagram of σ - and π -bonds forming from atomic orbitals between the carbon atoms in ethene (i.e. the two $2sp^2$ -orbitals forming σ -bonds with the hydrogen atoms are omitted). Figure adapted from [1] A. Köhler and H. Bässler, *Electronic Processes in Organic Semiconductors: An Introduction*. Weinheim: Wiley-VCH, 2015. Copyright 2015 Wiley-VCH Verlag GmbH & Co. KGaA.

Since the block of filled orbitals ends with the Highest Occupied Molecular Orbital (HOMO) and the sequence of unfilled ones starts with the Lowest Unoccupied Molecular Orbital (LUMO), are collectively termed *frontier molecular orbitals*. These orbitals play a pivotal role in the optical and electrical processes of the molecule if employed as an OSC, e.g., in an optoelectronic device. When an electron is introduced into a molecule from an electrode, it occupies the vacant molecular orbital with the lowest binding energy, which is the LUMO. Conversely, the introduction of a hole involves removing an electron from the highest occupied molecular orbital, the HOMO, and transferring it to the electrode. [1]

Due to significant resonance interaction, σ and σ^* orbitals are positioned at relatively low and high electron energies with respect to vacuum level, respectively, making charge injection from electrodes into molecular solids particularly challenging. In contrast, when the frontier orbitals are comprised of π -orbitals, their moderate degree of splitting results in a moderate energy difference compared to the typical electrode work function. [1, 17]

In a similar scenario, light absorption occurs by promoting an electron from the HOMO to the LUMO. When the frontier orbitals are σ -orbitals, the ($\sigma \rightarrow \sigma^*$) transition happens in the ultraviolet spectral range, whereas the lower splitting associated with π -orbitals allows $\pi \rightarrow \pi^*$ transitions to occur in the visible spectral range, especially for large π -orbitals that extend over several carbon atoms. [1]

The common characterization techniques for experimentally determining the HOMO and LUMO energies of COMs/CPs are cyclic voltammetry (CV), photoelectron spec-

troscopy (UPS), and inverse photoelectron spectroscopy (IPES). They have their limitations which are discussed below.

The primary drawback of CV—a technique based on varying the potential of a working electrode while recording the resulting current—stems from the challenge of solvating radical ions generated within the polar solvent as typically used. As the polarity of the solvent increases, so does the polarization energy of the ions, leading to a systematic error of 100 meV in HOMO and LUMO values. Additionally, a common issue arises in determining both oxidation and reduction potentials. Due to the constraints of the potential "window" determined by the specific electrode/electrolyte combination, often only one of the potentials—either oxidation or reduction—can be accurately measured. This limitation arises from the fact that the energy gap between the HOMO and LUMO levels, represented by the difference $E_{ox} - E_{red}$, can be substantial, typically around 2.5 to 3.0 eV. This leads to the common fact that one of the potentials, typically the reduction potential, may fall outside the experimentally accessible range. [1] The technical introduction to CV setup is in section 2.3

In turn, photoelectron spectroscopy measures the kinetic energy of photoelectrons which are usually emitted from a few nanometers below the surface, and is constrained in its ability to largely provide insights into material surfaces only.

In this thesis, CV has been used for determining the IE and EA of the molecules; note that their values are given on a positive binding energy scale throughout this work.

A *conjugated system* forms where the molecular structure exhibits alternating single and multiple bonds, with 'conjugation' referring to the interaction between p-orbitals across the σ -bond positioned between the multiple bonds. [18] The planarity of a conjugated polymer segment or conjugated oligomer molecule is crucial for the extent of coherent π -electron delocalization, termed as *conjugation length*, which significantly influences intra- and intermolecular charge transport due to the lower binding energy of π -electrons compared to σ -electrons. [1] The conjugation length also plays an important role in optical properties, as wider conjugated systems result in lower-energy transitions, impacting optical absorption and emission. [1] However, coherence in π -electron delocalization can be compromised in CPs due to conformational variations arising from solvent interaction and solid-state deposition, as well as torsional disorder along the polymer chain, chemical defects, and phonon scattering. [1]

Spectroscopically, a CP can be approximated by oligomers with a number of repeat units equivalent to the CP's conjugation length. For polythiophenes, like those employed in this thesis, the conjugation length in a completely planar configuration in the solid state can surpass 20 units. [1] This thesis focuses on poly(3-hexylthiophene-2,5-diyl) (P3HT) compared to a custom-synthesized oligomer; 3,3''''',3''''',3''''',3''''',4',4'',4'''-octahexyl 2,2':5',2'':5'',2''':5''',2''':5''', 2''''':5''''',2''''':5''''',2''''':5''''', 2''''''':5''''''',2''''''':5'''''''-decithiophene (h10T).

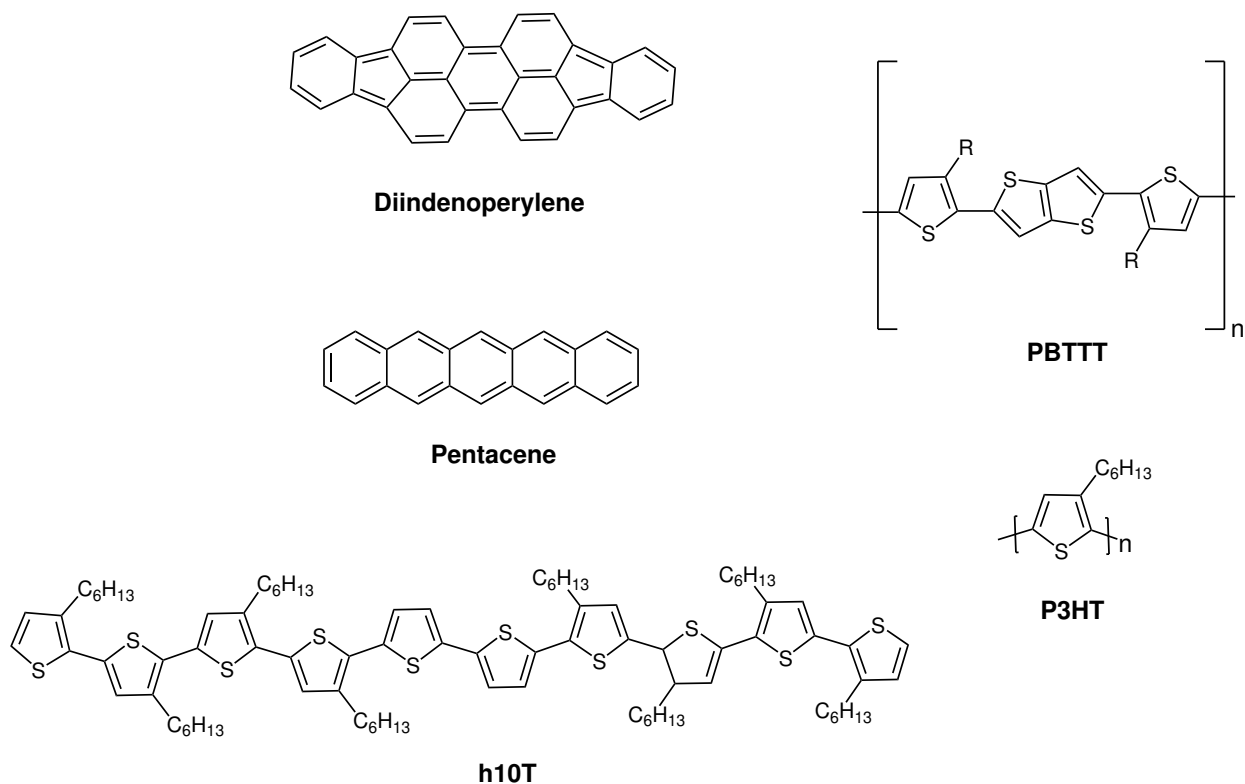


Figure 1.2: Chemical structures of some conjugated polymers (CPs) and conjugated organic molecules (COMs).

1.2 Organic *versus* Inorganic Semiconductors

The most distinguishing feature of organic semiconductors is the intermolecular van der Waals interactions. This stands in contrast to inorganic materials composed of chemically bonded atomic species, as outlined in standard textbooks on solid-state physics, e.g., by Ashcroft and Mermin (1976). [19] Chemical bonds in inorganic semiconductors (ISC) are covalent, involving the sharing of electrons between atoms within the semiconductor (as observed in Si and Ge), or primarily ionic, arising from Coulombic attraction between anion/cation atomic pairs (as seen in CdTe, ZnSe, etc.). In certain semiconductor alloys, bonding is achieved through a combination of both covalent and ionic bonds, as exemplified by InP, GaAs, GaN, and TiP. [17] Specifically, covalent bonds, such as those present in silicon, are relatively strong (78 kcal mol^{-1} in Si), in contrast to van der Waals interactions, which are weaker (approximately 10 kcal mol^{-1}). [20]

Traditional ISCs like silicon, germanium, and GaAs possess narrow band gaps (as defined as the energy difference between valence and conduction band), for example, 0.67 eV (Ge), 1.1 eV (Si), or 1.4 eV (GaAs). At room temperature, the generation of free charges occurs through thermal excitation from the valence band to the conduction band, and the concentration of charge carriers is given by $N = N_{\text{eff}} e^{-\frac{E_g}{2kT}}$, where N_{eff} represents the effec-

tive density of valence or conduction band states, E_g is the band gap, k is the Boltzmann constant, and T is the temperature. The intrinsic conductivities typically fall within the range of approximately 10^{-8} to $10^{-2} \Omega^{-1} \text{cm}^{-1}$ at room temperature. [1] Moreover, the dielectric constant in ISCs is substantial, reaching up to $\epsilon_r = 11$. This large dielectric constant ensures that Coulomb effects between electrons e^- and holes h^+ are negligible due to strong dielectric screening already on a small length scale. Thus, at room temperature, light absorption can easily lead to the immediate creation of free electrons and holes.

In contrast, the conductivity of organic "semiconductors" is extrinsic and arises from the injection of charges at electrodes, doping, and the dissociation of photogenerated electron-hole pairs bound by their mutual Coulomb attraction. This stems from two distinctive characteristics of conjugated organic materials. Firstly, absorption and emission often occur in the 2–3 eV range (approximately 600–400 nm) which corresponds to the magnitude of their fundamental energy gap between HOMO and LUMO, making it impossible to establish a significant charge-carrier concentration through thermal excitation at room temperature. Additionally, the low dielectric constant, approximately $\epsilon_r = 3.5$, signifies substantial Coulomb interactions. As a result, any electron-hole pair created by optical excitation is bound by a Coulomb energy which is typically significant (around 0.5–1.0 eV) and far beyond the thermal energy at room temperature. [1, 17]

As mentioned earlier, the weak van der Waals interactions impart soft mechanical characteristics to molecular solids and polymers, thereby creating extensive opportunities for applications that are not accessible to conventional ISCs. For instance, organic solids exhibit flexibility, whereas ISCs are frequently characterized by hardness, brittleness, and susceptibility to fracture. Despite being soft and prone to damage through handling, organic materials also possess the ability to bend, conform to various irregularly shaped surfaces, and even be folded without experiencing cracking, [17] as exploited in today's flexible electronics (smartphones with foldable displays etc.)

The relatively low intermolecular binding energy in OSCs translates in a comparatively low temperature for dissociating the molecules from the solid (around 100–500°C). However, most ISCs undergo thermal decomposition only at temperatures double to triple the highest temperatures tolerated by organic solids. [17]

Moreover, a broad array of organic (macro-) molecules, when appropriately synthesized and/or functionalized, can be dissolved in suitable solvents. Consequently, they can be capable of solution-processing methods. [20] The processability from a solution opens up the opportunity to evolve organic electronics into printed electronics. [21, 22]

The "tunable properties" of OSCs pertain to the ease with which a material or structural composition can be altered to fulfill specific requirements of the target application. The extensive adaptability in properties achieved through the synthesis of precisely designed organic compounds to meet application needs is a genuinely unique advantage of OSCs exploited in organic electronics. This field is built upon the exceptional versatility offered by organic chemistry. [17]

In ISCs, the Density of States (DOS), which is the number of states per interval of energy at each energy level that can be occupied by electrons, exhibits in good approximation a parabolic distribution at the band edges, and in the band gap, it drops to zero. [23, 24] In contrast, in OSCs the DOS has an exponential distribution in the band edges and Gaussian DOS is used for modeling the electronic state distribution. [25, 26]

In conclusion, OSC-based electronics do typically not aim to *generally* compete with today's high-performance electronics based on ISCs but strive to exploit the fact that OSCs are lightweight, flexible materials compatible with large-area processing on flexible substrates and allow for low-temperature device manufacturing techniques. [1, 17, 20]

1.3 Organic Semiconductor Doping Mechanisms

The principle underlying doping involves the addition of electron donors or acceptors to COMs or CPs, thereby generating additional mobile charge carriers. In OSCs, achieving n-type doping requires the dopant to donate electrons to the LUMO states of the OSCs, while p-type dopants extract electrons from the HOMO states, thus creating holes in OSCs. (Figure 1.3)

In the last three decades, the field of organic electronics emerged from the finding that conjugated polymers such as polyacetylene can be electrically doped to increase their conductivity by more than ten orders of magnitude. At this time, doping has been done analogously to ISCs by the admixture of inorganic dopants such as bromide, iodide, or chlorine to extract an electron from the polymer valence band (referred to as p-type doping) or sodium, lithium, and potassium to inject an electron into the polymer conduction band (n-type doping). [27–30] However, in contrast to ISCs, this doping strategy proved unable to provide stable p-/n-doped layers. These inorganic dopants are not covalently bonded to the semiconductor host and, therefore, readily diffuse throughout the semiconductor layer(s). [3, 31]

In the late 1990s, molecular dopants as organic acceptors and donor molecules were introduced to remedy these issues, which finally led to the breakthrough of doping OSCs in practical applications. Today, essentially all organic electronic devices such as organic light-emitting diodes (OLEDs) based displays [32, 33], organic photovoltaic devices (OPVCs)[32, 33], or organic field-effect transistors (OFETs) comprise OSC layers doped with molecular dopants. [34] Molecular doping is there used to tune both conductivity and the electronic properties at interfaces with electrodes [32, 35] in order to reduce charge injection barriers in OLEDs [34] and charge trap densities and depths, [36–39] as well as generating mobile holes in the host material to increase its conductivity by orders of magnitude. [40, 41]

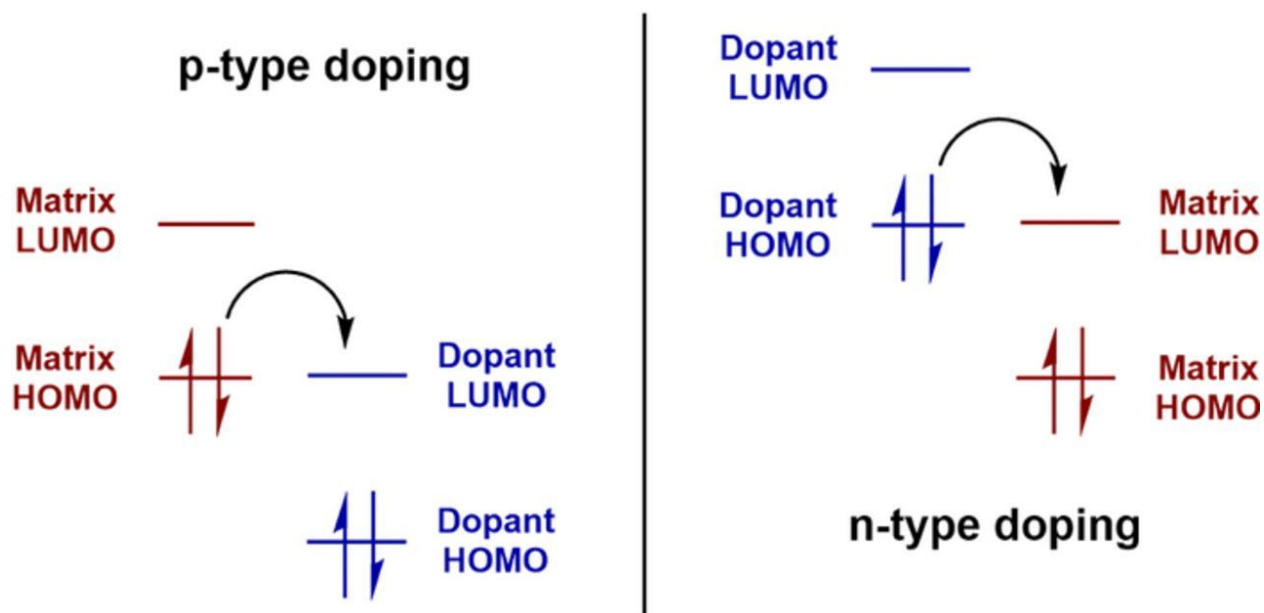


Figure 1.3: p-type and n-type doping of the organic semiconductor. Figure has adapted from [2] L. M. Cowen, J. Atoyo, M. J. Carnie, D. Baran, and B. C. Schroeder, “Review—organic materials for thermoelectric energy generation,” *ECS Journal of Solid State Science and Technology*, vol. 6, no. 3, p. N3080, Jan 2017. Published 2017 by ECS under CC BY 4.0.

One of the two fundamental mechanisms for doping OSC is integer charge transfer (ICT), where immediate charge transfers from the HOMO of OSC to the LUMO of the p-dopant (and vice versa for n-type doping) occur. As a result, a localized electron is stabilized on the dopant, and a mobile hole is generated in the OSC matrix. The spectroscopic confirmation of this phenomenon has been documented in various OSCs, as indicated by the observation of diagnostic ion absorption features in both the visible (related to electronic transitions) and the infrared (associated with vibrations) spectral regions. [6, 42] Regarding p-type doping, the fundamental prerequisite for ICT is that the EA of the p-dopant must equal or exceed the IE of the OSC in question. [42–45]

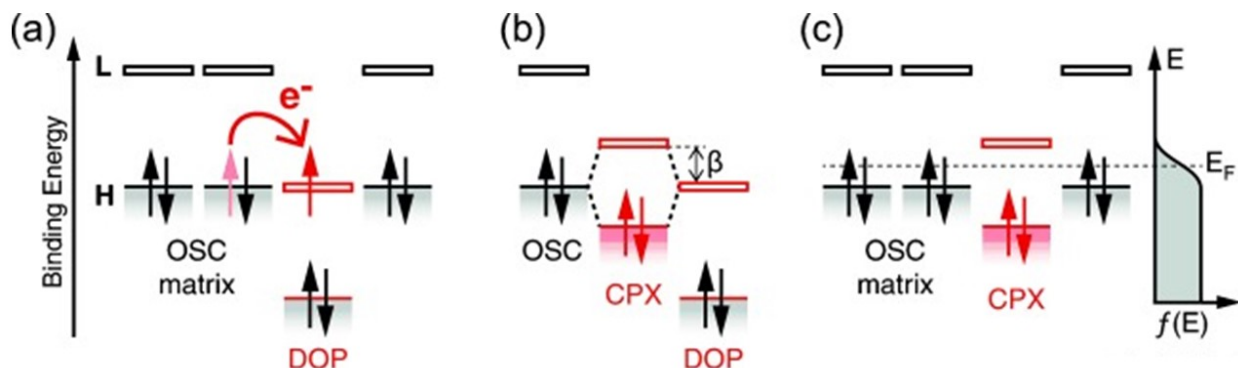


Figure 1.4: a) ICT upon integer charge transfer from the HOMO (H) of the OSC to the LUMO (L) of the p-dopant (DOP) leads to ionized molecules. b) Alternative model assuming the hybridization of the frontier molecular orbitals of the OSC and the p-dopant in a supramolecular ground-state charge transfer complex (CPX); β denotes the resonance integral. c) Complexes within the OSC matrix: within the OSC matrix, complexes exhibit low-lying unoccupied states in the OSC gap, which are being occupied according to the Fermi–Dirac distribution ($f(E)$); shaded/white boxes denote HOMO/LUMO levels. The figure has adapted from [3] H. Mendez, G. Heimel, A. Opitz, K. Sauer, P. Barkowski, M. Oehzelt, J. Soeda, T. Okamoto, J. Takeya, J.-B. Arlin, J.-Y. Balandier, Y. Geerts, N. Koch, and I. Salzmann, “Doping of Organic Semiconductors: Impact of Dopant Strength and Electronic Coupling,” *Angewandte Chemie International Edition*, vol. 52, no. 30, pp. 7751–7755, Jul. 2013. Copyright 2013 WILEY-VCH Verlag GmbH Co. KGaA, Weinheim

The second fundamental doping mechanism is the formation of ground-state charge transfer complexes (CPXs) where frontier molecular orbital hybridization between the HOMO of OSC and LUMO of the dopant occurs instead. (1.4) The amount of charge transfer δ , can be determined by the relative amplitude of the CPX’s HOMO and LUMO on the parent molecules, and it takes on noninteger values. The CPX maintains an overall charge neutrality. Within a Huckel-type model, the energy associated with the CPX’s frontier levels $E_{CPX,H}$ and $E_{CPX,L}$ can be given by

$$E_{CPX,H/L} = \frac{IE + EA}{2} \pm \sqrt{(IE - EA)^2 + 4\beta^2} \quad (1.1)$$

This equation depends on various factors such as IE, EA, and the resonance integral β . [46] Hybridization can, in principle, occur regardless of whether L_{dop} is higher or lower in

energy compared to H_{OSC} or in other words, where the EA of the dopant is either higher or lower than the IE of the OSC. [3, 47] CPXs show a significant energy gap between a doubly occupied bonding supramolecular hybrid orbital and an unoccupied antibonding one. In these CPXs, both charges reside in the bonding orbital, while the antibonding orbital is shifted well into the OSC gap and assumes the role of the dopant acceptor site.[46] The process of CPX formation is notable for its ability to operate even when the ICT mechanism does not occur. Some examples of CPX formation with COMs have been documented [3, 33, 47–49], along with a few cases involving CPs. [6] It is important to note that CPXs typically show diagnostic absorption bands, which has been shown for P3HT films doped with F_2 -TCNQ in chapter 4.

1.4 Common p-Dopants (Cyclohexadiene and Cyclopropane Core-Based Dopants)

This section offers a comprehensive literature summary of commonly used p-dopants derived from cyclohexadiene (CHD) and cyclopropane (CP) cores.

Initial investigations into p-type molecular dopants primarily focused on quinone molecules [50, 51], which are conjugated molecules derived from aromatic compounds possessing a cyclic dione structure. Tetracyanoquinodimethane (TCNQ) exemplifies one such p-type molecular dopant. However, TCNQ's doping efficiency is limited for most OSCs due to its relatively low EA, with its LUMO around 4.8 eV [52], compared to the general HOMO levels of most OSCs.

Kanai et al. investigated the impact of fluorination on the aromatic core structure of TCNQ and demonstrated that increasing the number of fluorine atoms increases the electron affinity. [53] Consequently, 2,3,5,6-Tetrafluorotetracyanoquinodimethane (F_4 -TCNQ), obtained by replacing the aromatic core's 2,3,5,6 hydrogens with fluorine atoms, exhibited the enhancement in electron affinity [52]; it is one of the most extensively utilized p-type molecular dopants to date. Furthermore, novel molecular structures have been proposed to achieve high electron affinities, including 1,3,4,5,7,8-hexafluorotetracyanonaphthoquinodimethane (F_6 TCNNQ)[54], and 1,4,5,8,9,11-Hexaazatriphenylenehexacarbonitrile ($HAT - CN$)[55], with planar molecular structures.

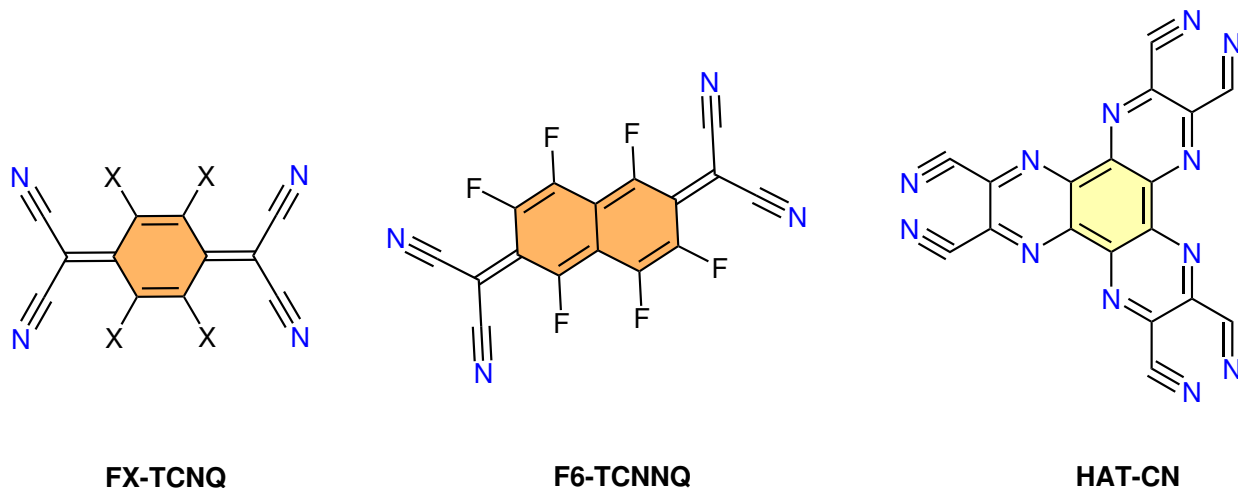


Figure 1.5: Chemical structure of TCNQ- based p-dopants discussed in this work . a) *FX – TCNQ*; where X shows the substitution of 1, 2, or 4 hydrogen atoms by fluorine atoms. b) *F6 – TCNNQ*. c) *HAT – CN*.

Lately, in a patent filed in 2012,[4] Werner et al. suggested a novel molecular dopants capable of doping high IE organic semiconductors, with reasonable stability in the air, of high purity and thermal stability in the semiconductor layer, and which are processable both from solution and vacuum. The patent claims that the above-mentioned improved properties are provided by a mesomeric radialene compound with the chemical formula shown in figure 1.6.

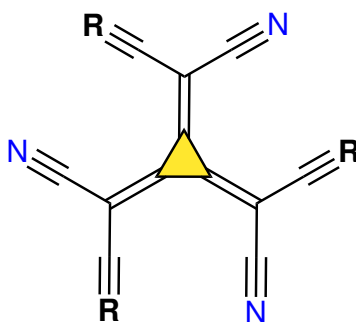


Figure 1.6: Schematic structure of a CP-core based molecular dopant as suggested in Ref. [4]

The chemical structure depicted in Figure 1.6, is based on a CP-core, and each *R* is independently selected from aryl and heteroaryl groups that are partially, or preferably completely substituted with electron-withdrawing groups. The authors reported that the doping of typical organic semiconductor matrix materials such as MeO-TPD (N,N,N',N'-Tetrakis(4-methoxyphenyl) benzidine), 2-TNATA (4,4',4''-Tris(2-naphthyl(phenyl)amino)triphenylamine), or Spiro-TTB (2,2',7,7'-tetrakis(N,N-

diphenylamino)-9,9-spirobifluorene) with these dopants leads to excellent charge transport layers, with low absorption, high conductivity, thermal stability, and operational stability with essentially no alteration of these properties in the long term.

In 2016, Karpov et al., presented a work on a variation of this dopant with six cyano groups denoted as $(CN)_6-CP$, which, however, showed low stability in the solid state under exposure to air, and no suitable solvent was found, as $(CN)_6-CP$ tends to react immediately with both protic and aprotic solvents [56]. This dopant has a record high EA of 5.87 eV and has been shown to dope the hole transport materials TAPC (4,4'-cyclohexylidenebis[N,N-bis(4-methylphenyl)benzenamine]) (IE = 5.50 eV), TCTA (tris(4-carbazoyl-9-ylphenyl)amine) (IE = 5.85 eV), and, surprisingly, CBP (4,4-Bis(carbazol-9-yl)-2,2-biphenyl) with an ionization energy as high as 6.05 eV. Despite these practical issues, in 2019, Liu et al. presented a proof-of-principle study of OLEDs based on layers doped with $(CN)_6-CP$, where the devices were fabricated under ultra-high vacuum conditions (pressure < 10^{-8} mbar) and encapsulated under an inert atmosphere for device characterization. [57] Although $(CN)_6-CP$ has the highest known EA of all molecular p-dopants to date, its use in commercial applications is therefore highly limited, and more stable alternatives must be sought.

Later, in 2019, Saska et al. introduced another variant featuring methyl ester substitutions on each R position of the compound depicted in Figure 1.6. This dopant, referred to as $TMCN3-CP$, possesses an EA of 5.5 eV. It demonstrated the capability to p-type dope high IE alternating copolymers such as PDPP-4T, PDPP3T, and PDPP-T-TT-T, resulting in high conductivities through sequential solution processing of OSC and dopant. [58]

Recently, additional variants emerged such as $PD-A$ [59, 60] (EA= N/A; not yet reported), $ECN5-CP$ (EA= 5.75 eV)[12], and $DMCN4-CP$ (EA= 5.61 eV). [12] The main advantage of $ECN5-CP$ and $DMCN4-CP$ over $(CN)_6-CP$ is that it can be processed from a solution, enabling more control over the film morphology and making it promising for use in large-area processing. [12] As for $PD-A$, there is currently no available literature data on its properties as a p-dopant. In this thesis, we have synthesized a novel variant known as $PFPP3CN3-CP$ with an EA of 5.03 eV, which will be discussed in detail in Chapter 4.

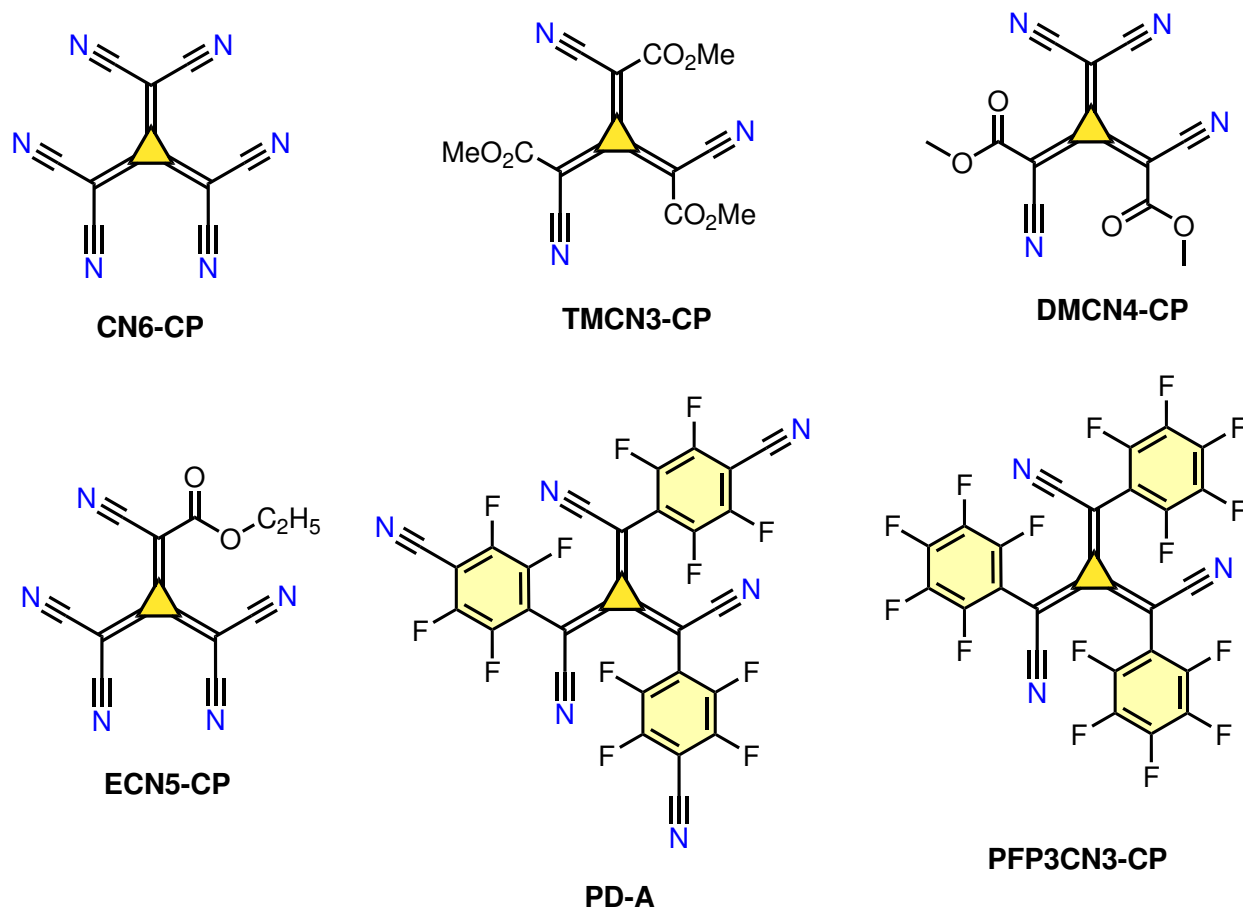


Figure 1.7: Chemical structures of CP-based p-dopants discussed in this thesis

1.5 Statement of the Problem

The effective integration of p-type dopants in OSCs is crucial for the advancement of organic electronic devices. This section outlines the statement of the problem and the subsequent subsections delve into specific challenges encountered in p-doping, each representing critical aspects in the quest for efficient and versatile molecular dopants.

1.5.1 Electron affinity

Achieving doping-related charge transfer relies on the EA of the p-dopant being in close proximity to or exceeding the IE of the OSC. This poses a significant challenge, especially for commercially relevant COMs and CPs, particularly those designated as large bandgap (>2 eV) hole transport materials (HTMs) with IEs exceeding 5 eV. [44, 61] Currently, most molecular p-dopants demonstrate most efficient performance only in host materials with comparably low IE. However, their doping efficiency significantly diminishes in host materials with IEs higher than 5 eV. Consequently, they cannot be reasonably employed

for the electrical doping of wide energy gap host materials with high IE, such as TCTA (5.85 eV), CBP (6.05 eV), and mCP (6.10 eV). [62, 63] The quest for suitable p-dopants remains a challenge, as only a few dopants meet the crucial criterion for such IE ranges.

1.5.2 Doping efficiency (inhibiting the CPX formation)

As we discussed earlier in 1.3, in the molecular doping of COMs and CPs, two competing mechanisms have been identified: ICT, involving integer charge transfer between the semiconductor and dopant, and CPX formation, where only fractional charge transfer occurs. Unlike ISCs such as Si, which essentially provide one mobile charge carrier per dopant at room temperature, OSCs exhibit lower doping efficiency. This inefficiency stems from both the significant energy offset between the p-dopant's EA and the OSC's IE, and the occurrence of CPX formation.

In CPX formation, hybridization of the LUMO of the dopant and the HOMO of the OSC results in supramolecular hybrid orbitals with fractional charge transfer. This process pushes the effective electron acceptor level of the CPX, that is, the empty antibonding supramolecular hybrid orbital, well into the OSC band gap, thus adversely affecting doping efficiency. [3, 46] Therefore, optimized dopants must control the overlap of frontier orbitals of dopant and OSC, and aim to minimize CPX formation to enhance doping efficiency. [3, 46, 64]

1.5.3 Diffusibility

The most common dopants are low molecular weight molecules such as fluorinated TCNQ derivatives. The molecular weight and geometry of these dopants play a crucial role in their diffusibility within the OSC layers. [65] This diffusibility poses a significant stability concern, as these molecules can readily diffuse through OSC layers and interdiffuse between multilayers in OSC heterostructures, which leads to potential degradation of device performance. [44, 45, 66, 67]

For instance, F_4 -TCNQ can diffuse at room temperature through common OSCs like MeO-TPD, while higher molecular weight alternatives like C60F36 exhibit significantly lower diffusibility due to their bulkier structure. [68] The optimization of the molecular weight and geometry of molecular dopants becomes critical to reduce these stability concerns and ensures the reliable performance of organic electronic devices.

1.5.4 Processibility

Currently, vacuum evaporation is the most common fabrication technique employed in the organic electronic device industry. [69] However, it presents challenges, particularly when dealing with small dopants, which may sublime at room temperature. This necessitates sample cooling and can potentially lead to contamination of vacuum equipment. Additionally, the sublimation of small molecular dopants at room temperature can lead to their diffusion through OSC layers (see above), and depleting the OSC layer under vacuum conditions. Higher molecular weight dopants not only enhance device performance but also address practical processing concerns.

An alternative approach involves the development of solution-processable semiconductors and dopants, offering a more cost-effective means of fabricating large-area, flexible electronic devices. [70] Dopants compatible with solution processing, allowing methods such as coating, screen printing, and inkjet printing with OSCs, have become of paramount interest. [58] However, the poor solubility of many molecular dopants in common organic solvents poses a significant challenge, hindering the mass production of organic electronic circuitry from solution. [35, 71] The processing of doped polymers to fabricate thin films can entail practical difficulties such as the precipitation of OSC/dopant agglomerates, where charge transfer in solution leads to the formation of complexes of poor solubility (as compared to the individual components). [72, 73]

Recent research has demonstrated innovative strategies to enhance the solubility of molecular dopants. For instance, replacing the CF_3 group with CO_2Me in the otherwise insoluble dopant $\text{Mo}(\text{tfd})_3$ resulted in increased solubility, facilitating the doping of P3HT from a solution. [74] In another notable study, Li et al. achieved remarkable solubility by substituting the cyano-group in $F_4\text{-TCNQ}$ with an ester group. [75] Furthermore, Rainbolt et al. contributed to advancing $F_4\text{-TCNQ}$ solubility by replacing one fluorine atom with a bulky alkyl group, leading to a significant increase in solubility. [76] These findings highlight the potential for tailored molecular modifications to overcome solubility challenges in the solution processing of doped polymers, paving the way for more efficient fabrication of electronic devices.

1.6 Thesis Objectives/ Research Goal

In this thesis, the overarching goal is to pioneer the development of an "ideal molecular p-dopant" designed for OSCs. This ideal dopant is envisioned to possess high EA, demonstrate superior doping efficiency, exhibit low diffusibility in the solid state, and showcase enhanced solution processability in common solvents with OSCs. We hypothesize that molecular dopants based on the CP core are, in principle, highly promising to overcome the issues. To achieve these ambitious objectives, we adopted a knowledge-based chemical design approach for novel doping agents. Employing Density Functional Theory (DFT) calculations on a diverse library of potential candidates, we aimed to elevate the dopant's EA through the introduction of electron-withdrawing substituents. Simultaneously, our strategy involved suppressing CPX formation via steric hindrance, reducing dopant diffusibility by increasing bulkiness, and improving solubility without compromising EA through the incorporation of solubilizing groups.

The DFT methodology employed for this research is a systematic pre-characterization tool that allowed us to identify compounds with high EA and optimize their geometry, providing insights into their three-dimensional structure. The details have been discussed in chapter 3. The most promising candidate, considering electronic and real-space structure, synthetic feasibility, and cost-effectiveness of starting materials, underwent then chemical synthesis. The synthesized dopant (PFP3CN3-CP) was then rigorously tested by doping benchmark materials, including P3HT and the shorter thiophene oligomer (H10T). Doping efficiency was assessed in comparison to the well-characterized F_xTCNQ p-type dopant series ($F_2\text{-TCNQ}$ and $F_4\text{-TCNQ}$). Structural, electronic, and

electrical characterizations of p-doped films provided valuable insights into their behavior and application potential. The more details can be found in chapter 4.

The results obtained not only contributed to the current understanding of p-doping in organic semiconductors but also provided guidance for future modifications to the molecular structure. Our ultimate objective is to develop, synthesize, and characterize improved p-dopants for OSCs, addressing challenges related to high EA, enhanced doping efficiency, low diffusibility, and superior solution processability. This research set the stage for advancements in organic electronics by overcoming existing limitations in p-doping strategies.

1.7 Thesis Organization

Chapter 1 of this thesis is an introduction to organic semiconductors, their comparison with inorganic semiconductors, and p-doping mechanisms. This introductory chapter also provides a literature review on various types of p-dopants (cyclohexadiene and cyclopropane-based dopants) and their behavior as dopants in organic semiconductors. This chapter aims to deliver background information complementary to the introduction sections found in the subsequent chapters of the thesis.

Chapter 2 describes the experimental methods that have been used in studies featured in this thesis and provides basic principles behind each technique. Detailed information is provided within the next chapters.

Chapter 3 provides a design strategy based on DFT calculations for potential p-dopants on both cyclopropane and cyclohexadiene cores. This work with the title of *Design Strategies for Optimized Molecular p-Dopants: Decoupling Electronic and Geometric Effects*, is submitted in Physical Review Materials.

Chapter 4 presents a novel p-dopant (*PFP3CN3 – CP*) with a sterically hindered core and emphasizes the structure design of this dopant in inhibiting the CPX formation. This work with the title of *Sterically-Hindered Molecular p-Dopants Promote Integer Charge Transfer in Organic Semiconductors*, is published in *Angewandte Chemie International Edition*.

Chapter 5 is a follow-up on the previous chapter, regarding the ability of the *PFP3CN3 – CP* to participate in radical-radical dimerization. The manuscript is in preparation.

Chapter 6 presents concluding remarks encompassing the research presented in the previous sections, and finally, Chapter ?? provides an appendix.

Chapter 2

Experimental Methods

While the studies featured in this thesis provide detailed experimental procedures in sections 3.2, 4.2, and 5.2, the objective of this chapter is to familiarize the reader with the fundamental principles underlying the employed techniques. Additionally, it addresses the resolutions applied to technical challenges experienced during the experiments conducted for this thesis and offers details into the processing of experimental data.

Primarily, discussions delve into Optical Absorption across the Ultraviolet (UV), Visible Light, and Near-Infrared (NIR) regions (UV-vis/NIR; section 2.1), and Fourier-Transform Infrared Spectroscopy (FTIR; section 2.2), which play important roles in identifying dopant mechanisms within a given sample.

Following this, Cyclic Voltammetry (CV; section 2.3) and Grazing-Incidence X-ray Diffraction (GIXRD; section 2.6) are examined as techniques for explaining the energetic influences and structural consequences, respectively, of observed doping behavior.

Lastly, to underscore the practical relevance of these techniques, determinations of thin-film conductivities are elaborated upon in section 2.4, alongside a discussion of Atomic Force Microscopy (AFM; section 2.5), which was utilized to determine sample dimensions (film thickness) that is crucial for conductivity calculations.

2.1 Optical Absorption Spectroscopy (UV-vis/NIR)

To assess optical absorption features and gain insight into doping phenomena for this thesis, UV-vis/NIR spectroscopy was conducted.

The instrument Cary 5000, produced by Agilent Technologies, with range of 0.38-7.1 eV (3300–180 nm) has employed here for assessment of optical absorption features in this thesis, in near-infrared (NIR; 0.41–1.6 eV, 3000–800 nm), visible light (vis; 1.6–3.1 eV, 800–400 nm), and ultraviolet (UV; near- to far-UV: 3.1–10 eV, 400–230 nm).

2.1.1 Setup fundamentals

In our spectrometer setups, absorbance is measured as a proxy to the investigated absorption. If I_0 is the incident light intensity at the frequency of interest and I_t is the intensity of transmitted light, the dependence of I_t / I_0 on the molar concentration of solute (c)

and the length of the sample cell (l), and molar extinction coefficient (ϵ) is described by Beer-Lambert's law:

$$A = \log\left(\frac{I_0}{I_t}\right) = \epsilon \cdot c \cdot l \quad (2.1)$$

The molar extinction coefficient ϵ is a measure of the strength of the transition and is characteristic of the chromophore and wavelength.

The typical ultraviolet-visible spectrophotometer consists of a light source, a monochromator, and a detector. This light source can be a deuterium lamp for the UV region and a tungsten or halogen lamp for the visible and near-infrared regions.

All measurements were done in double-beam mode. The emitted light is split into two beams – the sample beam and the reference beam. This split is usually achieved using a beamsplitter, which can be a prism or a diffraction grating. The rotating three-section chopper periodically directs the incident light alternately toward the sample and the reference. The three sections include a mirrored section (for the sample), a cut-out section (for the reference), and a matte black section (blocks it to provide time to move to the next wavelength step in a scan). The sample beam passes through the sample cell, where it interacts with the sample. Meanwhile, the reference beam travels through a reference cell containing a substance transparent across the measured spectral range. This cell provides a baseline for comparison. Both the sample and reference beams are then directed towards a detector system.

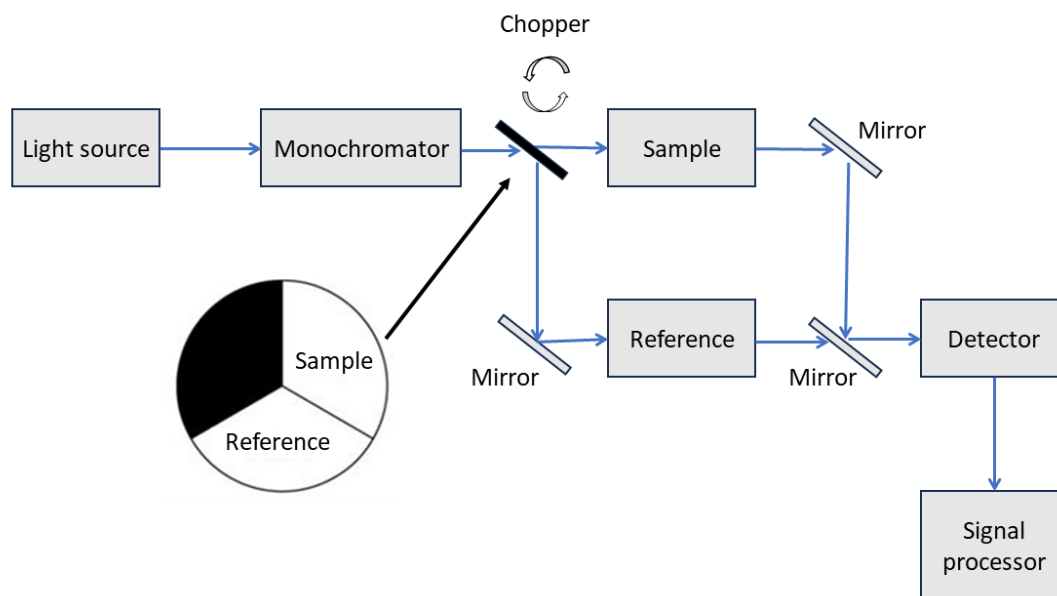


Figure 2.1: A typical double-beam configuration of optical absorbance; the simplified figure is missing filters, additional monochromator gratings, and variable slits.

2.1.2 Inert atmosphere sample holder and cuvette

Hannes Hase, in collaboration with William Chicoine from the Science Technical Center, designed a sample holder (refer to Figure 2.2). The holder is crafted from an aluminum base plate with long edges shaped into rails that seamlessly fit into the spectrometer's designated slot for standard glass-slide sample holders. The holder features an inset quartz glass window, sealed with epoxy at its contact points with the plate. A 1.0 cm \times 1.0 cm \times 0.5 mm sample can be positioned on the window opening and secured by a 3D-printed plastic brace. The brace's inner bevels only touch the substrate's edges, minimizing the risk of contamination from or of the deposited film. This configuration was utilized for experiments conducted under ambient conditions.

To secure the sample, flexible metal strips clamp it onto a holder perpendicularly attached to the base plate. The base plate incorporates a trench for a KF-25 o-ring, and the sample is oriented perpendicular to the base plate. The top compartment accommodates both windows, with thinner rails designed to fit the spectrometer slots. Additionally, each rail accommodates a bent metal strip acting as a spring to ensure the holder sits flush with the slot. This modification aims to minimize measurement discrepancies resulting from varied path lengths through the windows and the sample due to varying angles with respect to the beam.

A rectangular aluminum plate serves as a spacer, lifting the holder into the beam path. While the holder's height is adjustable through bolts in the spectrometer, the range of this adjustment is limited.

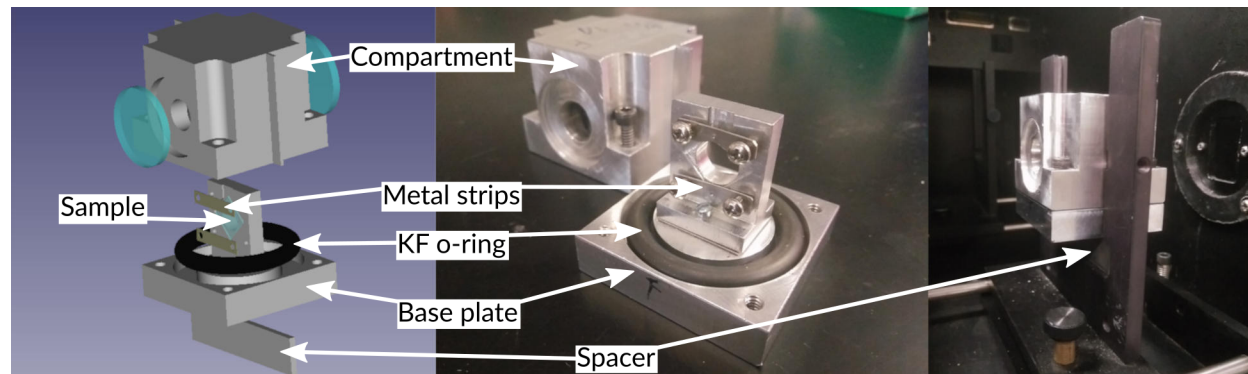


Figure 2.2: A spectroscopy sample holder for measurements in an inert atmosphere is used in this thesis. The figure adapted from: Hase, H. (2023). Integer and fractional charge transfer in the doping of poly- and oligothiophenes (Unpublished doctoral dissertation). Concordia University. (Figure 3.2, p. 24).

2.1.3 Sample spectra acquisition and treatment

During each measurement session, a baseline spectrum was recorded to eliminate features associated with the setup and substrate from the sample spectra. This baseline spectrum utilized the same setup as the sample measurement. The acquisition software

employed an automatic process to subtract the pre-recorded baseline absorbance while recording the sample spectrum.

UV-vis/NIR spectrometers are typically equipped with separate lamps, diffraction gratings, and detectors catering to different spectral ranges. The Cary 5000, for instance, integrates two sets of gratings along with a photomultiplier tube (PMT) and a PbS photocell serving as detectors for the UV-vis and NIR regions, respectively. Despite being automated within a single instrument, this configuration represents a substantial modification to the setup. The transition from the NIR to the vis range is considered an interruption in an otherwise nearly continuous scan. This interruption can manifest in the spectrum, with changes in both detectors and gratings leading to sudden increases or decreases in absorbance after passing their changeover wavelengths during the scan. To maintain clarity in the spectrum, it is advisable to mitigate the impact of these transitions by setting both changeovers to the same wavelength.

Moreover, another notable transition occurs when the instrument shifts from utilizing its quartz halogen lamp to the deuterium lamp, which is necessary for accessing the lowest wavelengths detectable by the Cary 5000. However, the specific focus of the studies conducted here did not necessitate investigations beyond 5.4 eV (< 230 nm), and higher energy levels were intentionally avoided to keep the samples safe from radiation damage in the ultraviolet range. To concentrate exclusively on relevant absorption features all spectra in this study are cut above 4.5 eV (< 275 nm).

2.2 Fourier-Transform Infrared Spectroscopy

In addition to UV-vis/NIR, Fourier-transform infrared spectroscopy (FTIR) in the mid-infrared range (MIR; 0.025–0.41 eV, 50000–3000 nm, 200–3300 cm^{-1}) has been employed in this thesis.

For resolving low-energy doping-related electronic transition features, particularly around 4000 cm^{-1} (0.50 eV), FTIR and UV-vis/NIR spectra have merged. The MIR spectrum reveals vibrational fingerprint bands, such as the $\text{C}\equiv\text{N}$ and ring $\text{C}=\text{C}$ stretching modes of $F_2\text{-TCNQ}$ and PFP3CN3-CP around 2200 and 1500 cm^{-1} , respectively. These bands aid in assessing charge transfer degrees, indicating integer charge transfer (ICT) or ground-state charge-transfer complex (CPX) formation, complementing UV-vis/NIR data.

The Thermo Scientific Nicolet 6700 FT-IR Spectrometer used in this study is equipped with an EverGlo glowbar infrared (IR) source, a KBr beam splitter, and an MCT-A liquid nitrogen-cooled HgCdTe detector, enabling optimal operation in the 650–4000 cm^{-1} (0.081–0.50 eV) range in transmission mode. To minimize CO_2 and H_2O peaks, the instrument undergoes periodic purging every 5 min. Sealable sample holders with KBr-crystal windows, designed for transparency in the MIR, allow measurements in an inert atmosphere as detailed in section 2.1.2.

2.2.1 Setup and fundamentals

The FT-IR employs an interferometer to process the energy directed towards the sample, its workings are here exemplified by the Michelson interferometer (Figure 2.3).

Within the interferometer, the source energy undergoes several steps. It passes through a beam splitter and a mirror positioned at a 45° angle to the incoming radiation, allowing the radiation to pass through while dividing it into two perpendicular beams. One beam (beam reflected), oriented at 90° as shown in Figure 2.3, travels to a stationary or "fixed" mirror before returning to the beam splitter.

Simultaneously, the undeflected beam (beam transmitted) travels to a moving mirror and then returns to the beam splitter. The moving-mirror displacement ξ_d , here, is defined with $\xi_d = 0$ being the position where the moving mirror has the same distance to the beam splitter as the fixed one. The motion of this moving mirror introduces variations in the pathlength traversed by the second beam.

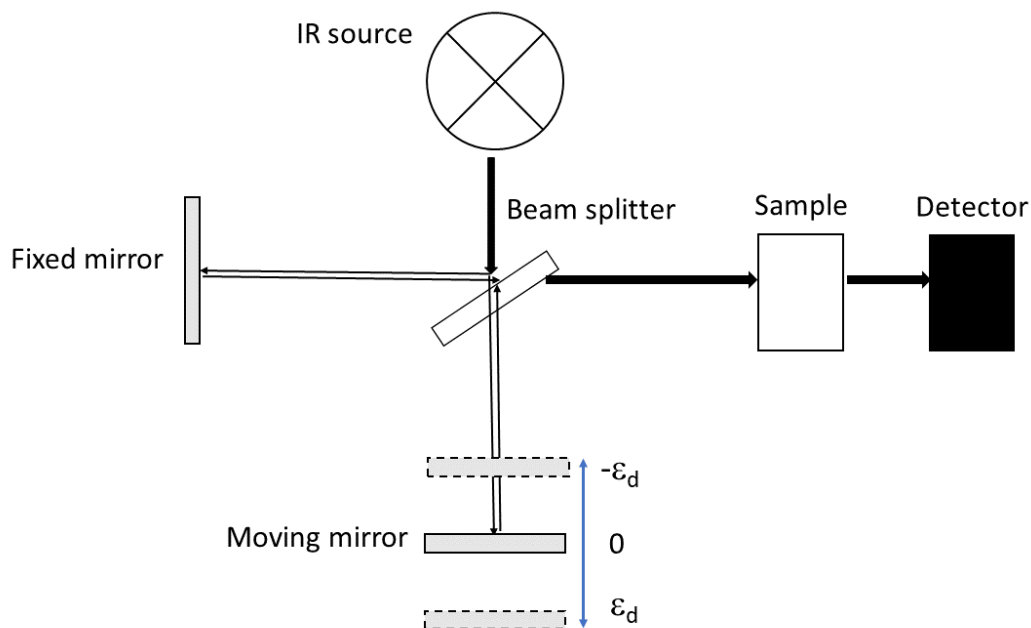


Figure 2.3: The standard configuration for a Fourier-transform infrared spectrometer in transmission mode utilizing a Michelson interferometer. The figure missing details such as filters, aperture control, and mirrors.

The beam parts reflected at the mirrors reunite again at the beam splitter. Here, they are both transmitted and reflected again, thus forming a unified beam path back to the source and, perpendicular to the fixed mirror, another path directed toward the detector. The allocation between the portion directed toward the detector and that directed back to the source relies on the phase differences after the second beam-splitter passes.

When $\xi_d = 0$, the phase shifts at the beam splitter, with 90° for reflection and zero for transmission, combine to result in fully constructive interference for the beam directed

towards the detector. Simultaneously, the beam directed towards the source is effectively extinguished through destructive interference.

As the moving mirror deviates by ξ_d from this position, a path difference $\xi = 2\xi_d$ introduces another phase shift. For a given wavelength λ , increasing $|\xi|$ to $\lambda/2$ adds a 180° shift, reversing the situation where all beam power is redirected at the source and none at the detector. Displacing the moving mirror to $|\xi| = \lambda$ then redirects the beam power, for a specific λ , back to the detector.

Recording the intensity I_ξ for continuous ξ generates an interferogram. For a monochromatic source, this takes the form of a cosine with a wavelength of $\lambda/2$ and an offset I_{const} aligning the otherwise negative cosine minima to $I = 0$. In IR spectroscopy, the reciprocal of the period is commonly used, known as the wavenumber ν , typically provided in cm^{-1} because the reciprocal of the maximal ξ in cm yields the spectral resolution in cm^{-1} . [77] With I_ν as the intensity for the given ν , affected by mirror and beam-splitter efficiencies, sample absorbance (if applicable), and detector sensitivity, I_ξ becomes:

$$I_\xi(\xi) = I_{\text{const}} + I_\nu(\nu) \cos(2\pi\nu\xi) \quad (2.2)$$

Mathematically, I_ν represents the Fourier transformation (FT) of $I'_\xi = I_\xi - I_{\text{const}}$. For a non-monochromatic, continuous source, the interferogram becomes more intricate, as each wavenumber obeys the equation above. Hence, I'_ξ needs to be integrated over all wavenumber:

$$I'_\xi(\xi) = \int_{-\infty}^{\infty} I_\nu(\nu) \cos(2\pi\nu\xi) d\nu \quad (2.3)$$

This forms a cosine FT pair with:

$$I_\nu(\nu) = \int_{-\infty}^{\infty} I'_\xi(\xi) \cos(2\pi\nu\xi) d\xi \quad (2.4)$$

This can be rewritten due to $I'_\xi(\xi)$ being an even function [77], providing intensities for only the physically sensible, positive wavenumber values:

$$I_\nu(\nu) = 2 \int_0^{\infty} I'_\xi(\xi) \cos(2\pi\nu\xi) d\xi \quad (2.5)$$

The experimental constraints of an infinitely long beam path difference ξ and infinitesimally small sampling $d\xi$ are limiting factors for resolution and range, respectively.

2.2.2 Data acquisition and treatment

The process of removing non-sample elements from the sample absorbance spectrum requires subtracting a background spectrum obtained with a blank substrate in the sample holder, as discussed for UV-vis/NIR in section 2.1.3. Nevertheless, FTIR spectra, lacking a reference beam, are more susceptible to artifacts stemming from source energy fluctuations, stray radiation, beam intensity variations, and electronic noise. It is recommended to record background spectra before and after to assess fluctuations. Still, it is essential

to acknowledge that these spectra do not precisely mirror the conditions during sample measurement. The spectroscopist holds the responsibility for determining the validity of background subtraction, underscoring the importance of continuous data evaluation during acquisition.

In the thesis, this is particularly relevant for doping-related electronic transitions around 4000 cm^{-1} (0.50 eV), the lowest-energy polaron transitions ('P1' in figure 4.3). The low-energy flank of these transitions may extend deeply into the MIR range. To distinguish peaks rather than flanks, a cautious approach was employed: FTIR spectra were methodically converted from wavenumber to an energy scale in eV and correlated with UV-vis/NIR spectra to capture the complete feature shape.

This process necessitates caution due to fundamental differences between FTIR and UV-vis/NIR experiments, encompassing variations in substrates, sample film thickness, and distinct instrument setups. Beyond the alignment achieved through a linear shift along the ordinate, similar to the procedure between UV-vis and NIR spectra, scaling of the FTIR spectrum is essential to ensure the seamless continuity of merged curves. It is crucial to emphasize that this method is suitable for qualitative analysis only, as certain fluctuations unaccounted for in FTIR may introduce a skewed baseline unnoticed in the curve-merging process.

Although a skewed baseline poses fewer challenges when examining the spectrum closely, for the detailed analysis of smaller peaks, including those associated with the $\text{C}\equiv\text{N}$ and ring $\text{C}=\text{C}$ stretching modes, it becomes essential to eliminate broader background features. This process involves subtracting a linear or low-order polynomial function fitted through points assumed to represent only the background. The outcome is a nearly flat baseline that facilitates the fitting of narrower peaks and the extraction of their parameters.

2.3 Cyclic Voltammetry (CV)

One commonly used approach for assessing the redox potential (V_{redox}), as well as the ionization energy IE and electron affinity EA of host and dopant materials in OSC research, is employing cyclic voltammetry (CV). This method serves as a cost-effective alternative to (inverse) photoelectron spectroscopy.

In our experimental setup, a CH Instruments CHI604d potentiostat was utilized along with a Pt-wire counter electrode, an Ag-wire pseudo-reference electrode, and a 0.1 M solution of tetrabutylammonium hexafluorophosphate in acetonitrile for TCNQ derivatives and P3HT, and dichloromethane for *PPF3CN3-CP*. For TCNQ derivatives, a glassy carbon working electrode and a scan rate of 0.05 V/s were employed. In the case of P3HT, the compound was spin-coated onto an indium-tin-oxide (ITO)-coated glass slide, with a scan rate of 0.02 V/s.

All measurements were conducted under N_2 atmosphere within a glovebox, and the potentials were referenced against the ferrocene/ferrocenium (Fc/Fc^+) redox couple, serving as an internal standard.

2.3.1 Setup fundamentals

The standard setup for cyclic voltammetry (CV) involves an electrochemical cell containing a solution of the analyte and a supporting electrolyte, with a working electrode (WE), reference electrode (RE), and a counter electrode (CE) immersed within. It is important to purge the cell with an inert gas (e.g., Ar) to prevent unintended chemical reactions. [78, 79] Here, all measurements were done in a N₂ glovebox.

A pseudo-reference is often made of simple Ag or Pt wires in the same electrolyte solution, to provide a reference potential. [79] In all measurements, a Fc/Fc⁺ is internally added to the solution right after the sample measurement, to provide a reproducible reference potential to align the data.

The experiment records the current (y-axis) as a function of the applied potential (x-axis) during the cyclic scan of the potential, which is known as a voltammogram. The shape and features of the voltammogram reveal details about redox reactions, including the potential at which oxidation or reduction occurs and the kinetics of these processes. The cyclic nature of the voltammetry scan, which involves sweeping the potential linearly and alternately between two preset values, results in characteristic patterns on the voltammogram. The measurement process revolves around the application of a potential difference V_{appl} , between working and counter electrodes. (2.4)

The potential difference induces a charge transfer between the working electrode and the molecular orbitals (highest occupied molecular orbital in the ground state (HOMO) and the lowest unoccupied molecular orbital in the ground state (LUMO)) of the analyte.

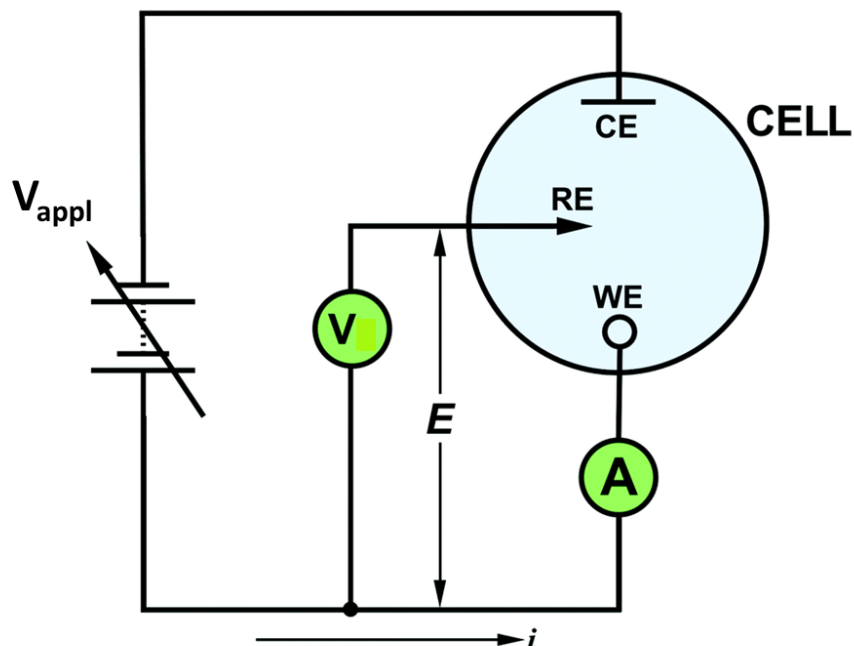


Figure 2.4: Schematic of a typical three electrode electrochemical set-up. Current flows between CE and WE whilst E is controlled between WE and RE. The figure has been edited and adapted from: Colburn, A. W., Levey, K. J., O'Hare, D., Macpherson, J. V. (2021). Lifting the lid on the potentiostat: a beginner's guide to understanding electrochemical circuitry and practical operation. *Phys. Chem. Chem. Phys.*, 23, 8100. <https://doi.org/10.1039/D1CP00661D>. [Creative Commons Attribution 3.0 Unported License]

As a result, a change in current (I) occurs and is then recorded as a function of the potential V detected independently by the reference electrode. The change in I serves as an indicator of the redox potential (V_{redox}), which can subsequently be translated into ionization energy (IE) or electron affinity (EA) values. Higher applied potential (V) initiates an anodic scan, offering valuable insights into oxidizing reactions and the exploration of occupied states. Conversely, a cathodic scan, accomplished in lower V , allows the observation of reducing reactions, providing a means to investigate unoccupied states.

2.3.2 Data acquisition and treatment

In case of TCNQ derivatives, and *PPF3CN3-CP*, we have calculated the V_{redox} , so-called half-wave potential as: $V_{1/2} = (V_{\text{p,a}} + V_{\text{p,c}})/2$. [78, 79] While, in the case of the P3HT film, due to the close overlap of peaks, the V_{redox} is estimated from the onset of the oxidation features in line with previous V_{redox} determination for P3HT in literature. [80]

To this point, all V_{redox} values would be derived with respect to the pseudo-reference potential which offers insufficient reproducibility between experiments. [78, 79] Therefore, in our measurements we have added Fc as a choice of *internal standard* to the so-

lution after measurement of the analyte—without any changes to the setup—and the V scale was subsequently zeroed on $V_{1/2} \approx V_{\text{redox}}$ of the Fc/Fc^+ redox couple. [81] The redox potentials, originally measured in Volts (V), were transformed into energy units (eV) through multiplication by the elementary charge e and referenced to the vacuum energy, to obtain IE (ionization energy) and EA (electron affinity). For clarity, these values are presented as positive, aligning higher EA with increased dopant strength.

The -5.1 eV has used here, as V_{redox} of Fc/Fc^+ *versus* vacuum energy. [82] An error margin of ± 0.1 eV [82] was assumed for all values.

Consequently, the conversion follows:

$$IE \text{ or } EA = 5.1 \text{ eV} + eV_{\text{redox}} \quad (2.6)$$

2.4 Electrical Characterization (thin-film conductivity)

The conductivity of the doped films has been measured, to assess the application-related effectiveness of doping. Sample films were spin-coated onto glass slides featuring a patterned ITO layer functioning as electrodes. The film is then deposited atop, while the electrodes are structured to allow probing of the segment of the film situated between them. For measuring the current-voltage (I - V) curves, a Keithley 2400 source-measure unit, with an Ossila OFET test board, was utilized to establish contact with the ITO substrates patterned by Ossila. Voltage sweeps ranging from -1 to 1 to -1 V, were applied, covering a total of 101 voltage steps with a 0.06 s settling time on the Keithley 2400. All measurements were performed inside a glovebox under a nitrogen (N_2) atmosphere. The dimensions of the probed film were determined using both optical and atomic force microscopy, as detailed in Section 2.5.

2.4.1 Setup fundamentals

The electrical conductivity γ , considered from a charge-carrier standpoint, is defined by the elementary charge e , the density of charge carriers n , and their mobility μ as described in [1].

$$\gamma = en\mu \quad (2.7)$$

The conductivity can also be determined from the resistance R of a well-defined dimension sample, namely the cross-section A and the channel length L between electrodes, which charge carriers need to pass. In an electrode configuration, A is defined by the channel width w and the film thickness t . Therefore, the conductivity can be calculated as:

$$\gamma = \frac{L}{RA} = \frac{L}{Rwt} \quad (2.8)$$

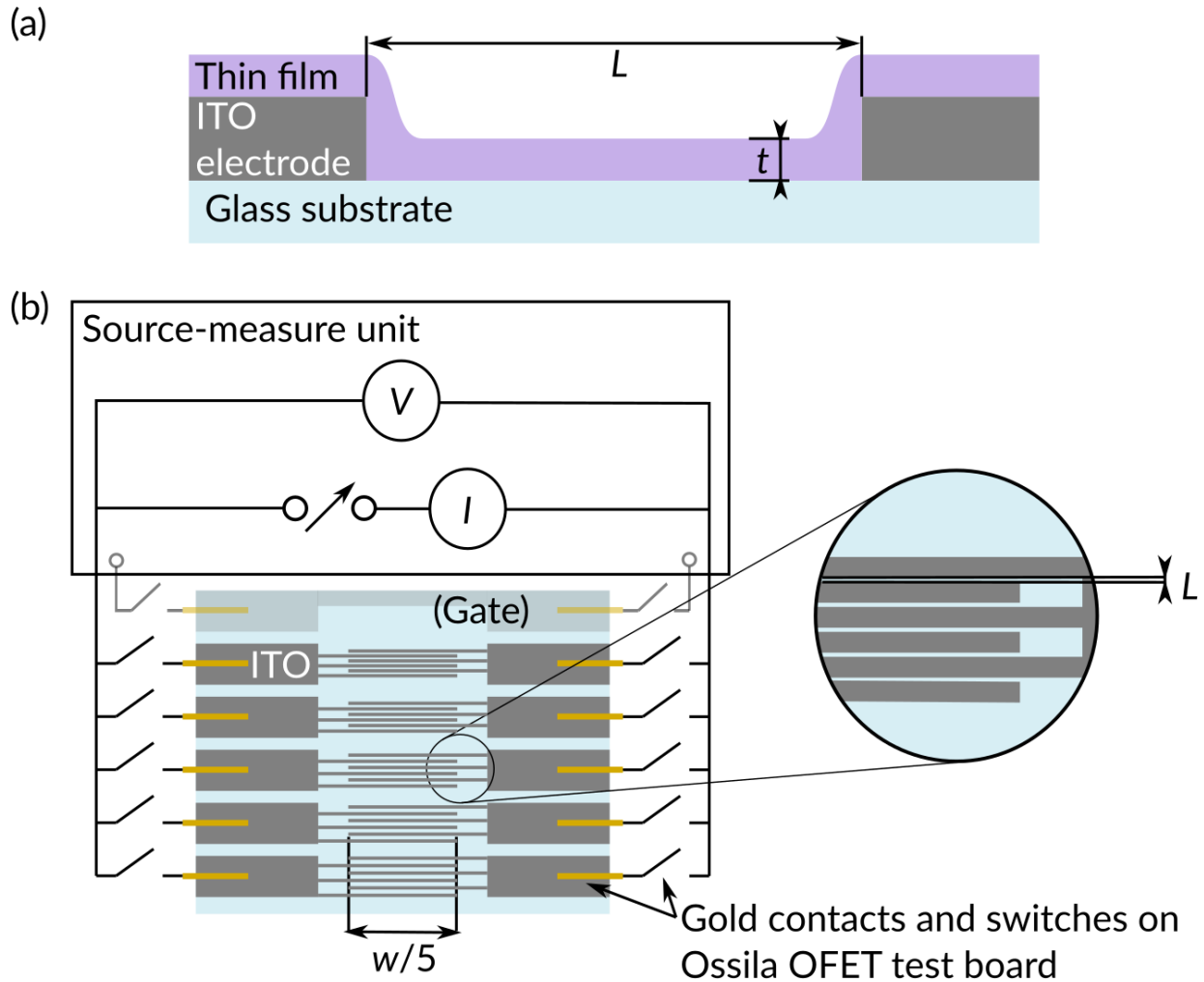


Figure 2.5: Visualization sample dimensions in thin-film conductivity measurements. These dimensions include the film thickness t , channel length L , and channel width w . (a) Offers a side view into the channel between electrodes. (b) Provides a top view onto the substrate, with connections to the source-measure unit illustrated (no thin film depicted for clarity). At the interdigitated regions of the three fingers of each electrode, five electrically parallel channels are formed, with their widths summing up to w . The figure has been adapted from: Hase, H. (2023). Integer and fractional charge transfer in the doping of poly- and oligothiophenes (Unpublished doctoral dissertation). Concordia University. (Figure 3.9, p. 40)

2.4.2 Data acquisition and treatment

A symmetrical voltage (V) sweep around $V = 0$ is conducted, and resistance (R) is derived from the slope of a linear fit. This indicates whether $V(I)$ exhibits a linear trend and thus adheres to Ohm's law ($V = RI$) in the first place.

To be noted that, determining the R using Ohm's law by measuring a single data point

of V and current (I), is not helpful in whether the applied voltage (V) falls within the ohmic regime.

Typically, 4-point probe setups are utilized, where V is sensed with a separate pair of electrodes, as the current-providing electrodes might encounter contact resistance R_{contact} , an unknown factor contributing to the measured resistance $R_{\text{measured}} = R + R_{\text{contact}}$.

However, establishing proper contacts can be challenging, especially with soft materials like P3HT. Therefore, a different approach is adopted with the patterned-ITO substrates offered by Ossila (Figure 2.5). These substrates feature multiple electrode pairs with varying L values on a single substrate, allowing for the resolution of γ with minimal influence from R_{contact} .

Applying equation 2.8 to R_{measured} yields:

$$R_{\text{measured}} = (\gamma wt)^{-1}L + R_{\text{contact}} = m_{R(L)}L + R_{\text{contact}} \quad (2.9)$$

where $m_{R(L)}$ represents the slope obtainable through linear regression of the $R_{\text{measured}}(L)$ data points. Subsequently, conductivity can be determined as:

$$\gamma = (m_{R(L)}wt)^{-1} \quad (2.10)$$

The uncertainty $\Delta\gamma$ is then propagated via:

$$\Delta\gamma = \frac{1}{wt} \sqrt{\Delta m_{R(L)}^2 + m_{R(L)}^2 \left(\frac{\Delta w^2}{w^2} + \frac{\Delta t^2}{t^2} \right)} \quad (2.11)$$

where $\Delta m_{R(L)}$, Δw , and Δt represent the uncertainties of $m_{R(L)}$, w , and t , respectively.

2.5 Atomic Force Microscopy (AFM)

AFM data presented in this thesis (relating to chapter 4, in the appendix) were either provided by Hannes Hase, to determine the relevant dimensions for thin-film conductivity calculations(2.4), or by Shubham Bhagat for the morphology study of P3HT doped films with F_2 -TCNQ and $PFP3CN3CP$.

The samples examined in this thesis have film thicknesses t ranging from 1 to 100 nm. These thicknesses can be effectively characterized using tapping-mode atomic force microscopy (AFM)[83], as implemented in this study. The film thickness P3HT doped films with F_2 -TCNQ and $PFP3CN3-CP$ were determined by atomic force microscopy (AFM) on a Bruker Dimension Icon (under ambient conditions) with a silicon nitride tip (AppNano ACTA, 125 $\mu\text{m} \times 30 \mu\text{m} \times 4.0 \mu\text{m}$ cantilever, < 10 nm tip radius, 14-16 μm 7 tip height, 200-400 kHz, 13-77 N/m) in its proprietary PeakForce Tapping Mode. Channel dimensions (L and W) were determined using the optical microscope as part of the same AFM.

Morphology study of the P3HT doped films with F_2 -TCNQ and $PFP3CN3-CP$ studied with AFM was performed on a Bruker Multimode 8HR (under ambient conditions) with a silicon nitride tip (AppNano ACTA-50, 125 $\mu\text{m} \times 30 \mu\text{m} \times 4.0 \mu\text{m}$ cantilever, < 10 nm tip radius, 14-16 μm tip height, 200-400 kHz, 13-77 N/m) in Tapping Mode.

2.5.1 Setup fundamentals

Atomic force microscopy (AFM) is a versatile technique widely employed for analyzing surface structures without the need for chemical etching or scratching. Unlike electron microscopy methods, AFM does not use a destructive electron beam, allowing for the investigation of diverse mechanical attributes. In this high-resolution scanning probe microscopy, a cantilever with a sharp tip scans the sample surface (Figure 2.6). The cantilever deflection causes by tip-surface interaction which is dominated by attraction through the van der Waals force. The deflections are measured and subsequently employed in determining the sample height at the raster point.

Deflection measurement in atomic force microscopy commonly involves reflecting a laser beam off the cantilever's back and tracking the movement on a quadrant photodiode. The reflected light collected by the photodiodes generates an output signal, while piezoelectric elements moving the probe, controlling its height over the sample.

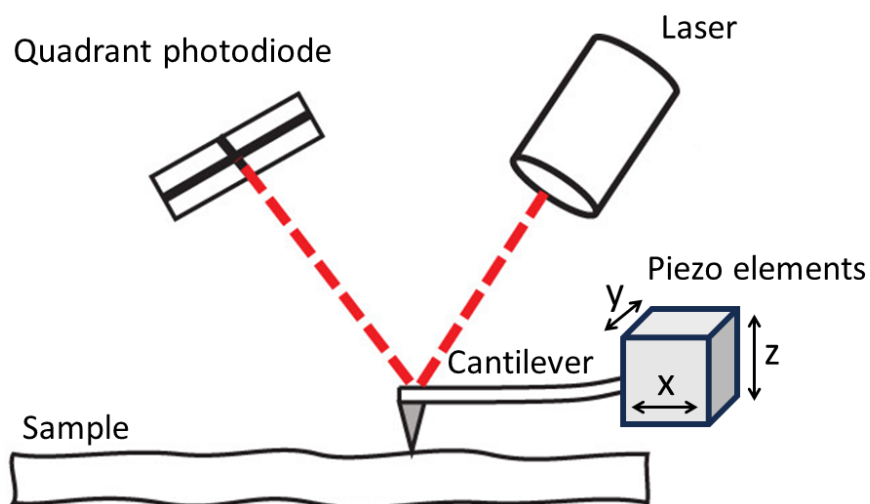


Figure 2.6: Schematic depiction of an atomic force microscopy (AFM). The figure has been edited and adapted from: Walker, Jack; Jamal, Umer; Mohammadpour, Mahdi; Theodossiadis, Stephanos; Bewsher, Stephen R.; Offner, Guenter; Bansal, Hemant; Leighton, Michael; Braunstingl, Michael; Flesch, Heinz-Georg. (2021). "Asperity level characterization of abrasive wear using atomic force microscopy." *Proceedings of the Royal Society A*, 477(2021), 20210103. DOI: <http://doi.org/10.1098/rspa.2021.0103>

The mode used in the discussed thesis is Bruker's PeakForce QNM, an evolution of tapping mode, emphasizing peak-force analysis to enhance control and reduce energy dissipation into the sample, which is crucial for preserving the integrity of soft samples like polymers.

2.5.2 Data acquisition and treatment

To measure the polymer-film thickness, light trenches were gently created within it using soft, flexible syringe needles. AFM scans were performed on $1\ \mu\text{m} \times 20\ \mu\text{m}$ areas with the long axis perpendicular to the trench edge and within the channel of the central and the two outermost electrode pairs (*cf.* substrate in figure 2.5) in order to account for film non-uniformity, which usually leads to a standard deviation in the range of 10%–40%.

The data underwent processing and analysis using Gwyddion (licensed under the GNU General Public License (GPL) v2.0; accessible at <http://gwyddion.net/>). The images were semi-automatically flattened by manually fine-tuning the parameters of the to-be-subtracted 2-dimensional polynomial. This process involved comparing the flatness of both the trench bottom and the pristine film, under omission of debris at the trench edge, which is easily identifiable by its location and at least one order of magnitude higher thickness.

The film thickness t was then derived from a profile cut through the image and averaged over the values obtained from the three electrode pairs. Image capture was stopped as soon as a satisfactory image, devoid of imaging artifacts and with a sufficiently large area for profiling, was obtained.

2.6 Grazing-Incidence X-Ray Diffraction

For the characterization of crystalline structures in thin films, and also for studying the dopant intercalation in OSC (as highlighted in chapter 4), grazing-incidence x-ray diffraction (GIXRD) technique is employed in this thesis.

The dataset (presented in figure B.17) was recorded at the Canadian Light Source Saskatoon, SK, Canada on beamline BXDS-IVU. The primary beam with $\lambda = 0.92\ \text{\AA}$ (14 keV) was employed at $\alpha = 0.15^\circ$ (close to the critical angle of total reflection) and exhibited beam dimensions of $100\ \mu\text{m}$ vertical, $2\ \text{mm}$ horizontal. Data acquisition was done using a stationary Rayonix MX300 detector and without sample rotation.

2.6.1 Setup and fundamentals

Although x-rays fall under the category of ionizing radiation, their interaction with matter, as utilized in x-ray diffraction, involves Thomson (elastic) scattering. This means that the photon energy remains conserved and is not transferred to the electron acting as the scatterer. Instead, the incident and outgoing wavevectors, denoted as \mathbf{k}_i and \mathbf{k}_o respectively, only experience a momentum transfer defined by the scattering vector $\mathbf{q} = \mathbf{k}_o - \mathbf{k}_i$, where $|\mathbf{k}_i| = |\mathbf{k}_o| = 2\pi/\lambda$. [84]

When an incident plane wave scatters at a point-charge scattering center, it generates a spherical wave around the center. In the presence of multiple scattering centers, the differences in path lengths for each center result in phase shifts between the outgoing spherical waves. These phase shifts lead to the formation of patterns characterized by constructive and destructive interference. When the path difference is an integer m multiple of the wavelength λ constructive interference occurs for scattering centers organized in a regular lattice, such as the electron clouds of atoms in a crystal. [84]

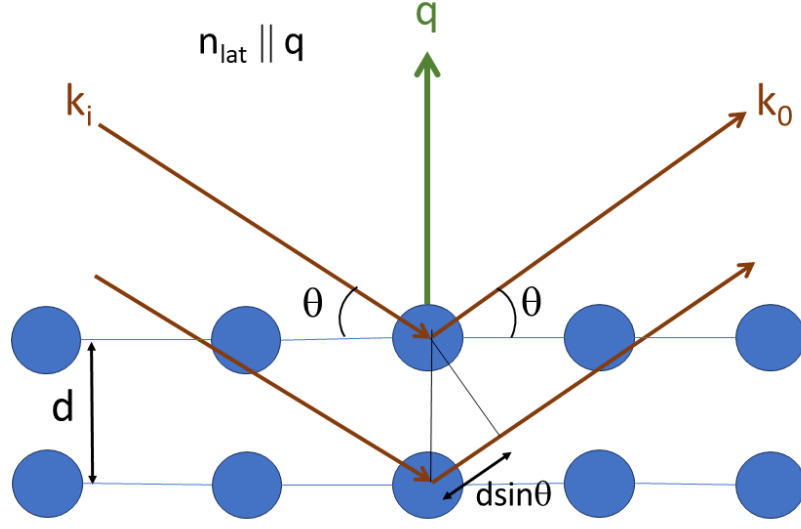


Figure 2.7: Visualization of the Bragg equation; depicted are the incoming and outgoing wavevectors \mathbf{k}_i and \mathbf{k}_o respectively, their angle θ with the lattice plane, the lattice plane distance d , the lattice normal \mathbf{n}_{lat} , and the scattering vector \mathbf{q} .

Considering a lattice plane with an angle θ towards \mathbf{k}_i and its plane normal \mathbf{n}_{lat} parallel to \mathbf{q} (refer to figure 2.7), the condition for constructive interference is described by the Bragg equation:

$$2d \sin \theta = m\lambda \quad (2.12)$$

Here, the lattice plane distance d is experimentally accessible and is connected to θ . It is a parameter to be scanned for intensity maxima of the outgoing beam, referred to as *Bragg reflections* or *Bragg peaks*. In a broader context, the lattice plane distance d can be related to the scattering-vector length $q = |\mathbf{q}|$ through geometric considerations of $\sin \theta = m \frac{q/2}{|\mathbf{k}_i|}$ and the wavevector length $|\mathbf{k}_i| = 2\pi/\lambda$:

$$d = m \frac{2\pi}{q} \quad (2.13)$$

This equation becomes pertinent in setups where θ is not directly measured, and data, based on more complex geometry, are often presented in *reciprocal space*, representing a function of \mathbf{q} (*vide infra*).

The overall lattice structure, defined by vectors \mathbf{a}_1 , \mathbf{a}_2 , \mathbf{a}_3 within its unit cell, a lattice plane labeled as ‘ (hkl) ’ can be set up using three points: \mathbf{a}_1/h , \mathbf{a}_2/k , and \mathbf{a}_3/l . These points feature Miller indices denoted as h , k , and l . In the context of this thesis, an exploration is undertaken on the changes in the spacing of the (100), (200), (300), and (020) planes in crystalline P3HT, as defined by Kayunkid et al. [85] (refer to section B.8)

It is essential to acknowledge that equation 2.12 or 2.13 exclusively addresses the θ or q position, respectively, of the Bragg reflections. Nevertheless, the actual intensity of a specific Bragg peak is influenced by factors such as the number of electrons in the atoms serving as scattering centers and the configuration of the electron distribution, contributing to the *atomic form factor*. [84, 86] Additionally, the intensity is further determined by the *structure factor*, which takes into account the arrangement of atoms within the unit cell. [84, 86]

In *specular* x-ray diffraction, equation 2.12 is directly employed by aligning the lattice planes of interest to enable the scanning of θ . This alignment is typically accomplished in a configuration known as a $\theta/2\theta$ setup. In this setup, the sample undergoes rotation by θ around an axis perpendicular to \mathbf{n}_{lat} for the set of parallel lattice planes under investigation. This rotation controls their angle with \mathbf{k}_i while the detector simultaneously moves by 2θ around the same axis, forming an angle of θ between the planes and \mathbf{k}_o . [84]

In the context of the thesis, since P3HT thin films have a low degree of crystallinity, the geometry of $\theta/2\theta$ would allow the beam to pass through an insufficient amount of sample material, specifically, too small or too few crystalline phases. To overcome this challenge, in GIXRD, a small incidence angle α between \mathbf{k}_i and the film plane, near the angle of total reflection, is selected. This configuration ensures that the beam travels the film over an extended distance. For instance, at $\alpha = 0.15^\circ$, the beam could penetrate through a $0.5 \mu\text{m}$ film for a distance of up to $190 \mu\text{m}$ before reaching the substrate.

The $\theta/2\theta$ geometry necessitates measurements only for the sets of parallel lattice planes with \mathbf{n}_{lat} in the $\theta/2\theta$ -plane at a time. Conversely, the fixed α in GIXRD means that θ remains constant for all lattice planes parallel to the film plane, making it impractical to probe these planes in this configuration. This characteristic positions GIXRD as a technique complementary to specular x-ray diffraction.

To comprehensively cover diffraction from all accessible lattice planes and minimize sample exposure, 2-dimensional array detectors are employed to capture the Bragg reflections. The acquired angular data is then transformed into reciprocal space, generating a reciprocal space map. [86] It is important to note that azimuthal rotation of the sample is still necessary (*vide infra*). Considering the instrument geometry, the array pixels are mapped to the coordinates of \mathbf{q} , specifically its components in parallel and perpendicular to \mathbf{n}_{film} , denoted as q_z and q_{xy} , respectively. Utilizing these coordinates, $q = |\mathbf{q}| = \sqrt{q_z^2 + q_{xy}^2}$ can be inserted into equation 2.13 to compute d . [87]

The GIXRD configuration also imposes a limitation on sample rotation, which is confined to the film-plane normal \mathbf{n}_{film} . Consequently, θ changes only for lattice planes where \mathbf{n}_{lat} has a non-zero component perpendicular to \mathbf{n}_{film} . This rotation is frequently omitted to decrease sample exposure and experiment time, especially when the crystalline domains of a sample exhibit a preferred orientation towards the film plane but are randomly rotated around \mathbf{n}_{film} —a characteristic known as *fiber texture*. [84] This situation applies to the P3HT samples investigated in [5].

2.6.2 Data Treatment

The analysis of reciprocal space maps was primarily conducted using the GIDVis software. [87] This tool, equipped with beamline specifications and geometry obtained in-situ from a reference scan using a NIST standard of LaB6 [88], can perform various functions, including the conversion of detector pixel data into q_z and q_{xy} coordinates.

To minimize interference from air scattering, data were initially recorded with a blank substrate to replicate the same geometry as in a sample measurement. Subsequently, this blank substrate data was subtracted from the sample data using a custom Mathematica script. For a more detailed examination of peaks, particularly focusing on (near-)out-of-plane (small q_{xy}) and (near-)in-plane (small q_z) features, integrated line scans along constant $q = \sqrt{q_z^2 + q_{xy}^2}$ within 3-13° off the q_z and q_{xy} axis were extracted using GIDVis.

Chapter 3

Design Strategies for Optimized Molecular p-Dopants: Decoupling Electronic and Geometric Effects

Abstract

The design of efficient molecular p-dopants for organic semiconductors relies on maximizing their electron affinity for promoting integer-charge transfer and effectively generating holes in the semiconductor host. Recently, it has been found that effects detrimental to doping efficiency such as the formation of ground-state charge transfer complexes, which results in fractional charge transfer only and in strong electron-hole interaction that reduces hole mobility, can be overcome by increasing the steric bulk of the doping agents. However, while electron affinity is typically sought to be increased by adding electron-withdrawing groups to the dopant core, enhancing its steric demand is done *via* the substitution of bulky side groups, where the latter strategy may be detrimental to the former. Here, we attempt to systematically analyze the interplay between electronic and geometric effects induced by side group addition and their impact on electron affinity. For a library of existing and proposed new molecular p-dopants based on cyclohexadiene and cyclopropane cores, we use density functional theory based modeling to contrast the effect of direct bonding of electron-withdrawing groups to the core and their bridging by a phenyl moiety, thereby decoupling electronic from geometric effects. We first demonstrate the direct relationship of the dopant EAs with the Hammett parameters of the substituents. This approach is contrasted with an analysis of the partial atomic charges at the molecular core, which reveals that its charge deficiency drives the electron affinity. To assess the dopants' capability of double doping, that is, the transfer of two electrons per dopant, we further examined their second electron affinities and the ensuing (non-)linearity of shifts in cyano vibrational modes characteristic of the degree of charge transfer with respect to the molecular charge. Our study not only provides guidelines for achieving high electron affinity dopants but also predicts several three-dimensional doping agents of record-high electron affinity, thereby, allowing to disentangle the roles of substituents, steric bulk, and that of the molecular core, which may inform the de-

sign of novel p-dopants balancing high electron affinity and steric demand. Given the agreement between the quantitative predictions (calculated EAs) and the mechanistic explanation (based on the Hammett index and the partial atomic charges), the results can serve as a solid basis for the development of future dopants.

3.1 Introduction

The p-doping of organic semiconductors (OSCs) is typically achieved by the admixture of strong molecular electron acceptors as dopants in order to induce charge transfer. [35, 46, 89, 90] Doping OSCs achieves several crucial objectives for applications not only in organic electronics such as for organic light emitting diodes (OLEDs), [91, 92] and thermoelectric energy harvesting, [93, 94] but also in hybrid (organic-inorganic) electronics, such as for the transport layer of perovskite solar cells. [95, 96] The objectives include reducing charge-injection barriers at interfaces to electrodes, [97, 98] reducing charge trap densities and depths, [36–39] as well as generating mobile holes in the host material to increase its conductivity by orders of magnitude. [40, 41, 99]

For charge transfer to efficiently occur, the electron affinity (EA) of the p-dopant should match or be higher than the ionization energy (IE) of the OSC, [32, 90] resulting in integer charge transfer (ICT) between p-dopant and OSC. However, alternatively, ground-state charge-transfer complexes (CPX) can form between them with only fractional charge transfer, which occurs following the hybridization of the frontier molecular orbitals, that is, the dopant’s lowest unoccupied molecular orbital (LUMO) and the OSC’s highest occupied molecular orbital (HOMO), [100, 101]. This process generally competes with ICT. For structurally similar dopants, CPX formation is less likely for larger EAs, but can persist even if the dopant EA exceeds the IE of the OSC, as it has been demonstrated in several works [5, 47]. To such concerns need to be added the fact that CPX and ICT tend to form preferentially in different phases of OSCs [5, 90, 102] and that the effective EA of p-dopants has been shown to be impacted both by the presence of surrounding OSC and the material phase [103, 104]. Nevertheless, efficient p-dopants should clearly feature both high EA and a molecular structure that minimizes/inhibits CPX formation.

For increasing EA, the typical strategy is to deplete the core of a conjugated molecule by the substitution of electron-withdrawing groups (EWGs) on its periphery. Notably, a large body of works has been dedicated to electron acceptors comprising a cyclohexadiene (CHD) core, where attaching cyano groups in the form of two ylidene-malononitrile groups leads to tetracyanoquinodimethane (TCNQ), [105] a molecule with an (experimental) EA of 4.23 eV. [53] Its EA can be increased by replacing the remaining hydrogens on the core with fluorine atoms as EWGs to obtain F^- , F_2^- and F_4^- -TCNQ with an EA of 4.55, 4.59 and 5.08 eV, respectively. [53] Extending the size of the core also plays a role in obtaining dopants of higher EA, both due to the possibility of attaching more EWGs and the intrinsically higher EA of molecules with more extended conjugation. Related to the former, metallic complexes can also feature a high electron affinity due to their hypervalent configurations, see for instance molybdenum tris(1,2-bis(trifluoromethyl)ethane-1,2-dithiolene) ($Mo(tfd)_3$), which has an electron affinity of 5.6 eV and has been extensively employed for the doping of OSCs. [106]

In terms of conjugated molecular dopants, hexafluorotetracyanonaphthoquinodimethane (F_6 -*TNAP*, also known as F_6 -*TCNNQ*), the direct naphthalene-like analogue to F_4 -*TCNQ*, features an even higher EA of 5.37 eV. [107] An extended computational study of substituted quinone derivatives [108] points in a similar direction: anthraquinone derivatives can achieve higher EAs than their benzoquinone and naphthoquinone counterparts. Furthermore, quinones containing stronger EWGs such as cyano and sulfonyl, have higher EAs than those with weaker EWGs such as halogen-containing groups. It is therefore not surprising that other conjugated molecules featuring a different core and several cyano substituents display very high EAs, such as hexaazatriphenylenehexacarbonitrile (*HAT-CN*) and hexacyanotrimethylenecyclopropane ($(CN)_6$ -*CP*), the former with an experimentally-determined EA of 5.4 eV [55] and the latter being the molecule with the highest reported experimental EA of 5.87 eV and is used as a dopant in the hole transport layer of OLEDs. [56, 57] It is unclear whether the higher number of cyano substituents on $(CN)_6$ -*CP* compared to F_x -*TCNQs* is responsible for the higher EA or if this difference is due to the functional core (cyclopropane (CP) versus CHD).

The synthesis of substituted *TCNQ*-like dopants has not only been done to increase the EA but also to control other functional aspects including increased solubility, miscibility with OSCs, [75] or reduced diffusivity, [68, 76].

However, such modifications often result in a decrease in EA. In a similar vein, despite the severe core strain present in cyclopropane which can lead to difficulties in synthesis, several works have been dedicated to the synthesis of dopants which such cores, and the study of their applications in electronic devices [12, 15, 57, 58, 109]. $(CN)_6$ -*CP* analogues were synthesized by Saska et al. to feature better solubility, with three of the six cyano groups being replaced with methyl esters (i.e. a trimethyl ester analogue) in *TMCN3-CP* [58], followed by dimethyl ester (*DMCN4-CP*) and monoethyl ester (*ECN5-CP*) analogues showing EAs closer to that of the parent species [12].

Chemical structures of some of the dopants discussed here and their nomenclature for the remaining of the work are shown in Figure 3.1, with $(CN)_6$ -*CP* in Figure 3.1d, and its soluble analogues in Figure 3.1e.

Furthermore, substituting three of the six cyano groups of $(CN)_6$ -*CP* by bulky perfluorophenyl groups to obtain *PF3CN3-CP* (Figure 3.1f; here we refer to it as $(F_5-Ph)_3(CN)_3$ -*CP*) was experimentally found to suppress the formation of CPX upon doping OSCs [15] by preventing intermolecular hybridization, as previously suggested [3, 46, 48]. There, reducing/eliminating CPX formation solely follows peripheral substitution and can, therefore, be achieved by chemical modification of well-established dopants. This substitution by three rings was found to be sufficient to shield the core, and comparing the doping behavior of *PF3CN3-CP* with that of F_2 -*TCNQ* of identical EA, confirmed that CPX formation can be readily suppressed by steric hindrance of the bulky dopant, as F_2 -*TCNQ* itself features no steric shielding. *PF3CN3-CP* is highly similar to a dopant referred to as PD-A (Figure 3.1f) [109] for which the same steric effects can be expected. However, the presence of cyano groups instead of fluorine atoms at the para position of the three fluorinated rings leads to a higher EA, sufficient to dope OSCs with IEs as high as 5.6 eV [59, 60]. Using bulky substituents also has the added benefit of reducing electrostatic interaction between the dopant anions and the holes generated on the OSC after integer charge transfer. This reduction in electrostatic interaction improves

the delocalization of mobile holes, thereby enhancing conductivity [110]. These results found probing CP-core dopants illustrate that planar dopants based on a CHD-core are in fact not "ideal" dopants due to their tendency to undergo CPX formation as well as the necessity to investigate other substitutions with varying electron-withdrawing strengths and steric hindrance, as well as alternative core structures to CHDs.

Altogether, existing data suggest that the number and strength of the EWGs present on conjugated molecules are controlling the EA, presumably mediated by a charge depletion of the core. Such internal charge redistribution in conjugated molecules was recently also observed experimentally by Kelvin probe force microscopy for halogen-substituted polyaromatic hydrocarbons. [111]

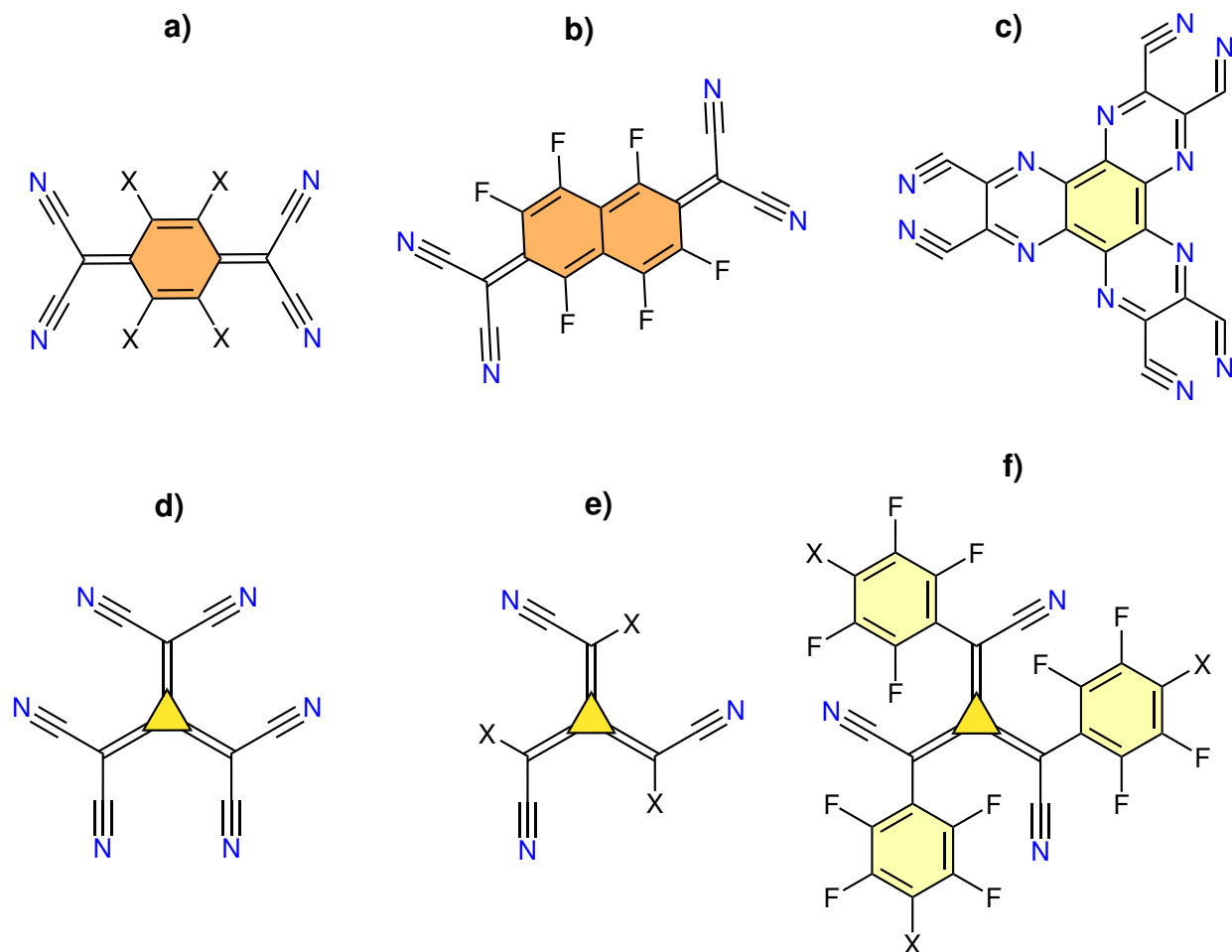


Figure 3.1: Chemical structure of some p-dopants discussed in this work. a) F_x -TCNQ; where X indicates the substitution of 1, 2, 3 or 4 hydrogen atoms by fluorine atoms. b) F_6 -TCNNQ. c) HAT-CN. d) $(CN)_6$ -CP. e) $(CO_2CH_3)_3(CN)_3$ -CP, and its higher EA analogues, $(CO_2CH_3)_2(CN)_4$ -CP, and $(CO_2CH_2CH_3)(CN)_5$ -CP, where X shows the substitution of 1, 2 or 3 cyano groups by either 1 $CO_2CH_2CH_3$ group, 2 CO_2CH_3 groups, or 3 CO_2CH_3 groups respectively. f) $(F_5-Ph)_3(CN)_3$ -CP, and its higher EA analogue $(F_4CN-Ph)_3(CN)_3$ -CP, where X represents either a fluorine atom or a cyano group.

To determine the ionicity (δ) of the charge transfer process (i.e., integer versus fractional), characteristic shifts in the cyano vibrational modes inferred from Fourier transform infrared spectroscopy (FTIR) are commonly used, where a linear relation between the shift and δ is typically assumed. [112–114] Some of us recently noted that the presence of bulky, electron-rich EWGs and/or non-monoatomic substituents in *TCNQ*- and $(CN)_6$ -*CP*-analogues can dramatically impact these modes [115] and induce large nonlinearities of the vibrational frequency shift with respect to the molecular charge, a result which was obtained by probing the second ionization of such molecules. This phenomenon is therefore likely to occur in the case of ring-containing substituents attached to dopant cores as well. It becomes particularly relevant as recent works highlighted both experimentally, using F_4 -*TCNQ*, [116] and computationally, using $(CN)_6$ -*CP*, [117, 118] the possibility of using the double ionization of a molecular dopant to inject a second charge carrier into the OSC, making the relationship between cyano vibrations and the three molecular charge states (neutral, radical anion and dianion) extremely relevant for the design of high-efficiency double-ionization dopants.

Overall, the electron-withdrawing effect of substituents has a defining impact on both the first EA (EA_1) and second EA (EA_2) of molecular p-dopants. In addition, the reduction of CPX-formation through steric shielding of the core by bulky, phenyl-like substituents comes with a cost to their EAs, which concomitantly reduces the doping strength of p-dopants. Therefore, a trade-off exists between the benefits resulting from increased EAs and sterically shielding molecular dopants for CPX suppression and electron-hole separation, since both cannot be maximized simultaneously. This trade-off likely depends on the molecular structure, influenced by the substitution patterns, the type of functional side-group, and the molecular core, all of which play a defining role in the resulting values of EA_1 and EA_2 . In addition, the experimental realization of double doping lacks systematic investigations of the relation between dopants' EA_2 and other pertinent molecular features such as the presence of EWGs and their strength, steric hindrance of the core, or even EA_1 . So far, all of these factors and relationships can only be qualitatively described, when at all possible, and therefore call for an equally systematic and comprehensive investigation.

In this work, we attempt to fill this gap in knowledge by quantitatively analyzing a large series of $(CN)_6$ -*CP*- and *TCNQ*-analogues using density functional theory (DFT), where substitution with EWGs was done both directly at the dopant's core or through phenyl groups. The present direct comparison of substituted molecular analogues allows us to derive both fundamental and practically-relevant results that can now be used to optimize the molecular design of novel p-dopants prior to their synthesis. Given the convergence of both quantitative predictions (calculated electron affinities) and mechanistic explanations (based on the Hammett index and partial atomic charges parameters), these calculations serve as a solid foundation to guide experiments.

3.2 Methods

All presented DFT calculations were carried out within Gaussian (version 09 revision E.01), [10] performed using the ω B97X-D range-separated functional from Chai and

Head-Gordon [119] and the 6-31+G(d,p) basis set. All molecular geometries for the neutral, radical anionic, and dianionic species have been optimized. Vibrational frequencies were calculated to verify the ground state nature of all molecules. The energy of the cyano stretch mode has been extracted from the same vibrational frequency calculations and was scaled according to the precomputed vibrational scaling factors from the Computational Chemistry Comparison and Benchmark Database (CCCBDB) corresponding to our model chemistry. [13] When several cyano stretch modes were present, only the highest energy one that belonged to the isolated cyano groups (and not to the cyano groups on substituents, where this is the case) was selected. For each molecule, we obtained the adiabatic first EA (referred to as EA_1) from the difference in electronic energy between neutral and radical anionic molecules as the following:

$$EA_1 = -\Delta E = E_{neutral(0,1)} - E_{radical\ anion(-1,2)} \quad (3.1)$$

Where the first number in parentheses refers to the charge and the second to the spin multiplicity. The adiabatic second EA (referred to as EA_2) was obtained in a similar way:

$$EA_2 = -\Delta E = E_{radical\ anion(-1,2)} - E_{dianion(-2,1)} \quad (3.2)$$

Wavefunctions of all optimized molecules were exported to calculate partial atomic charges from the quantum theory of atoms in molecules (QTAIM) using the software Multiwfn,[120] at the highest quality available. We used a range separation parameter ω of 0.20 (which coincides with the value by default) for all calculations, based on a benchmarking procedure that we followed in our previous work with similar molecules.[15]

Predicted EA_1 values, referred to as $EA_1^{pred.}$, were obtained from the linear fit of experimental against DFT-calculated EAs (for molecules with available experimental EA values) in analogy to our previous work. [15] The following molecules have been used in the fitting process: $(CN)_6$ -CP, $(CO_2CH_3)_2(CN)_4$ -CP, $(CO_2CH_2CH_3)(CN)_5$ -CP, $(F_5-Ph)_3(CN)_3$ -CP, F_4 -TCNQ, F_2 -TCNQ, F -TCNQ, and TCNQ. More details can be found in Figure A.1. This procedure is used to obtain quantitatively correct predictions for EA_1 (but it is not employed for EA_2 due to a lack of experimental EA_2 values). Nevertheless, the *relative* comparison of EA_2 values is reliable, as is typically the case with DFT-based methods, and as expected from the identical mechanistic and fundamental behaviors of EA_1 and EA_2 that will be demonstrated in several Figures of this work. The following equation for $EA_1^{pred.}$ is obtained based on the fitting process:

$$EA_1^{pred.}(eV) = 0.97 * EA_1^{(DFT)} + 1.128 \quad (3.3)$$

Because molecules with a different number of substituents were investigated, to quantify their electron withdrawing strength, we defined the Hammett index, which is obtained by summing Hammett substituent parameters of all the substituents on a molecule (therefore summing 6 substituents for CP cores and 8 substituents for CHD cores). In order to mediate experimental uncertainties related to the determination of Hammett parameters, the average value of both meta and para parameters was taken:

Substituent		Cyclohexadiene		Cyclopropane	
Name	Hammett index	(1)	(2)	(3)	(4)
SO_2H	0.660 ¹	$(SO_2H)_4-TCNQ$	$(PhSO_2H)_4-TCNQ$	$(SO_2H)_3(CN)_3-CP$	$(PhSO_2H)_3(CN)_3-CP$
SO_2F	0.855	$(SO_2F)_4-TCNQ$	$(PhSO_2F)_4-TCNQ$	$(SO_2F)_3(CN)_3-CP$	$(PhSO_2F)_3(CN)_3-CP$
SO_2CN	1.180	$(SO_2CN)_4-TCNQ$	$(PhSO_2CN)_4-TCNQ$	$(SO_2CN)_3(CN)_3-CP$	$(PhSO_2CN)_3(CN)_3-CP$
SO_2Cl	1.155	$(SO_2Cl)_4-TCNQ$	$(PhSO_2Cl)_4-TCNQ$	$(SO_2Cl)_3(CN)_3-CP$	$(PhSO_2Cl)_3(CN)_3-CP$
SO_2CH_3	0.620	$(SO_2CH_3)_4-TCNQ$	$(PhSO_2CH_3)_4-TCNQ$	$(SO_2CH_3)_3(CN)_3-CP$	$(PhSO_2CH_3)_3(CN)_3-CP$
SO_2CF_3	0.895	$(SO_2CF_3)_4-TCNQ$	$(PhSO_2CF_3)_4-TCNQ$	$(SO_2CF_3)_3(CN)_3-CP$	$(PhSO_2CF_3)_3(CN)_3-CP$
$COCH_3$	0.440	$(COCH_3)_4-TCNQ$	$(PhCOCH_3)_4-TCNQ$	$(COCH_3)_3(CN)_3-CP$	$(PhCOCH_3)_3(CN)_3-CP$
$COCF_3$	0.715	$(COCF_3)_4-TCNQ$	$(PhCOCF_3)_4-TCNQ$	$(COCF_3)_3(CN)_3-CP$	$(PhCOCF_3)_3(CN)_3-CP$
CO_2CH_3	0.410	$(CO_2CH_3)_4-TCNQ$	$(PhCO_2CH_3)_4-TCNQ$	$(CO_2CH_3)_3(CN)_3-CP$	$(PhCO_2CH_3)_3(CN)_3-CP$
CO_2CF_3	0.685 ²	$(CO_2CF_3)_4-TCNQ$	$(PhCO_2CF_3)_4-TCNQ$	$(CO_2CF_3)_3(CN)_3-CP$	$(PhCO_2CF_3)_3(CN)_3-CP$
CH_3	0.050	$(CH_3)_4-TCNQ$	$(PhCH_3)_4-TCNQ$	$(CH_3)_3(CN)_3-CP$	$(PhCH_3)_3(CN)_3-CP$
CF_3	0.485	$(CF_3)_4-TCNQ$	$(PhCF_3)_4-TCNQ$	$(CF_3)_3(CN)_3-CP$	$(PhCF_3)_3(CN)_3-CP$
CN	0.610	$(CN)_4-TCNQ$	$(PhCN)_4-TCNQ$	$(CN)_6-CP$	$(PhCN)_3(CN)_3-CP$
Ph	0.025	$(Ph)_4-TCNQ$	N/A	$(Ph)_3(CN)_3-CP$	N/A
F_5-Ph	0.265	$(F_5-Ph)_4-TCNQ$	N/A	$(F_5-Ph)_3(CN)_3-CP$	N/A
F_4CN-Ph	N/A ³	$(F_4CN-Ph)_4-TCNQ$	N/A	$(F_4CN-Ph)_3(CN)_3-CP$	N/A
F	0.200	F_4-TCNQ	N/A	N/A	N/A
H	0.000	$TCNQ$	N/A	N/A	N/A

Table 3.1: Substituents and molecular nomenclature employed for molecules with the same number of cyano groups and substituents (Figures 3.2a-d). The first two columns refer to the substituents used and their Hammett index, calculated from values found in Ref. [11], except when specified otherwise. The four other columns contain the names of the molecules either with a CHD or CP core, both when substituents are connected directly to the core (substitution patterns (1) and (3)) or through phenyl groups (substitution patterns (2) and (4)). Note that we did not include the two molecules from Ref. [12] in this table, as molecules with a very analogous substituent ($(CO_2CH_3)_3(CN)_3-CP$) are already listed. N/A indicates molecules that have not been studied – the three phenyl-containing substituents (Ph , F_5-Ph , F_4CN-Ph) were not considered on a bridging phenyl group, as discussed in the Methodology, and the two monoatomic substituents (F , H) are provided as reference, because $TCNQ$ and F_4-TCNQ are experimentally well studied dopants.

¹No value found; added the difference between SO_2CH_3 and SO_2CF_3 to SO_2F .

²Similarly added the difference between between $COCF_3$ and $COCH_3$ to CO_2CH_3 .

³No value found.

$$Hammett_{index} = \sum_{substituents} \frac{1}{2} (Hammett_{para} + Hammett_{meta}) \quad (3.4)$$

Given that the ability of substituents to withdraw electrons is often quantified using their Hammett substituent parameters, this allows to index all molecules with an independent metric according to their substitution.

3.3 Results and discussion

3.3.1 Choice of molecules

Chemically-diverse functional side-groups with highly different electron withdrawing abilities were selected for our study and are given in the first column of Tables 3.1 and 3.2. The choice was informed by the Hammett substituent parameters found in the popular reference by Hansch et al. (Ref. [11]); all cases where parameters were taken from elsewhere are identified in Tables 3.1 and 3.2. All substituents are either connected directly to the core, following substitution patterns (1) and (3), or in the para position of a phenyl group connected to the core, following substitution patterns (2) and (4), as illustrated in the left column of Figure 3.2. This is done for both CHD and CP cores such that each substituent is featured on four different molecules (patterns (1)-(4)), except for the perfluorophenyl, phenyl, and F_4CN-Ph groups, which were themselves not considered connected through a phenyl. In addition, we also explored the effect of the number of substituents by replacing all cyano groups with a given substituent (for a selection of the substituents probed in this work), as schematized in the right column of Figure 3.2, patterns (5)-(7). Molecules logically corresponding to the missing pattern (8) were not included given the high number of possible conformations and the resulting complexity of the analysis (see Figure A.2). To align with pertinent literature, we also considered additional molecules featuring a CP core (Figures 3.1e and 3.1f) that have been recently synthesized and employed as molecular dopants.[12, 59, 60]

For the CHD-based pattern (1), we found in the early stages of this work that the presence of large and strongly electron-withdrawing substituents can lead to significant bending of the core, and that in such cases boat conformations (all substituents pointing in the same direction) are more stable than chair conformations (every two substituents pointing in opposite direction); additional details are provided in Figure A.3. Note that for the smaller monoatomic substituents (i.e. leading to molecules such as *TCNQ* and F_4-TCNQ), the CHD core remains completely planar. For the CP-based pattern (3), while the presence of substituents does not lead to bending of the core, two configurations are possible, and we found lower electronic energy solutions in molecules where the three substituents point in the same direction (leading to a higher dipole but lower energy) rather than one substituent in the direction opposite to the two others (leading to a lower dipole but higher energy). For patterns (2) and (4), no bending of the core was observed, and configurations where all the phenyl groups share the same dihedral angle – with the same sign with respect to the core – were found to lead to lower energy solutions than other conceivable scenarios. The impact of the substituents’ orientation on phenyl groups (patterns (2) and (4)) is discussed in Figure A.4. Only molecules in their lowest electronic energy conformation were used in this work.

All molecules have been summarized in the following way: First, molecules of *equal number of substituents and cyano groups* are given in Table 3.1 (patterns (1)-(4)). Second, molecules with *all cyano groups replaced by the same substituents* (patterns (5)-(7)) are listed in Table 3.2. The properties of all molecules most relevant for the upcoming sections (Hammett indices, EAs, QTAIM charges) are listed in Tables A.1-A.4.

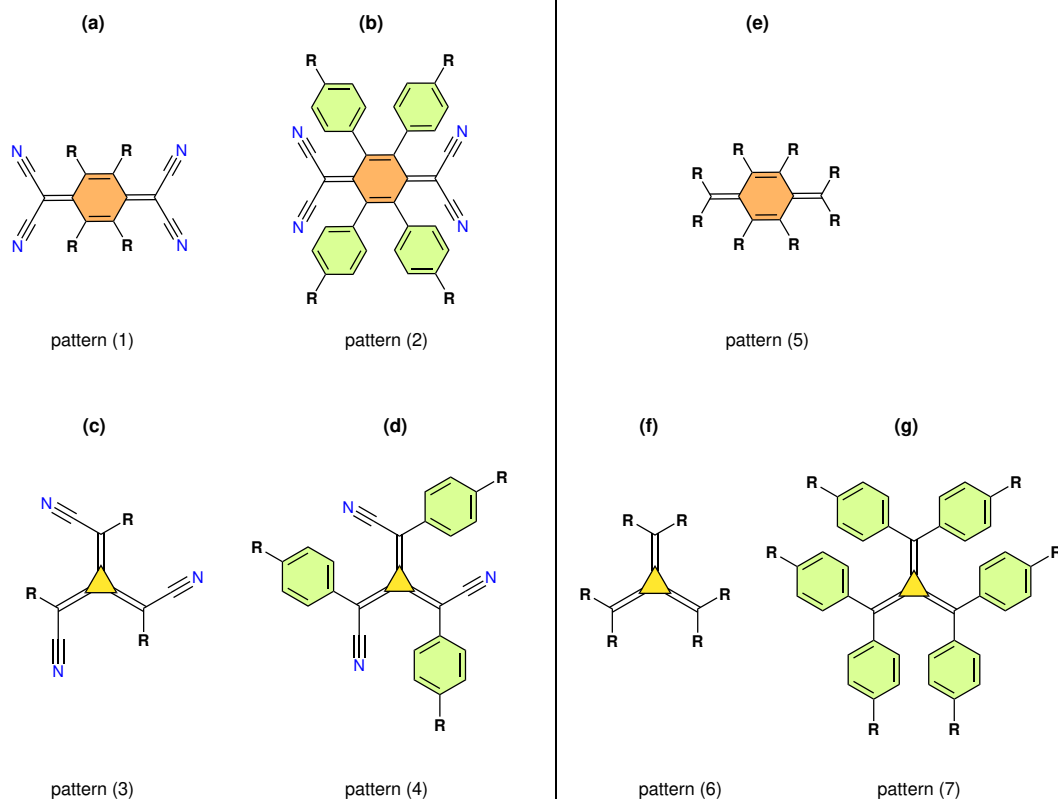


Figure 3.2: Substitution pattern nomenclature. a) Pattern (1): four substituents (R) directly on a CHD core. b) Pattern (2): same as a) but through phenyl groups. c) Pattern (3): three substituents directly on a CP core. d) Pattern (4): same as c) but through phenyl groups. e) Pattern (5): 8 substituents directly on a CHD core. f) Pattern (6): six substituents directly on a CP core. g) Pattern (7): same as f) but through phenyl groups.

3.3.2 Hammett indices predict electron affinities

First considering the CHD core (substitution patterns (1), (2) and (5)), EA_1 and EA_2 show a slightly increasing trend with the Hammett index (Figure 3.3a), however, with large spread and an apparent saturation for the species where the substituents are connected directly to the core ((1) and (5)) – see Figures A.5 and A.6). This is due to the fact that both larger and stronger electron-withdrawing groups tend to break the molecular planarity when close to the CHD core in the neutral state (although molecules with monoatomic or very weakly electron-withdrawing substituents still feature a planar core in the neutral state). The additional electron of the radical anion helps support the structure of the molecule, notably by restoring most of the core planarity. However, the reorganization energy involved in re-stabilizing the molecules then leads to lower-than-expected EAs.

Geometric distortions induced by EWGs connected directly to CHD cores thus lead to electronic instabilities and prevent the molecules from reaching high EAs. Instead, connecting EWGs through phenyl rings offers an elegant solution to (i) the issue of core bending, as it effectively decouples the substituents from the backbone geometry, and (ii) to that of CPX formation as it induces steric bulk, which also increases electron hole

Substituent		Cyclohexadiene	Cyclopropane
Name	Hammett	(5)	(6,7)
CH_3	0.050	$(CH_3)_8$ -CHD	$(CH_3)_6$ -CP
CF_3	0.485	$(CF_3)_8$ -CHD	$(CF_3)_6$ -CP
Ph	0.025	$(Ph)_8$ -CHD	$(Ph)_6$ -CP
F_5 -Ph	0.265	$(F_5$ -Ph) $_8$ -CHD	$(F_5$ -Ph) $_6$ -CP
SO_2F	0.855	N/A	$(SO_2F)_6$ -CP
SO_2CN	1.180	N/A	$(SO_2CN)_6$ -CP
SO_2Cl	1.155	N/A	$(SO_2Cl)_6$ -CP
PhF	0.200	N/A	$(PhF)_6$ -CP
$PhCF_3$	0.485	N/A	$(PhCF_3)_6$ -CP
$PhCCl_3$	0.430	N/A	$(PhCCl_3)_6$ -CP
$PhCBr_3$	0.285	N/A	$(PhCBr_3)_6$ -CP
$PhCO_2CH_3$	0.410	N/A	$(PhCO_2CH_3)_6$ -CP
$PhOH$	-0.125	N/A	$(PhOH)_6$ -CP

Table 3.2: Substituents and molecular nomenclature employed for molecules with only substituents and no cyano groups (Figures 3.2e-g). The table follows the same idea as Table 3.1 but all molecules follow patterns (5), (6) or (7). The Hammett indices of the last six substituents (PhF to $PhOH$) are the same as if connected directly to the core (Table 3.1); N/A indicates molecules that have not been studied due to the excessive number of possible configurations as discussed in Figure A.2.

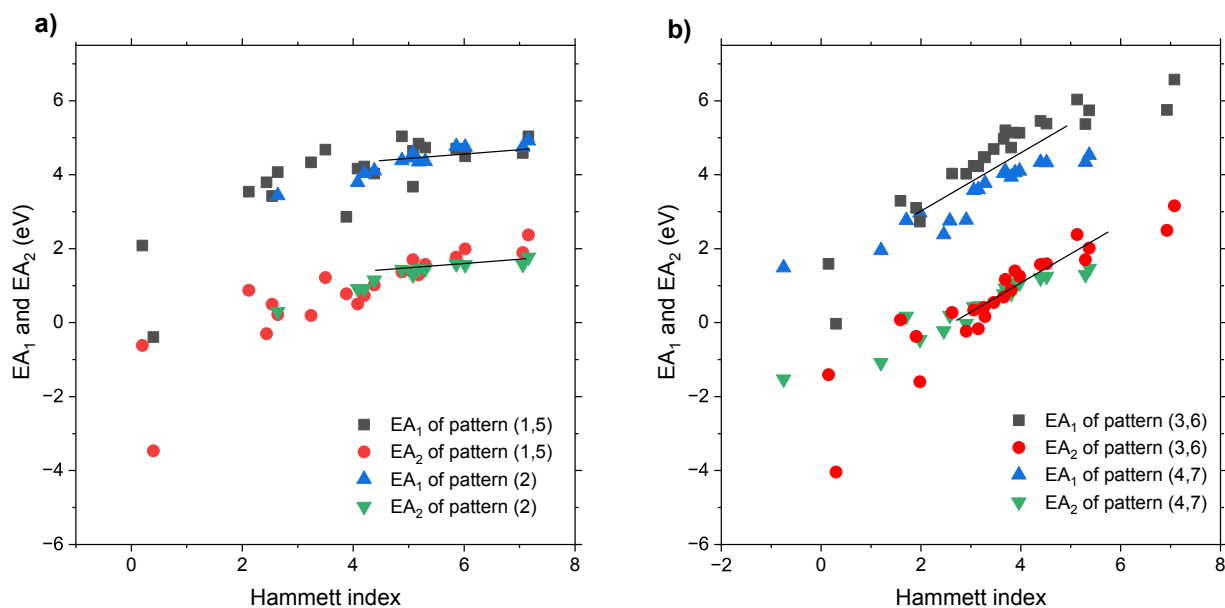


Figure 3.3: Relationship between the Hammett index and EAs for the molecules listed in Tables 3.1 and 3.2. a) EA_1 and EA_2 of CHD-based molecules, for substitution patterns (1), (2), and (5); trend quality is particularly poor for EA_1 of patterns (1) and (5) (black squares). b) EA_1 and EA_2 of CP molecules, for patterns (3), (4), (6), and (7). The lines have been added as guides to the eye to highlight the general behavior discussed in the text.

separation after charge transfer. Figure 3.3a also shows EA_1 and EA_2 of CHD molecules with the substituents connected through a phenyl (pattern (2)), where clear linear trends between Hammett index and EAs can now be observed because the phenyl groups allow connecting the substituents to the core without disturbing its geometry in the neutral state.

We now turn to the investigation of the same substituents on the CP-based molecules (patterns (3), (4), (6), and (7)), where the relation between Hammett index and the EAs is shown in Figure 3.3b. Most noteworthy, even without phenyl, both EA_1 and EA_2 display clear linear trends against the Hammett index (aside from slight saturation at very high values), and trends become again sharper with the phenyl groups. This reflects the fact that CP-core molecules feature a planar core even in neutral state as can be inferred from the Cartesian coordinates of the relevant atoms provided in the last section of the SI.

Linear fits for all molecular patterns (1) - (7) were performed, details and fit parameters are reported in Table A.5, and in Figures A.5-A.8. As expected, all molecules have a lower EA_2 than EA_1 . When connected through the phenyl, substituents become less effective at increasing the EA, which can be inferred from the smaller slopes of the linear fits of patterns (2), (4) and (7), as summarized in Table A.5. This can be explained by the fact that they are further away and the (dihedral) angle between the phenyl and core planes decreases the electron-withdrawing effect of the substituents, leading to generally lower EAs. CP cores (patterns (3) and (6)) have vastly superior EA_1 than their CHD counterparts due to the fact that the core is not destabilized even with the substituents directly connected to it. Finally, it is possible to directly use the linear fit equations (Table A.5) for patterns (2), (3), and (4)-(7) to predict EA_1 and EA_2 , solely from the Hammett index of the molecules. This can considerably simplify the future exploration of possible analogues molecular dopants.

The insights gained from analyzing the electron-withdrawing abilities of substituents and their impact on EAs lead to three key conclusions. (i) For the CP core, substituents can be connected directly to the neutral core without significantly distorting the molecule. This is in marked contrast to neutral molecules with a CHD core, thus, leading for a given substituent to much higher EA_1 for the CP-based species. (ii) Connecting substituents through phenyl groups significantly lowers the electronic impact of the substituents (as deduced from the comparison of the fit slopes). (iii) Nevertheless, the presence of phenyl groups might be otherwise beneficial to inhibit CPX formation through steric bulk and reduce electron hole interaction; in this case, molecules with a CHD core feature systematically higher EA_1 than those with CP, which is related to the unsubstituted core itself and will be discussed more in-depth below.

3.3.3 Relation between atomic charge on the core and electron affinity

As a next step, we aim to more formally probe the mechanistic relationship between EWGs and the resulting EAs. If the EAs stem from electron-depletion of the core, then the calculation of partial atomic charges on the molecules *before* undergoing charge transfer should allow to quantify the total effect of the substituents on the charge density and predict the tendency to accept electrons. The relationship between the sum of partial atomic charges on core atoms of neutral species and their EA_1 is shown in Figure 3.4 for sub-

stitution patterns (2), (3), (4), (6), and (7). For molecules with substituents connected directly to CHD cores (substitution patterns (1) and (5)), the EA_1 cannot be predicted by the atomic charges on the core of the neutral molecule, again, because of geometric distortions induced by the substituents (Figure A.9a).

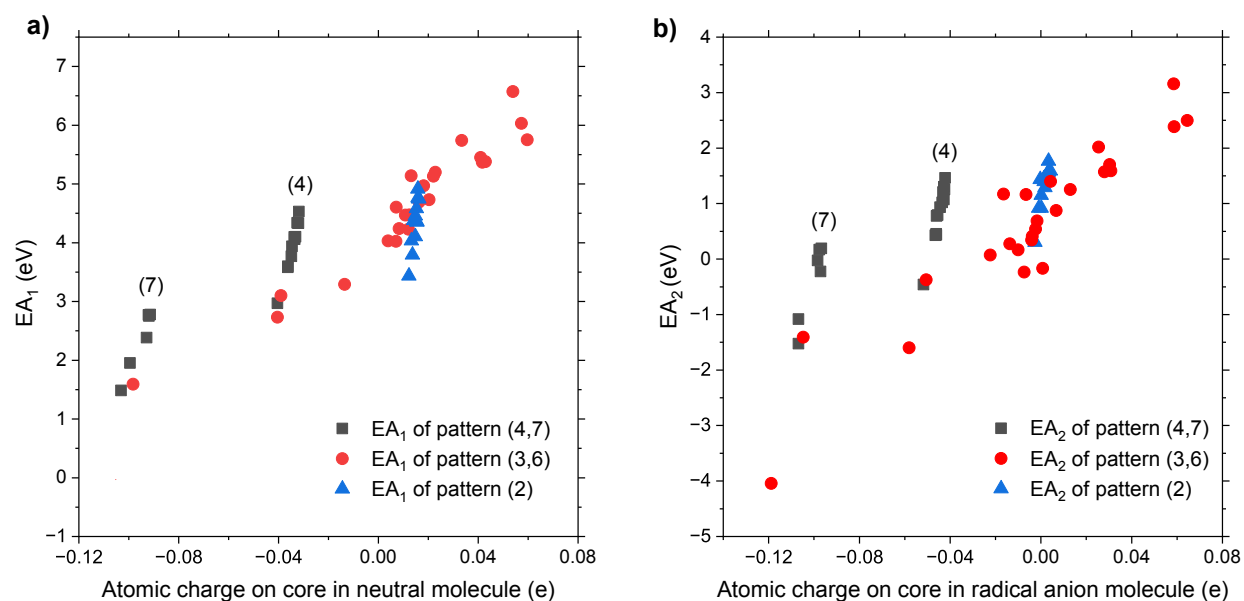


Figure 3.4: Relationship between atomic charges and EAs. The sum of partial atomic charges on the core atoms in neutral molecules against their EA_1 is shown in a) while the sum of partial atomic charges on the core atoms in radical anionic molecules against their EA_2 is shown in b), in both cases for substitution patterns (2), (3), (4), (6), and (7). Data points for patterns (4) and (7) segregate on individual lines which have been identified directly on the Figure (this cannot be done for patterns (3) and (6) since they are mixed). The relationship for patterns (1) and (5) is poor because of geometric distortions, see Figure A.9.

However, for substitution patterns (1) and (5), contrary to the relationship between EAs and Hammett indices (Figure 3.3), the situation is *not* largely improved when moving to the relationship between EA_2 and atomic charge on the core of the radical anion (see Figure A.9b), indicating that partial atomic charges are more sensitive to geometric disturbances for the prediction of EAs than Hammett indices, which reinforces the interest of the latter for screening large numbers of molecules.

In marked contrast, when the substituent is geometrically decoupled from the core using phenyl groups (substitution patterns (2), (4), and (7)), extremely sharp linear trends are obtained, where less negative atomic charge on the core directly leads to higher EA. For substitution patterns (3) and (6), linear trends can be observed, although less sharp than for patterns (2), (4) and (7). Notably, the range covered by the atomic charges of patterns (3) and (6) is much larger than with phenyl groups, which is expected given that for the former the core is directly exposed to the electron withdrawing effect of the sub-

stituents. Similar trends are found for EA_2 in Figure 3.4b, which is here predicted by the sum of partial atomic charge on the core atoms of the radical anion. Linear fit parameters for all molecular patterns (1)-(7) are reported in Table A.6, and in Figures A.9-A.12. Altogether, these data conclusively demonstrate the direct relationship between charge depletion of the core of a molecule and its tendency to accept an electron.

3.3.4 Cyano vibrational modes

In a recent work,[115] we highlighted that the shift of cyano vibrations with the molecular charge can be highly non-linear, with severe implications for the experimental quantification of the degree of charge transfer in doping applications. This was hypothesized to be more likely the case for molecules with a CP core than a CHD core due to the lower cyano-substituent distance (a side effect of the different molecular symmetry), and was found to occur in molecules featuring more electron-rich and larger substituents. For example, this was the case for $(SO_2Cl)_3(CN)_3-CP$, which is also probed here in addition to other similar sulfonyl-containing molecules of pattern (3). Given the high number of molecules covered in the present work, the non-linearity of cyano vibrations shifts can now be systematically probed. DFT-calculated shifts of cyano vibrations were investigated for all the molecules across their three different charge states (neutral, radical anionic, and dianionic). We selected only the highest wavenumber cyano vibration that belongs to the backbone cyano groups instead of those at the substituents, if present (e.g., for SO_2CN); wavenumbers corresponding to these vibrations for all molecules are given in Tables A.7-A.10.

Closer inspection of individual trends suggests that our chosen range of molecules covers the complete realm of possibilities, from completely linear, in the case of planar molecules, to molecules featuring pronounced second-order behavior of both signs, even reaching a maximum shift *before* reaching the dianionic state (i.e., the dianion exhibits a smaller shift than the radical anion). A selection of molecules representative of this diversity of behaviors is shown in Figure 3.5a.

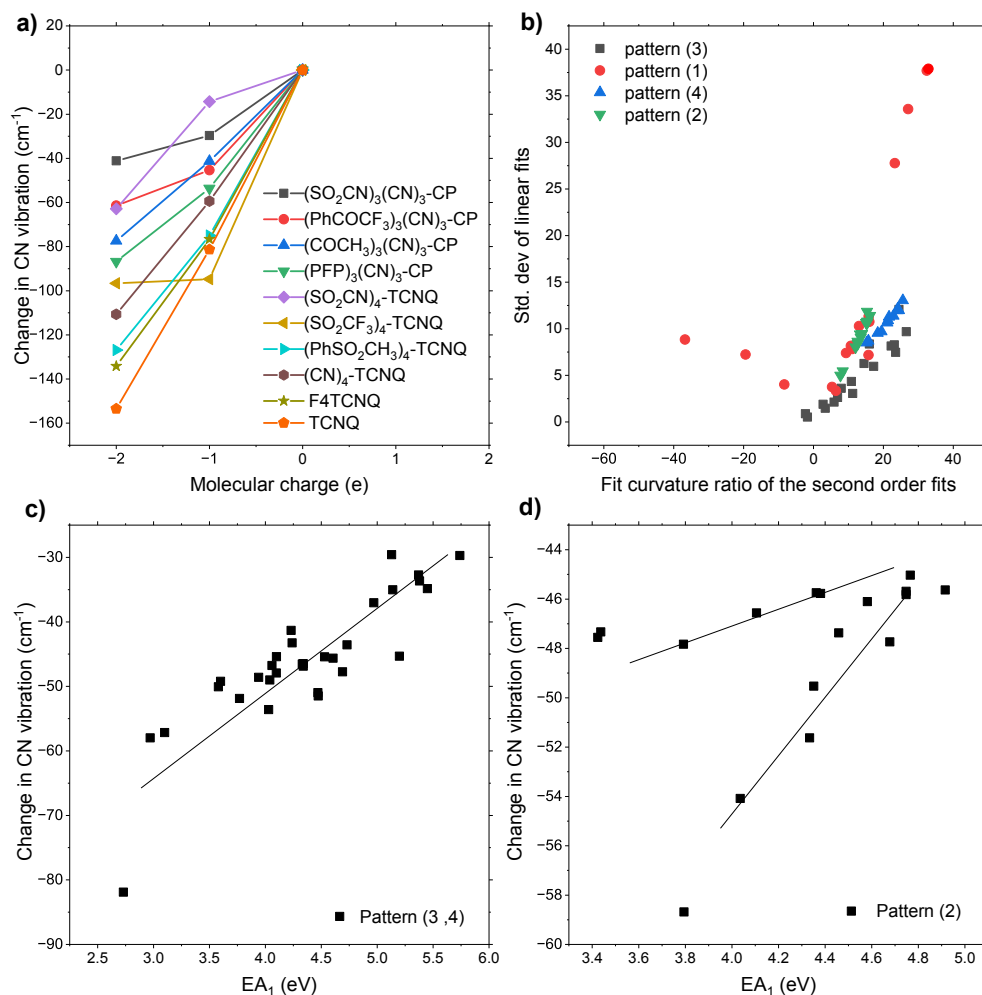


Figure 3.5: Cyano vibration shifts across the three different charge states of the molecules (neutral, radical anionic and dianionic). a) Shifts of the highest wavenumber cyano vibrational mode as a function of the molecular charge for a selection of electron acceptors. b) Standard deviation of the linear fits for CHD-based (patterns (1) and (2)) and CP-based molecules (patterns (3) and (4)) plotted against the fit curvature ratio (see text); $(\text{SO}_2\text{CN})_4\text{-TCNQ}$ was excluded from the plot because the ratio is extremely high (622%) due to coupling between the backbone cyano and (SO_2CN) vibrations. c) Relationship between EA_1 and cyano vibration shifts between the radical anionic and neutral molecules for molecules with a CP core (patterns (3) and (4)). d) Relationship between EA_1 and cyano vibration shifts between the radical anionic and neutral molecules for molecules with a CHD core (pattern (2)).

Following the approach introduced in previous work, [115] to quantify the deviation from linearity, first and second-order fits to the position of cyano vibrations against the molecular charge are performed as follows:

$$\text{First order fit} = B_1x + C \quad (3.5)$$

$$\text{Second order fit} = B_2x^2 + B_1x + C \quad (3.6)$$

Results are compiled in Tables A.11-A.14. Even slight deviations from linearity can induce significant error due to the uncertainty in the proper fitting model to assume (first or second order) in the quantification of charge transfer on the basis of cyano vibration shifts, as illustrated in Figure A.13. As a figure of merit to simply quantify non-linearity, a fit curvature ratio (FCR) is introduced, which we define for *second-order fits* as the division of the second-order coefficient (B_2) by the first-order one (B_1):

$$\text{Fit Curvature Ratio} = B_2/B_1 \quad (3.7)$$

A positive FCR indicates that the cyano shift towards the dianion is less pronounced than a linear fit suggests, a FCR of zero indicates that the shift is perfectly predicted by a linear fit, and a negative FCR indicates that the shift is more pronounced than suggested by a linear fit. Then, to quantify how much this non-linearity leads to an error in the correspondence between cyano vibration wavenumber and the molecular charge when assuming a *linear fit*, the standard deviation of each linear fit is calculated as follows:

$$\text{Standard Deviation} = \sqrt{\text{Residual Sum of Squares}} \quad (3.8)$$

Where the $1/\sqrt{n}$ term was omitted because it is always equal to 3. The standard deviation is then represented against the FCR for each molecule in Figure 3.5b.

The different substitution patterns are found on distinct trends, although these trends mostly coincide for CHD cores. Interestingly, the resulting standard deviation for the same FCR is generally higher for CHD cores, as visible from the y-axis position of points with the same fit curvature ratio in Figure 3.5b, and this remains true even for the substituents on the phenyl groups. This can be traced back to the fact that the error is more symmetrically spread out across the charge states for CPs than for CHDs, while the error is more pronounced for the diaionic states than for the radical anionic and neutral states. This reflects fundamentally distinct behaviors of the two cores regarding EA_2 and is presumably related to restoring aromaticity in CHDs (see discussion in the next section).

Furthermore, for positive FCRs, CP-core molecules are found to feature much higher non-linearity of the cyano shift than CHD-core molecules, as can be inferred from the fact that the majority of CP molecules extend further right on the x-axis. The four CHD molecules extending very far right ($(SO_2Cl)_4$ -TCNQ, $(SO_2CH_3)_4$ -TCNQ, $(SO_2CF_3)_4$ -TCNQ and $(CO_2CF_3)_4$ -TCNQ) and the three CHD molecules extending far into negative FCRs ($(CF_3)_4$ -TCNQ, $(SO_2H)_4$ -TCNQ, and $(SO_2F)_4$ -TCNQ) are all molecules that have large amount of physical reorganization upon charging.

On this basis, the relationship between vibrational mode shifts and the electronic properties probed in this work can now be explored. Strongly linear relationships between the cyano shift upon accepting the first electrons and EA_1 (Figures 3.5c and 3.5d) are found. This aligns perfectly with our previous discussion: molecules with higher EA_1 may exhibit less change in atomic charge on the *cyano* atoms, as the core has already been depleted of charge towards these substituents in the neutral state. Atomic charges on the core themselves do not predict the shift of cyano vibrations well, in line with past work highlighting that cyano vibrations are predicted instead by the product of atomic

charges on the cyano carbon and nitrogen atoms, within the limit that the cyano groups do not interact with the other substituents [115]. This is rather surprising as the charge on the core was shown to be responsible for the EAs in the previous section. This analysis suggests that the EA better captures the sum of intricate changes between the neutral and radical anionic molecules, both electronic and physical, that also lead to the shift of cyano vibrations. Altogether, the results presented in this section clarify fundamental aspects related to a non-linearity of cyano vibration shifts upon charging, i.e., the error that these can induce in deducing the degree of charge transfer as well as the relationship with various substitution patterns.

3.3.5 Comparison of molecular factors and selected molecules of interest

We now focus on the role of molecular factors in defining the EAs, that is, the presence of phenyl groups and the type of core. A series of molecules of interest for CP and CHD based cores are selected, and the balance between their EAs and steric shielding is discussed in the context of molecules that have not yet been experimentally employed (Table 3.3). This section demonstrates how the results presented in this work can be used to guide predictive design of molecular p-type dopants.

To simplify the analysis of the role of phenyl groups, only molecules with CP cores are displayed in Figure 3.6, since trends tend to be clearer than for CHDs (for which the data are still both qualitatively and quantitatively similar, see Figure A.14). Figure 3.6a illustrates the EAs of molecules with the same substituent connected either directly to the core (pattern (3)) or through a phenyl group (pattern (4)). The connection through a phenyl decreases the impact of the substituent, as molecules of (3) have systematically lower EAs than their equivalents in (4). From the slopes of linear fits for molecules with a CP core (0.59 and 0.54 for EA_1 and EA_2 , respectively) we find that connecting substituents through phenyl rings decreases their ability to elevate EA_1 and EA_2 by 41% and 46% respectively, while the intercept in the fits reflects the impact of the phenyl substituents alone (see fit data in Table A.15).

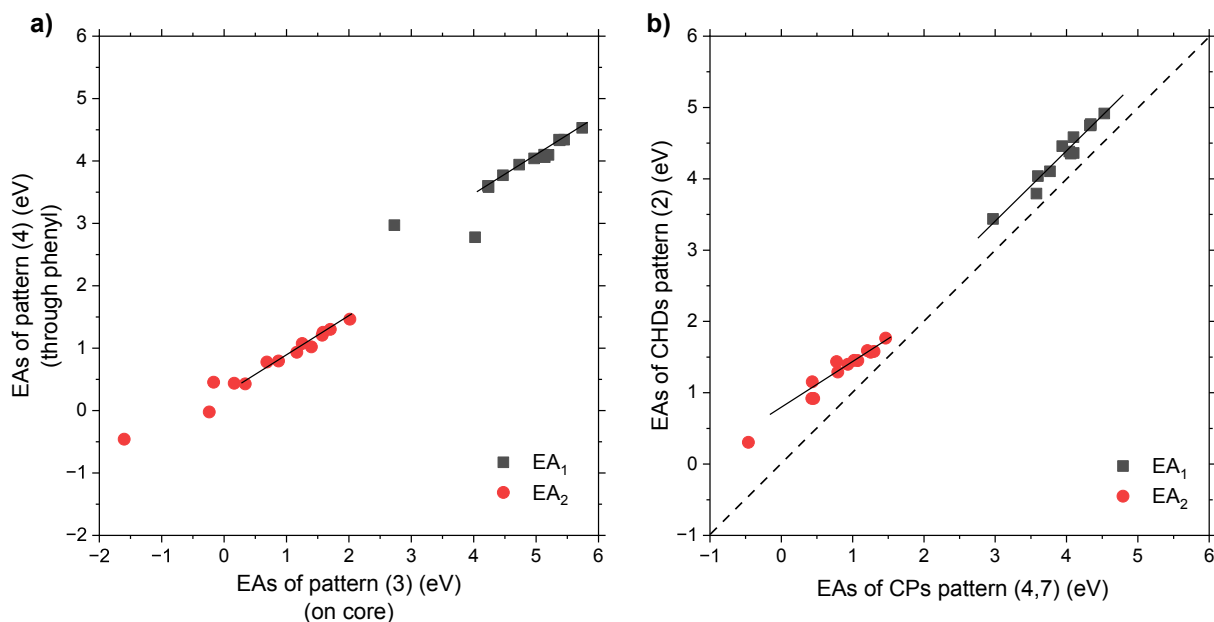


Figure 3.6: Impact of molecular factors on EAs. a) Role of through-phenyl-substitution on the EA_1 and EA_2 of molecules with a CP core. Note that to supplement the comparison $(CF_3)_6$ -CP and $(PhCF_3)_6$ -CP were added despite not being part of patterns (3) or (4). b) Role of the core type on EA_1 and EA_2 for molecules with a phenyl group. The dashed line represents the identity line, i.e. where the points would lie if molecules with the same substituents but different cores had identical EAs.

Then, the role of the core is isolated by representing the electron affinities of CHDs against those of CPs in Figure 3.6b for molecules where significant geometrical changes between charge states can be excluded (i.e. with phenyl groups – patterns (2), (4) and (7)). Trends are visibly strongly linear; linear fits were performed and the resulting parameters are listed in Table A.16. The same analysis was performed for molecules without phenyl groups – patterns (1), (3), (5) and (6) – in Figure A.15. For EA_2 , the trend is linear but more dispersed while for EA_1 the lack of clear trend due to the geometrical changes of the molecules with a CHD core can be seen.

Two major conclusions can be drawn from Figure 3.6b and the corresponding fits. First, the slope for EA_1 is *exactly* 1, which shows that the substituents on different cores have the same impact on EA_1 (provided they follow the same substitution patterns as done in this work). The differences in values must then be ascribed to an intrinsic effect of the core which is reflected in the intercept (i.e., substituents on a CP molecule yielding an EA_1 of 0 eV, would lead to a molecule with EA_1 of 0.39 eV on a CHD core). Note that it can be excluded that the higher EA_1 values of the CHDs are due to the higher number of substituents, as this would be reflected in the slope. Second, this does *not* hold for EA_2 where the slope is 0.74, meaning that same substituents have a *higher* ability with CP cores to increase EA_2 . However, the intercept of 0.68 eV implies that the CHD core intrinsically features a higher EA_2 , and that the difference between both cores is more pronounced than for EA_1 . This higher intrinsic EA_2 of CHD cores counterbalances the

fact that substituents are more effective at increasing EA_2 on CP cores. The parameters of this linear fit imply that beyond a DFT-calculated EA_2 of 2.61 eV, CP-core-based molecules become increasingly more advantageous for double doping purposes [116–118] than their CHD-based analogues, while the reverse is true below 2.61 eV. This value is higher than all calculated molecules except one, and is well above the DFT-calculated EA_2 of F_4 -TCNQ and CN_6 -CP (0.19 and 0.69 eV respectively). Many of the molecules in this work, with both core types, feature EA_2 values higher than F_4 -TCNQ and CN_6 -CP and are, therefore, sufficient to induce double doping to OSCs. It is noted that the parameters extracted from the fits of Figure 3.6b are qualitatively in line with results of the past section showing that EA_1 and EA_2 behave differently across the two cores.

A selection of molecules taken from those calculated thus far and which we regard as particularly interesting are highlighted in the summary Table 3.3. There, we included molecules that have been used experimentally for doping OSCs as well as some of the, in our view, most exciting molecules studied here to facilitate the rational molecular design of p-dopants featuring both high EA and steric bulk.

First focusing on molecules with a CP core in Table 3.3, by adding phenyl groups to obtain $(Ph)_3(CN)_3$ -CP (molecule **B**) from $(CN)_6$ -CP (molecule **A** in Table 3.3) in order to induce steric bulk, a stark *decrease* in both $EA_1^{pred.}$ and EA_2 is obtained. EAs of sterically-shielded molecules like **B** can be increased by connecting EWGs on phenyl groups and, as established above, with the effect of the substituents being decreased by around half in this configuration; $(PhCN)_3(CN)_3$ -CP (**C**) is expected to be very similar to $(F_5-Ph)_3(CN)_3$ -CP (**D**) given that half of the Hammett index of a cyano group is very close to the Hammett index of a perfluorophenyl group (see Tables 3.1 and 3.2), and we find that this is indeed the case. While the two molecules are very similar, we note that (**D**) should, in principle, be more effective at shielding the core in the solid state due to the higher rotation barrier of perfluorophenyl rings[115] which helps maintaining its twisting out of the plane defined by the core.

This molecule was synthesized recently [15], where it was demonstrated that the molecule does not undergo formation of charge transfer complexes while doping OSCs. Also noting the largely superior (more than twice) Hammett index of cyano groups compared to fluorine atoms and perfluorophenyl groups, the higher $EA_1^{pred.}$ and EA_2 of (**A**) compared to (**D**) is not surprising, and naturally suggests tetrafluorocyanophenyl groups as highly promising substituents. Note that $(F_4CN-Ph)_3(CN)_3$ -CP (**E**) indeed showcases an excellent $EA_1^{pred.}$ of 5.59 eV, and has been employed for the doping of relatively high IE OSCs (5.6 eV). [59, 60] This species approaches what could be considered an ideal dopant in terms of doping performances, with excellent steric shielding, as well as high $EA_1^{pred.}$ and EA_2 . Its $EA_1^{pred.}$ compares for instance favorably with that of $(CO_2CH_3)_3(CN)_3$ -CP (**F**, with 5.24 eV) and that of analogues derivatives synthesized recently to feature better solubility than **A**, [12, 58] while additionally benefiting from steric bulk. The fit of EA_1 against the Hammett index for patterns (**3**) and (**6**) shown in Figure 3.3b allows us to calculate a Hammett index for the tetrafluorocyanophenyl group of 0.68 ± 0.18 , which is similar to that of the cyano group itself.

It is worth pointing out that substituents based on sulfonyl groups emerge as ex-

Label	Name	EA_1^{DFT}	EA_2^{DFT}	$EA_1^{pred.}$
A	$(CN)_6-CP$	4.97	0.69	5.95
B	$(Ph)_3(CN)_3-CP$	3.10	-0.38	4.14
C	$(PhCN)_3(CN)_3-CP$	4.04	0.78	5.05
D	$(F_5-Ph)_3(CN)_3-CP$	4.03	0.27	5.04
E	$(F_4CN-Ph)_3(CN)_3-CP$	4.61	1.16	5.59
F	$(CO_2CH_3)_3(CN)_3-CP$	4.24	0.34	5.24
G	$(PhSO_2CN)_3(CN)_3-CP$	4.53	1.46	5.52
H	$(SO_2CN)_3(CN)_3-CP$	5.74	2.02	6.70
I	$(SO_2CN)_6-CP$	6.57	3.16	7.51
J	$TCNQ$	3.79	-0.30	4.81
K	$(Ph)_4-TCNQ$	3.42	0.49	4.45
L	$(PhCN)_4-TCNQ$	4.38	1.44	5.37
M	$(F_5-Ph)_4-TCNQ$	4.68	1.22	5.67
N	F_4-TCNQ	4.33	0.19	5.30
O	$(F_4CN-Ph)_4-TCNQ$	5.22	1.81	6.19
P	$(CN)_4-TCNQ$	5.04	1.37	6.02
Q	$(SO_2CN)_4-TCNQ$	5.04	2.37	6.02
R	$(PhSO_2CN)_4-TCNQ$	4.92	1.77	5.90

Table 3.3: Selected molecules of interest for the discussion of EAs and steric shielding. Relevant experimentally-characterized species were added for comparison; $EA_1^{pred.}$ values were calculated as described in the Methodology section, all energies are given in eV. The color scale reflects the $EA_1^{pred.}$ values with a minimum of 4.14 eV (**B**) in red, the range of “strong” molecular p-dopants starting around the $EA_1^{pred.}$ value of F_4-TCNQ (**N**) (5.30 eV) in yellow, and the highest derived value of 7.51 eV (**I**) in green.

tremely promising from our analysis, including triflyl groups (SO_2CF_3) and, in particular, sulfonyl cyanide (SO_2CN). Connecting the latter to phenyl groups to obtain $(PhSO_2CN)_3(CN)_3-CP$ (**G**) is, in fact, enough to match the $EA_1^{pred.}$ of (**E**), at 5.52 eV; connecting it directly on the CP core to obtain $(SO_2CN)_3(CN)_3-CP$ (**H**) yields a molecule with a moderately better $EA_1^{pred.}$ (6.70 eV) than (**A**) (5.95 eV) but an intriguingly much better EA_2 . In the same vein, saturating the CP core with such substituents to obtain $(SO_2CN)_6-CP$ (**I**) even leads to a molecule with vastly superior $EA_1^{pred.}$ and EA_2 . In fact, (**I**) has an estimated $EA_1^{pred.}$ of 7.51 eV, making it, to the best of our knowledge, by a large amount the molecule with the highest EA_1 proposed in the field. It remains to be seen if our current attempts to find synthesis routes towards such CP-based dopants comprising sulfonyl groups will be successful, as those molecules might not have reasonable stability, which will be subject to a forthcoming study. There, it is noted that, in direct analogy to our investigation of substituents bridged through a phenyl group, a single bridging carbon atom could be used to connect these sulfonyl substituents, slightly increasing the distance from the core and overall improving the stability of the molecules. This should lead to much less dramatic decreases of the EAs than bridging through a phenyl group, although the resulting molecule would not benefit from the added steric shielding.

The well-known CHD-core molecules such as $TCNQ$ (**J**) and F_4-TCNQ (**N**), which are planar and not sterically hindered, have EAs that are in fact not comparatively competi-

tive to other dopants, when considering the color scale in Table 3.3. An analogous analysis can therefore be carried out to improve their properties. *TCNQ* (**J**) can be sterically shielded by replacing the hydrogen atoms with phenyl groups to obtain $(Ph)_4$ -*TCNQ* (**K**) with slightly lower $EA_1^{pred.}$ (4.45 instead of 4.81 eV). Synthesis of (**K**) has been reported [121], but to our knowledge, this species was not yet analyzed regarding its doping behavior, possibly due to its even lower $EA_1^{pred.}$ than the parent species *TCNQ* (**J**), which itself does not undergo integer charge transfer even with low IE OSCs such as P3HT [5, 47]. Adding a cyano group to the phenyl on the para position, however, yields $(PhCN)_4$ -*TCNQ* (**L**) with much higher $EA_1^{pred.}$ and EA_2 than its CP counterpart (**B**). This follows our result that molecules with CHD cores have higher EAs than their CP analogues when substituents are connected *via* phenyl rings, and vice versa without. (**L**) is expectedly similar in EAs to $(F_5-Ph)_4$ -*TCNQ* (**M**) as well as F_4 -*TCNQ* (**N**), and could replace the latter in practical applications because of its superior steric bulk and lower diffusibility. On this basis we propose a molecule analogous to (**E**) but with a CHD core, $(F_4CN-Ph)_4$ -*TCNQ* (**O**), which is found to feature even better $EA_1^{pred.}$ than (**E**) with 6.19 eV, again with the benefit of increased steric bulk (because the rings are connected closer to the core). To our knowledge, this molecule has not yet been synthesized but based on our results might come close to an ideal p-type dopant in terms of doping performance.

While connecting cyano groups directly to the core to obtain $(CN)_4$ -*TCNQ* (**P**) yields comparable characteristics to (**A**), the substitution of sulfonyl cyanide groups to obtain $(SO_2CN)_4$ -*TCNQ* (**Q**) does not yield an appreciable increase in $EA_1^{pred.}$, but does instead provide a large increase in EA_2 . Following the explanations put forward earlier that the EA_1 values of this substitution pattern are lower than trivially expected due to the pronounced bending of the core, EA_2 values do not suffer that fate. This is because the neutral molecules experience a significant geometry change by adding an electron (which restores most of the core planarity), while the geometry changes involved in adding the second electron to form the radical anion are of much smaller amplitude. In fact, the penalty on $EA_1^{pred.}$ due to core bending is so pronounced here that connecting the same substituent through phenyl groups to obtain $(PhSO_2CN)_4$ -*TCNQ* (**R**) yields a molecule with an $EA_1^{pred.}$ (5.90 eV) very similar to that of (**Q**) (6.02 eV). This is despite the reduction of the EWG effects through the phenyl, while the EA_2 of (**Q**) (2.31 eV) is distinctively higher than that of (**R**) (1.77 eV). We note that the absolute EA_2 values that we obtain do not bear direct predictive value (and in practice should be much higher than those calculated here), as opposed to our $EA_1^{pred.}$ values which are obtained through a careful comparison and fitting process to experimental values. Nevertheless, the relative comparison of the values is reliable, as is typically the case with DFT-based methods, and as expected from the identical mechanistic and fundamental behaviors of EA_1 and EA_2 demonstrated in several Figures of this work.

3.4 Conclusion

In this work, a series of molecular p-dopants based on CP and CHD cores were investigated using DFT-based modeling. The systematic comparison of several electron-withdrawing substituents on the two cores and in different substitution patterns allows to derive rational dopant design rules through the comparison of group properties and trends. This approach allows to distinguish the impact of the core from the substituent and the role of geometric effects from electronic effects in defining EA_1 and EA_2 . Immediate practical results of our study include that electron affinities can be predicted directly from the substituents' Hammett parameters, which considerably facilitates dopant screening prior to synthesis efforts. It enables the proposition of several new molecules with compelling EA_1 and EA_2 , some of them featuring three-dimensional structures with a shielded core which should therefore directly translate into higher-performance dopants in practical applications.

Fundamentally, we demonstrated partial atomic charges on the cores to be the driving factor of the molecules' EAs and that the cores behave differently when accepting the first (EA_1) and the second (EA_2) electron, directly implying different dopant design rules for applications involving double doping. To support their experimental analysis *via* vibrational spectroscopy and assess applicability as dopants in functional structures, we examined the energy change of cyano vibrations of all molecules in relation to their charge states. Studying EA_2 of these molecules sheds light on the non-linearity of the cyano vibration energy with the molecular charge, which goes against the still common perception of cyano vibration shifts being linearly proportional to the molecular charge. Several species feature a high degree of non-linearity between excess charge on the molecule and the cyano vibration energy, which is of high relevance to correctly assess the degree of charge transfer upon doping and to confirm double doping.

Several critical conclusions are reached concerning the relationship between electronic and geometric factors in the molecular design of dopants. The design of superior CHD-based dopants is severely limited, because retaining planarity of the core region is necessary to maintain high EA , but is easily lost for larger substituents. When the substituents are, however, geometrically decoupled from the core through a phenyl ring, molecules with a CHD core generally display higher EAs than their CP analogues allowing us to propose (**O**) as very promising species for efficient ionization of OSCs. This behavior is due to a different intrinsic affinity of the core rather than a different core-substituent interplay. However, decoupling the substituent from the core effectively lowers the achievable EA , as the electron-withdrawing effect is transmitted through the phenyl ring which reduces the electronic impact of substituents by about 50%. As opposed to CHDs, it is possible to connect substituents directly to the CP cores without distorting its structure, finally leading to higher EAs , as for example, in species (**I**) of record-high EA . For the CHD cores, it is again the core bending which prevents the analogue species (**Q**) to reach its full potential. Furthermore, EA_2 of CP-based molecules is increasing faster with the electron-withdrawing abilities of the substituents than that of their CHD-based analogues, although this effect is more than compensated for by the intrinsically higher EA_2 values found for the CHD core. While both cores allow obtaining molecules with high EA_2 , molecules with a CP core shine because of their dramatically

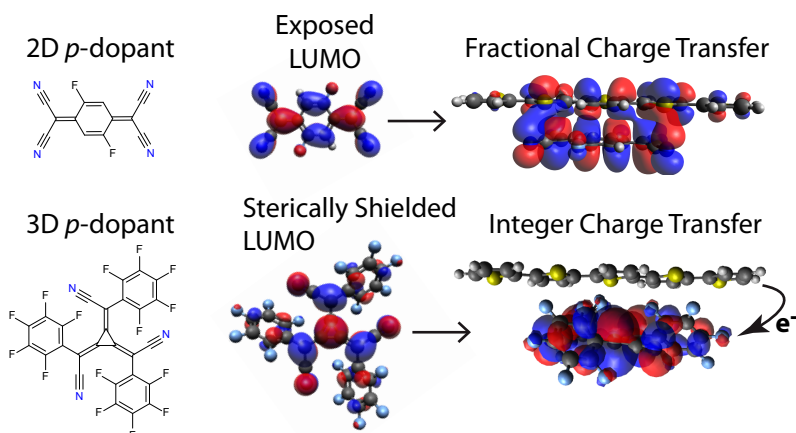
higher EA_1 . This is, again, due to the fact that core planarity is maintained even without connecting the substituents through phenyl groups, making such molecules highly interesting prospects for designing p-dopants with superior single and double electron-accepting abilities. However, the challenges involved in synthesizing these molecules should be taken into account. Altogether, in addition to the practical aspects of the present study, our results can provide a rationale for various fundamental aspects underlying the molecular design and behavior of strong electron acceptors which pave the way for their optimization through knowledge-based molecular design.

Chapter 4

Sterically-Hindered Molecular p-Dopants Promote Integer Charge Transfer in Organic Semiconductors

Abstract

Molecular p-dopants designed to undergo electron transfer with organic semiconductors are typically planar molecules with high electron affinity. However, their planarity can promote the formation of ground-state charge transfer complexes with the semiconductor host and results in fractional instead of integer charge transfer, which is highly detrimental to doping efficiency. Here, we show this process can be readily overcome by targeted dopant design exploiting steric hindrance. To this end, we synthesize and characterize the remarkably stable p-dopant 2,2',2''-(cyclopropane-1,2,3-triylidene)tris(2-(perfluorophenyl)acetonitrile) comprising pendant functional groups that sterically shield its central core while retaining high electron affinity. Finally, we demonstrate it outperforms a planar dopant of identical electron affinity and increases the thin film conductivity by up to an order of magnitude. We believe exploiting steric hindrance represents a promising design strategy towards molecular dopants of enhanced doping efficiency.



4.1 Introduction

Conjugated organic molecules (COMs) and polymers (COPs) have attracted much interest for their use as organic semiconductors in (opto-)electronic devices including organic light emitting diodes (OLEDs), [34, 122] photovoltaic cells, [123, 124] transistors, [124–126] or sensors [127, 128].

Most applications employ layers of electrically doped COMs/COPs, where p-doping is generally done by adding molecular acceptors of high electron affinity (EA) to promote electron transfer from the COM/COP, [35, 126] which can be augmented by subsequent anion exchange with an ionic liquid, as put forward recently. [129] This process of integer charge transfer (ICT) between p-dopant and COM/COP results in a localized charge on the dopant forming a radical anion, and a mobile hole in the organic semiconductor host. It increases its conductivity by several orders of magnitude and concomitantly reduces charge injection barriers at interfaces to electrodes. [45, 54, 130]

For efficient electron transfer, a common assumption is that the dopant EA must be equal to or greater than the ionization energy (IE) of the COM/COP. [32, 90, 131] As hole transport materials in organic electronic devices typically exhibit IEs of > 5.0 eV, efficient p-dopants require EAs in that range as well. [46, 90] Designing dopants of both high EA and stability is an ongoing challenge. Much work has been dedicated to derivatives of tetracyanoquinodimethane (*TCNQ*, EA = 4.91 eV), where fluorination of the quinoid core increases EA to 5.01 eV (*F₂-TCNQ*) and 5.31 eV (*F₄-TCNQ*), Figure B.1). [5] More recently, hexacyano-trimethylenecyclopropane (*(CN)₆-CP*, Figure 4.1) was introduced as a record strong dopant with an EA of 5.87 eV, thus, in principle, capable of ionizing high-IE materials, but at the expense of chemical stability in air and solvents. [56, 57, 132] For practical applicability, derivatives of *(CN)₆-CP* have been presented with cyano-groups being replaced to form trimethyl 2,2,2-(cyclopropane-1,2,3-triylidene)-tris(cyanoacetate) (*TMCN3-CP*, EA = 5.50 eV, Figure 4.1)[58] or the analogous dimethyl (*DMCN4-CP*, EA = 5.61 eV, Figure B.1) and monoethyl esters (*ECN5-CP*, EA = 5.75 eV, Figure B.1). [12] While they successfully p-dope high-IE copolymers, stability issues remain. [12, 58]

An additional challenge in doping can arise from the molecular shape of the dopants. In previous work, we established that integer charge transfer (ICT) does not necessarily happen efficiently upon doping because ground-state charge-transfer complexes (CPXs) may form instead, where only fractional charge transfer occurs. [5, 46, 47] This is due to the hybridization of the frontier molecular orbitals of the dopant and COM/COP, where the lowest unoccupied molecular orbital (LUMO) of the p-dopant and the highest occupied molecular orbital (HOMO) of the COM/COP split into doubly occupied bonding and empty antibonding supramolecular hybrid orbitals. The latter become the effective acceptor levels for electron transfer and take over the role of the pristine dopant LUMO, but are energetically less favorable, which limits their doping efficiency. [3, 46, 64] *TCNQ* and its fluorinated derivatives are fully planar dopants and thus highly susceptible to CPX formation with common COMs [46, 47, 133] and COPs [5, 6, 46, 47, 134] including the homopolymer poly(3-hexylthiophene-2,5-diyl) (P3HT, IE = 5.21 eV, Figure B.1) [5] which has been found to show both ICT and CPX formation even with *F₄-TCNQ* of an EA exceeding the IE of P3HT. [5, 102, 135, 136]

As the energy level splitting between the supramolecular hybrid orbitals upon CPX

formation depends on the electronic coupling between the dopant and host frontier molecular orbitals, we earlier proposed reducing their coupling via steric hindrance to remedy this issue through directed molecular design. [3, 46, 48] We suggested this can be done by adding bulky and chemically inert side groups to the dopant, which further helps reduce their unwanted diffusibility through organic semiconductor films. [68, 76, 137] In addition, it increases the spatial separation between the dopant radical anion and COM/COP, promoting the formation of delocalized polarons [110]—the ultimate goal of molecular doping. Here, we now explore the feasibility of suppressing CPX formation by exploiting steric hindrance to increase the doping efficiency. We first analyze several $(CN)_6$ -CP derivatives via density functional theory (DFT) modeling and then synthesize the most promising compound of high EA, which is non-planar, bulky, and exhibits remarkable chemical stability, even in air. Its doping behavior is juxtaposed to F_2 -TCNQ as a fully planar dopant of identical EA, which allows us to isolate the impact of steric hindrance in molecular doping. We demonstrate that the presence of bulky side groups that shield the p-dopant LUMO effectively suppresses the adverse consequences of CPX formation for oligo- and polythiophene. This eventually translates into enhanced conductivity in doped P3HT films.

4.2 Methods

4.2.1 Materials

The thiophene oligomer 3,3',3'',3'''-octahexyl 2,2':5',2'':5'',2''':5''', 2'''':5''''', 2''''':5''''', 2'''''':5''''''', 2''''''':5''''''''- decithiophene (h10T) was synthesized according to the method published in earlier work by some of the authors. [133] 2,3,5,6-Tetrafluoro-7,7,8,8-tetracyanoquinodimethane (F_4 -TCNQ), and 2,5-difluoro-7,7,8,8-tetracyanoquinodimethane (F_2 -TCNQ) were purchased from Tokyo Chemical Industry Co., Ltd. (TCI) (all: purity > 98.0%) and used as is. P3HT (MW > 45 kDa; 93% regio-regularity) was used as purchased from Luminescence Technology Corp. (Lumtec, Taiwan). Potassium iodide ($\geq 99.8\%$) was purchased from Sigma-Aldrich. Anhydrous chloroform (Sigma-Aldrich, amylenes as stabilizer, purity $\geq 99\%$), anhydrous dichloromethane (Sigma-Aldrich, purity $\geq 99.8\%$), and anhydrous acetonitrile (Sigma-Aldrich, purity $\geq 99.8\%$) were used as solvents. Sample preparations and measurements were performed under an inert atmosphere (N_2) in a glovebox ($H_2O < 0.1$ ppm, $O_2 < 5.0$ ppm); all compounds and solvents were stored therein unless stated otherwise.

Pentafluorophenyl acetonitrile (TCI, purity > 97%), perchlorocycloprop-1-ene (Fisher Scientific, purity 98%), Lithium hydride (Sigma Aldrich, powder, 95%, 30mesh), 1,2-dimethoxyethane (DME) (Sigma Aldrich, anhydrous, 99.5% inhibitor-free), hydroboronic acid (Sigma Aldrich, ACS reagent, 48%), nitric acid (Thermo Fisher Scientific, 70%). Dichloromethane, hexane, chloroform, $NaSO_4$ were purchased as ACS grade from Sigma Aldrich, Thermo Fisher Scientific, and ACP chemical, respectively, and used without further purification. Distilled water was obtained from an in-house water distillery. Reactions were carried out in flame-dried glassware under an argon atmosphere unless otherwise noted.

4.2.2 Sample preparation

P3HT films doped with F2TCNQ and F4TCNQ: Dopants (0.3 g/L) were dissolved in chloroform by stirring on a heating plate set to 60 °C for 1 h and left to cool at room temperature for at least 1 h before mixing with P3HT. P3HT (10 g/L) was dissolved in chloroform directly before application. Blend solutions were mixed to yield ratios of 100, 50, 20, 10, and 5 P3HT repeat units per dopant molecule, i.e., dopant molar ratios of 1%, 2%, 5%, 9%, and 17%, respectively.

P3HT films doped with PFP3CN3-CP: Blend solutions of PFP3CN3-CP (0.8 g/L) and P3HT (3 g/L) were mixed to yield ratios of 100, 50, 20, 10, and 5 P3HT repeat units per dopant molecule, i.e., dopant molar ratios of 1%, 2%, 5%, 9%, and 17%, respectively.

h10T films doped with F2TCNQ: F₂-TCNQ (0.3 g/L) was dissolved in chloroform by stirring on a heating plate set to 60 °C, 24 h before mixing blend solutions and used without cooling to avoid precipitation. h10T (3 g/L) was dissolved directly in chloroform prior to application. Blend solutions were mixed to yield ratios of 100, 50, 20, 10, and 5 thiophene rings per dopant molecule (to allow for a direct comparison with P3HT), i.e., dopant molar ratios of 9%, 17%, 33%, 50%, and 67%.

h10T films doped with PFP3CN3-CP: Blend solutions of PFP3CN3-CP (1 g/L) and h10T (1 g/L) were mixed to yield a ratio of 100, 50, 20, 10, and 5 thiophene rings per dopant molecule (for comparison with P3HT), i.e., a dopant molar ratio of 9%, 17%, 33%, 50%, and 67%.

Substrates were cleaned in chloroform, acetone, deionized water, and isopropyl alcohol (in that order) for 10 min each in an ultrasonic bath. Substrates were: 1 cm × 0.5 cm × 0.5 mm pieces of n-doped Si wafer (single-side polished; phosphorous-doped) for grazing-incidence X-ray diffraction (GIXRD) and Atomic Force Microscopy (AFM), 1 cm × 1 cm × 0.5 mm pieces of undoped Si wafer (double-side polished, prime grade) for Fourier-transform infrared (FTIR) spectroscopy, 1 cm × 1 cm × 0.5 mm electrically fused quartz slides for ultraviolet to near-infrared (UV-vis/NIR) spectroscopy, and 1.5 cm × 2.0 cm glass substrates with each 5 pre-patterned ITO electrodes (Ossila; 42 μm channel length, 3 cm electrode width) for conductivity measurements. Films for conductivity measurements and (some supporting) UV-vis/NIR experiments (Figure B.13) were spin-coated (static dispense, 30 s, 1000 rpm, 150 μL). To increase the signal-to-noise ratio, films for GIXRD, FTIR, and UV-vis/NIR (Figure 4.3) were drop-cast (50 μL).

4.2.3 Column Chromatography

Compounds were purified using column chromatography on silica-gel (Zeoprep 60 Eco, 40–63 μm, Zeochem AG).

4.2.4 Mass Spectra

High-resolution mass spectra (HRMS) were obtained using a LTQ Orbitrap Velos with ETD (Thermo Fisher Scientific); exact masses were determined with ESI negative mode through direction inject of sample in chloroform solution.

4.2.5 NMR

^{19}F NMR (470 MHz) Spectra were obtained in CD_3CN with 500 MHz Agilent DD2 NMR Spectrometer. Spectral features are reported in the following format: chemical shift (δ , ppm); multiplicity (s singlet, d-doublet, t-triplet, q-quartet, dd-doublet of doublets, m-multiplet, ddd-doublet of doublets of doublets); coupling constants (J, Hz).

4.2.6 Cyclic Voltammetry

Cyclic voltammetry (CV) was recorded employing a CH Instruments CHI604d potentiostat, Ag/Ag^+ reference electrode, Pt-wire counter-electrode, glassy carbon working electrode, and a scan rate of 50 mV/s and 100 mV/s under inert N_2 atmosphere in the glovebox. Before each experiment, the glassy carbon working electrode was polished using 1.0, 0.3, 0.05 μm alumina powder, and the counter electrode was polished using 0.05 μm alumina powder.

First, a background scan was performed to ensure there is no contamination before adding the analyte. The electrolyte solutions were 0.1 M tetrabutylammonium hexafluorophosphate ($n\text{ Bu}_4\text{NPF}_6$) in Dichloromethane (CH_2Cl_2) for *PPF3CN3 – CP* and acetonitrile for *F₂-TCNQ* and *F₄-TCNQ*. Reduction potentials were recorded as halfwave potentials $E_{1/2,\text{red vs. Fc/Fc}^+}$ between corresponding anodic and cathodic peak potentials and referenced to the halfwave potential of ferrocene added internally to the electrolyte. The energies of the lowest unoccupied molecular orbitals (LUMOs) were calculated by using the equation: $E_{\text{LUMO}} = -(5.09\text{ V} + E_{1/2,\text{red vs. Fc/Fc}^+})$. [82] Uncertainties were estimated as ± 0.1 eV following the recommendation by Cardona et al. [82]

4.2.7 UV-vis/NIR and FTIR Spectroscopy

Ultraviolet to near-infrared (UV-vis/NIR) spectroscopy and Fourier-transform infrared (FTIR) absorbance spectra were recorded on an Agilent (ex. Varian) Cary 5000 and a Thermo Scientific Nicolet 6700 using a liquid-nitrogen cooled mercury cadmium telluride (MCT) detector; all film samples were kept under inert N_2 atmosphere from the glovebox in custom-built, sealed boxes with quartz and KBr windows, respectively.

Quartz cuvettes [Alpha Nanotech Inc., spectral range 190-2500 nm, path length of 2 mm (0.7 ml)] were used for solution samples of UV-vis/NIR absorbance spectra. The thicknesses of the spin-coated films (UV-vis/NIR data in Figure S13) were determined by atomic force microscopy (AFM) on a Bruker Multimode 8HR (under ambient conditions) with a silicon nitride tip (AppNano ACTA-50, 125 $\mu\text{m} \times 30 \mu\text{m} \times 4.0 \mu\text{m}$ cantilever, <10 nm tip radius, 14-16 μm tip height, 200-400 kHz, 13-77 N/m) in Tapping Mode.

4.2.8 Conductivity

Conductivity measurements were done using a Keithley 2612B source measure unit employing an Ossila OFET test board to collect conductance data. The film thickness was determined by atomic force microscopy (AFM) on a Bruker Dimension Icon (under ambient conditions) with a silicon nitride tip (AppNano ACTA, 125 $\mu\text{m} \times 30 \mu\text{m} \times 4.0 \mu\text{m}$

cantilever, <10 nm tip radius, 14-16 μm tip height, 200-400 kHz, 13-77 N/m) in its proprietary PeakForce Tapping Mode. Channel dimensions were determined using the optical microscope as part of the same AFM.

4.2.9 GIXRD Experiments

Grazing-incidence X-ray diffraction (GIXRD) data was collected at Canadian Light Source Saskatoon, SK, Canada on beamline BXDS-IVU employing a Rayonix MX300 detector, 0.92 Å primary beam wavelength, an incidence angle of 0.15°, and beam dimensions of 100 μm vertical, 2 mm horizontal. The open-source software GIDvis (<https://www.if.tugraz.at/amd/GIDvis/>), GPL v3.0, was used for general GIXRD data analysis (transformation into reciprocal space). [87]

4.2.10 AFM

Atomic Force Microscopy (AFM) was performed on a Bruker Multimode 8HR (under ambient conditions) with a silicon nitride tip (AppNano ACTA-50, 125 μm \times 30 μm \times 4.0 μm cantilever, <10 nm tip radius, 14-16 μm tip height, 200-400 kHz, 13-77 N/m) in Tapping Mode. Spin coating of the films was performed using the same parameters as for the samples on quartz for UV-vis/NIR (Figure B.13).

4.2.11 DFT calculations

DFT calculations were performed within the Gaussian computational package (version 09 revision E.01) [10] using the $\omega\text{B97x-D}$ functional [119] and 6-31+G(d,p) as the basis set. Molecular geometries for the neutral and radical anions were optimized, and the absence of imaginary vibrational frequencies was subsequently verified to confirm the proper ground state nature of all species. The range separation parameter ω was modified using Gaussian's internal options (IOps) controls and fixed to 0.20 following a tuning procedure (which coincides with the value by default) for all calculations presented in the main text. Molecular orbital isosurfaces were drawn using the software Avogadro, Version 1.2.0. [138]

4.3 Results and discussion

We start by investigating the impact of different substitutions on the electron affinity (EA) for various $(\text{CN})_6\text{-CP}$ derivatives (Figure 4.1), all of which have a three-dimensional (3D) shape as inferred from density functional theory (DFT) structure optimizations. We then benchmark our DFT-calculated EA values (EA_{calc}) of known molecules against their reported experimental values (EA_{exp}) to obtain predicted experimental values (EA_{pred} , equation 3.3) in excellent agreement (Table 4.11), which assures reliable predictive power for the unknown species (see details in the Appendix B.2).

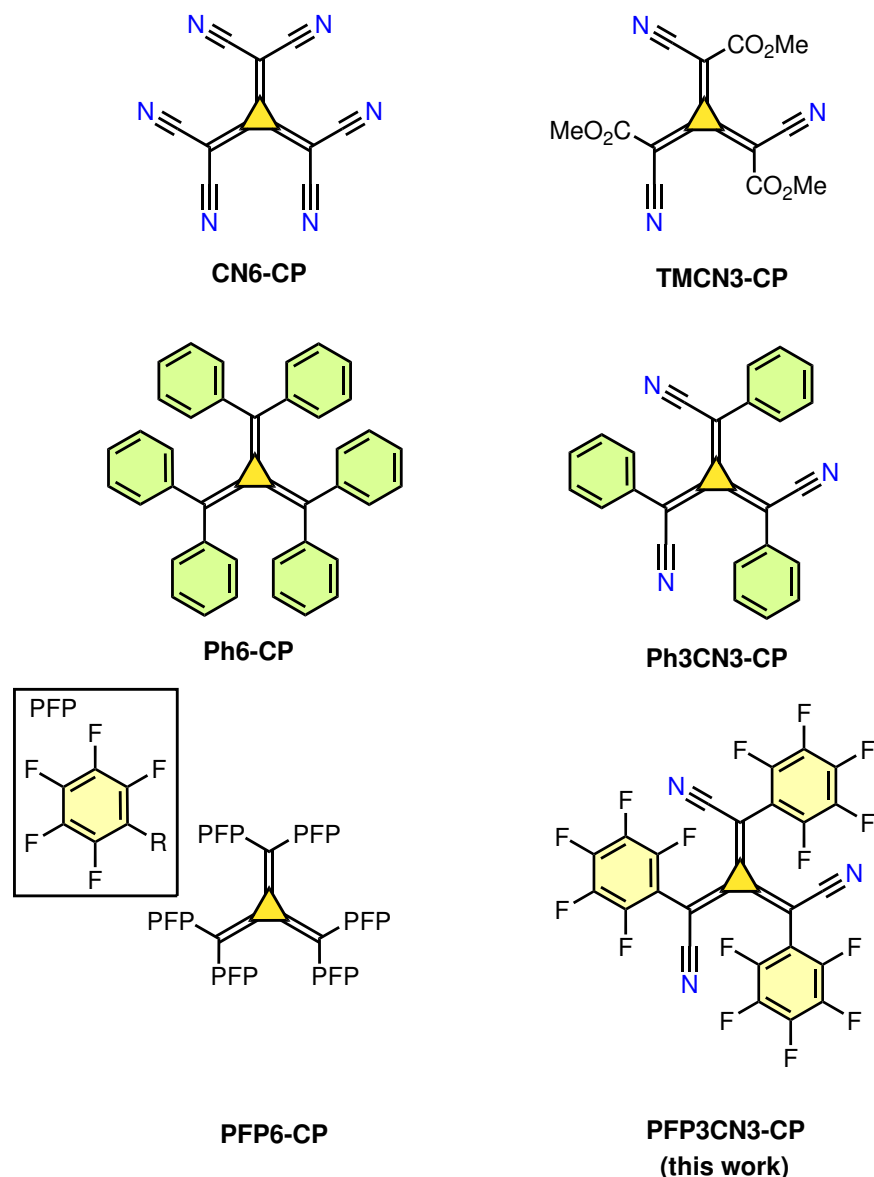


Figure 4.1: Chemical structures of p-dopants discussed in this work; additional structures are depicted in Figure B.1.

As expected for its six cyano substitutions (CN)₆-CP has the highest EA (Table 4.1), its EA_{calc} value is in excellent agreement with that modeled by Karpov et al. (4.87 eV), as is our EA_{pred} with their experimental value ($EA_{\text{exp}} = 5.87$ eV). [56] Replacing cyano groups with bulky substituents such as phenyl (Ph) and pentafluorophenyl (PFP) rings we obtain bulky, 3D dopants where PFP generally provides higher EA due to the high electronegativity of fluorine. Importantly, with three PFP substitutions, we obtain 2,2',2''-(cyclopropane-1,2,3-triylidene)tris(2-(perfluorophenyl) acetonitrile) ($PFP3CN3-CP$, Figure 4.1) and find, for steric reasons, a 3D molecular structure almost identical to that of the non-fluorinated species $Ph3CN3-CP$ (see Table B.2 and Figure

Dopants	EA_{exp} (eV)	EA_{calc} (eV)	EA_{pred} (eV)
CN6-CP	5.87	4.96	5.85
TMCN3-CP	5.50	4.24	5.20
Ph6-CP	N/A	1.59	2.83
Ph3CN3-CP	N/A	3.10	4.18
PFP6-CP	N/A	3.29	4.35
PFP3CN3-CP	5.07	4.03	5.02

Table 4.1: Comparison of DFT-calculated EA values (EA_{calc}) with experimental (EA_{exp}) and predicted experimental values (EA_{pred}).

B.6), but with an EA_{pred} higher by almost 1 eV. Figure 4.2 juxtaposes the isosurface plots for the LUMOs of $(\text{CN})_6\text{-CP}$ and PFP3CN3-CP illustrating how efficiently the PFP substitutions shield the p-dopant LUMO. Based on its promising 3D structure and high EA , we selected PFP3CN3-CP for chemical synthesis. We note this dopant is similar to a commercial one (denoted as $PD-A$ by Merck KGaA) introduced recently [59], which comprises three 2,3,5,6-tetrafluorobenzonitrile substitutions instead (structure shown in Figure B.1, our EA_{pred} for $PD-A$ is 5.53 eV).

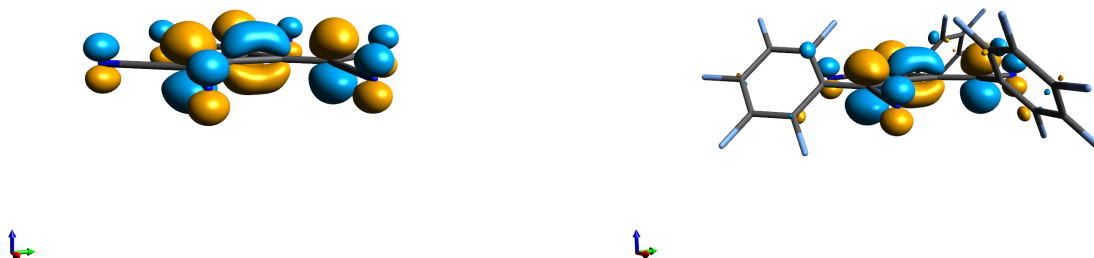
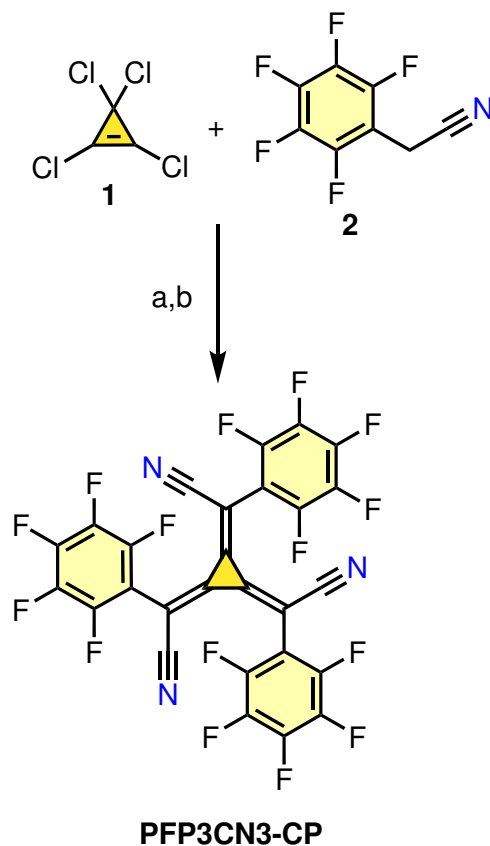


Figure 4.2: Isosurface plots of the exposed and shielded LUMOs of $(\text{CN})_6\text{-CP}$ (left) and PFP3CN3-CP (right), respectively; the average twisting angle of the PFP rings is 36.1° .

PFP3CN3-CP was synthesized following a reported procedure [4] using tetrachlorocyclopropene (1) and pentafluorophenyl acetonitrile (2) (Scheme 4.1). The dopant is isolated by column chromatography and further characterized with HRMS, FTIR, and ^{19}F NMR (Supporting Information). Cyclic voltammetry (Figure B.11) yields $EA_{\text{exp}} = 5.07$ eV (± 0.1 eV) [82] in excellent agreement with our EA_{pred} value of 5.02 eV.



Scheme 4.1: a. LiH, DME, $-5\text{ }^{\circ}\text{C}$ to $20\text{ }^{\circ}\text{C}$, 48h. b. HBr, HNO_3 , Acetic acid, $-5\text{ }^{\circ}\text{C}$ to $20\text{ }^{\circ}\text{C}$, 2 h. 32% over 2-step.

Next, we systematically compare the doping behavior of *PFP3CN3-CP* with that of *F₂-TCNQ*, a fully planar dopant of the same EA_{exp} , as equally determined by cyclic voltammetry (5.05 ± 0.1 eV), see Table B.3 and cf. Ref. [52] This allows investigating whether the shielded LUMO of *PFP3CN3-CP* and the openly exposed one of *F₂-TCNQ* translate into a different doping phenomenology. To this end, we used both to p-dope films of P3HT from a common solution, as charge transfer complex (CPX) formation is common for this conjugated organic polymer (COP). [5, 102, 135, 136] We performed ultraviolet-visible-near-infrared absorption spectroscopy (UV-vis/NIR), which has been extensively employed before to study doping-related charge transfer [3, 5, 42, 47, 56, 57, 102, 132–134]; the results are shown in Figure 4.3.

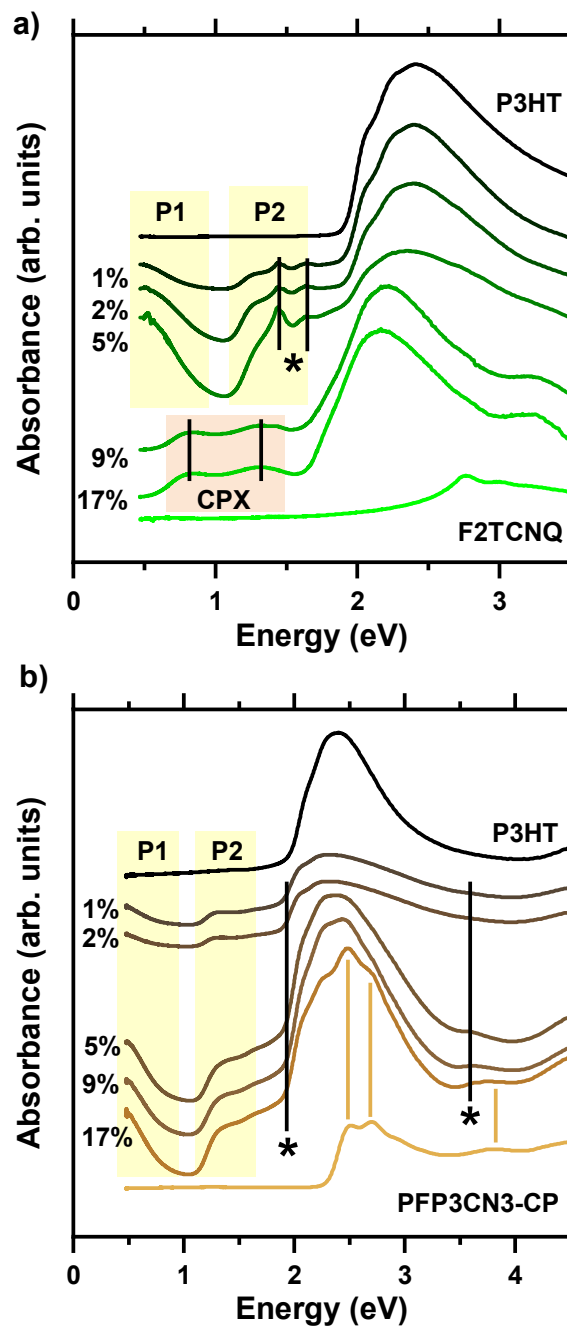


Figure 4.3: UV-vis/NIR absorption spectra of dropcast P3HT films doped with increasing molar ratios of *PFP3CN3-CP*. Data obtained under identical conditions as in (a). P1 and P2 indicate optical transitions assigned to the positive polaron in P3HT. [5–8] Stars mark transitions assigned to the *PFP3CN3-CP* radical anions ($PFP3CN3-CP^{\cdot-}$; see Refs. [3, 5] and Figure B.12, respectively). Transitions of neutral *PFP3CN3-CP* are assigned by supporting DFT calculations (Figure B.7).

Pure P3HT has its fundamental absorption at 1.95 eV (onset), broad peaks in the sub-gap region occurring upon doping are transitions related to positive polarons known to lie around 0.5 eV (P1) and 1.5 eV (P2). [5–8] For F_2 -TCNQ doping, we find them up to 5% dopant loading together with the characteristic transitions of the F_2 -TCNQ radical anion (marked with asterisks) [5, 47, 52], which both are indicative of ICT. For elevated doping ratios ($\geq 9\%$), however, P1 and P2 are attenuated, and two different transitions are found around 0.8 and 1.3 eV, which are characteristic for the CPX. [5] We note this is analogous to various systems, including oligo- and polythiophene forming mixed crystals with the planar TCNQ derivatives. [3, 47, 102] Their solid-state packing typically exhibits an alternating, cofacial stacking motif [3, 102, 139] that enables pronounced frontier-molecular orbital overlap promoting CPX formation. Importantly, this process represents a driving force for the formation of such structures as CPX formation contributes to the overall binding energy. [48]

In marked contrast, and despite its identical EA, $PFP3CN3 - CP$ doped P3HT shows all fingerprints of ICT for the whole range of doping concentrations with no indication of CPX formation (Figure 4.3b); we note the same is true for spin-coated films (Figure B.13), for which atomic force microscopy shows smooth films of unaltered morphology upon doping with $PFP3CN3 - CP$ while CPX formation increases the surface roughness (Figure B.9).

To independently assess the susceptibility of $PFP3CN3 - CP$ to CPX formation, we further evaluated it in combination with the COM decithiophene (h10T, Figure B.1) for which we recently showed that ICT occurs alongside CPX formation with F_4 -TCNQ. [133] We regard h10T as an excellent model system to probe the ability of a dopant to hybridize, as it is liquid at room temperature, and, therefore, crystalline order inhibiting or promoting frontier molecular orbital overlap (as required for CPX formation) can be excluded. For F_2 -TCNQ, with its EA insufficient to ionize h10T, we find exclusive CPX formation inferred from pronounced sub-gap absorption features in UV-vis/NIR, which are absent for $PFP3CN3 - CP$ (Figure B.14). This demonstrates that CPX formation is successfully suppressed.

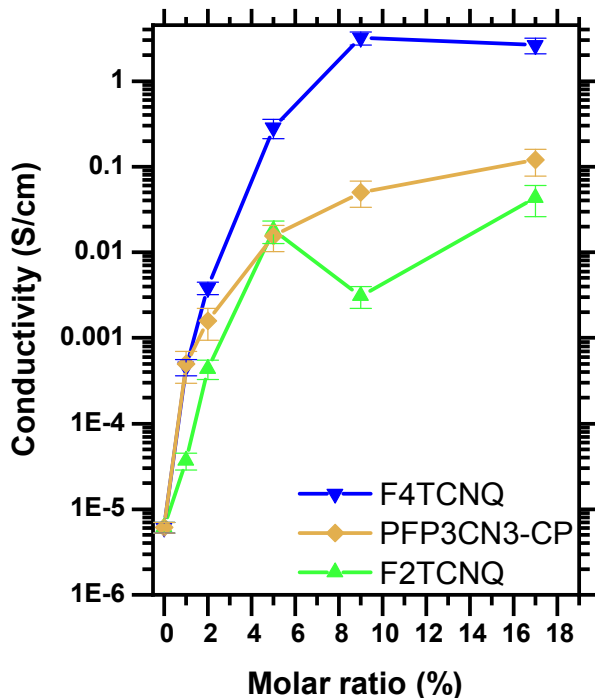


Figure 4.4: Conductivity of P3HT films doped with F_4 -TCNQ, F_2 -TCNQ, and PFP3CN3 – CP versus the molar doping ratio (%); F_4 -TCNQ and F_2 -TCNQ data taken from our own previous study [5] and obtained under identical conditions as the PFP3CN3 – CP data.

Finally, the conductivity (σ) of doped P3HT films highlights how PFP3CN3 – CP outperforms the planar dopant (Figure 4.4). At a 1% ratio, σ is even equal to that of F_4 -TCNQ-doped P3HT despite the ca. 0.2 eV lower electron affinity (EA) of PFP3CN3 – CP. Given that for F_4 -TCNQ-doped P3HT essentially all dopants are ionized at low dopant loading [5, 6, 42], this indicates the same to be true for our dopant as well. At higher ratios, σ falls behind owing to the lower EA, which can be understood by the occupation of the Gaussian density of states of dopant and host frontier molecular orbitals. [46] It dictates that more dopants remain neutral at higher doping ratios as the electron chemical potential (often referred to as the Fermi energy, E_F) is stabilized between these energies. Note the spectral features of the neutral dopant accordingly become visible for >5% (Figure 4.3b). In the same vein, this is in line with σ being systematically lower for F_2 -TCNQ, which is prone to CPX formation. Again, this is understood from the occupation of the density of states: the CPX contributes acceptor levels of lower EA, and therefore, fewer holes are generated in the p-doped organic semiconductor. The (highly reproducible) non-uniform increase in σ observed for F_2 -TCNQ can be ascribed to a complex microstructure of the semicrystalline P3HT films forming a mixed crystalline phase with F_2 -TCNQ [5]. For PFP3CN3 – CP, the dopants are intercalated with the alkyl chains (see Figures B.17 and B.18 for grazing-incidence X-ray diffraction data).

Most notably, in marked contrast to the parent species $(CN)_6$ -CP [56] and TMCN3 –

CP [58], *PFP3CN3 – CP* is highly stable over time, as evident from time-dependent UV-vis/NIR (Figure B.6) and conductivity (Figure B.7) measurements. Under N_2 , σ does not decline (tested for 7 days), only in air it is reduced by about one order of magnitude (see Figure B.7). We thus speculate shielding the dopant core not only inhibits CPX formation but also helps maintain its stability in the air. While not the focus of the present study, we note that exploiting steric hindrance might be equally beneficial for n-doping as well, where recent breakthroughs paved the way to more efficient n-doping strategies based on organometallic dimers [140] or transition-metal-catalyzed n-doping. [141]

4.4 Conclusion

To summarize, we have investigated whether shielding the LUMO of a molecular p-dopant can serve to suppress the formation of ground-state charge transfer complexes and increase the doping efficiency. To this end, we synthesized the sterically hindered three-dimensional dopant *PFP3CN3 – CP* and juxtaposed its doping phenomenology to that of the planar p-dopant *F₂-TCNQ* of the same electron affinity (EA). We find complex formation can indeed be effectively suppressed by this simple design rule leading to a significant improvement in doping efficiency. In marked contrast to chemically similar dopants, *PFP3CN3 – CP* is remarkably stable, assumably another side effect of its sterically shielded central core. We consider the exploitation of steric hindrance a promising general route to more efficient molecular dopants, which are required to achieve maximum doping response at lower dopant loading so that functional films remain less affected by the presence of dopant radical anions, and the charge carrier mobility is increased.

Chapter 5

Reversible Dimerization of *PFP3CN3-CP*

Abstract

We investigate the dimerization behavior of 2,2',2''-(cyclopropane-1,2,3-triylidene) tris(2-(perfluorophenyl)acetonitrile) (*PFP3CN3-CP*) introduced in Chapter 4. A combination of ^{19}F NMR, Density Functional Theory (DFT) modeling, and Powder X-ray diffraction (PXRD) is performed to characterize the propensity of *PFP3CN3-CP* to form non-covalent dimers under various conditions. ^{19}F NMR spectroscopy in toluene and acetonitrile revealed additional peaks at higher concentrations which point towards a reversible dimerization of the neutral *PFP3CN3-CP* species. DFT modeling suggests possible dimer conformations, which is supported by PXRD analysis indicating a hexagonal unit cell with a threefold rotational symmetry like the monomer itself, which exhibits a unit-cell volume that can hold two molecules. These combined results suggest that *PFP3CN3-CP* undergoes neutral dimerization, which is further in line with findings for differently substituted analogues.

5.1 Introduction

Recently, a study on hexacyano[3]radialene ($(\text{CN})_6\text{-CP}$) and related compounds suggested that $(\text{CN})_6\text{-CP}$ consistently maintains its status as a free radical anion (i.e., non-dimerized) across various solvents (such as acetonitrile, brine (Aq.NaCl), and water) and at various temperatures.[9] However, substituting cyano groups with ester moieties (resulting in trimethyl 2,2',2''-(cyclopropane-1,2,3-triylidene)-tris(cyanoacetate) (*TMCN3-CP*) and dimethyl 2,2'-(3-(dicyanomethylene)cyclopropane-1,2-diylidene)-bis(2-cyanoacetate) (*DMCN4-CP*)) improves solubility and facilitates radical anion-radical anion dimerization.[9]

In contrast to $(\text{CN})_6\text{-CP}$, the *TMCN3-CP* radical anion has been reported to undergo solvent-dependent dimerization, forming a σ radical-radical dimer in water, which transforms into a free radical anion upon introduction of organic solvents (acetonitrile, methanol, or acetone), or to a π radical-radical dimer in brine solutions.[9] However, the *DMCN4-CP* radical anion exists as a π radical-radical dimer in aqueous environments and as a free radical anion in organic solvents (acetonitrile, methanol, or acetone) (Figure

5.1).

Additionally, Hasan et al., have reported that temperature variations in methanol solution influence the dimerization mode of both *TMCN3-CP* and *DMCN4-CP*, in particular, the presence of a so-called σ radical-radical dimerization mode at low temperatures (10°C), which is reported to transform into a π dimerization mode upon heating (45°C), evidenced by Variable temperature electron paramagnetic spectroscopy (VT-EPR) measurements.[9] However, this hypothesis is surprising given the high energy requirement associated with breaking covalent bonds, i.e., thermal energy provided *via* heating a sample to 45°C cannot be expected to be sufficient to break a C-C covalent bond.

The reported mode of radical-radical dimerization is affected by solvent type, temperature, and salt additives[9], which, in turn, represents a way to deliberately manipulate dimer formation and select between different modes of dimerization. Studying the different dimerization modes of molecules such as *TMCN3-CP* and *DMCN4-CP*, which are used as p-dopants for organic semiconductors (OSCs) in their neutral form, is crucial since dimerization *per se*, and different modes of dimerization may significantly impact the doping behavior of these species. Most obviously, the formation of a dimer between a dopant radical anion—generated *via* integer charge transfer in common solution with the OSC—and a neutral dopant may impact the ability of the latter to undergo charge transfer itself, e.g., by modifying the energy position of the acceptor electronic states provided by the neutral dopant. In the same vein, the electronic properties of dopants in neutral dimers, if formed under certain preparation conditions of doped OSC films may be modified and their tendency to undergo charge transfer with an OSC may be reduced.

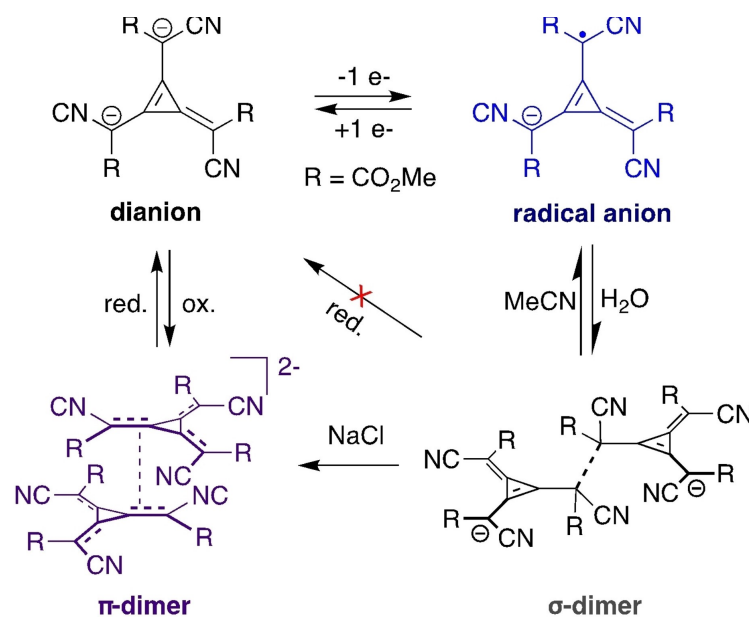


Figure 5.1: The σ and π radical dimerization modes for *TMCN3-CP* and *DMCN4-CP* respectively; $\text{R} = \text{CO}_2\text{Me}$. The figure has been edited and adapted from: Hasan, F., Gillen, J. H., Jayaweera, A. T., McDearmon Jr., W. D., Winter, A. H., Bejger, C. M. (2023).[9] The σ dimerization mode forms through a single covalent bond.

Here, we have investigated the dimerization behavior of *PFP3CN3-CP* by ^{19}F NMR, DFT calculations, and PXRD. This p-dopant as discussed in chapter 4 has shown sufficiently high EA to p-dope P3HT without showing evidence of charge complex (CPX) formation even at high dopant ratios. [15] As reported in chapter 4, the dopant has a sterically-shielded core, due to the bulky pentafluorophenyl (PFP) rings, which inhibits the hybridization between frontier molecular orbitals: the HOMO of the OSC, and the LUMO of the p-dopant.

The ^{19}F -NMR spectra for the neutral *PFP3CN3-CP* in acetonitrile and toluene exhibit six dominant peaks, indicating the presence of three additional peaks alongside the three ^{19}F NMR peaks expected for *PFP3CN3-CP* (Figure B.9). This phenomenon is observed only at high concentrations (30 g/l), whereas diluting the sample (3 g/l) results in the attenuation of the three additional peaks. This finding suggests that neutral *PFP3CN3-CP* undergoes dimerization in solution at high concentrations, a process that is reversible upon dilution. This points to non-covalent interactions between *PFP3CN3-CP* monomers, ruling out the occurrence of a σ dimerization mode (covalent bond). Notably, as the practical doping of OSC films happens from a common solution and dimerization depends on concentration, dimerization is expected upon thin film formation from a common solution (e.g., after spin-coating doped films) when the solvent evaporates during film formation.

To assess possible modes of dimerization, we performed DFT calculations which reveal three possible geometries for the *PFP₃CN₃-CP* dimer, highlighting either the π -dipole (between the PFP rings and CN bonds) or π - π intermolecular interactions between monomers. Synchrotron PXRD analysis supports these findings, as it shows that *PFP₃CN₃-CP* crystallizes in a hexagonal unit cell with threefold rotational symmetry that matches the dimer symmetry, and the unit cell volume is sufficient to accommodate the dimer.

5.2 Methods

5.2.1 Materials

Anhydrous acetonitrile (Sigma-Aldrich, purity $\geq 99.8\%$), and anhydrous toluene (Sigma-Aldrich, purity $\geq 99.8\%$) were used as solvents. The 2,2',2''-(cyclopropane-1,2,3-triylidene)tris(2-(perfluorophenyl)acetonitrile) (*PFP3CN3-CP*) has been synthesized in our previous work. [15] Sample preparations and measurements were performed under an inert atmosphere (N_2) in a glovebox ($\text{H}_2\text{O} < 0.1$ ppm, $\text{O}_2 < 5.0$ ppm); all compounds and solvents were stored therein unless stated otherwise.

5.2.2 Sample preparation

5.2.3 NMR

^{19}F NMR (470 MHz) Spectra were obtained in acetonitrile and toluene with 500 MHz Agilent DD2 NMR Spectrometer. Spectral features are reported in the following format:

chemical shift (δ , ppm).

5.2.4 DFT calculations

All presented DFT calculations were carried out within Gaussian (version 09 revision E.01), [10] performed using the ω B97X-D range-separated functional from Chai and Head-Gordon [119] and the 6-31+G(d,p) basis set. All molecular geometries for the neutral, radical anionic, and dianionic species have been optimized in the gas phase as well as in toluene and acetonitrile using the polarizable continuum model (PCM). Wavefunctions were exported from Gaussian and subsequently used for analyses based on the charge density using the software Multiwfn [120]. Molecular visualization and images were obtained using Avogadro 1.2.0. [138].

5.2.5 PXRD

Grazing-incidence X-ray diffraction (GIXRD) data was collected at Canadian Light Source Saskatoon, SK, Canada on beamline BXDS-IVU employing a Rayonix MX300 detector, 0.92 Å primary beam wavelength, an incidence angle of 0.15°, and beam dimensions of 100 μ m vertical, 2 mm horizontal. The powder was in 0.4 mm Kapton capillaries. The open-source software GIDvis (<https://www.if.tugraz.at/amd/GIDvis/>), GPL v3.0, was used for general GIXRD data analysis (transformation into reciprocal space). [87] The data was analyzed using the software suite Expo2014 [142] employing the McMaille 4.0 [143] analysis algorithm implemented therein.

5.3 Results and discussion

Overall, this study shows reversible dimerization of the neutral species for the *PFP3CN3 – CP*. First, the ^{19}F NMR in two different organic solvents (toluene and acetonitrile) in high concentrations (30 g/l) show three extra peaks (δ -136.96, -148.97, -161.31 in acetonitrile) in addition to the three expected ^{19}F NMR peaks in low concentrations (3 g/l) (δ -143.38, -156.20, -163.76 in acetonitrile) (see Figure 5.2). This finding indicates a reversible neutral-neutral dimerization of *PFP3CN3 – CP* and aligns with the observation that the dimer peaks shift upfield due to redistribution of electron density arising from different reasons such as conformational change, intermolecular interactions, and shielding effect from PFP rings, which all are changing the chemical environment of the nucleus. Furthermore, as we expected, there is a downfield shift by changing the solvent from toluene (non-polar) to acetonitrile (polar).

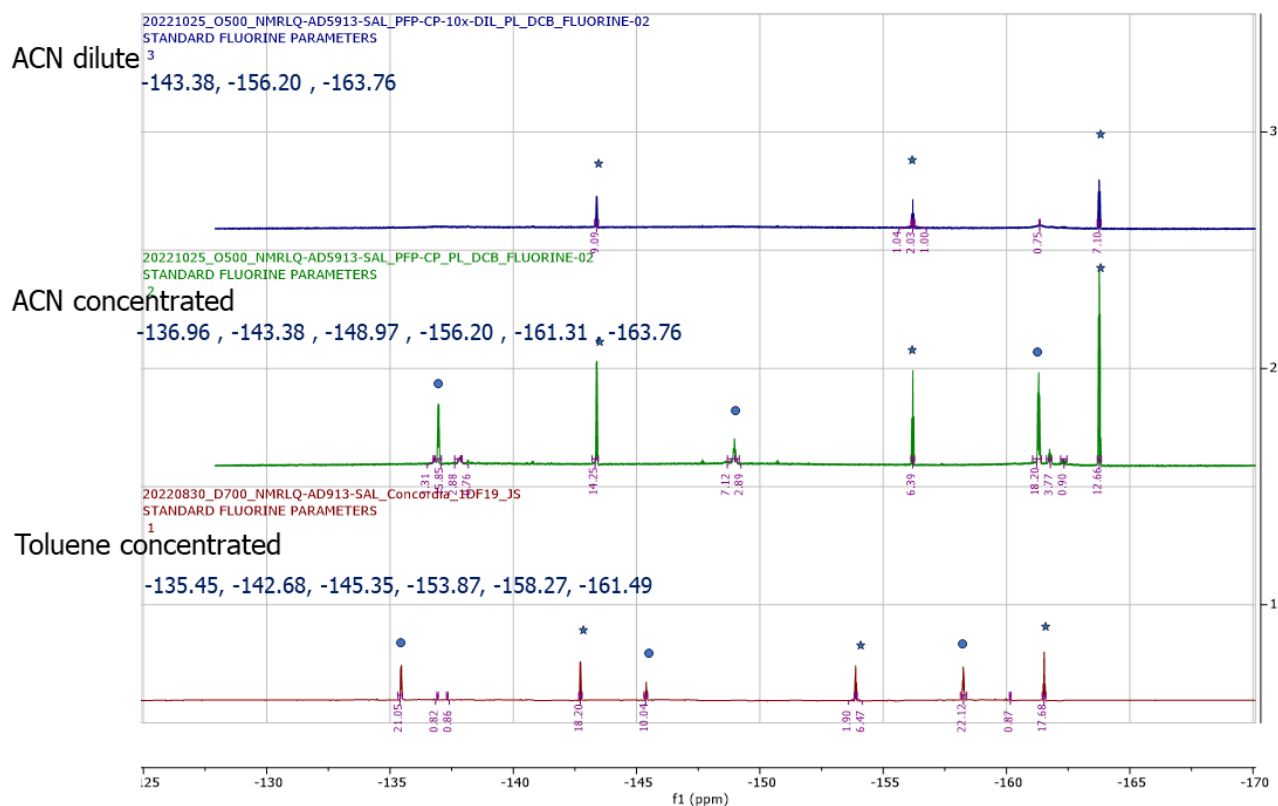


Figure 5.2: ^{19}F NMR spectrum of *PFP3CN3-CP* in acetonitrile (dilute (3 g/l) and concentrated (30 g/l)) and toluene (concentrated (30 g/l)). The star signs relate to monomers, and the circle signs rise from dimers in high concentrations.

Our DFT calculations identified three potential dimer conformations for *PFP3CN3-CP* by considering the possible types of intermolecular interactions between monomers. Figure 5.3 presents these conformations: (a) and (b) are face-to-face stacked geometries that feature intermolecular π - π interactions, while (c) is an arrangement involving dipole- π interactions between CN bonds and the PFP rings.

We also studied how the polarity of solvents can affect the dimerization modes by selecting acetonitrile as a polar solvent and toluene as a non-polar solvent. Our calculations in these two different solvents did not indicate any change in the dimerization modes of *PFP3CN3-CP*. In both solvents, we observed dimer conformations (a), (b), and (c), featuring either π - π or dipole- π intermolecular interactions between the monomers. The PFP rotation and the dihedral angles between the core and CN bonds for each dimer conformation are reported below.

Importantly, only the DFT-optimized dimer conformation (b) would be in line with our experimental ^{19}F NMR results, which would be expected to show six ^{19}F NMR peaks: three peaks from the non-dimerized species (monomer) and three peaks from the dimer, which, therefore, must have a fully symmetric structure. Further ^{19}F NMR measurements are necessary to observe changes in ^{19}F NMR peak intensities where the sample is being

gradually diluted, to conclusively determine whether the fully symmetric dimer configuration is the only dominant species or if other dimer modes can occur, which would provide additional peaks in ^{19}F NMR.

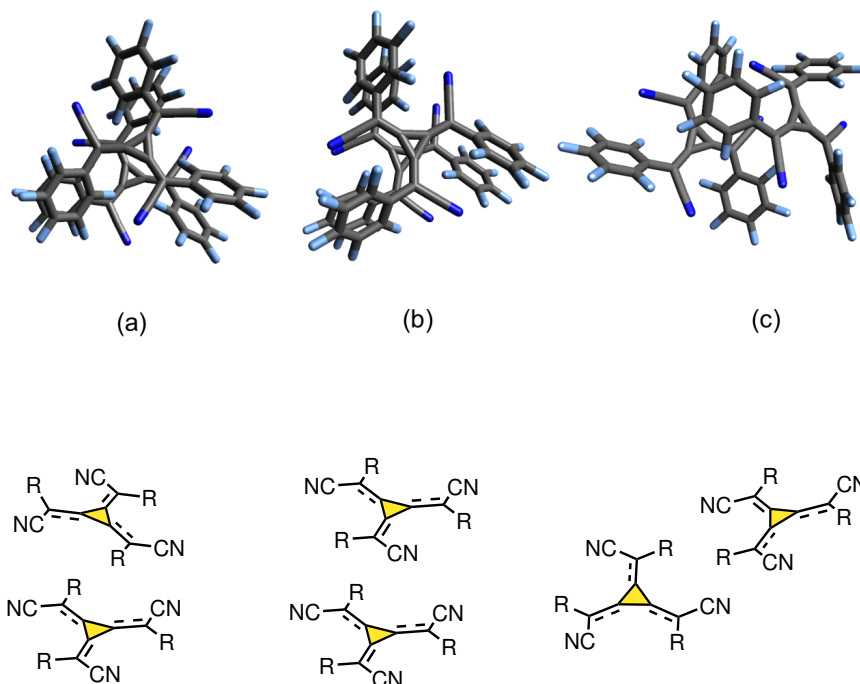


Figure 5.3: Three different possible dimer conformations for *PFP3CN3-CP* based on our DFT calculations, and their corresponding schematics; R=PFP. The average PFP ring rotation angle and the dihedral angles between CN and the core are $(41^\circ, 9^\circ)$, $(47^\circ, 1.9^\circ)$, and $(45^\circ, 1.3^\circ)$ respectively for (a), (b), and (c) in the gas phase.

To further assess the hypothesis of dimer formation in dense solution we aimed to investigate the solid-state structure of *PFP3CN3-CP*. The finding of a crystal structure comprising a dimerized structure, e.g., of sandwich herringbone type, would provide strong support for the above interpretation of the ^{19}F NMR data as being indicative of (reversible) dimerization in dense solution. To this end, first, we dissolved 10 mg of the *PFP3CN3-CP* in 5 ml of chloroform and then added 10 ml methanol slowly to the vial to grow macroscopic single crystals of *PFP3CN3-CP* for crystal-structure solution via single-crystal X-ray diffraction. However, despite week-long efforts of trying to crystallize *PFP3CN3-CP* no notable crystals could be obtained. Therefore, we performed powder X-ray diffraction of the source material at the Canadian Light Source to gain insight into the solid-state packing; the data is shown in Figure 5.4 in angular (2θ) and reciprocal (\AA^{-1}) units.

The unit-cell determination algorithm yielded a hexagonal unit cell solution with unit cell parameters of $a = 13.40\text{\AA}$, $b = 13.40\text{\AA}$, $c = 8.93\text{\AA}$, $\gamma = 120^\circ$, with a cell volume of

1388.96Å³, with a high M20-quality metric of the structure solution of 46.36. Given that the Van der Waals volume of a single *PFP3CN3 – CP* molecule is 586.094Å³, the volume would be well compatible with two molecules per unit cell. The hexagonal unit cell is a very plausible solution for the given compound as its symmetry is compatible with the threefold rotational symmetry of the *PFP3CN3 – CP* molecule, as well as the DFT-optimized dimer conformations (a) and (b).

Currently, in an ongoing collaboration with Prof. Mihails Arhangeliskis (Faculty of Chemistry, University of Warsaw, Poland) the modeling of the molecular orientation in the experimentally determined unit cell is being attempted using force field calculations. To this end, both the optimized structure of the single *PFP3CN3 – CP* molecule is used and two such molecules are being put into the unit cell and treated as rigid bodies, as well as the DFT-optimized dimers are used as starting geometries for modeling the structure solution.

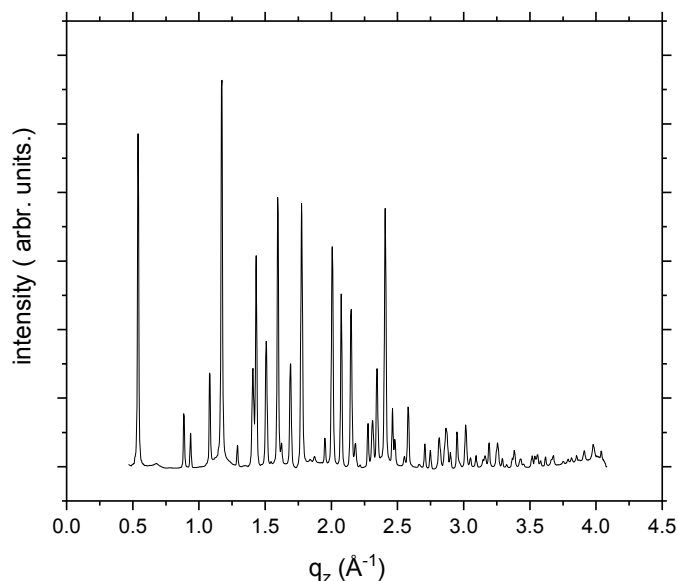


Figure 5.4: Powder X-ray Diffraction (PXRD) pattern of *PFP3CN3 – CP* showing the intensity (in arbitrary units) as a function of the scattering vector q_z (corresponding to specific d-spacings)

5.4 Conclusion

In conclusion, our study provides strong evidence for the dimerization of *PFP3CN3-CP* in solution at higher concentrations. The ¹⁹F NMR analysis in various solvents (toluene and acetonitrile) revealed additional peaks alongside the expected ones, with these supplementary peaks becoming more pronounced at higher concentrations. Our findings suggest the occurrence of reversible neutral-neutral dimerization of *PFP3CN3-CP* in dense

solution.

DFT calculations support this hypothesis by identifying three possible dimer conformations for PFP_3CN_3-CP , featuring either intermolecular $\pi-\pi$ or dipole- π interactions. Among these, conformation (b) is consistent with the ^{19}F NMR data, indicating that the $\pi-\pi$ dimerization mode is the most plausible in solution.

Further ^{19}F NMR experiments are required to confirm the final dimer conformation and to explore any potential transitions between conformations as the concentration is varied. Monitoring the changes in peak intensities upon gradual dilution would be especially useful in refining our understanding of the dimerization process.

Additionally, to independently assess the plausibility of dimerization, synchrotron PXRD data provided structural insights, suggesting that PFP_3CN_3-CP crystallizes in the hexagonal crystal class, compatible with the threefold rotational symmetry observed in DFT-optimized conformations (a) and (b). Based on the unit cell volume, we infer that one dimer per unit cell exists in the crystalline state, further supporting the conclusion that PFP_3CN_3-CP , similar to its analogues, tends to dimerize, here in the form of a dimer formed by neutral molecules in a dense solution, which might translate into the solid state.

Chapter 6

Conclusion

The work (chapters 3, 4 and 5) presented in this thesis brings together comprehensive studies on molecular p-dopants and the role of steric hindrance in enhancing p-doping efficiency. By leveraging density functional theory (DFT) calculations, along with various spectroscopic and electrical characterization techniques, we have contributed new insights into the fundamental aspects of the p-dopant design.

First, chapter 3, provides a comprehensive analysis of the interplay between electronic and geometric effects in the design of molecular p-dopants based on cyclohexadiene (CHD) and cyclopropane (CP) cores. By systematically comparing various electron-withdrawing substituents on the two cores with different substitution patterns, we derived rational design principles for p-dopants. This approach enabled us to separate the influence of the core from the substituent and distinguish the geometric effects from the electronic effects in determining EA_1 and EA_2 . A key outcome of this work is that electron affinities can be directly predicted from the Hammett parameters of the substituents, significantly streamlining the screening of p-dopants before synthesis. Fundamentally, we demonstrated that partial atomic charges on the cores are the primary factor driving the electron affinities of the molecules. The design of highly efficient CHD-based p-dopants is constrained by the need to retain core planarity for high electron affinity, which is easily disrupted by bulky substituents. However, when the substituents are geometrically decoupled from the core via a phenyl ring, CHD-based dopants typically exhibit higher electron affinities than their CP analogues. This distinction arises from the intrinsic affinity of the core rather than a specific core-substituent interaction. However, this decoupling reduces the electron-withdrawing effect of the substituent, lowering achievable electron affinities by around 50%. Unlike CHD cores, CP cores can accommodate direct substituent connections without distorting their structure, leading to higher electron affinities. Furthermore, while EA_2 of CP-based molecules increases more rapidly with electron-withdrawing substituents than their CHD analogues, this effect is offset by the higher intrinsic EA_2 values of CHD cores. Despite both cores being capable of yielding molecules with high EA_2 , CP-based molecules excel due to their significantly higher EA_1 , as their core planarity is preserved without requiring phenyl rings. These findings reveal the potential of CP-based molecules for designing p-dopants with superior single and double electron-accepting abilities. This study offers practical insights into the design of strong electron acceptors and provides a deeper understanding of the molecu-

lar factors, which guides future optimization efforts through knowledge-based molecular design.

Second, chapter 4, addresses the challenges associated with p-doping efficiency. The conventional approach of using planar dopants with high EAs has been shown to lead to the formation of ground-state charge transfer complexes (CPX), hindering integer charge transfer (ICT) and compromising doping efficiency. To overcome this limitation, it is hypothesized that steric hindrance in dopant design can suppress CPX formation and promote ICT. A novel three-dimensional dopant, 2,2',2''-(cyclopropane-1,2,3-triylidene)tris(2-(perfluorophenyl)acetonitrile) ($PF_3CN_3 - CP$), with pendant functional groups that shield its central core while maintaining high electron affinity is synthesized. The study demonstrates that incorporating steric hindrance in dopant design effectively suppresses CPX formation. This is experimentally validated through the comparison with an equally strong planar dopant, F_2-TCNQ . The remarkable stability exhibited by $PF_3CN_3 - CP$ over time, further adds to its appeal as a promising molecular p-dopant. The steric hindrance in $PF_3CN_3 - CP$ not only enhances doping efficiency but also helps the stability issues commonly associated with similar dopants. Furthermore, this improvement in doping efficiency is further highlighted by an order-of-magnitude increase in thin film conductivity compared to the planar dopant; F_2-TCNQ . This study highlights the potential of a steric hindrance as a general and promising route for designing efficient molecular p-dopants in OSCs.

Third, chapter 5, explores the dimerization behavior of $PF_3CN_3 - CP$ using a combination of ^{19}F NMR spectroscopy, DFT, and Powder X-ray Diffraction (PXRD). This study proves that $PF_3CN_3 - CP$ undergoes reversible neutral-neutral dimerization in dense solutions. Through ^{19}F NMR spectroscopy in both toluene and acetonitrile, the appearance of additional peaks at high concentrations, points to the formation of dimers. Complementary DFT calculations identified three possible dimer conformations, highlighting the presence of either $\pi-\pi$ stacking or dipole- π intermolecular interactions between monomers. Additionally, synchrotron PXRD data further validated these conclusions by demonstrating that $PF_3CN_3 - CP$ crystallizes within a hexagonal unit cell, consistent with the molecule's threefold rotational symmetry. The combination of ^{19}F NMR, DFT modeling, and PXRD provides compelling evidence for the neutral dimerization of $PF_3CN_3 - CP$. Although these findings provide strong insights into the dimerization behavior of $PF_3CN_3 - CP$, further ^{19}F NMR experiments are essential to confirm the dominant dimer conformation and to track any transitions between dimer conformations as a function of concentration.

In conclusion, this thesis provides a valuable contribution to the more efficient molecular p-doping of organic semiconductors. The findings not only improve our understanding of the intricate balance between molecular structure and electronic properties but also offer practical strategies for developing p-dopants with enhanced efficiency. Future studies could focus on the synthesis of other potential p-dopants that are proposed in the thesis, to optimize doping efficiency and investigate their performance in organic semiconductors and model devices. Another promising direction for future research is examining the feasibility of potential p-dopants for double doping, as inferred from the DFT modeling study presented. This approach could involve the use of relevant organic semiconductors such as P3HT and more recent and application relevant conjugated poly-

mers to enhance charge transport properties and improve the device performance while retaining low dopant loading.

Bibliography

- [1] A. Köhler and H. Bässler, *Electronic Processes in Organic Semiconductors: An Introduction*. Weinheim: Wiley-VCH, 2015.
- [2] L. M. Cowen, J. Atoyo, M. J. Carnie, D. Baran, and B. C. Schroeder, “Review—organic materials for thermoelectric energy generation,” *ECS Journal of Solid State Science and Technology*, vol. 6, no. 3, p. N3080, Jan 2017. [Online]. Available: <https://dx.doi.org/10.1149/2.0121703jss>
- [3] H. Méndez, G. Heimel, A. Opitz, K. Sauer, P. Barkowski, M. Oehzelt, J. Soeda, T. Okamoto, J. Takeya, J.-B. Arlin, J.-Y. Balandier, Y. Geerts, N. Koch, and I. Salzmann, “Doping of Organic Semiconductors: Impact of Dopant Strength and Electronic Coupling,” *Angewandte Chemie International Edition*, vol. 52, no. 30, pp. 7751–7755, Jul. 2013.
- [4] W. Ansgar, N. Makato, and K. Shigeru, “Diaryl-amino matrix material doped with a mesomeric radialene compound,” Patent EP-2 684 932A1, 2012.
- [5] H. Hase, M. Berteau-Rainville, S. Charoughchi, W. Bodlos, E. Orgiu, and I. Salzmann, “Critical dopant concentrations govern integer and fractional charge-transfer phases in doped P3HT,” *Journal of Physics: Materials*, vol. 6, no. 1, p. 014004, Jan. 2023.
- [6] F. Ghani, A. Opitz, P. Pingel, G. Heimel, I. Salzmann, J. Frisch, D. Neher, A. Tsami, U. Scherf, and N. Koch, “Charge transfer in and conductivity of molecularly doped thiophene-based copolymers,” *Journal of Polymer Science Part B: Polymer Physics*, vol. 53, no. 1, pp. 58–63, Jan. 2015.
- [7] G. Heimel, “The Optical Signature of Charges in Conjugated Polymers,” *ACS Central Science*, vol. 2, no. 5, pp. 309–315, May 2016.
- [8] P. J. Brown, H. Sirringhaus, M. Harrison, M. Shkunov, and R. H. Friend, “Optical spectroscopy of field-induced charge in self-organized high mobility poly(3-hexylthiophene),” *Phys. Rev. B*, vol. 63, p. 125204, Mar 2001. [Online]. Available: <https://link.aps.org/doi/10.1103/PhysRevB.63.125204>
- [9] F. Hasan, J. H. Gillen, A. T. Jayaweera, W. D. McDearmon Jr., A. H. Winter, and C. M. Bejger, “Simple air-stable [3]radialene anion radicals as environmentally switchable catholytes in water,” *Chemistry – A European*

- Journal*, vol. 30, no. 7, p. e202302829, 2024. [Online]. Available: <https://chemistry-europe.onlinelibrary.wiley.com/doi/abs/10.1002/chem.202302829>
- [10] M. J. Frisch, G. W. Trucks, H. B. Schlegel, G. E. Scuseria, M. A. Robb, J. R. Cheeseman, G. Scalmani, V. Barone, B. Mennucci, G. A. Petersson, H. Nakatsuji, M. Caricato, X. Li, H. P. Hratchian, A. F. Izmaylov, J. Bloino, G. Zheng, J. L. Sonnenberg, M. Hada, M. Ehara, K. Toyota, R. Fukuda, J. Hasegawa, M. Ishida, T. Nakajima, Y. Honda, O. Kitao, H. Nakai, T. Vreven, J. A. Montgomery Jr., J. E. Peralta, F. Ogliaro, M. J. Bearpark, J. Heyd, E. N. Brothers, K. N. Kudin, V. N. Staroverov, R. Kobayashi, J. Normand, K. Raghavachari, A. P. Rendell, J. C. Burant, S. S. Iyengar, J. Tomasi, M. Cossi, N. Rega, N. J. Millam, M. Klene, J. E. Knox, J. B. Cross, V. Bakken, C. Adamo, J. Jaramillo, R. Gomperts, R. E. Stratmann, O. Yazyev, A. J. Austin, R. Cammi, C. Pomelli, J. W. Ochterski, R. L. Martin, K. Morokuma, V. G. Zakrzewski, G. A. Voth, P. Salvador, J. J. Dannenberg, S. Dapprich, A. D. Daniels, Farkas, J. B. Foresman, J. V. Ortiz, J. Cioslowski, and D. J. Fox, *Gaussian, Inc., Gaussian, Inc.*, Wallingford, CT, USA, 2009.
- [11] C. Hansch, A. Leo, and R. W. Taft, "A survey of hammett substituent constants and resonance and field parameters," *Chemical Reviews*, vol. 91, no. 2, pp. 165–195, 1991. [Online]. Available: <https://doi.org/10.1021/cr00002a004>
- [12] J. Saska, N. E. Shevchenko, G. Gonel, Z. I. Bedolla-Valdez, R. M. Talbot, A. J. Moulé, and M. Mascal, "Synthesis and characterization of solution processable, high electron affinity molecular dopants," *Journal of Materials Chemistry C*, vol. 9, no. 44, pp. 15 990–15 997, 2021.
- [13] R. D. Johnson III, "Nist 101. computational chemistry comparison and benchmark database," 05 2022. [Online]. Available: <https://cccbdb.nist.gov/>
- [14] H. Hase, M. Berteau-Rainville, S. Charoughchi, E. Orgiu, and I. Salzmann, "Doping-related broadening of the density of states governs integer-charge transfer in P3HT," *Applied Physics Letters*, vol. 118, no. 20, p. 203301, May 2021.
- [15] S. Charoughchi, J. T. Liu, M. Berteau-Rainville, H. Hase, M. S. Askari, S. Bhagat, P. Forgione, and I. Salzmann, "Sterically-Hindered Molecular p-Dopants Promote Integer Charge Transfer in Organic Semiconductors," *Angewandte Chemie International Edition*, vol. 62, no. 31, p. e202304964, Aug. 2023.
- [16] P. Atkins and J. de Paula, *Atkins' Physical Chemistry*. OUP Oxford, 2014. [Online]. Available: <https://books.google.ca/books?id=sWTYAwAAQBAJ>
- [17] S. R. Forrest, *Organic Electronics: Foundations to Applications*. Oxford University Press, 08 2020. [Online]. Available: <https://doi.org/10.1093/oso/9780198529729.001.0001>
- [18] V. Gold, Ed., *The IUPAC Compendium of Chemical Terminology: The Gold Book*, 4th ed. Research Triangle Park, NC: International Union of Pure and Applied Chemistry (IUPAC), 2019.

- [19] N. W. Ashcroft, "Solid state physics [by] neil w. ashcroft [and] n. david mermin." 1976. [Online]. Available: <https://api.semanticscholar.org/CorpusID:126694383>
- [20] D. Natali, "1 - fundamentals of organic electronic devices," in *Organic Flexible Electronics*, ser. Woodhead Publishing Series in Electronic and Optical Materials, P. Cosseddu and M. Caironi, Eds. Woodhead Publishing, 2021, pp. 1–25. [Online]. Available: <https://www.sciencedirect.com/science/article/pii/B9780128188903000011>
- [21] M. Caironi and Y.-Y. Noh, *Front Matter*. John Wiley Sons, Ltd, 2015. [Online]. Available: <https://onlinelibrary.wiley.com/doi/abs/10.1002/9783527679973.fmatter>
- [22] S. Ogawa, Ed., *Organic Electronics Materials and Devices*, 1st ed. Springer Tokyo, 2015. [Online]. Available: <https://doi.org/10.1007/978-4-431-55654-1>
- [23] G. Horowitz, "Validity of the concept of band edge in organic semiconductors," *Journal of Applied Physics*, vol. 118, no. 11, p. 115502, Sep. 2015.
- [24] S. M. Sze, *Physics of Semiconductor Devices*, 2nd ed. New York: Wiley, 1981.
- [25] H. Bässler, "Charge Transport in Disordered Organic Photoconductors a Monte Carlo Simulation Study," *physica status solidi (b)*, vol. 175, no. 1, pp. 15–56, Jan. 1993.
- [26] M. Oehzelt, N. Koch, and G. Heimel, "Organic semiconductor density of states controls the energy level alignment at electrode interfaces," *Nature Communications*, vol. 5, no. 1, p. 4174, Sep. 2014.
- [27] H. Shirakawa, E. J. Louis, A. G. MacDiarmid, C. K. Chiang, and A. J. Heeger, "Synthesis of electrically conducting organic polymers: Halogen derivatives of polyacetylene, $(\text{CH})_x$," *Journal of the Chemical Society, Chemical Communications*, no. 16, p. 578, 1977.
- [28] C. K. Chiang, C. R. Fincher, Y. W. Park, A. J. Heeger, H. Shirakawa, E. J. Louis, S. C. Gau, and A. G. MacDiarmid, "Electrical Conductivity in Doped Polyacetylene," *Physical Review Letters*, vol. 39, no. 17, pp. 1098–1101, Oct. 1977.
- [29] N. Basescu, Z.-X. Liu, D. Moses, A. J. Heeger, H. Naarmann, and N. Theophilou, "High electrical conductivity in doped polyacetylene," *Nature*, vol. 327, no. 6121, pp. 403–405, Jun. 1987.
- [30] Y. Yamamoto, K. Yoshino, and Y. Inuishi, "Electrical Properties of Phthalocyanine-Halogen Complexes," *Journal of the Physical Society of Japan*, vol. 47, no. 6, pp. 1887–1891, Dec. 1979.
- [31] G. Parthasarathy, C. Shen, A. Kahn, and S. R. Forrest, "Lithium doping of semi-conducting organic charge transport materials," *Journal of Applied Physics*, vol. 89, no. 9, pp. 4986–4992, May 2001.

- [32] B. Lüssem, M. Riede, and K. Leo, "Doping of organic semiconductors," *physica status solidi (a)*, vol. 210, no. 1, pp. 9–43, Jan. 2013.
- [33] I. Salzmann and G. Heimel, "Toward a comprehensive understanding of molecular doping organic semiconductors (review)," *Journal of Electron Spectroscopy and Related Phenomena*, vol. 204, pp. 208–222, Oct. 2015.
- [34] S. Reineke, F. Lindner, G. Schwartz, N. Seidler, K. Walzer, B. Lüssem, and K. Leo, "White organic light-emitting diodes with fluorescent tube efficiency," *Nature*, vol. 459, no. 7244, pp. 234–238, May 2009.
- [35] I. E. Jacobs and A. J. Moulé, "Controlling Molecular Doping in Organic Semiconductors," *Advanced Materials*, vol. 29, no. 42, p. 1703063, Nov. 2017.
- [36] E. Lim, B.-J. Jung, M. Chikamatsu, R. Azumi, Y. Yoshida, K. Yase, L.-M. Do, and H.-K. Shim, "Doping effect of solution-processed thin-film transistors based on polyfluorene," *J. Mater. Chem.*, vol. 17, pp. 1416–1420, 2007. [Online]. Available: <http://dx.doi.org/10.1039/B615720C>
- [37] M. Matters, D. de Leeuw, P. Herwig, and A. Brown, "Bias-stress induced instability of organic thin film transistors," *Synthetic Metals*, vol. 102, no. 1, pp. 998–999, 1999. [Online]. Available: <https://www.sciencedirect.com/science/article/pii/S037967799801162X>
- [38] G. Horowitz, R. Hajlaoui, D. Fichou, and A. El Kassmi, "Gate voltage dependent mobility of oligothiophene field-effect transistors," *Journal of Applied Physics*, vol. 85, no. 6, pp. 3202–3206, 03 1999. [Online]. Available: <https://doi.org/10.1063/1.369661>
- [39] H. F. Haneef, A. M. Zeidell, and O. D. Jurchescu, "Charge carrier traps in organic semiconductors: A review on the underlying physics and impact on electronic devices," *Journal of Materials Chemistry C*, vol. 8, no. 3, pp. 759–787, 2020.
- [40] K.-H. Yim, G. L. Whiting, C. E. Murphy, J. J. M. Halls, J. H. Burroughes, R. H. Friend, and J.-S. Kim, "Controlling Electrical Properties of Conjugated Polymers via a Solution-Based p-Type Doping," *Advanced Materials*, vol. 20, no. 17, pp. 3319–3324, Sep. 2008.
- [41] E. F. Aziz, A. Vollmer, S. Eisebitt, W. Eberhardt, P. Pingel, D. Neher, and N. Koch, "Localized Charge Transfer in a Molecularly Doped Conducting Polymer," *Advanced Materials*, vol. 19, no. 20, pp. 3257–3260, Sep. 2007.
- [42] P. Pingel and D. Neher, "Comprehensive picture of p-type doping of P3HT with the molecular acceptor F4TCNQ," *Physical Review B*, vol. 87, no. 11, p. 115209, Mar. 2013.
- [43] K. Harada, M. Riede, K. Leo, O. R. Hild, and C. M. Elliott, "Pentacene homojunctions: Electron and hole transport properties and related photovoltaic

- responses,” *Phys. Rev. B*, vol. 77, p. 195212, May 2008. [Online]. Available: <https://link.aps.org/doi/10.1103/PhysRevB.77.195212>
- [44] K. Walzer, B. Maennig, M. Pfeiffer, and K. Leo, “Highly Efficient Organic Devices Based on Electrically Doped Transport Layers,” *Chemical Reviews*, vol. 107, no. 4, pp. 1233–1271, Apr. 2007.
- [45] W. Gao and A. Kahn, “Controlled p doping of the hole-transport molecular material N,N'-diphenyl-N,N'-bis(1-naphthyl)-1,1'-biphenyl-4,4'-diamine with tetrafluorotetracyanoquinodimethane,” *Journal of Applied Physics*, vol. 94, no. 1, pp. 359–366, Jun. 2003.
- [46] I. Salzmann, G. Heimel, M. Oehzelt, S. Winkler, and N. Koch, “Molecular Electrical Doping of Organic Semiconductors: Fundamental Mechanisms and Emerging Dopant Design Rules,” *Accounts of Chemical Research*, vol. 49, no. 3, pp. 370–378, Mar. 2016.
- [47] H. Méndez, G. Heimel, S. Winkler, J. Frisch, A. Opitz, K. Sauer, B. Wegner, M. Oehzelt, C. Röthel, S. Duhm, D. Többens, N. Koch, and I. Salzmann, “Charge-transfer crystallites as molecular electrical dopants,” *Nature Communications*, vol. 6, no. 1, p. 8560, Dec. 2015.
- [48] I. Salzmann, G. Heimel, S. Duhm, M. Oehzelt, P. Pingel, B. M. George, A. Schnegg, K. Lips, R.-P. Blum, A. Vollmer, and N. Koch, “Intermolecular Hybridization Governs Molecular Electrical Doping,” *Physical Review Letters*, vol. 108, no. 3, p. 035502, Jan. 2012.
- [49] J. Yang, Y. Li, S. Duhm, J. Tang, S. Kera, and N. Ueno, “Molecular structure-dependent charge injection and doping efficiencies of organic semiconductors: Impact of side chain substitution,” *Advanced Materials Interfaces*, vol. 1, no. 3, p. 1300128, 2014. [Online]. Available: <https://onlinelibrary.wiley.com/doi/abs/10.1002/admi.201300128>
- [50] V. P. Parkhutik and E. Matveeva, “Effects of molecular doping by hydroquinones on morphology and optical properties of polyaniline,” *The Journal of Physical Chemistry B*, vol. 102, no. 9, pp. 1549–1555, 1998. [Online]. Available: <https://doi.org/10.1021/jp972471m>
- [51] E. Matveeva, “Could the acid doping of polyaniline represent the charge transfer interaction?” *Synthetic Metals*, vol. 83, no. 2, pp. 89–96, 1996. [Online]. Available: <https://www.sciencedirect.com/science/article/pii/S0379677997800598>
- [52] B. Wegner, L. Grubert, C. Dennis, A. Opitz, A. Röttger, Y. Zhang, S. Barlow, S. R. Marder, S. Hecht, K. Müllen, and N. Koch, “Predicting the yield of ion pair formation in molecular electrical doping: Redox-potentials *versus* ionization energy/electron affinity,” *Journal of Materials Chemistry C*, vol. 7, no. 44, pp. 13 839–13 848, 2019.

- [53] K. Kanai, K. Akaike, K. Koyasu, K. Sakai, T. Nishi, Y. Kamizuru, T. Nishi, Y. Ouchi, and K. Seki, "Determination of electron affinity of electron accepting molecules," *Applied Physics A*, vol. 95, no. 1, pp. 309–313, Apr. 2009.
- [54] F. Zhang and A. Kahn, "Investigation of the High Electron Affinity Molecular Dopant F6-TCNNQ for Hole-Transport Materials," *Advanced Functional Materials*, vol. 28, no. 1, p. 1703780, Jan. 2018.
- [55] H. Lee, J. Lee, S. Park, Y. Yi, S. W. Cho, J. W. Kim, and S. J. Kang, "Hole injection enhancement of a single-walled carbon nanotube anode using an organic charge-generation layer," *Carbon*, vol. 71, pp. 268–275, 2014. [Online]. Available: <https://www.sciencedirect.com/science/article/pii/S000862231400075X>
- [56] Y. Karpov, T. Erdmann, I. Raguzin, M. Al-Hussein, M. Binner, U. Lappan, M. Stamm, K. L. Gerasimov, T. Beryozkina, V. Bakulev, D. V. Anokhin, D. A. Ivanov, F. Günther, S. Gemming, G. Seifert, B. Voit, R. Di Pietro, and A. Kiriy, "High Conductivity in Molecularly p-Doped Diketopyrrolopyrrole-Based Polymer: The Impact of a High Dopant Strength and Good Structural Order," *Advanced Materials*, vol. 28, no. 28, pp. 6003–6010, Jul. 2016.
- [57] Y. Liu, B. Nell, K. Ortstein, Z. Wu, Y. Karpov, T. Beryozkina, S. Lenk, A. Kiriy, K. Leo, and S. Reineke, "High electron affinity molecular dopant cn6-cp for efficient organic light-emitting diodes," *ACS Appl. Mater. Interfaces*, vol. 11, pp. 11 660–11 666, 2019. [Online]. Available: <https://pubmed.ncbi.nlm.nih.gov/30810028/>
- [58] J. Saska, G. Gonel, Z. I. Bedolla-Valdez, S. D. Aronow, N. E. Shevchenko, A. S. Dudnik, A. J. Moulé, and M. Mascal, "A Freely Soluble, High Electron Affinity Molecular Dopant for Solution Processing of Organic Semiconductors," *Chemistry of Materials*, vol. 31, no. 5, pp. 1500–1506, Mar. 2019.
- [59] M. Frericks, C. Pflumm, E. Mankel, T. Mayer, and W. Jaegermann, "Space charge regions at organic p-i-homointerfaces from advanced modeling of in situ-prepared interfaces analyzed by photoelectron spectroscopy," *ACS Applied Electronic Materials*, vol. 3, no. 3, pp. 1211–1227, 2021. [Online]. Available: <https://doi.org/10.1021/acsaelm.0c01062>
- [60] V. Wißdorf, M. Frericks, M. Tzschoppe, P. Connor, S. Beck, C. Pflumm, A. Pucci, W. Jaegermann, and E. Mankel, "Impedance spectra analysis of p-doped organic thin films by charge carrier distribution evaluation," *ACS Applied Electronic Materials*, vol. 1, no. 10, pp. 1994–2006, 2019. [Online]. Available: <https://doi.org/10.1021/acsaelm.9b00279>
- [61] W. Gao and A. Kahn, "Controlled p-doping of zinc phthalocyanine by coevaporation with tetrafluorotetracyanoquinodimethane: A direct and inverse photoemission study," *Applied Physics Letters*, vol. 79, no. 24, pp. 4040–4042, Dec. 2001.

- [62] F. Zhang and A. Kahn, "Investigation of the high electron affinity molecular dopant f6-tcnnq for hole-transport materials," *Advanced Functional Materials*, vol. 28, no. 1, p. 1703780, 2018. [Online]. Available: <https://onlinelibrary.wiley.com/doi/abs/10.1002/adfm.201703780>
- [63] J.-H. Lee, S.-H. Cheng, S.-J. Yoo, H. Shin, J.-H. Chang, C.-I. Wu, K.-T. Wong, and J.-J. Kim, "An exciplex forming host for highly efficient blue organic light emitting diodes with low driving voltage," *Advanced Functional Materials*, vol. 25, no. 3, pp. 361–366, 2015. [Online]. Available: <https://onlinelibrary.wiley.com/doi/abs/10.1002/adfm.201402707>
- [64] S. Bhagat, H. Hase, and I. Salzmann, "Chemical doping of organic semiconductors," in *Organic Flexible Electronics*, P. Cosseddu and M. Caironi, Eds. Elsevier, 2021, pp. 107–141.
- [65] P. Tyagi, M. K. Dalai, C. K. Suman, S. Tuli, and R. Srivastava, "Study of 2,3,5,6-tetrafluoro-7,7,8,8-tetracyano quinodimethane diffusion in organic light emitting diodes using secondary ion mass spectroscopy," *RSC Adv.*, vol. 3, pp. 24 553–24 559, 2013. [Online]. Available: <http://dx.doi.org/10.1039/C3RA43218A>
- [66] S. Olthof, W. Tress, R. Meerheim, B. Lüssem, and K. Leo, "Photoelectron spectroscopy study of systematically varied doping concentrations in an organic semiconductor layer using a molecular p-dopant," *Journal of Applied Physics*, vol. 106, no. 10, p. 103711, Nov. 2009.
- [67] J.-H. Lee, J. Lee, Y. H. Kim, C. Yun, B. Lüssem, and K. Leo, "Effect of trap states on the electrical doping of organic semiconductors," *Organic Electronics*, vol. 15, no. 1, pp. 16–21, 2014. [Online]. Available: <https://www.sciencedirect.com/science/article/pii/S1566119913004564>
- [68] J. Li, C. W. Rochester, I. E. Jacobs, S. Friedrich, P. Stroeve, M. Riede, and A. J. Moulé, "Measurement of Small Molecular Dopant F4TCNQ and C₆₀F₃₆ Diffusion in Organic Bilayer Architectures," *ACS Applied Materials & Interfaces*, vol. 7, no. 51, pp. 28 420–28 428, Dec. 2015.
- [69] B. Lüssem, M. L. Tietze, H. Kleemann, C. Hoßbach, J. W. Bartha, A. Zakhidov, and K. Leo, "Doped organic transistors operating in the inversion and depletion regime," *Nature Communications*, vol. 4, no. 1, Dec. 2013.
- [70] Y. Karpov, N. Kiriy, M. Al-Hussein, M. Hambsch, T. Beryozkina, V. Bakulev, S. C. B. Mannsfeld, B. Voit, and A. Kiriy, "Hexacyano-[3]-radialene anion-radical salts: A promising family of highly soluble p-dopants," *Chemical Communications*, vol. 54, no. 3, pp. 307–310, 2018.
- [71] A. C. Arias, J. D. MacKenzie, I. McCulloch, J. Rivnay, and A. Salleo, "Materials and applications for large area electronics: Solution-based approaches," *Chemical Reviews*, vol. 110, no. 1, pp. 3–24, 2010, PMID: 20070114. [Online]. Available: <https://doi.org/10.1021/cr900150b>

- [72] P. Pingel, R. Schwarzl, and D. Neher, "Effect of molecular p-doping on hole density and mobility in poly(3-hexylthiophene)," *Applied Physics Letters*, vol. 100, no. 14, p. 143303, Apr. 2012.
- [73] J. E. Cochran, M. J. N. Junk, A. M. Glaudell, P. L. Miller, J. S. Cowart, M. F. Toney, C. J. Hawker, B. F. Chmelka, and M. L. Chabinyc, "Molecular Interactions and Ordering in Electrically Doped Polymers: Blends of PBTBT and F₄ TCNQ," *Macromolecules*, vol. 47, no. 19, pp. 6836–6846, Oct. 2014.
- [74] A. Dai, Y. Zhou, A. L. Shu, S. K. Mohapatra, H. Wang, C. Fuentes-Hernandez, Y. Zhang, S. Barlow, Y.-L. Loo, S. R. Marder, B. Kippelen, and A. Kahn, "Enhanced charge-carrier injection and collection via lamination of doped polymer layers p-doped with a solution-processible molybdenum complex," *Advanced Functional Materials*, vol. 24, no. 15, pp. 2197–2204, 2014. [Online]. Available: <https://onlinelibrary.wiley.com/doi/abs/10.1002/adfm.201303232>
- [75] J. Li, G. Zhang, D. M. Holm, I. E. Jacobs, B. Yin, P. Stroeve, M. Mascal, and A. J. Moulé, "Introducing Solubility Control for Improved Organic P-Type Dopants," *Chemistry of Materials*, vol. 27, no. 16, pp. 5765–5774, Aug. 2015.
- [76] J. E. Rainbolt, P. K. Koech, E. Polikarpov, J. S. Swensen, L. Cosimbescu, A. L. V. Ruden, L. Wang, L. S. Sapochak, A. B. Padmaperuma, and D. J. Gaspar, "Synthesis and characterization of p-type conductivity dopant 2-(3-(adamantan-1-yl)propyl)-3,5,6-trifluoro-7,7,8,8-tetracyanoquinodimethane," *Journal of Materials Chemistry C*, vol. 1, pp. 1876–1884, 2013. [Online]. Available: <https://api.semanticscholar.org/CorpusID:96301013>
- [77] P. R. Griffiths and J. A. de Haseth, *Fourier Transform Infrared Spectrometry*. Hoboken, NJ, USA: John Wiley & Sons, Inc., Apr. 2007.
- [78] N. Elgrishi, K. J. Rountree, B. D. McCarthy, E. S. Rountree, T. T. Eisenhart, and J. L. Dempsey, "A Practical Beginner's Guide to Cyclic Voltammetry," *Journal of Chemical Education*, vol. 95, no. 2, pp. 197–206, Feb. 2018.
- [79] F. Scholz, A. Bond, R. Compton, D. Fiedler, G. Inzelt, H. Kahlert, Š. Komorsky-Lovrić, H. Lohse, M. Lovrić, F. Marken, A. Neudeck, U. Retter, F. Scholz, and Z. Stojek, Eds., *Electroanalytical Methods*. Berlin, Heidelberg: Springer Berlin Heidelberg, 2010.
- [80] S. Sweetnam, K. R. Graham, G. O. Ngongang Ndjawa, T. Heumüller, J. A. Bartelt, T. M. Burke, W. Li, W. You, A. Amassian, and M. D. McGehee, "Characterization of the Polymer Energy Landscape in Polymer:Fullerene Bulk Heterojunctions with Pure and Mixed Phases," *Journal of the American Chemical Society*, vol. 136, no. 40, pp. 14078–14088, Oct. 2014.
- [81] R. R. Gagne, C. A. Koval, and G. C. Lisensky, "Ferrocene as an internal standard for electrochemical measurements," *Inorganic Chemistry*, vol. 19, no. 9, pp. 2854–2855, Sep. 1980.

- [82] C. M. Cardona, W. Li, A. E. Kaifer, D. Stockdale, and G. C. Bazan, "Electrochemical Considerations for Determining Absolute Frontier Orbital Energy Levels of Conjugated Polymers for Solar Cell Applications," *Advanced Materials*, vol. 23, no. 20, pp. 2367–2371, May 2011.
- [83] R. García, "Dynamic atomic force microscopy methods," *Surface Science Reports*, vol. 47, no. 6-8, pp. 197–301, Sep. 2002.
- [84] M. Birkholz, *Thin Film Analysis by X-Ray Scattering*. Weinheim, FRG: Wiley-VCH Verlag GmbH & Co. KGaA, Oct. 2005.
- [85] N. Kayunkid, S. Uttiya, and M. Brinkmann, "Structural Model of Regioregular Poly(3-hexylthiophene) Obtained by Electron Diffraction Analysis," *Macromolecules*, vol. 43, no. 11, pp. 4961–4967, Jun. 2010.
- [86] I. K. Robinson and D. J. Tweet, "Surface X-ray diffraction," *Reports on Progress in Physics*, vol. 55, no. 5, pp. 599–651, May 1992.
- [87] B. Schrode, S. Pachmajer, M. Dohr, C. Röthel, J. Domke, T. Fritz, R. Resel, and O. Werzer, "GIDVis: A comprehensive software tool for geometry-independent grazing-incidence X-ray diffraction data analysis and pole-figure calculations," *Journal of Applied Crystallography*, vol. 52, no. 3, pp. 683–689, Jun. 2019.
- [88] B. Toby and M. Suchoamel, "Mail-in synchrotron powder diffraction at the APS." *Synchrotron Radiation in Natural Science*, vol. 10, no. 1-2, pp. 77–80, Jan. 2011.
- [89] B. Lüssem, C.-M. Keum, D. Kasemann, B. Naab, Z. Bao, and K. Leo, "Doped organic transistors," *Chemical Reviews*, vol. 116, no. 22, pp. 13 714–13 751, Oct. 2016.
- [90] A. D. Scaccabarozzi, A. Basu, F. Aniés, J. Liu, O. Zapata-Arteaga, R. Warren, Y. Firdaus, M. I. Nugraha, Y. Lin, M. Campoy-Quiles, N. Koch, C. Müller, L. Tsetseris, M. Heeney, and T. D. Anthopoulos, "Doping Approaches for Organic Semiconductors," *Chemical Reviews*, vol. 122, no. 4, pp. 4420–4492, Feb. 2022.
- [91] H. Fukagawa, T. Sasaki, T. Tsuzuki, Y. Nakajima, T. Takei, G. Motomura, M. Hasegawa, K. Morii, and T. Shimizu, "Long-Lived Flexible Displays Employing Efficient and Stable Inverted Organic Light-Emitting Diodes," *Advanced Materials*, vol. 30, no. 28, p. 1706768, Jul. 2018.
- [92] D. Shen, W.-C. Chen, M.-F. Lo, and C.-S. Lee, "Charge-transfer complexes and their applications in optoelectronic devices," *Materials Today Energy*, vol. 20, p. 100644, Jun. 2021.
- [93] J. Pope and C. Lekakou, "Thermoelectric polymer composite yarns and an energy harvesting wearable textile," *Smart Materials and Structures*, vol. 28, no. 9, p. 095006, Sep. 2019.

- [94] N. Okada, K. Sato, M. Yokoo, E. Kodama, S. Kanehashi, and T. Shimomura, "Thermoelectric Properties of Poly(3-hexylthiophene) Nanofiber Aerogels with a Giant Seebeck Coefficient," *ACS Applied Polymer Materials*, vol. 3, no. 1, pp. 455–463, Jan. 2021.
- [95] C. Momblona, L. Gil-Escrig, E. Bandiello, E. M. Hutter, M. Sessolo, K. Lederer, J. Blochwitz-Nimoth, and H. J. Bolink, "Efficient vacuum deposited p-i-n and n-i-p perovskite solar cells employing doped charge transport layers," *Energy & Environmental Science*, vol. 9, pp. 3456–3463, 2016. [Online]. Available: <http://dx.doi.org/10.1039/C6EE02100J>
- [96] V. M. Le Corre, M. Stolterfoht, L. Perdigón Toro, M. Feuerstein, C. Wolff, L. Gil-Escrig, H. J. Bolink, D. Neher, and L. J. A. Koster, "Charge transport layers limiting the efficiency of perovskite solar cells: How to optimize conductivity, doping, and thickness," *ACS Applied Energy Materials*, vol. 2, no. 9, pp. 6280–6287, 2019. [Online]. Available: <https://doi.org/10.1021/acsaem.9b00856>
- [97] H. Ishii and K. Seki, "Energy level alignment at organic/metal interfaces studied by uv photoemission: breakdown of traditional assumption of a common vacuum level at the interface," *IEEE Transactions on Electron Devices*, vol. 44, no. 8, pp. 1295–1301, 1997.
- [98] W. Gao and A. Kahn, "Electrical doping: the impact on interfaces of π -conjugated molecular films," *Journal of Physics: Condensed Matter*, vol. 15, no. 38, p. S2757, 09 2003. [Online]. Available: <https://dx.doi.org/10.1088/0953-8984/15/38/014>
- [99] Z. Wang, D. P. McMeekin, N. Sakai, S. van Reenen, K. Wojciechowski, J. B. Patel, M. B. Johnston, and H. J. Snaith, "Efficient and air-stable mixed-cation lead mixed-halide perovskite solar cells with n-doped organic electron extraction layers," *Advanced Materials*, vol. 29, no. 5, p. 1604186, 2017. [Online]. Available: <https://onlinelibrary.wiley.com/doi/abs/10.1002/adma.201604186>
- [100] J. Ferraris, D. O. Cowan, V. Walatka, and J. H. Perlstein, "Electron transfer in a new highly conducting donor-acceptor complex," *Journal of the American Chemical Society*, vol. 95, no. 3, pp. 948–949, 1973. [Online]. Available: <https://doi.org/10.1021/ja00784a066>
- [101] K. P. Goetz, D. Vermeulen, M. E. Payne, C. Kloc, L. E. McNeil, and O. D. Jurchescu, "Charge-transfer complexes: New perspectives on an old class of compounds," *J. Mater. Chem. C*, vol. 2, no. 17, pp. 3065–3076, 2014.
- [102] I. E. Jacobs, C. Cendra, T. F. Harrelson, Z. I. Bedolla Valdez, R. Faller, A. Salleo, and A. J. Moulé, "Polymorphism controls the degree of charge transfer in a molecularly doped semiconducting polymer," *Materials Horizons*, vol. 5, no. 4, pp. 655–660, 2018.
- [103] M. Comin, V. Lemaur, A. Giunchi, D. Beljonne, X. Blase, and G. D'Avino, "Doping of semicrystalline conjugated polymers: dopants within alkyl chains do

- it better,” *J. Mater. Chem. C*, vol. 10, pp. 13 815–13 825, 2022. [Online]. Available: <http://dx.doi.org/10.1039/D2TC01115H>
- [104] J. Li, I. Duchemin, O. M. Roscioni, P. Friederich, M. Anderson, E. Da Como, G. Kociok-Köhn, W. Wenzel, C. Zannoni, D. Beljonne, X. Blase, and G. D’Avino, “Host dependence of the electron affinity of molecular dopants,” *Mater. Horiz.*, vol. 6, pp. 107–114, 2019. [Online]. Available: <http://dx.doi.org/10.1039/C8MH00921J>
- [105] D. S. Acker and W. R. Hertler, “Substituted quinodimethans. i. preparation and chemistry of 7,7,8,8-tetracyanoquinodimethan,” *Journal of the American Chemical Society*, vol. 84, no. 17, pp. 3370–3374, 1962. [Online]. Available: <https://doi.org/10.1021/ja00876a028>
- [106] Y. Qi, T. Sajoto, M. Kröger, A. M. Kandabarow, W. Park, S. Barlow, E.-G. Kim, L. Wielunski, L. C. Feldman, R. A. Bartynski, J.-L. Brédas, S. R. Marder, and A. Kahn, “A molybdenum dithiolene complex as p-dopant for hole-transport materials: A multitechnique experimental and theoretical investigation,” *Chemistry of Materials*, vol. 22, no. 2, pp. 524–531, 2010. [Online]. Available: <https://doi.org/10.1021/cm9031623>
- [107] P. K. Koech, A. B. Padmaperuma, L. Wang, J. S. Swensen, E. Polikarpov, J. T. Darsell, J. E. Rainbolt, and D. J. Gaspar, “Synthesis and application of 1,3,4,5,7,8-hexafluorotetracyanonaphthoquinodimethane (f6-tnap): A conductivity dopant for organic light-emitting devices,” *Chemistry of Materials*, vol. 22, no. 13, pp. 3926–3932, 2010. [Online]. Available: <https://doi.org/10.1021/cm1002737>
- [108] S. Er, C. Suh, M. P. Marshak, and A. Aspuru-Guzik, “Computational design of molecules for an all-quinone redox flow battery,” *Chemical Science*, vol. 6, pp. 885–893, 2015. [Online]. Available: <http://dx.doi.org/10.1039/C4SC03030C>
- [109] O. Zeika, S. Willmann, A. Lux, H. Hartmann, S. Dorok, and A. Werner, “United states patent application 20100102709: Radialene compounds and their use,” Patent 20 100 102 709, April, 2010. [Online]. Available: <https://www.freepatentsonline.com/y2010/0102709.html>
- [110] T. J. Aubry, J. C. Axtell, V. M. Basile, K. J. Winchell, J. R. Lindemuth, T. M. Porter, J.-Y. Liu, A. N. Alexandrova, C. P. Kubiak, S. H. Tolbert, A. M. Spokoyny, and B. J. Schwartz, “Dodecaborane-Based Dopants Designed to Shield Anion Electrostatics Lead to Increased Carrier Mobility in a Doped Conjugated Polymer,” *Advanced Materials*, vol. 31, no. 11, p. 1805647, 2019.
- [111] B. Mallada, M. Ondráček, M. Lamanec, A. Gallardo, A. Jiménez-Martín, B. de la Torre, P. Hobza, and P. Jelínek, “Visualization of -hole in molecules by means of kelvin probe force microscopy,” *Nature Communications*, vol. 14, no. 1, p. 4954, 2023.

- [112] J. S. Chappell, A. N. Bloch, W. A. Bryden, M. Maxfield, T. O. Poehler, and D. O. Cowan, "Degree of charge transfer in organic conductors by infrared absorption spectroscopy," *Journal of the American Chemical Society*, vol. 103, no. 9, pp. 2442–2443, May 1981.
- [113] E. Kampar and O. Neilands, "Degree of Charge Transfer in Donor–Acceptor Systems of the π – π Type," *Russian Chemical Reviews*, vol. 55, no. 4, pp. 334–342, Apr. 1986.
- [114] M. Meneghetti and C. Pecile, "Charge–transfer organic crystals: Molecular vibrations and spectroscopic effects of electron–molecular vibration coupling of the strong electron acceptor TCNQF₄," *The Journal of Chemical Physics*, vol. 84, no. 8, pp. 4149–4162, Apr. 1986.
- [115] M. Berteau-Rainville, E. Orgiu, and I. Salzmann, "On validity and limits of deducing the degree of charge transfer from shifts of cyano vibrations," *Electronic Structure*, vol. 5, no. 3, p. 034002, Sep. 2023.
- [116] D. Kiefer, R. Kroon, A. I. Hofmann, H. Sun, X. Liu, A. Giovannitti, D. Stegerer, A. Cano, J. Hynynen, L. Yu, Y. Zhang, D. Nai, T. F. Harrelson, M. Sommer, A. J. Moulé, M. Kemerink, S. R. Marder, I. McCulloch, M. Fahlman, S. Fabiano, and C. Müller, "Double doping of conjugated polymers with monomer molecular dopants," *Nature Materials*, Jan. 2019.
- [117] T. Bathe, C.-D. Dong, and S. Schumacher, "Microscopic study of molecular double doping," *The Journal of Physical Chemistry A*, vol. 126, no. 13, pp. 2075–2081, 2022.
- [118] C.-d. Dong and S. Schumacher, "Molecular doping in few-molecule polymer-dopant complexes shows reduced coulomb binding," *Journal of Materials Chemistry. C*, vol. 8, pp. 11 929–11 935, 2020. [Online]. Available: <http://dx.doi.org/10.1039/D0TC02185G>
- [119] J.-D. Chai and M. Head-Gordon, "Long-range corrected hybrid density functionals with damped atom–atom dispersion corrections," *Physical Chemistry Chemical Physics*, vol. 10, no. 44, p. 6615, 2008.
- [120] T. Lu and F. Chen, "Multiwfn: A multifunctional wavefunction analyzer," *Journal of Computational Chemistry*, vol. 33, no. 5, pp. 580–592, Feb. 2012.
- [121] T. Eicher and R. Graf, "Zur photochemie der triafulvene i," *Tetrahedron Letters*, vol. 16, no. 46, pp. 4021–4024, 1975. [Online]. Available: <https://www.sciencedirect.com/science/article/pii/S0040403900912255>
- [122] J. H. Burroughes, D. D. C. Bradley, A. R. Brown, R. N. Marks, K. Mackay, R. H. Friend, P. L. Burn, and A. B. Holmes, "Light-emitting diodes based on conjugated polymers," *Nature*, vol. 348, pp. 352–352, 1990.

- [123] K. M. Coakley and M. D. McGehee, "Conjugated polymer photovoltaic cells," *Chemistry of Materials*, vol. 16, no. 23, pp. 4533–4542, 2004. [Online]. Available: <https://doi.org/10.1021/cm049654n>
- [124] A. Facchetti, "-conjugated polymers for organic electronics and photovoltaic cell applications," *Chemistry of Materials*, vol. 23, no. 3, pp. 733–758, 2011. [Online]. Available: <https://doi.org/10.1021/cm102419z>
- [125] J. Yang, Z. Zhao, S. Wang, Y. Guo, and Y. Liu, "Insight into high-performance conjugated polymers for organic field-effect transistors," *Chem*, vol. 4, no. 12, pp. 2748–2785, 2018. [Online]. Available: <https://www.sciencedirect.com/science/article/pii/S2451929418303577>
- [126] B. Lüssem, C.-M. Keum, D. Kasemann, B. Naab, Z. Bao, and K. Leo, "Doped Organic Transistors," *Chemical Reviews*, vol. 116, no. 22, pp. 13 714–13 751, Nov. 2016.
- [127] D. T. McQuade, A. E. Pullen, and T. M. Swager, "Conjugated polymer-based chemical sensors," *Chemical Reviews*, vol. 100, pp. 2537–2574, 2000.
- [128] D. A. Bernards, R. M. Owens, and G. G. Malliaras, *Organic Semiconductors in Sensor Applications*. Berlin - Heidelberg: Springer, 2008.
- [129] Y. Yamashita, J. Tsurumi, M. Ohno, R. Fujimoto, S. Kumagai, T. Kurosawa, T. Okamoto, J. Takeya, and S. Watanabe, "Efficient molecular doping of polymeric semiconductors driven by anion exchange," *Nature*, vol. 572, pp. 634–638, 2019.
- [130] M. Pfeiffer, A. Beyer, T. Fritz, and K. Leo, "Controlled doping of phthalocyanine layers by cosublimation with acceptor molecules: A systematic Seebeck and conductivity study," *Applied Physics Letters*, vol. 73, no. 22, pp. 3202–3204, 11 1998. [Online]. Available: <https://doi.org/10.1063/1.122718>
- [131] B. Nell, K. Ortstein, O. V. Boltalina, and K. Vandewal, "Influence of dopant-host energy level offset on thermoelectric properties of doped organic semiconductors," *Journal of Physical Chemistry C*, vol. 122, pp. 11 730–11 735, 2018. [Online]. Available: <https://api.semanticscholar.org/CorpusID:104121160>
- [132] T. Fukunaga, M. D. Gordon, and P. J. Krusic, "Negatively substituted trimethylenecyclopropanes and their radical anions," *Journal of the American Chemical Society*, vol. 98, no. 2, pp. 611–613, 1976. [Online]. Available: <https://doi.org/10.1021/ja00418a051>
- [133] J. T. Liu, H. Hase, S. Taylor, I. Salzmann, and P. Forgione, "Approaching the Integer-Charge Transfer Regime in Molecularly Doped Oligothiophenes by Efficient Decarboxylative Cross-Coupling," *Angewandte Chemie International Edition*, vol. 59, no. 18, pp. 7146–7153, Apr. 2020.

- [134] M. Cui, H. Rui, X. Wu, Z. Sun, W. Qu, W. Qin, and S. Yin, "Coexistent Integer Charge Transfer and Charge Transfer Complex in F₄-TCNQ-Doped PTAA for Efficient Flexible Organic Light-Emitting Diodes," *The Journal of Physical Chemistry Letters*, vol. 12, no. 35, pp. 8533–8540, Sep. 2021.
- [135] K. E. Watts, B. Neelamraju, E. L. Ratcliff, and J. E. Pemberton, "Stability of Charge Transfer States in F₄TCNQ-Doped P3HT," *Chemistry of Materials*, vol. 31, no. 17, pp. 6986–6994, Sep. 2019.
- [136] O. Zapata-Arteaga, B. Döring, A. Perevedentsev, J. Martín, J. S. Reparaz, and M. Campoy-Quiles, "Closing the Stability–Performance Gap in Organic Thermoelectrics by Adjusting the Partial to Integer Charge Transfer Ratio," *Macromolecules*, vol. 53, no. 2, pp. 609–620, Jan. 2020.
- [137] S. Duhm, I. Salzmann, B. Bröker, H. Glowatzki, R. L. Johnson, and N. Koch, "Interdiffusion of molecular acceptors through organic layers to metal substrates mimics doping-related energy level shifts," *Applied Physics Letters*, vol. 95, no. 9, p. 093305, Aug. 2009.
- [138] M. D. Hanwell, D. E. Curtis, D. C. Lonie, T. Vandermeersch, E. Zurek, and G. R. Hutchison, "Avogadro: an advanced semantic chemical editor, visualization, and analysis platform," *Journal of Cheminformatics*, vol. 4, no. 1, p. 17, 2012, published 2012 Aug 13.
- [139] T. Salzillo, M. Masino, G. Kociok-Köhn, D. Di Nuzzo, E. Venuti, R. G. Della Valle, D. Vanossi, C. Fontanesi, A. Girlando, A. Brillante, and E. Da Como, "Structure, Stoichiometry, and Charge Transfer in Cocrystals of Perylene with TCNQ-F_x," *Crystal Growth & Design*, vol. 16, no. 5, pp. 3028–3036, May 2016.
- [140] S. K. Mohapatra, S. R. Marder, and S. Barlow, "Organometallic and organic dimers: Moderately air-stable, yet highly reducing, n-dopants," *Accounts of Chemical Research*, vol. 55, no. 3, pp. 319–332, 2022, pMID: 35040310. [Online]. Available: <https://doi.org/10.1021/acs.accounts.1c00612>
- [141] H. Guo, C. Yang, X. Zhang *et al.*, "Transition metal-catalysed molecular n-doping of organic semiconductors," *Nature*, vol. 599, pp. 67–73, 2021. [Online]. Available: <https://doi.org/10.1038/s41586-021-03942-0>
- [142] A. Altomare, C. Cuocci, C. Giacovazzo, A. Moliterni, R. Rizzi, N. Corriero, and A. Falcicchio, "EXPO2013: a kit of tools for phasing crystal structures from powder data," *Journal of Applied Crystallography*, vol. 46, no. 4, pp. 1231–1235, Aug 2013. [Online]. Available: <https://doi.org/10.1107/S0021889813013113>
- [143] A. L. Bail, "Monte carlo indexing with mcmaille," *Powder Diffraction*, vol. 19, pp. 249–254, 2004.
- [144] U. Salzner and A. Aydin, "Improved prediction of properties of π -conjugated oligomers with range-separated hybrid density functionals," *Journal of Chemical Theory and Computation*, vol. 7, no. 8, pp. 2568–2583, 2011.

- [145] T. Vikramaditya and S. Lin, "Assessing the role of hartree-fock exchange, correlation energy and long range corrections in evaluating ionization potential, and electron affinity in density functional theory," *Journal of Computational Chemistry*, vol. 38, pp. 1844 – 1852, 2017. [Online]. Available: <https://api.semanticscholar.org/CorpusID:206037101>
- [146] T. Körzdörfer and J.-L. Brédas, "Organic electronic materials: Recent advances in the dft description of the ground and excited states using tuned range-separated hybrid functionals," *Accounts of Chemical Research*, vol. 47, no. 11, pp. 3284–3291, 2014, PMID: 24784485. [Online]. Available: <https://doi.org/10.1021/ar500021t>
- [147] C. Halsey-Moore, P. Jena, and J. T. McLeskey, "Tuning range-separated dft functionals for modeling the peak absorption of meh-ppv polymer in various solvents," *Computational and Theoretical Chemistry*, vol. 1162, p. 112506, 2019. [Online]. Available: <https://www.sciencedirect.com/science/article/pii/S2210271X19302002>
- [148] L. N. Anderson, M. B. Oviedo, and B. M. Wong, "Accurate electron affinities and orbital energies of anions from a nonempirically tuned range-separated density functional theory approach," *Journal of Chemical Theory and Computation*, vol. 13, no. 4, pp. 1656–1666, 2017, PMID: 28339200. [Online]. Available: <https://doi.org/10.1021/acs.jctc.6b01249>
- [149] M. Brinkmann, "Structure and morphology control in thin films of regioregular poly(3-hexylthiophene)," *Journal of Polymer Science Part B: Polymer Physics*, vol. 49, no. 17, pp. 1218–1233, Sep. 2011.
- [150] I. F. Perepichka and D. F. Perepichka, *Handbook of Thiophene-Based Materials: Applications in Organic Electronics and Photonics*. Chichester, U.K: Wiley, 2009.
- [151] D. A. Stanfield, Z. Mehmedović, and B. J. Schwartz, "Vibrational Stark Effect Mapping of Polaron Delocalization in Chemically Doped Conjugated Polymers," *Chemistry of Materials*, vol. 33, no. 21, pp. 8489–8500, Nov. 2021.
- [152] A. Hamidi-Sakr, L. Biniek, J.-L. Bantignies, D. Maurin, L. Herrmann, N. Leclerc, P. Lévêque, V. Vijayakumar, N. Zimmermann, and M. Brinkmann, "A Versatile Method to Fabricate Highly In-Plane Aligned Conducting Polymer Films with Anisotropic Charge Transport and Thermoelectric Properties: The Key Role of Alkyl Side Chain Layers on the Doping Mechanism," *Advanced Functional Materials*, vol. 27, no. 25, p. 1700173, Jul. 2017.
- [153] H. Hase, K. O'Neill, J. Frisch, A. Opitz, N. Koch, and I. Salzmänn, "Unraveling the Microstructure of Molecularly Doped Poly(3-hexylthiophene) by Thermally Induced Dedoping," *The Journal of Physical Chemistry C*, vol. 122, no. 45, pp. 25 893–25 899, Nov. 2018.

- [154] S. Nagamatsu and S. S. Pandey, "Ordered arrangement of F4TCNQ anions in three-dimensionally oriented P3HT thin films," *Scientific Reports*, vol. 10, no. 1, p. 20020, Dec. 2020.
- [155] V. Untilova, T. Biskup, L. Biniek, V. Vijayakumar, and M. Brinkmann, "Control of Chain Alignment and Crystallization Helps Enhance Charge Conductivities and Thermoelectric Power Factors in Sequentially Doped P3HT:F₄TCNQ Films," *Macromolecules*, vol. 53, no. 7, pp. 2441–2453, Apr. 2020.

Appendix A

Supporting Information of chapter 3

A.1 Predicted EAs

The linear fit of experimental against computational EA_1 is shown in Figure A.1 and allows to calculate $EA_1^{pred.}$ in the main text. Computational EA_1 values are calculated at the same level of theory as described in the main text. Molecules included in the fit are the following: $(CN)_6-CP$, $(CO_2CH_2CH_3)(CN)_5-CP$, $(CO_2CH_3)_3(CN)_3-CP$, $(F_5-Ph)_3(CN)_3-CP$, F_4-TCNQ , F_2-TCNQ , $F-TCNQ$, and $TCNQ$. The experimental values for F_x-TCNQ were taken from Ref.[52], and, for the other molecules, from their corresponding references as provided in the Introduction of the Main Text.

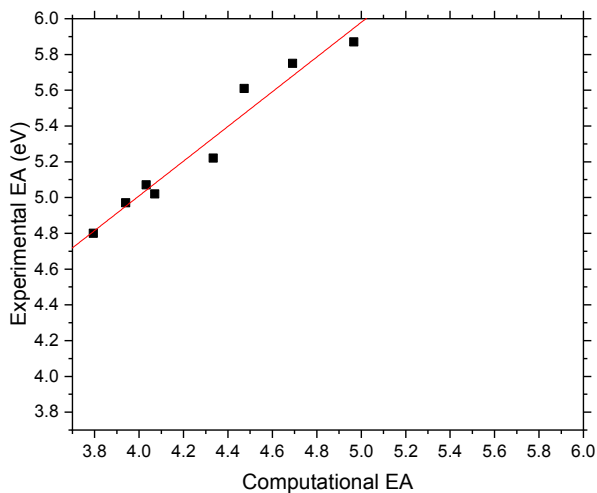


Figure A.1: Experimental against computational EA_1 for selected molecules. The slope (0.97) and intercept (1.13) of the linear fit have been used to calculate $EA_1^{pred.}$ in the main text.

A.2 Geometrical considerations

The effect of the number of substituents on CHD cores with phenyl groups (i.e. a missing pattern (**8**)) was not explored in this work. Such molecules have an out-of-plane offset between the phenyl rings which leads to a large number of possible molecular conformations that also depends on the charge state. This makes the process of investigating a large number of molecules extremely tedious and defeats the purpose of this work. Some of these conformations are shown in Figure A.2.

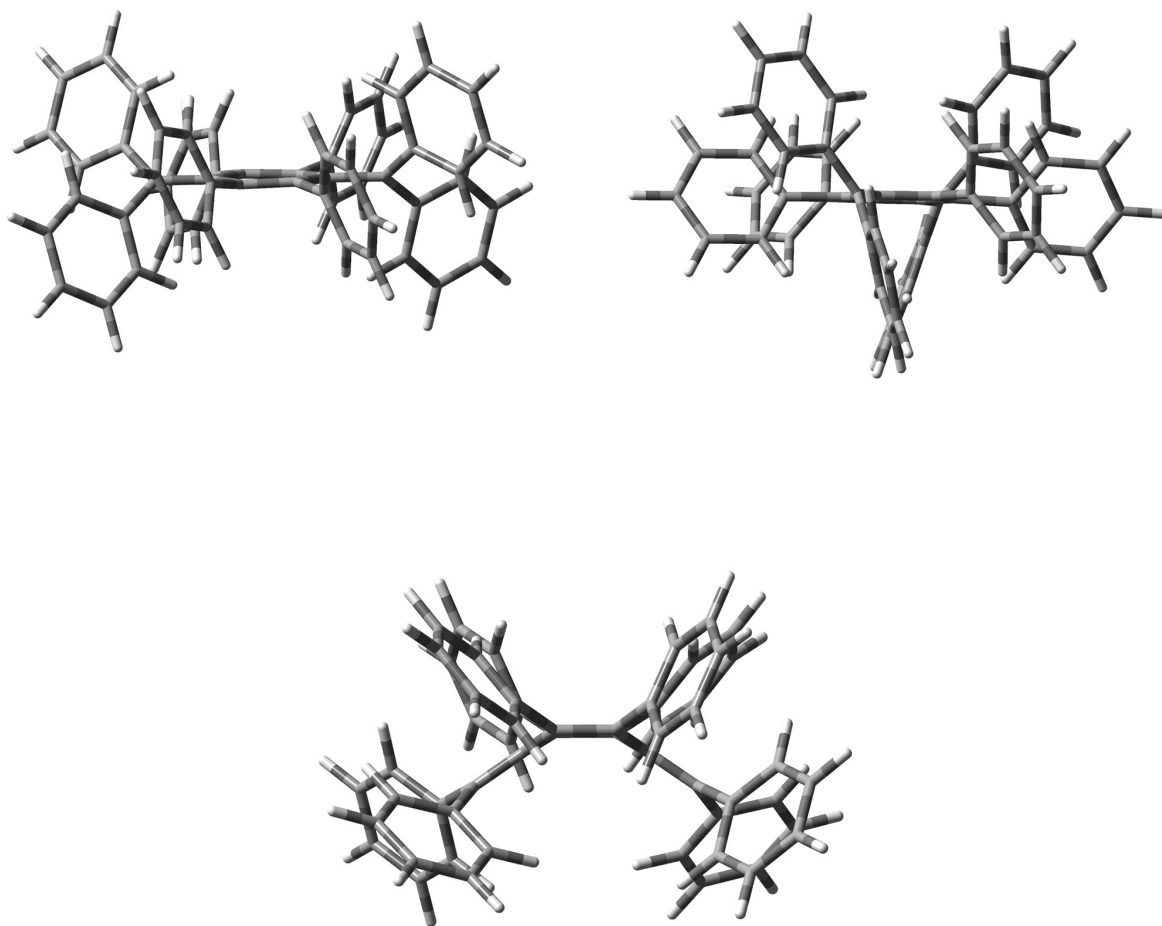


Figure A.2: Example conformations of $(Ph)_8$ -CHD.

Furthermore, as mentioned in the main text, patterns (1) and (5) lead to many molecules with pronounced core bending in the neutral state. Two main conformations are found for these: boat-like and chair-like. In all cases, boat-like conformations have lower energies, as exemplified below in Figure A.3 for $(SO_2F)_4-TCNQ$.

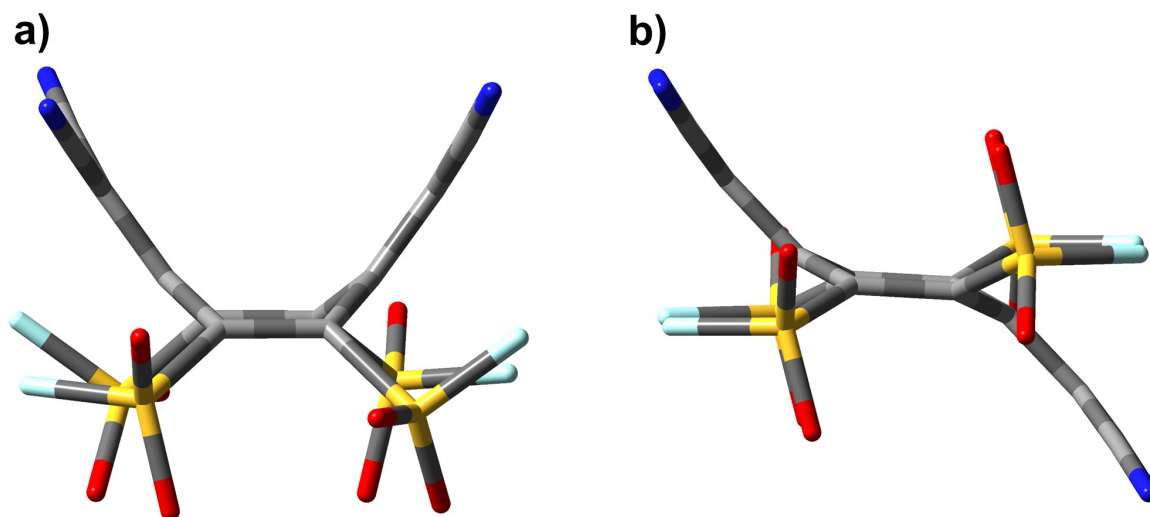


Figure A.3: Example of a) boat and b) chair conformations for neutral $(SO_2F)_4-TCNQ$ molecule.

For molecules following pattern (2), such as exemplified with $(PhSO_2CF_3)_4\text{-TCNQ}$, three different conformations are possible, based on the orientation of the substituents on the phenyl group with respect to each other. We again picked the most symmetric configurations in this work (corresponding to Figure A.4 a), as it is the lowest energy solution.

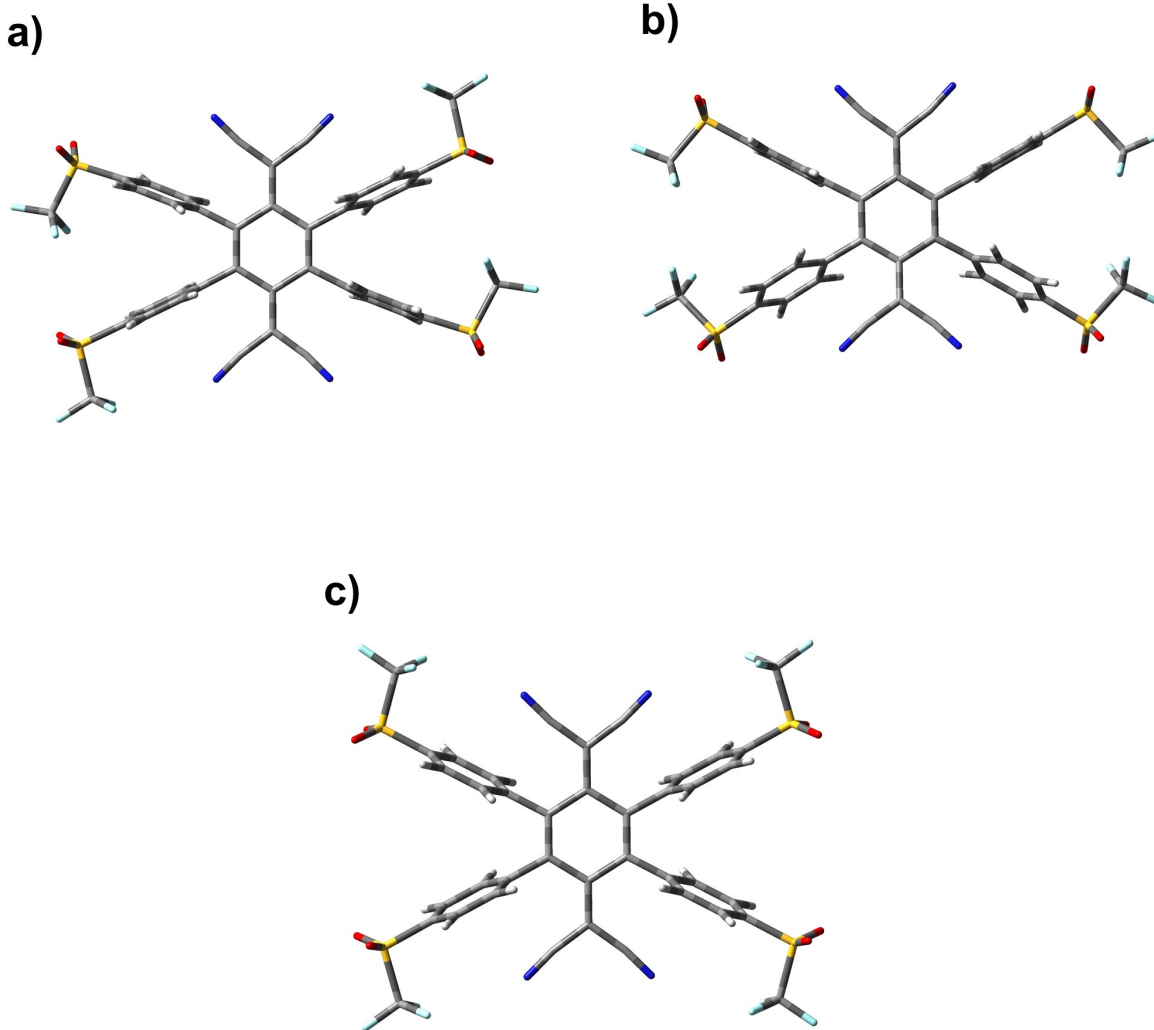


Figure A.4: Conformations of $(PhSO_2CF_3)_4\text{-TCNQ}$. Panel a) is the lowest energy conformation.

A.3 Molecular descriptors

Name	Hammett _{index}	EA ₁	EA ₂	AIM _(0,1)	AIM _(-1,2)
(SO ₂ H) ₄ -TCNQ	5.08	4.64	1.70	0.18207	-0.05543
(SO ₂ F) ₄ -TCNQ	5.86	4.74	1.77	-0.01717	0.02712
(SO ₂ CN) ₄ -TCNQ	7.16	5.04	2.37	-0.03907	-0.05113
(SO ₂ Cl) ₄ -TCNQ	7.06	4.59	1.89	-0.02443	-0.03180
(SO ₂ CH ₃) ₄ -TCNQ	5.08	3.67	1.35	-0.05100	-0.06010
(SO ₂ CF ₃) ₄ -TCNQ	6.02	4.49	1.99	-0.03503	-0.04753
(COCH ₃) ₄ -TCNQ	4.20	4.22	0.73	0.00224	-0.00275
(COCF ₃) ₄ -TCNQ	5.30	4.73	1.57	0.02978	0.02165
(CO ₂ CH ₃) ₄ -TCNQ	4.08	4.17	0.50	0.04668	0.03562
(CO ₂ CF ₃) ₄ -TCNQ	5.18	4.84	1.29	0.04482	0.04091
(CH ₃) ₄ -TCNQ	2.64	4.07	0.22	0.01763	0.00053
(CF ₃) ₄ -TCNQ	4.38	4.03	1.02	0.05680	0.04276
(Ph) ₄ -TCNQ	2.54	3.42	0.49	0.01214	-0.00229
(F ₅ -Ph) ₄ -TCNQ	3.50	4.68	1.22	0.06243	0.05036
(CH ₃) ₈ -CHD	0.40	-0.39	-3.47	-0.02554	-0.04108
(CF ₃) ₈ -CHD	3.88	2.86	0.78	0.05851	0.05427
(CN) ₄ -TCNQ	4.88	5.04	1.37	0.10296	0.08950
(Ph) ₈ -CHD	0.20	2.08	-0.61	-0.01815	-0.02459
(F ₅ -Ph) ₈ -CHD	2.12	3.54	0.88	0.03310	0.04093
(F ₄ CN-Ph) ₄ -TCNQ	N/A	5.22	1.81	0.06223	0.05141
TCNQ	2.44	3.79	-0.30	0.12422	0.00416
F ₄ -TCNQ	3.24	4.33	0.19	0.44907	0.40762

Table A.1: Molecular descriptors of patterns (1) and (5). EA₁ and EA₂ are provided in eV, AIM represents the sum of partial atomic charges on core atoms calculated from the quantum theory of atoms in molecules for neutral (AIM_(0,1)) and radical anionic (AIM_(-1,2)) molecules, the charge is given in fraction of the elementary charge e .

Name	Hammett _{index}	EA ₁	EA ₂	AIM _(0,1)	AIM _(-1,2)
(PhSO ₂ H) ₄ -TCNQ	5.08	4.58	1.40	0.01525	0.00146
(PhSO ₂ F) ₄ -TCNQ	5.86	4.77	1.59	0.01589	0.00422
(PhSO ₂ CN) ₄ -TCNQ	7.16	4.92	1.77	0.01584	0.00341
(PhSO ₂ Cl) ₄ -TCNQ	7.06	4.75	1.58	0.01607	0.00337
(PhSO ₂ CH ₃) ₄ -TCNQ	5.08	4.46	1.29	0.01483	0.00185
(PhSO ₂ CF ₃) ₄ -TCNQ	6.02	4.75	1.57	0.01621	0.00332
(PhCOCH ₃) ₄ -TCNQ	4.20	4.04	0.92	0.01327	0.00013
(PhCOCF ₃) ₄ -TCNQ	5.30	4.36	1.45	0.01543	0.00139
(PhCO ₂ CH ₃) ₄ -TCNQ	4.08	3.79	0.92	0.01371	-0.00090
(PhCO ₂ CF ₃) ₄ -TCNQ	5.18	4.35	1.45	0.01548	0.00166
(PhCH ₃) ₄ -TCNQ	2.64	3.44	0.30	0.01227	-0.00260
(PhCF ₃) ₄ -TCNQ	4.38	4.11	1.15	0.01487	0.00018
(PhCN) ₄ -TCNQ	4.88	4.38	1.44	0.01416	-0.00030

Table A.2: Molecular descriptors of pattern (2). Content follows Table A.1.

Name	Hammett _{index}	EA ₁	EA ₂	AIM _(0,1)	AIM _(-1,2)
(SO ₂ H) ₃ (CN) ₃ -CP	3.69	5.20	1.17	0.02285	-0.01643
(SO ₂ F) ₃ (CN) ₃ -CP	4.40	5.45	1.57	0.04102	0.02800
(SO ₂ CN) ₃ (CN) ₃ -CP	5.37	5.74	2.02	0.03341	0.02545
(SO ₂ Cl) ₃ (CN) ₃ -CP	5.30	5.37	1.70	0.04164	0.03032
(SO ₂ CH ₃) ₃ (CN) ₃ -CP	3.81	4.73	0.87	0.02034	0.00673
(SO ₂ CF ₃) ₃ (CN) ₃ -CP	4.52	5.38	1.59	0.04295	0.03086
(COCH ₃) ₃ (CN) ₃ -CP	3.15	4.23	-0.17	0.01208	0.00080
(COCF ₃) ₃ (CN) ₃ -CP	3.98	5.13	1.25	0.02208	0.01301
(CO ₂ CH ₃) ₃ (CN) ₃ -CP	3.06	4.24	0.34	0.00833	-0.00404
(CO ₂ CF ₃) ₃ (CN) ₃ -CP	3.89	5.14	1.40	0.01319	0.00429
(CH ₃) ₃ (CN) ₃ -CP	1.98	2.73	-1.60	-0.04040	-0.05802
(CF ₃) ₃ (CN) ₃ -CP	3.29	4.47	0.16	0.01080	-0.01000
(Ph) ₃ (CN) ₃ -CP	1.91	3.10	-0.38	-0.03903	-0.05051
(F ₅ -Ph) ₃ (CN) ₃ -CP	2.63	4.03	0.27	0.00392	-0.01369
(CH ₃) ₆ -CP	0.30	-0.03	-4.05	-0.10521	-0.11886
(CF ₃) ₆ -CP	2.91	4.02	-0.24	0.00707	-0.00740
(CN) ₆ -CP	3.66	4.97	0.69	0.01813	-0.00164
(Ph) ₆ -CP	0.15	1.59	-1.41	-0.09826	-0.10470
(F ₅ -Ph) ₆ -CP	1.59	3.29	0.07	-0.01349	-0.02231
(SO ₂ F) ₆ -CP	5.13	6.03	2.38	0.05735	0.05872
(SO ₂ CN) ₆ -CP	7.08	6.57	3.16	0.05389	0.05852
(SO ₂ Cl) ₆ -CP	6.93	5.75	2.49	0.05968	0.06455
(F ₄ CN-Ph) ₃ (CN) ₃ -CP	N/A	4.605	1.163	0.00718	-0.00652
(CO ₂ CH ₃) ₂ (CN) ₄ -CP	3.26	4.473	0.408	0.01245	-0.00377
(CO ₂ C ₂ H ₅)(CN) ₅ -CP	3.46	4.691	0.54	0.01632	-0.00231

Table A.3: Molecular descriptors of patterns (3) and (6). Content follows Table A.1.

Name	Hammett _{index}	EA ₁	EA ₂	AIM _(0,1)	AIM _(-1,2)
(PhSO ₂ H) ₃ (CN) ₃ -CP	3.69	4.10	0.93	-0.03366	-0.04440
(PhSO ₂ F) ₃ (CN) ₃ -CP	4.40	4.34	1.21	-0.03242	-0.04308
(PhSO ₂ CN) ₃ (CN) ₃ -CP	5.37	4.53	1.46	-0.03187	-0.04216
(PhSO ₂ Cl) ₃ (CN) ₃ -CP	5.30	4.34	1.30	-0.03239	-0.04274
(PhSO ₂ CH ₃) ₃ (CN) ₃ -CP	3.81	3.94	0.79	-0.03461	-0.04550
(PhSO ₂ CF ₃) ₃ (CN) ₃ -CP	4.52	4.33	1.25	-0.03198	-0.04250
(PhCOCH ₃) ₃ (CN) ₃ -CP	3.15	3.60	0.45	-0.03628	-0.04615
(PhCOCF ₃) ₃ (CN) ₃ -CP	3.98	4.10	1.07	-0.03319	-0.04278
(PhCO ₂ CH ₃) ₃ (CN) ₃ -CP	3.06	3.58	0.43	-0.03629	-0.04653
(PhCO ₂ CF ₃) ₃ (CN) ₃ -CP	3.89	4.06	1.02	-0.03347	-0.04343
(PhCH ₃) ₃ (CN) ₃ -CP	1.98	2.97	-0.46	-0.04044	-0.05169
(PhCF ₃) ₃ (CN) ₃ -CP	3.29	3.77	0.44	-0.03487	-0.04608
(PhCN) ₃ (CN) ₃ -CP	3.66	4.04	0.78	-0.03517	-0.04597
(PhF) ₆ -CP	1.20	1.95	-1.08	-0.09949	-0.1068
(PhCF ₃) ₆ -CP	2.91	2.66	0.00	-0.09144	-0.09839
(PhCCl ₃) ₆ -CP	2.58	2.75	0.19	-0.09188	-0.09674
(PhCBr ₃) ₆ -CP	1.71	2.77	0.17	-0.09207	-0.09768
(PhCO ₂ CH ₃) ₆ -CP	2.46	2.38	-0.23	-0.0928	-0.09706
(PhOH) ₆ -CP	-0.75	1.48	-1.53	-0.1031	-0.10685

Table A.4: Molecular descriptors patterns (4) and (7). Content follows Table A.1.

A.4 Hammett indices predict electron affinities

In this section, individual plots of EA_1 and EA_2 against the Hammett index are shown for all molecular patterns (1)-(7) (Figures A.5-A.8). The fit parameters are reported in Table A.5. EA_1 and EA_2 of the molecules can be predicted with their corresponding Hammett values based on the fit parameters. This is done by multiplying the slope with the Hammett index, and adding the intercept. Taking for example $(PhSO_2H)_4$ -TCNQ, belonging to pattern (2), an EA_1 value of $5.08 * 0.33 + 2.8 = 4.48$ eV is found, in good agreement with the value of 4.58 eV calculated using DFT.

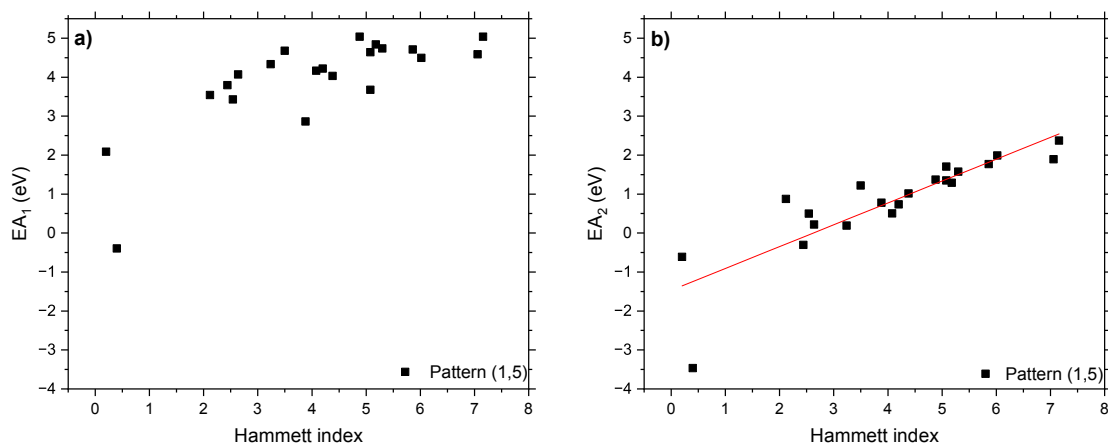


Figure A.5: Impact of the Hammett index on a) EA_1 and b) EA_2 of molecules following substitution patterns (1) and (5).

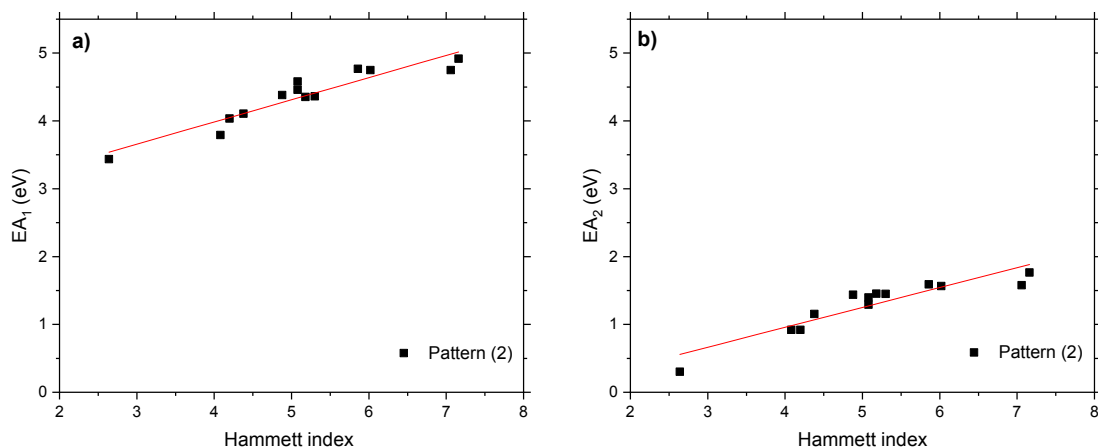


Figure A.6: Impact of the Hammett index on a) EA_1 and b) EA_2 of molecules following substitution pattern (2).

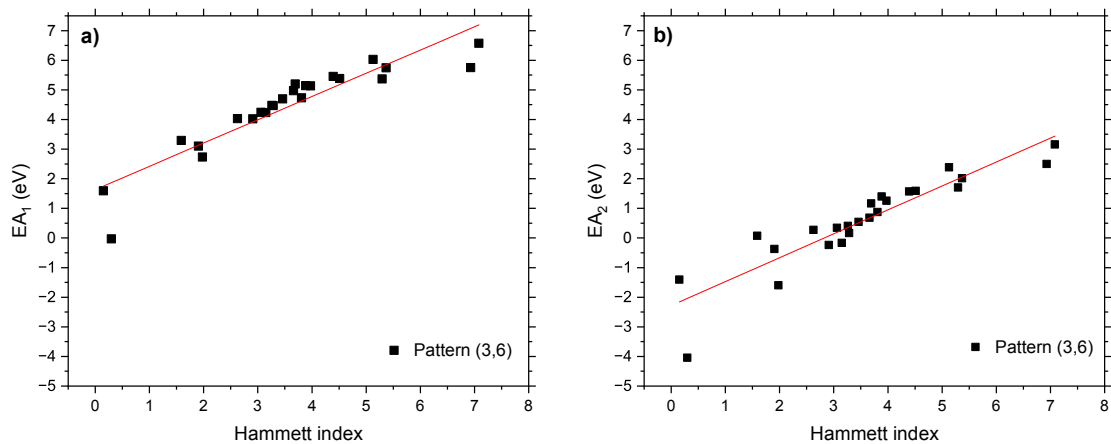


Figure A.7: Impact of the Hammett index on a) EA_1 and b) EA_2 of molecules following substitution patterns (3) and (6).

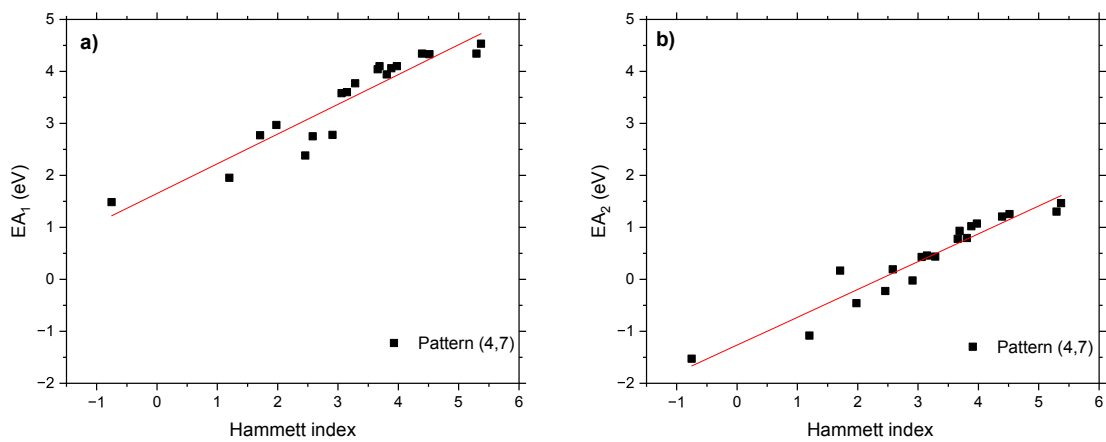


Figure A.8: Impact of the Hammett index on a) EA_1 and b) EA_2 of molecules following substitution patterns (4) and (7).

Substitution pattern	Slope	Intercept	R^2
EA1			
1,5	0.49 ± 0.10	1.92 ± 0.44	0.574
2	0.33 ± 0.04	2.68 ± 0.19	0.883
3,6	0.78 ± 0.07	1.63 ± 0.20	0.832
4,7	0.57 ± 0.05	1.65 ± 0.17	0.878
EA2			
1,5	0.56 ± 0.08	-1.47 ± 0.35	0.727
2	0.29 ± 0.04	-0.21 ± 0.20	0.845
3,6	0.81 ± 0.08	-2.28 ± 0.31	0.829
4,7	0.54 ± 0.04	-1.26 ± 0.13	0.915

Table A.5: Linear fit parameter (slope, intercept, and R^2 values) of the EAs against the Hammett index. Patterns (1) and (5) are CHDs without phenyl, patterns (3) and (6) are CPs without phenyl, patterns (4) and (7) are CPs with phenyl, pattern (2) is CHDs with phenyl. The standard errors of the parameters are reported as \pm values.

A.5 Relation between atomic charge on the core and electron affinity

In this section, individual plots of EA_1 and EA_2 against the sum of partial atomic charges of core atoms determined via the quantum theory of atoms in molecules (QTAIM) are shown for all molecular patterns (1)-(7) (Figures A.9-A.12). The fit parameters are reported in Table A.6.

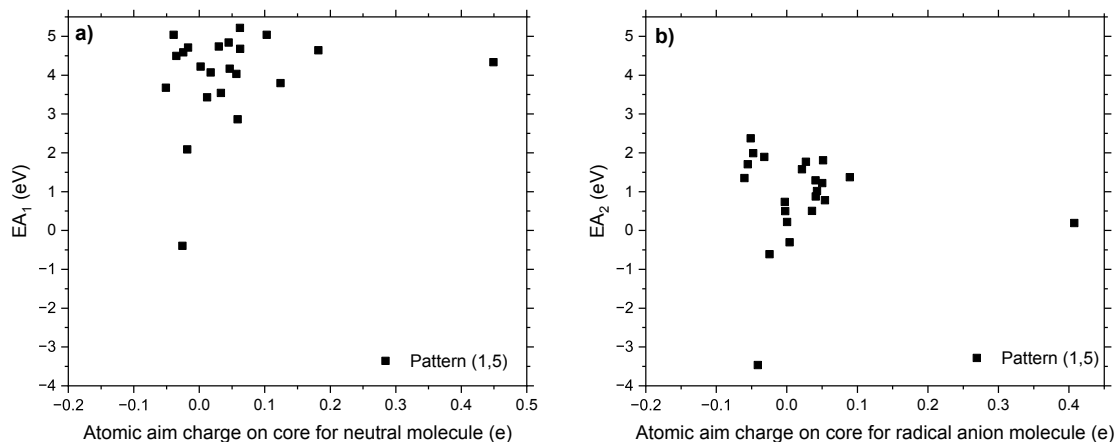


Figure A.9: Impact of the partial atomic charges of core atoms on EAs of molecules following substitution patterns (1) and (5). a) Impact of the charge in neutral molecules on EA_1 . b) Impact of the charge in radical anionic atoms on EA_2 .

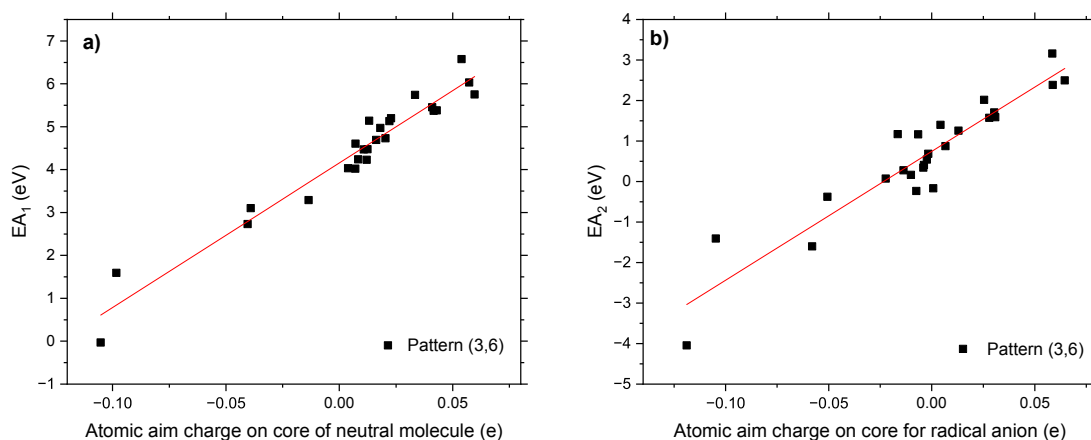


Figure A.10: Impact of the partial atomic charges of core atoms on EAs of molecules following substitution patterns (3) and (6). a) Impact of the charge in neutral molecules on EA_1 . b) Impact of the charge in radical anionic atoms on EA_2 .

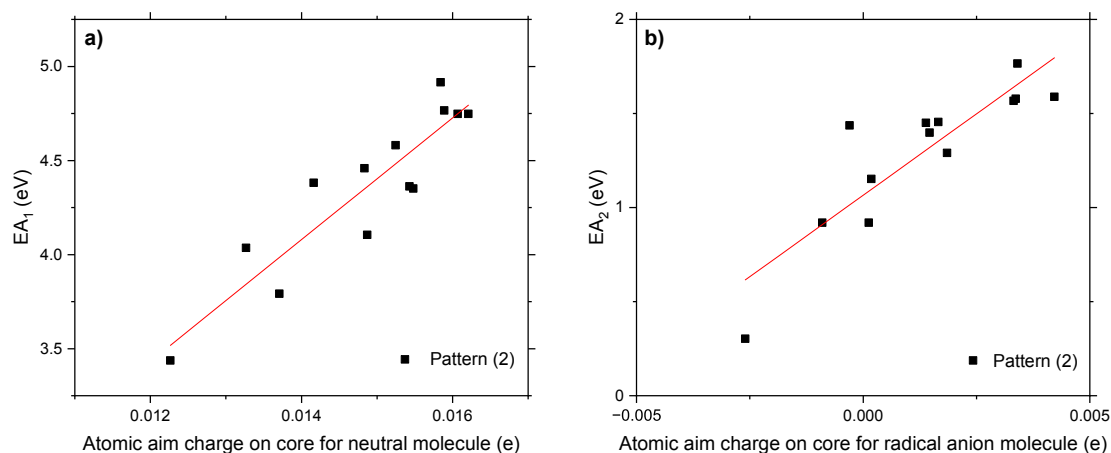


Figure A.11: Impact of the partial atomic charges of core atoms on EAs of molecules following substitution patterns (2). a) Impact of the charge in neutral molecules on EA_1 . b) Impact of the charge in radical anionic atoms on EA_2 .

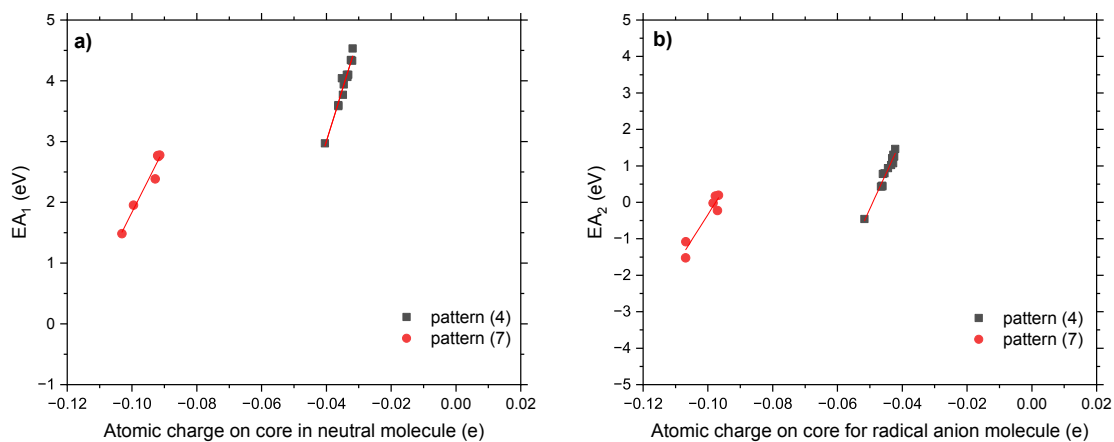


Figure A.12: Impact of the partial atomic charges of core atoms on EAs of molecules following substitution patterns (4) and (7). a) Impact of the charge in neutral molecules on EA_1 . b) Impact of the charge in radical anionic atoms on EA_2 .

Substitution pattern	Slope	Intercept	R^2
EA1			
1,5	2.27 ± 2.54	3.88 ± 0.29	0.038
2	323.69 ± 44.22	-0.45 ± 0.66	0.830
3,6	33.72 ± 1.76	4.16 ± 0.07	0.941
4	172.04 ± 11.27	9.89 ± 0.39	0.955
7	105.90 ± 11.45	12.43 ± 1.09	0.955
EA2			
1,5	-0.72 ± 2.80	0.87 ± 0.29	0.003
2	173.18 ± 28.50	1.07 ± 0.01	0.770
3,6	31.77 ± 2.52	0.74 ± 0.11	0.873
4	193.57 ± 12.11	9.50 ± 0.54	0.959
7	140.72 ± 22.13	13.74 ± 2.23	0.909

Table A.6: Linear fit parameters (slope, intercept, and R^2 values) of the EAs against the sum of partial atomic charges of core atoms. Patterns (1) and (5) are CHDs without phenyl, patterns (3) and (6) are CPs without phenyl, patterns (4) and (7) are CPs with phenyl, pattern (2) is CHDs with phenyl. The standard errors of the parameters are reported as \pm .

A.6 Cyano vibrational modes

Name	CN _(0,1)	CN _(-1,2)	CN _(-2,1)
(SO ₂ H) ₄ -TCNQ	2279.0	2224.6	2152.5
(SO ₂ F) ₄ -TCNQ	2281.8	2241.5	2179.6
(SO ₂ CN) ₄ -TCNQ	2280.0	2265.7	2217.2
(SO ₂ Cl) ₄ -TCNQ	2279.1	2182.9	2179.1
(SO ₂ CH ₃) ₄ -TCNQ	2281.3	2169.3	2125.4
(SO ₂ CF ₃) ₄ -TCNQ	2278.6	2183.9	2182.0
(COCH ₃) ₄ -TCNQ	2274.6	2186.8	2117.0
(COCF ₃) ₄ -TCNQ	2269.0	2199.8	2156.9
(CO ₂ CH ₃) ₄ -TCNQ	2268.3	2184.5	2125.8
(CO ₂ CF ₃) ₄ -TCNQ	2278.2	2167.5	2139.1
(CH ₃) ₄ -TCNQ	2251.9	2168.8	2105.5
(CF ₃) ₄ -TCNQ	2277.9	2213.9	2140.1
(Ph) ₄ -TCNQ	2249.8	2176.4	2115.3
(F ₅ -Ph) ₄ -TCNQ	2257.4	2183.6	2137.5
(F ₄ CN-Ph) ₄ -TCNQ	2260.0	2213.1	2183.8
(CH ₃) ₈ -CHD	N/A	N/A	N/A
(CF ₃) ₈ -CHD	N/A	N/A	N/A
(CN) ₄ -TCNQ	2271.0	2211.5	2160.3
(Ph) ₈ -CHD	N/A	N/A	N/A
(F ₅ -Ph) ₈ -CHD	N/A	N/A	N/A
TCNQ	2264.5	2183.1	2110.9
F ₄ -TCNQ	2272.9	2196.3	2138.7

Table A.7: Highest-energy cyano vibrational mode of molecules following substitution patterns (1) and (5). Energy is given in wavenumber (cm^{-1}). Where applicable, the vibration that belongs to isolated cyano groups and not to cyano groups on substituents were selected. (0,1) represents neutral molecules, (-1,2) represents radical anionic molecules, and (-2,1) represents dianionic molecules. The energies of the cyano vibrations were scaled according to the precomputed vibrational scaling factors from the Computational Chemistry Comparison and Benchmark Database (CCCBDB) corresponding to our model chemistry. [13] N/A indicates molecules that have no cyano groups.

Name	CN _(0,1)	CN _(-1,2)	CN _(-2,1)
(PhSO ₂ H) ₄ -TCNQ	2254.9	2181.3	2133.9
(PhSO ₂ F) ₄ -TCNQ	2255.3	2183.3	2137.2
(PhSO ₂ CN) ₄ -TCNQ	2257.1	2184.8	2140.5
(PhSO ₂ Cl) ₄ -TCNQ	2256.2	2183.8	2137.9
(PhSO ₂ CH ₃) ₄ -TCNQ	2256.2	2181.2	2129.3
(PhSO ₂ CF ₃) ₄ -TCNQ	2256.1	2183.6	2137.5
(PhCOCH ₃) ₄ -TCNQ	2258.6	2178.4	2127.2
(PhCOCF ₃) ₄ -TCNQ	2254.4	2183.5	2134.9
(PhCO ₂ CH ₃) ₄ -TCNQ	2253.0	2179.7	2127.5
(PhCO ₂ CF ₃) ₄ -TCNQ	2254.3	2182.6	2134.0
(PhCH ₃) ₄ -TCNQ	2247.3	2174.4	2114.9
(PhCF ₃) ₄ -TCNQ	2253.2	2181.3	2129.2
(PhCN) ₄ -TCNQ	2254.0	2183.0	2132.5

Table A.8: Highest-energy cyano vibrational mode of molecules following substitution pattern (2). Content follows Table A.7.

Name	CN _(0,1)	CN _(-1,2)	CN _(-2,1)
(SO ₂ H) ₃ (CN) ₃ -CP	2259.3	2214.0	2184.0
(SO ₂ F) ₃ (CN) ₃ -CP	2266.8	2231.9	2217.1
(SO ₂ CN) ₃ (CN) ₃ -CP	2263.6	2233.9	2222.5
(SO ₂ Cl) ₃ (CN) ₃ -CP	2264.7	2231.9	2222.9
(SO ₂ CH ₃) ₃ (CN) ₃ -CP	2256.7	2213.2	2180.2
(SO ₂ CF ₃) ₃ (CN) ₃ -CP	2263.6	2229.9	2216.6
(COCH ₃) ₃ (CN) ₃ -CP	2255.6	2214.3	2178.2
(COCF ₃) ₃ (CN) ₃ -CP	2264.8	2235.2	2213.1
(CO ₂ CH ₃) ₃ (CN) ₃ -CP	2268.7	2225.4	2188.5
(CO ₂ CF ₃) ₃ (CN) ₃ -CP	2272.3	2237.2	2216.8
(CH ₃) ₃ (CN) ₃ -CP	2250.0	2168.1	2090.9
(CF ₃) ₃ (CN) ₃ -CP	2268.5	2217.5	2175.4
(Ph) ₃ (CN) ₃ -CP	2250.1	2192.9	2157.0
(F ₅ -Ph) ₃ (CN) ₃ -CP	2257.6	2204.0	2170.8
(CH ₃) ₆ -CP	N/A	N/A	N/A
(CF ₃) ₆ -CP	N/A	N/A	N/A
(CN) ₆ -CP	2275.2	2238.2	2199.9
(Ph) ₆ -CP	N/A	N/A	N/A
(F ₅ -Ph) ₆ -CP	N/A	N/A	N/A
(SO ₂ F) ₆ -CP	N/A	N/A	N/A
(SO ₂ CN) ₆ -CP	N/A	N/A	N/A
(SO ₂ Cl) ₆ -CP	N/A	N/A	N/A
(F ₄ CN-Ph) ₃ (CN) ₃ -CP	2259.1	2213.5	2197.4
(CO ₂ CH ₃) ₂ (CN) ₄ -CP	2267.3	2215.8	2168.0
(CO ₂ C ₂ H ₅)(CN) ₅ -CP	2267.1	2219.3	2169.4

Table A.9: Highest-energy cyano vibrational mode of molecules following substitution pattern (3) and (6). Content follows Table A.7.

Name	CN _(0,1)	CN _(-1,2)	CN _(-2,1)
(PhSO ₂ H) ₃ (CN) ₃ -CP	2254.4	2206.5	2184.7
(PhSO ₂ F) ₃ (CN) ₃ -CP	2255.0	2208.1	2189.1
(PhSO ₂ CN) ₃ (CN) ₃ -CP	2255.4	2210.0	2193.9
(PhSO ₂ Cl) ₃ (CN) ₃ -CP	2255.0	2208.5	2193.9
(PhSO ₂ CH ₃) ₃ (CN) ₃ -CP	2253.4	2204.8	2182.3
(PhSO ₂ CF ₃) ₃ (CN) ₃ -CP	2255.2	2208.7	2191.4
(PhCOCH ₃) ₃ (CN) ₃ -CP	2252.4	2203.1	2180.6
(PhCOCF ₃) ₃ (CN) ₃ -CP	2253.9	2208.5	2192.5
(PhCO ₂ CH ₃) ₃ (CN) ₃ -CP	2252.2	2202.1	2179.6
(PhCO ₂ CF ₃) ₃ (CN) ₃ -CP	2253.6	2206.8	2189.8
(PhCH ₃) ₃ (CN) ₃ -CP	2249.2	2191.2	2154.0
(PhCF ₃) ₃ (CN) ₃ -CP	2252.9	2201.0	2172.5
(PhCN) ₃ (CN) ₃ -CP	2253.1	2204.1	2178.8
(PhF) ₆ -CP	N/A	N/A	N/A
(PhCF ₃) ₆ -CP	N/A	N/A	N/A
(PhCCl ₃) ₆ -CP	N/A	N/A	N/A
(PhCBr ₃) ₆ -CP	N/A	N/A	N/A
(PhCO ₂ CH ₃) ₆ -CP	N/A	N/A	N/A
(PhOH) ₆ -CP	N/A	N/A	N/A

Table A.10: Highest-energy cyano vibrational mode of molecules following substitution pattern (4) and (7). Content follows Table A.7.

As mentioned in the main text, first- and second-order fits of the cyano vibration energy against the molecular charge were performed for all molecules. A fit curvature ratio was introduced, defined (for second-order fits) as the division of the second-order coefficient (B_2) by the first-order one (B_1):

$$Fit\ Curvature\ Ratio = B_2/B_1 \quad (A.1)$$

All fit parameters are reported in Tables A.11-A.14.

Name	Intercept (2)	B1 (2)	B2 (2)	Intercept (1)	B1 (1)	R ² (1)	Curvature ratio (2)
(SO ₂ H) ₄ -TCNQ	2279.0	45.6	-8.9	2282.0	63.3	0.994	-19.4
(SO ₂ F) ₄ -TCNQ	2281.8	29.4	-10.8	2285.4	51.1	0.985	-36.8
(SO ₂ CN) ₄ -TCNQ	2280.0	-2.7	-17.1	2285.7	31.4	0.910	622.9
(SO ₂ Cl) ₄ -TCNQ	2279.1	142.3	46.2	2263.7	50.0	0.779	32.4
(SO ₂ CH ₃) ₄ -TCNQ	2281.3	145.9	34.0	2269.9	77.9	0.940	23.3
(SO ₂ CF ₃) ₄ -TCNQ	2278.6	141.1	46.4	2263.1	48.3	0.765	32.9
(COCH ₃) ₄ -TCNQ	2274.6	96.9	9.0	2271.6	78.8	0.996	9.3
(COCF ₃) ₄ -TCNQ	2269.0	82.4	13.2	2264.7	56.1	0.982	16.0
(CO ₂ CH ₃) ₄ -TCNQ	2268.3	96.5	12.6	2264.1	71.3	0.990	13.1
(CO ₂ CF ₃) ₄ -TCNQ	2278.2	151.8	41.1	2264.5	69.6	0.896	27.1
(CH ₃) ₄ -TCNQ	2251.9	93.2	10.0	2248.6	73.2	0.994	10.7
(CF ₃) ₄ -TCNQ	2277.9	59.1	-4.9	2279.5	68.9	0.998	-8.3
(Ph) ₄ -TCNQ	2249.8	79.5	6.1	2247.7	67.3	0.997	7.7
(F ₅ -Ph) ₄ -TCNQ	2257.4	87.7	13.9	2252.8	59.9	0.982	15.8
(F ₄ CN-Ph) ₄ -TCNQ	2260.0	55.7	8.8	2257.1	38.1	0.982	15.8
(CH ₃) ₈ -CHD	N/A	N/A	N/A	N/A	N/A	N/A	N/A
(CF ₃) ₈ -CHD	N/A	N/A	N/A	N/A	N/A	N/A	N/A
(CN) ₄ -TCNQ	2271.0	63.5	4.1	2269.6	55.3	0.998	6.4
(Ph) ₈ -CHD	N/A	N/A	N/A	N/A	N/A	N/A	N/A
(F ₅ -Ph) ₈ -CHD	N/A	N/A	N/A	N/A	N/A	N/A	N/A
TCNQ	2264.5	86.0	4.6	2262.9	76.8	0.999	5.3
F ₄ -TCNQ	2272.9	86.3	9.6	2269.7	67.1	0.993	11.1

Table A.11: Results of first and second order fits to the position of CN vibrations against the molecular charge for patterns (1) and (5). The number in parentheses identifies the order of the fit to which parameters belong. N/A indicates molecules that have no cyano groups.

Name	Intercept (2)	B1 (2)	B2 (2)	Intercept (1)	B1 (1)	R ² (1)	Curvature ratio (2)
(PhSO ₂ H) ₄ -TCNQ	2254.9	86.6	13.1	2250.5	60.5	0.985	15.1
(PhSO ₂ F) ₄ -TCNQ	2255.3	84.9	12.9	2251.0	59.0	0.984	15.2
(PhSO ₂ CN) ₄ -TCNQ	2257.1	86.3	14.0	2252.4	58.3	0.981	16.2
(PhSO ₂ Cl) ₄ -TCNQ	2256.2	85.5	13.2	2251.8	59.1	0.984	15.4
(PhSO ₂ CH ₃) ₄ -TCNQ	2256.2	86.5	11.5	2252.3	63.5	0.989	13.3
(PhSO ₂ CF ₃) ₄ -TCNQ	2256.1	85.8	13.2	2251.7	59.3	0.984	15.4
(PhCOCH ₃) ₄ -TCNQ	2258.6	94.7	14.5	2253.8	65.7	0.984	15.3
(PhCOCF ₃) ₄ -TCNQ	2254.4	82.0	11.1	2250.7	59.8	0.989	13.5
(PhCO ₂ CH ₃) ₄ -TCNQ	2253.0	83.9	10.6	2249.5	62.8	0.991	12.6
(PhCO ₂ CF ₃) ₄ -TCNQ	2254.3	83.3	11.6	2250.4	60.2	0.988	13.9
(PhCH ₃) ₄ -TCNQ	2247.3	79.5	6.7	2245.1	66.2	0.997	8.4
(PhCF ₃) ₄ -TCNQ	2253.2	81.7	9.8	2249.9	62.0	0.992	12.1
(PhCN) ₄ -TCNQ	2254.0	81.3	10.3	2250.5	60.7	0.991	12.7

Table A.12: Results of first and second order fits to the position of CN vibrations against the molecular charge for pattern (2). Content follows Table A.11.

Name	Intercept (2)	B1 (2)	B2 (2)	Intercept (1)	B1 (1)	R ² (1)	Curvature ratio (2)
(SO ₂ H) ₃ (CN) ₃ -CP	2259.3	53.0	7.7	2256.8	37.7	0.986	14.5
(SO ₂ F) ₃ (CN) ₃ -CP	2266.8	44.8	10.0	2263.5	24.9	0.949	22.3
(SO ₂ CN) ₃ (CN) ₃ -CP	2263.6	38.9	9.1	2260.5	20.6	0.938	23.5
(SO ₂ Cl) ₃ (CN) ₃ -CP	2264.7	44.6	11.9	2260.7	20.9	0.903	26.6
(SO ₂ CH ₃) ₃ (CN) ₃ -CP	2256.7	48.9	5.3	2254.9	38.2	0.994	10.9
(SO ₂ CF ₃) ₃ (CN) ₃ -CP	2263.6	43.8	10.1	2260.2	23.5	0.942	23.1
(COCH ₃) ₃ (CN) ₃ -CP	2255.6	43.9	2.6	2254.8	38.7	0.999	5.9
(COCF ₃) ₃ (CN) ₃ -CP	2264.8	33.3	3.7	2263.5	25.9	0.993	11.2
(CO ₂ CH ₃) ₃ (CN) ₃ -CP	2268.7	46.5	3.2	2267.6	40.1	0.998	6.9
(CO ₂ CF ₃) ₃ (CN) ₃ -CP	2272.3	42.3	7.3	2269.8	27.7	0.977	17.3
(CH ₃) ₃ (CN) ₃ -CP	2250.0	84.2	2.3	2249.2	79.6	1.000	2.8
(CF ₃) ₃ (CN) ₃ -CP	2268.5	55.4	4.4	2267.0	46.6	0.997	8.0
(Ph) ₃ (CN) ₃ -CP	2250.1	67.8	10.6	2246.5	46.5	0.983	15.7
(F ₅ -Ph) ₃ (CN) ₃ -CP	2257.6	63.8	10.2	2254.2	43.4	0.982	16.0
(CH ₃) ₆ -CP	N/A	N/A	N/A	N/A	N/A	N/A	N/A
(CF ₃) ₆ -CP	N/A	N/A	N/A	N/A	N/A	N/A	N/A
(CN) ₆ -CP	2275.2	36.4	-0.6	2275.4	37.7	1.000	-1.7
(Ph) ₆ -CP	N/A	N/A	N/A	N/A	N/A	N/A	N/A
(F ₅ -Ph) ₆ -CP	N/A	N/A	N/A	N/A	N/A	N/A	N/A
(SO ₂ F) ₆ -CP	N/A	N/A	N/A	N/A	N/A	N/A	N/A
(SO ₂ CN) ₆ -CP	N/A	N/A	N/A	N/A	N/A	N/A	N/A
(SO ₂ Cl) ₆ -CP	N/A	N/A	N/A	N/A	N/A	N/A	N/A
(F ₄ CN-Ph) ₃ (CN) ₃ -CP	2259.1	60.4	14.8	2254.2	30.9	0.929	24.5
(CO ₂ CH ₃) ₂ (CN) ₄ -CP	2267.3	53.3	1.8	2266.7	49.7	1.000	3.4
(CO ₂ C ₂ H ₅)(CN) ₅ -CP	2267.1	46.7	-1.1	2267.4	48.8	1.000	-2.3

Table A.13: Results of first and second order fits to the position of CN vibrations against the molecular charge for patterns (3) and (6). Content follows Table A.11.

Name	Intercept (2)	B1 (2)	B2 (2)	Intercept (1)	B1 (1)	R ² (1)	Curvature ratio (2)
(PhSO ₂ F) ₃ (CN) ₃ -CP	2255.0	60.8	13.9	2250.4	32.9	0.944	22.9
(PhSO ₂ CN) ₃ (CN) ₃ -CP	2255.4	60.1	14.6	2250.6	30.8	0.930	24.4
(PhSO ₂ Cl) ₃ (CN) ₃ -CP	2255.0	62.4	16.0	2249.6	30.5	0.916	25.6
(PhSO ₂ CH ₃) ₃ (CN) ₃ -CP	2253.4	61.6	13.0	2249.1	35.6	0.957	21.2
(PhSO ₂ CF ₃) ₃ (CN) ₃ -CP	2255.2	61.2	14.6	2250.3	31.9	0.934	23.9
(PhCOCH ₃) ₃ (CN) ₃ -CP	2252.4	62.6	13.3	2247.9	35.9	0.956	21.3
(PhCOCF ₃) ₃ (CN) ₃ -CP	2253.9	60.1	14.7	2249.0	30.7	0.929	24.4
(PhCO ₂ CH ₃) ₃ (CN) ₃ -CP	2252.2	63.9	13.8	2247.6	36.3	0.954	21.6
(PhCO ₂ CF ₃) ₃ (CN) ₃ -CP	2253.6	61.6	14.8	2248.6	31.9	0.933	24.1
(PhCH ₃) ₃ (CN) ₃ -CP	2249.2	68.4	10.4	2245.7	47.6	0.984	15.2
(PhCF ₃) ₃ (CN) ₃ -CP	2252.9	63.6	11.7	2249.0	40.2	0.973	18.4
(PhCN) ₃ (CN) ₃ -CP	2253.1	60.9	11.9	2249.1	37.1	0.967	19.5
(PhF) ₆ -CP	N/A	N/A	N/A	N/A	N/A	N/A	N/A
(PhCF ₃) ₆ -CP	N/A	N/A	N/A	N/A	N/A	N/A	N/A
(PhCCl ₃) ₆ -CP	N/A	N/A	N/A	N/A	N/A	N/A	N/A
(PhCBr ₃) ₆ -CP	N/A	N/A	N/A	N/A	N/A	N/A	N/A
(PhCO ₂ CH ₃) ₆ -CP	N/A	N/A	N/A	N/A	N/A	N/A	N/A
(PhOH) ₆ -CP	N/A	N/A	N/A	N/A	N/A	N/A	N/A

Table A.14: Results of first and second order fits to the position of CN vibrations against the molecular charge for patterns (4) and (7). Content follows Table A.11.

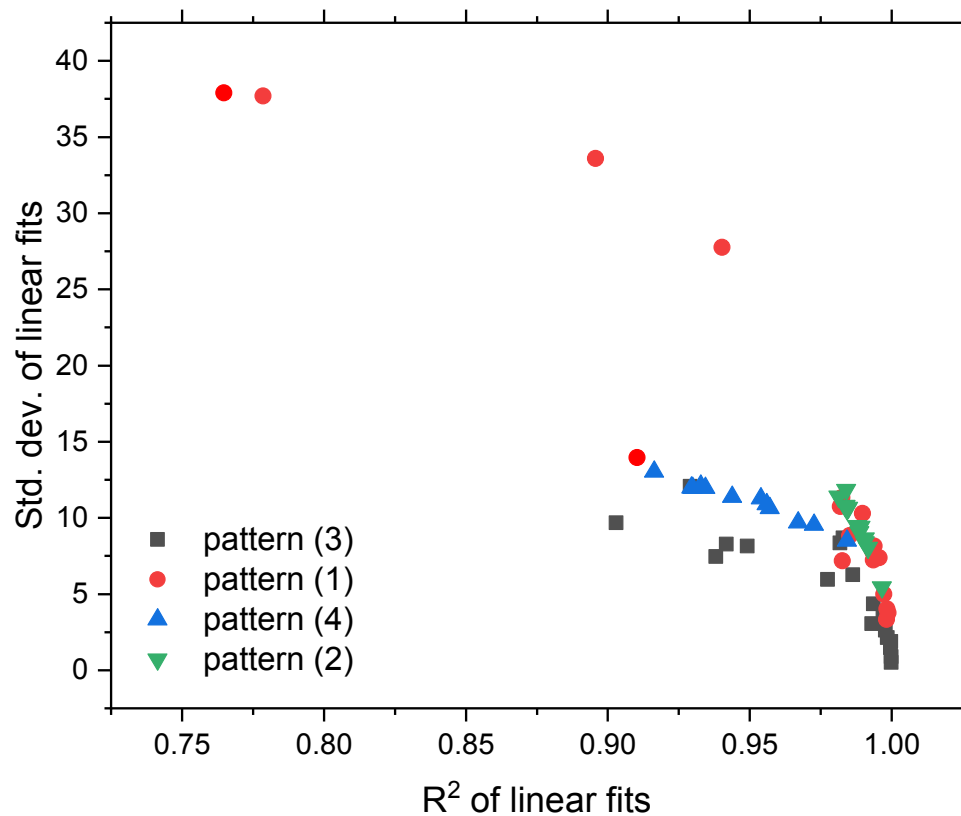


Figure A.13: Standard deviation of the linear fits against their coefficient of determination R^2 , to quantify how much this non-linearity leads to an error in the correspondence between cyano vibration wavenumber and the molecular charge when assuming a linear fit.

A.7 Comparison of molecular factors

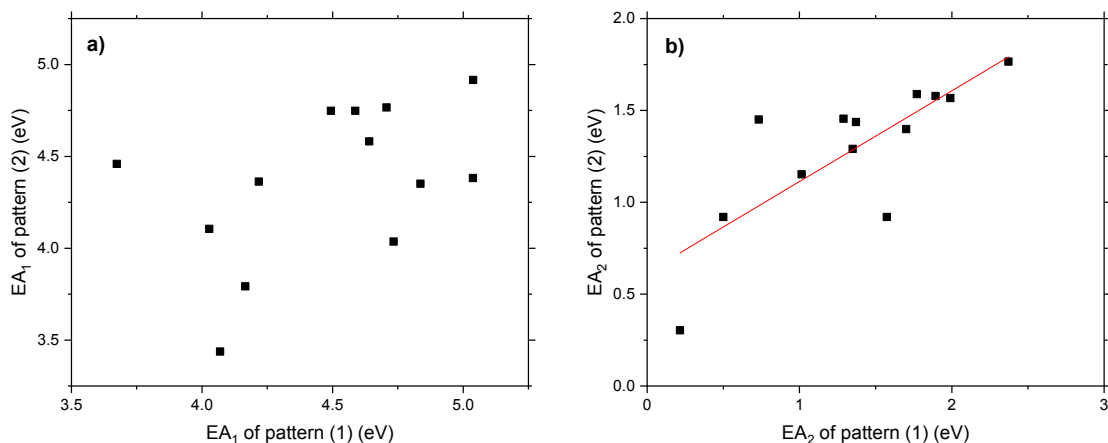


Figure A.14: Impact of phenyl groups on the EAs of molecules with a CHD core. a) For EA_1 , no clear trend is visible due to core bending of the neutral molecules when the substituents are attached directly to the CHD core. b) For EA_2 , a trend emerges as discussed in the main text, due to the fact that much of the physical reorganization of the CHD cores has already occurred during their first ionization.

Group	Intercept	Slope	R^2 (COD)
EA_1 of patterns (4) vs (3)	1.04 ± 0.37	0.59 ± 0.08	0.834
EA_2 of patterns (4) vs (3)	0.34 ± 0.04	0.54 ± 0.02	0.966
EA_1 of patterns (2) vs (1)	2.21 ± 1.22	0.48 ± 0.27	0.221
EA_2 of patterns (2) vs (1)	0.62 ± 0.17	0.49 ± 0.12	0.615

Table A.15: Linear fit parameters (intercept, slope, and R^2 values) of the EAs of molecules with phenyl groups against those of molecules without. Slopes smaller than 1 indicate that the connection of substituents via a phenyl group decreases their electronic impact, while the intercept reflects the impact of the phenyl itself.

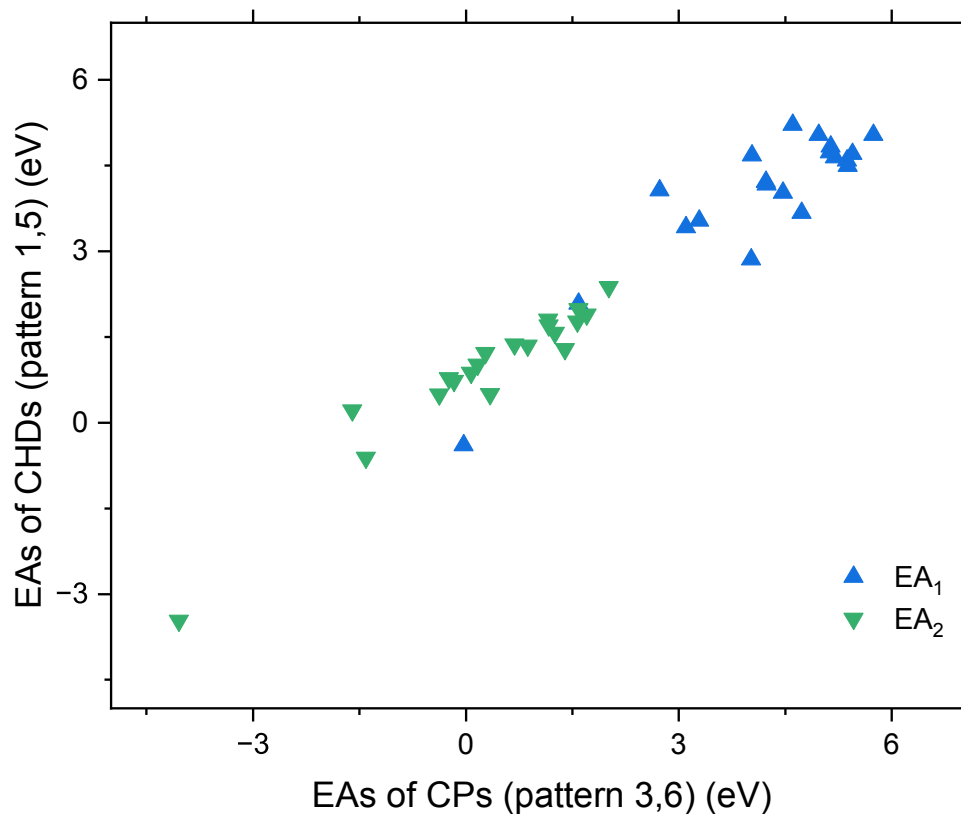


Figure A.15: Impact of the core on the EAs of molecules without phenyl groups; patterns (1), (5), (3), and (6).

Group	Intercept	Slope	R^2 (COD)
EA_1 , no phenyl	0.64 ± 0.42	0.80 ± 0.09	0.811
EA_2 , no phenyl	0.65 ± 0.05	0.83 ± 0.04	0.924
EA_1 , phenyl	0.39 ± 0.26	0.99 ± 0.06	0.955
EA_2 , phenyl	0.68 ± 0.04	0.74 ± 0.05	0.960

Table A.16: Linear fit parameters (intercept, slope, and R^2 values) of the EAs of molecules with a CHD core (patterns (1), (2) and (5)) against those with a CP core ((3), (4), (6) and (7)).

Appendix B

Supporting Information of chapter 4

B.1 Chemical structures

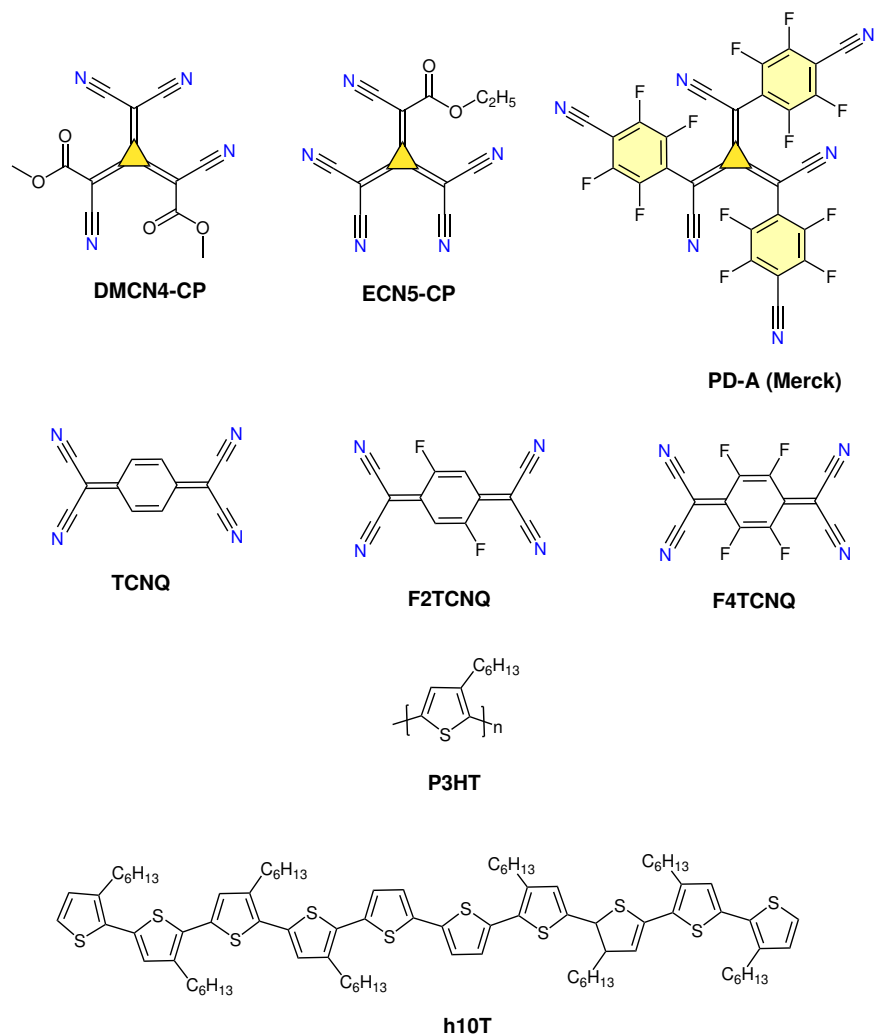


Figure B.1: Chemical structures in addition to those shown in Figure 4.11 of the main text.

B.2 DFT calculations

The objective of our density functional theory (DFT) calculations is twofold and will be detailed in the two subsections following the general DFT methodology (B.2 and B.2). First, the effects of tuning ω , the range separation parameter, are explored on a series of relevant molecular dopants with available experimental data, which allows us to identify and justify an optimal value of ω for the remaining work. Second, the optimal ω value is used to perform the calculations pertaining to this work.

DFT methodology

DFT calculations were performed within the Gaussian computational package (version 09 revision E.01) [10] using the ω B97x-D functional [119] and 6-31+G(d,p) as the basis set. Molecular geometries for the neutral and radical anions were optimized, and the absence of imaginary vibrational frequencies was subsequently verified to confirm the proper ground state nature of all species. The range separation parameter ω was modified using Gaussian’s internal options (IOPs) controls and fixed to 0.20 following a tuning procedure (which coincides with the value by default) for all calculations presented in the main text, as discussed below. Molecular orbital isosurfaces were drawn using the software Avogadro, Version 1.2.0. [138]

ω -tuning

It is common practice when working with range-separated functionals such as ω B97x-D to first perform the tuning of the range separation parameter ω , often referred to as a gap-tuning procedure. This procedure has been shown to be particularly important for molecules with extended conjugation [144] and, given recurring difficulties with high electron affinity molecules in computational chemistry (the electron affinity is systematically underestimated for such molecules, see Ref. [145] for a detailed discussion), was performed here as a preliminary step. Such a procedure is typically performed either by minimizing the difference between the ionization potential of the molecule and position of the HOMO, i.e., by enforcing manually Koopman’s theorem [146], or by observing the concomitant change of an observable of interest with ω [147], in scenarios where reasonable expectations on the observable can be formulated through other means. Given the scope of the present work, we select 7 molecules with known experimental electron affinities, allowing the results of both ω -tuning procedures to be compared within themselves and with experimental results. These molecules are *TCNQ*, *FTCNQ*, *F₂-TCNQ*, and *F₄-TCNQ*, extensively studied and referred to in this work, as well as *(CN)₆-CP*, *TMCN3 – CP*, and *PPF3CN3 – CP*. We note that the first ω -tuning approach is not of high relevance here given the interest in electron affinities instead of ionization potentials, and, further, that no theorem analogous to Koopman’s applies to the position of the LUMO and the electron affinity. If such a theorem would exist, it would be manually enforceable by finding the ω value minimizing the function $J^2(\omega)$:

$$J^2(\omega) = [-E_{\text{LUMO}} - \text{EA}]^2 \tag{B.1}$$

where E_{LUMO} is the energy of the LUMO in the ground state and EA is the adiabatic electron affinity obtained as the electronic energy difference between the molecule in its neutral and its radical anionic state. While this function based on the EA and the LUMO is formally incorrect, we note that EAs are routinely obtained via DFT, can be both qualitatively consistent and numerically reliable, and that EAs are typically extremely well correlated with LUMO energies. It is also possible to consider the radical anion as the starting point instead, where there should exist a relation between its HOMO and the LUMO of the neutral species, as well as between its ionization potential and the electron affinity of the neutral species. Such a modified procedure has been conducted at least once. [148] As such, these data are provided here and the roles of the HOMO and LUMO levels for both the neutral and radical anion species are inspected as a function of ω . We finally probe the evolution of the electron affinity with ω and compare these results with known, experimental values.

First, J_2 , as calculated from the LUMO and the EA of the neutral molecule, is shown in Figure B.2a. The function is minimized for $\omega = 0.15$; and the range between $\omega = 0.10$ and $\omega = 0.20$ appears to be reliable. J_2 is then calculated from the HOMO and the IE of the radical anion as shown in Figure B.2b, with very similar results, which provides confidence in the physical consistency of ω values within this range. This is not a coincidence as the difference between the HOMO of the radical anion and the LUMO of the neutral molecule follow the exact same trend (Figure B.2c). This last fact reveals that no additional error is added in the J_2 trends due to the electron affinity term (Figure B.2d), which benefits from error cancelation when calculated adiabatically. EA values increase over the low values of ω but saturate for the most part at higher ω , and never reach values as high as the experimental values. This suggests that the underestimation of the EA is not due to miscalibration of the transition between DFT and Hartree-Fock (HF) exchange, determined by ω , but rather due to the method itself, for instance from the % exchange contribution, since such parameters are optimized considering molecules with moderate electron affinities only.

In summary, molecules of extremely high electron-affinity, such as molecular p-dopants used for the doping of organic semiconductors as targeted in the present study, simply fall outside of the scope of most computational chemistry methods. Nevertheless, careful benchmarking against other methods or experimental values as demonstrated below allows using results predictively and quantitatively. The band gap (LUMO-HOMO difference) of the neutral molecules increases monotonically with ω (Figure B.2e), which is due to the inverse trends in HOMO and LUMO with ω as seen in Figure B.2f (only $(\text{CN})_6\text{-CP}$ shown; trends are representative of all molecules).

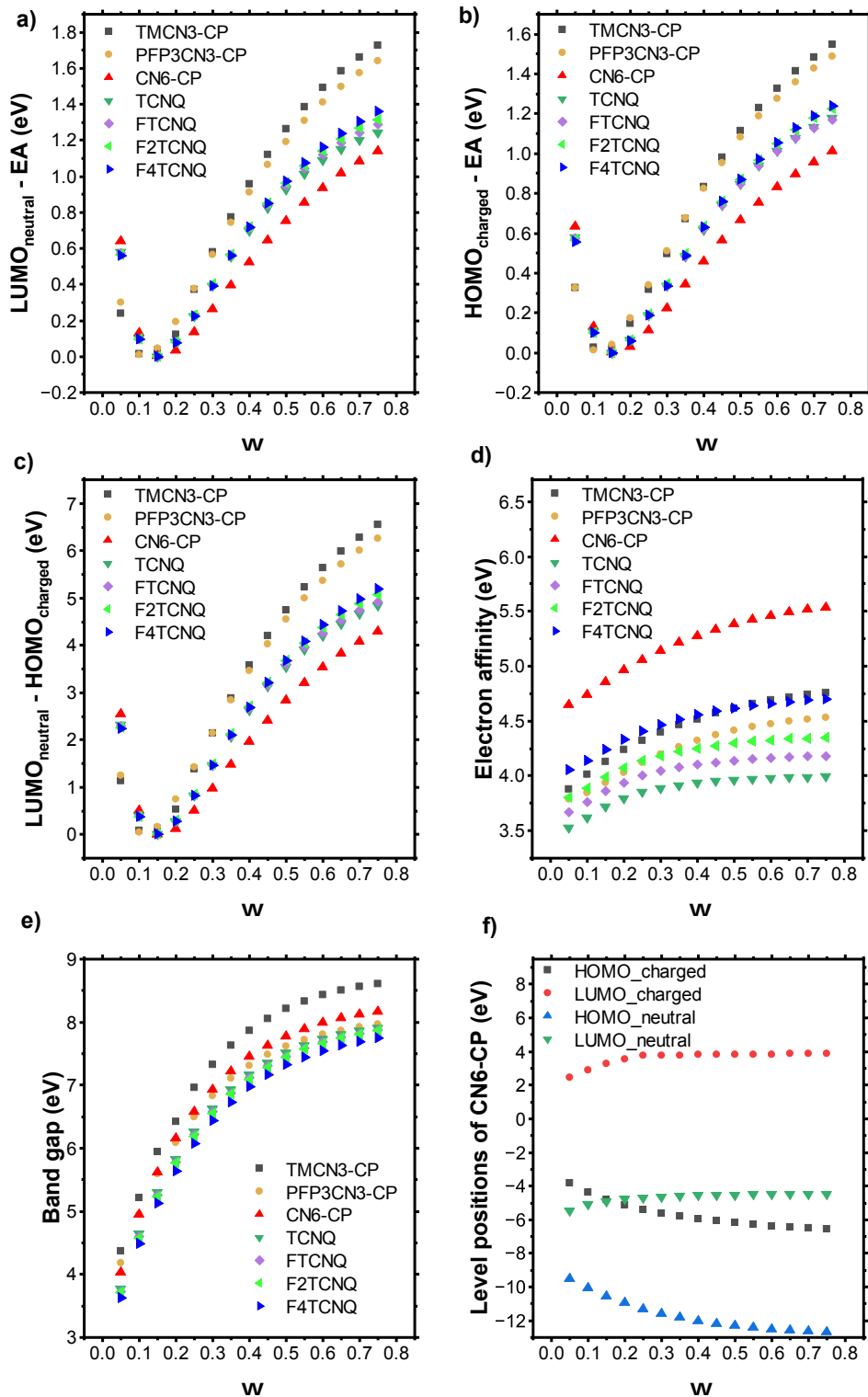


Figure B.2: a) $LUMO_{neutral} - EA$ b) $HOMO_{charged} - EA$ c) $LUMO_{neutral} - HOMO_{charged}$ d) EA e) Band gap for TMCN3-CP, PFP3CN3-CP, $(CN)_6-CP$, TCNQ, FTCNQ, F_2-TCNQ , and F_4-TCNQ molecules f) Level position of $(CN)_6-CP$, all as a function of ω . Charged refers to the radical anion.

While the results shown so far suggest an optimal $\omega = 0.15$, or at least ω within the range of 0.10 – 0.20, we also need to consider how well the electron affinity values at different ω correlate with those obtained experimentally. As apparent from Figure B.3a, computational values corresponding to *TMCN3-CP* appear to be quite underestimated compared to the trend, which could suggest that reported experimental values have been overestimated. The same trends obtained without this molecule are shown in Figure B.3b. Overall, computational and experimental electron affinities correlate very well and are linearly related; all parameters of the fits are given in the summary Table B.1.

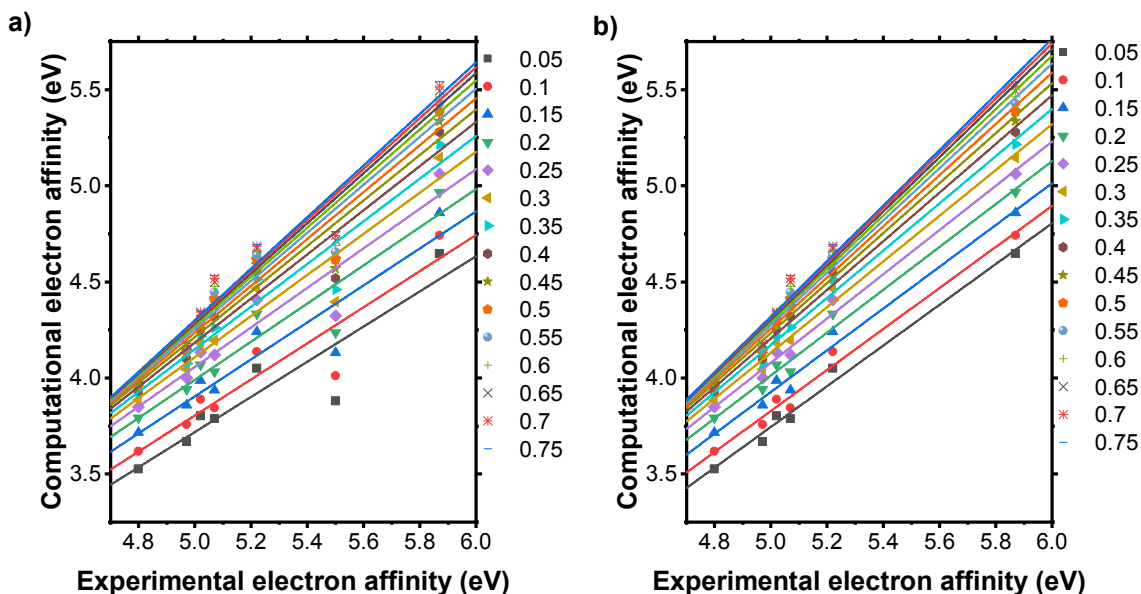


Figure B.3: Computational versus experimental electron affinity at different ω values for *PPF3CN3-CP*, *(CN)₆-CP*, *TCNQ*, *FTCNQ*, *F₂-TCNQ*, *F₄-TCNQ* a) with and b) without *TMCN3-CP* included in the fit.

Finally, we consider the difference between the computational and experimental electron affinity as shown in Figure B.4, as the optimal ω value should ideally not lead to huge error differences across molecules, and, therefore, the error spread should be minimized.

ω	With TMCN3-CP					Without TMCN3-CP				
	Intercept value	Intercept std. err.	Slope value	Slope std. err.	R^2	Intercept value	Intercept std. err.	Slope value	Slope std. err.	R^2
0.05	-0.85	0.93	0.91	0.18	0.84	-1.55	0.31	1.06	0.06	0.99
0.10	-0.89	0.84	0.94	0.16	0.87	-1.50	0.34	1.07	0.07	0.99
0.15	-0.90	0.82	0.96	0.16	0.88	-1.50	0.35	1.09	0.07	0.98
0.20	-0.97	0.81	0.99	0.16	0.89	-1.56	0.34	1.11	0.07	0.99
0.25	-1.08	0.80	1.03	0.15	0.90	-1.67	0.32	1.15	0.06	0.99
0.30	-1.23	0.79	1.07	0.15	0.91	-1.81	0.30	1.19	0.06	0.99
0.35	-1.39	0.78	1.11	0.15	0.92	-1.96	0.31	1.23	0.06	0.99
0.40	-1.55	0.77	1.15	0.15	0.92	-2.12	0.33	1.26	0.06	0.99
0.45	-1.70	0.77	1.18	0.15	0.93	-2.26	0.36	1.30	0.07	0.99
0.50	-1.85	0.77	1.22	0.15	0.93	-2.40	0.39	1.33	0.08	0.99
0.55	-1.99	0.77	1.25	0.15	0.94	-2.52	0.42	1.36	0.08	0.99
0.60	-2.11	0.77	1.28	0.15	0.94	-2.63	0.45	1.38	0.09	0.98
0.65	-2.22	0.77	1.30	0.15	0.94	-2.73	0.47	1.41	0.09	0.98
0.70	-2.32	0.77	1.32	0.15	0.94	-2.82	0.49	1.43	0.10	0.98
0.75	-2.40	0.77	1.34	0.15	0.94	-2.90	0.51	1.44	0.10	0.98

Table B.1: Linear fit parameters of computational versus experimental electron affinities (as plotted in Figure B.3) with different ω values

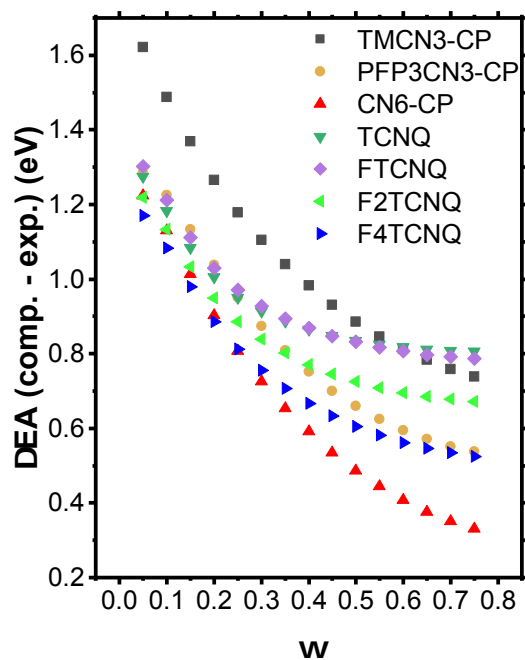


Figure B.4: Difference of computational and experimental electron affinity (EA) for *TMCN3-CP*, *PFP3CN3-CP*, *(CN)₆-CP*, *TCNQ*, *FTCNQ*, *F₂-TCNQ*, *F₄-TCNQ* molecules as a function of ω .

The spread of error across molecules as a function of ω , with and without *TMCN3-CP* respectively, are shown in Figures B.5a and B.5b. With *TMCN3-CP*, the spread is minimized in the region 0.25 – 0.35; while without, it is increasing monotonically except for a minimum at 0.20.

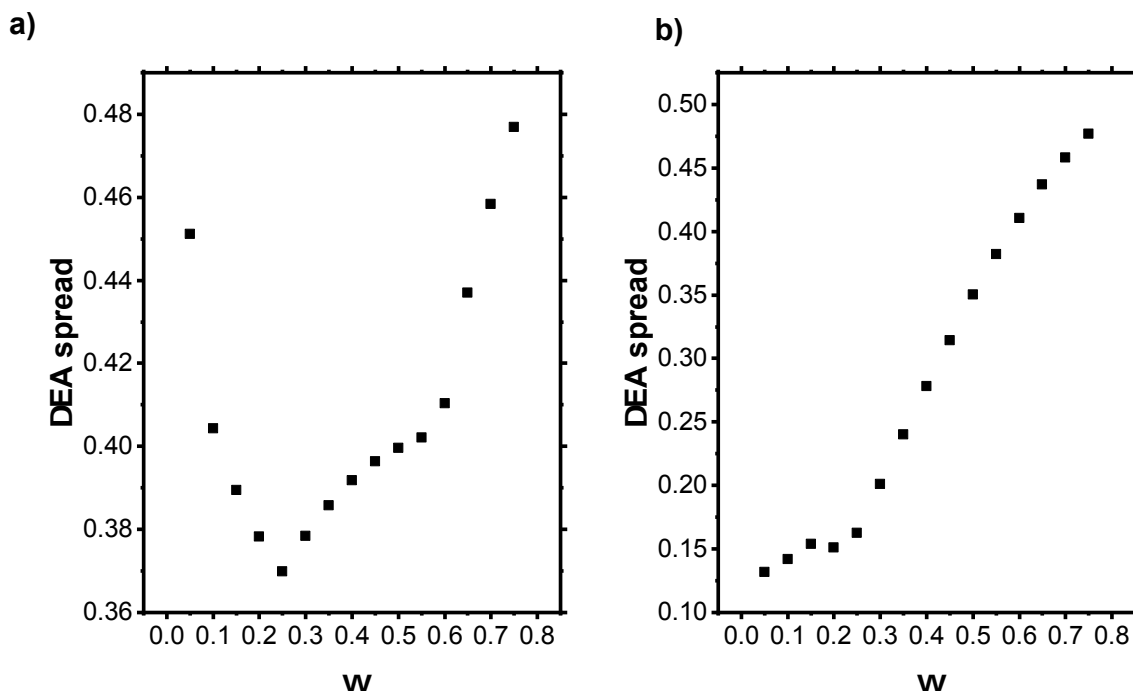


Figure B.5: Spread of the error as a function of ω for *PFP3CN3-CP*, *(CN)₆-CP*, *TCNQ*, *FTCNQ*, *F₂-TCNQ*, and *F₄-TCNQ* molecules: (a) With *TMCN3-CP* (b) Without *TMCN3-CP*.

To summarize, band gap tuning analyses reveal an ideal ω value between 0.10 and 0.20, in addition to showing that experimental EAs cannot be retrieved directly from the method employed. Further analysis of the scaling between computational and experimental EA values (referred to in the main text as EA_{calc} and EA_{exp} , respectively) suggests an overestimation of the *TMCN3-CP* molecule’s EA in experiments and a minimal overall discrepancy with experimental value for ω between 0.20 and 0.30; or between 0.15 and 0.25 if *TMCN3-CP* is being excluded. For these reasons, we find it appropriate to select an ω value that is founded both formally and in terms of expected outcome, where $\omega = 0.20$ fulfills this task best. Therefore, this value is being used for all calculations presented in the main text. Finally, from the fits of the computational electron affinities against the experimental ones (here selecting $\omega = 0.20$ without *TMCN3-CP*, since its inclusion leads to a rather large discrepancy in the intercept), we can derive an equation by inverting the fits to correct computational electron affinities (EA_{calc}) and retrieve expected experimental values for the molecules of interest. These values are referred to as “predicted experimental electron affinities” (EA_{pred}) in tables and the main text and are

obtained from the following equation:

$$EA_{\text{pred}} = 0.89746 * EA_{\text{calc}} + 1.39829 \quad (\text{B.2})$$

Calculations presented in main text

The calculated HOMO, LUMO, total energy for both neutral and charged molecules, and their EA are shown in Table B.2. Note that EA values are reported as positive numbers throughout this work. Corrected computational electron affinities have been obtained as described in the previous section. Average twisting angles (Figure B.6) of the rings for neutral molecules are provided when applicable. Finally, all optimized geometries are provided in Cartesian coordinates for the materials given in Table B.2 (see Appendix; pictures of the optimized geometries are provided for reference; there is no visible change for the radical anions).

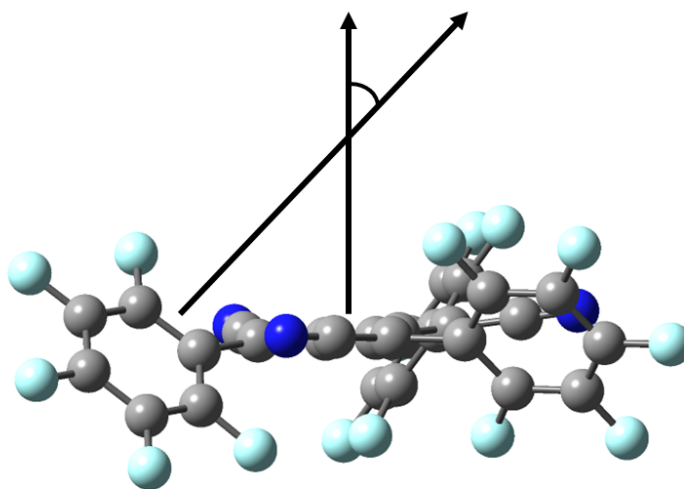


Figure B.6: Schematic of the ring twisting angle, which is defined as the angle between the vector normal to the plane of the PFP ring and the vector normal to the plane of the CP core; values for neutral molecules given in Table B.2.

Dopants	HOMO Neutral (eV)	LUMO Neutral (eV)	Energy Neutral (Hartree)	HOMO Charged (eV)	LUMO Charged (eV)	Energy Charged (Hartree)	E _{calc} (eV)	E _{pred} (eV)	Avg. Ring Twisting Angle (°)
CN6-CP	-10.94	-4.78	-785.23	-5.12	3.53	-785.42	4.96	5.85	NA
TMCN3-CP	-10.31	-3.81	-1192.09	-4.62	3.88	-1192.25	4.24	5.20	NA
Ph6-CP	-7.27	-1.02	-1618.02	-2.18	3.54	-1618.08	1.59	2.83	40.56
Ph3CN3-CP	-8.49	-2.66	-1201.64	-3.52	3.70	-1201.76	3.10	4.18	28.63
PFP6-CP	-9.13	-2.69	-4594.21	-0.28	4.63	-4594.33	3.29	4.35	50.75
PFP3CN3-CP	-9.68	-3.59	-2689.72	-4.44	2.87	-2689.86	4.03	5.02	36.13

Table B.2: The DFT calculated Highest Occupied Molecular Orbital (HOMO) energies, the Lowest Unoccupied Molecular Orbital (LUMO) energies, total energy of neutral and charged molecules (radical anion), $E_{A_{calc}}$ and $E_{A_{pred}}$ (see main text), and the average ring-twisting angles for neutral molecules (°).

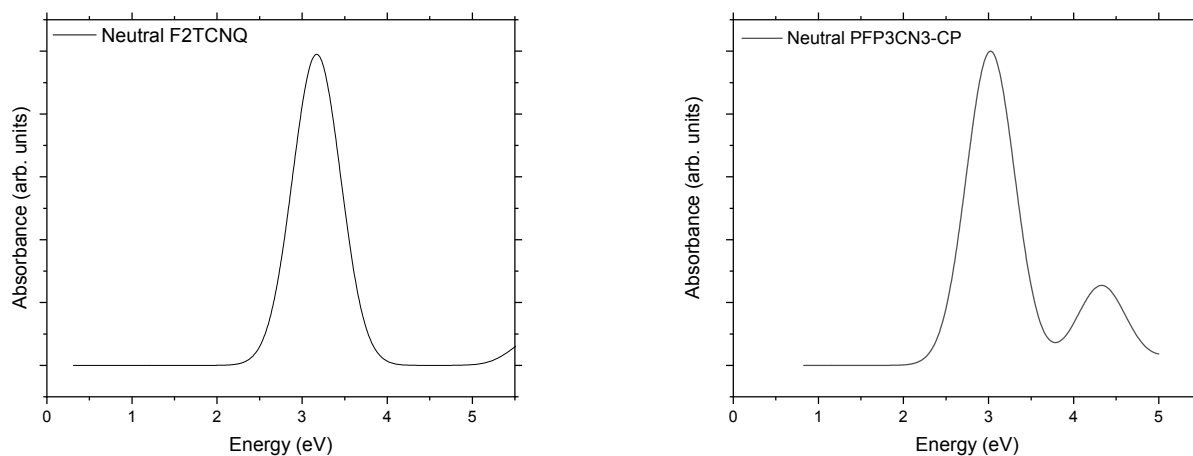


Figure B.7: DFT calculated UV-vis/NIR spectra of neutral F_2 -TCNQ (left) and $PFP3CN3-CP$ (right). Spectra were calculated using 25 singlet and 25 triplet excited states and were obtained using the default broadening in the software package Gaussian [10] (which assumes a Gaussian peak shape with $\sigma = 0.4$ eV).

B.3 Synthesis of PFP3CN3-CP

General synthetic procedure for PFP3CN3-CP (based on the procedure given in Ref.[4])

In a flamed-dry round bottom flask equipped with a stir bar, lithium hydride (8 equiv., 107.4 mg) was suspended in dry 1,2-dimethoxyethane (DME) (10 mL) and cooled to -5°C in a cooling bath under an argon atmosphere. Pentafluorophenyl acetonitrile (4 equiv, 0.842 mL) was dissolved in dry DME (2 mL) and added dropwise over a pe-

riod of 15 min while covered with aluminum foil. The mixture was slowly warmed to room temperature and stirred for 1h. It was then cooled again to -5°C in a cooling bath. Perchlorocycloprop-1-ene (1.0 equiv.; 0.206 mL) was dissolved in dry DME (2 mL) and added into the mixture dropwise. The resulting solution was slowly warmed to room temperature and stirred for 48h under an inert atmosphere. The dark red reaction mixture was then poured into 250 mL of ice/water. The solution was acidified to $\text{pH} = 1$ with cold concentrated hydrochloric acid (HCl) (12 M). The resulting dark purple mixture is transferred into an extraction funnel and extracted with dichloromethane (DCM) (3 \times 50 mL). The combined organic layer was washed with brine and then dried over anhydrous sodium sulfate (Na_2SO_4), and the filtrate is collected through filtration. Excess solvent is removed by rotatory evaporator at 25°C . The resulting crude is dissolved in cold glacial acetic acid 35 mL (500 mL) and purged with argon for 15 min. A mixture of cold 3 mL of nitric acid (HNO_3) (65% in water) and 9 mL of hydrobromic (HBr) (48% in water) is slowly added into the reaction mixture at 5°C . The resulting mixture is slowly warmed to room temperature and stirred for 2h and poured into 250 mL ice/water mixture, then settled in an ice-bath for 1h. The resulting orange precipitate was then collected by vacuum filtration and washed with distilled water (3 \times 50 mL). *PFP3CN3 – CP* is isolated by column chromatography (hexane: chloroform gradient from 10:1 to 1:1, $R_f = 0.31$). The compound is orange color oil, slowly crystallized in the freezer. ^{19}F NMR sample is prepared approximately with 3 mg/mL CD_3CN and is decoupled from ^{13}C (Figure B.9).

^{19}F NMR (470 MHz, CD_3CN): δ -143.38 (m), -156.20 (m), -163.76 (m).

HRMS (ESI): $\text{C}_{27}\text{F}_{15}\text{N}_3$, Calc.: 650.9852, Found: 650.9859.

Mass Spectroscopy, ^{19}F NMR, and FTIR

HRMS (ESI): $\text{C}_{27}\text{F}_{15}\text{N}_3$, Calc.: 650.9852, Found: 650.9859.

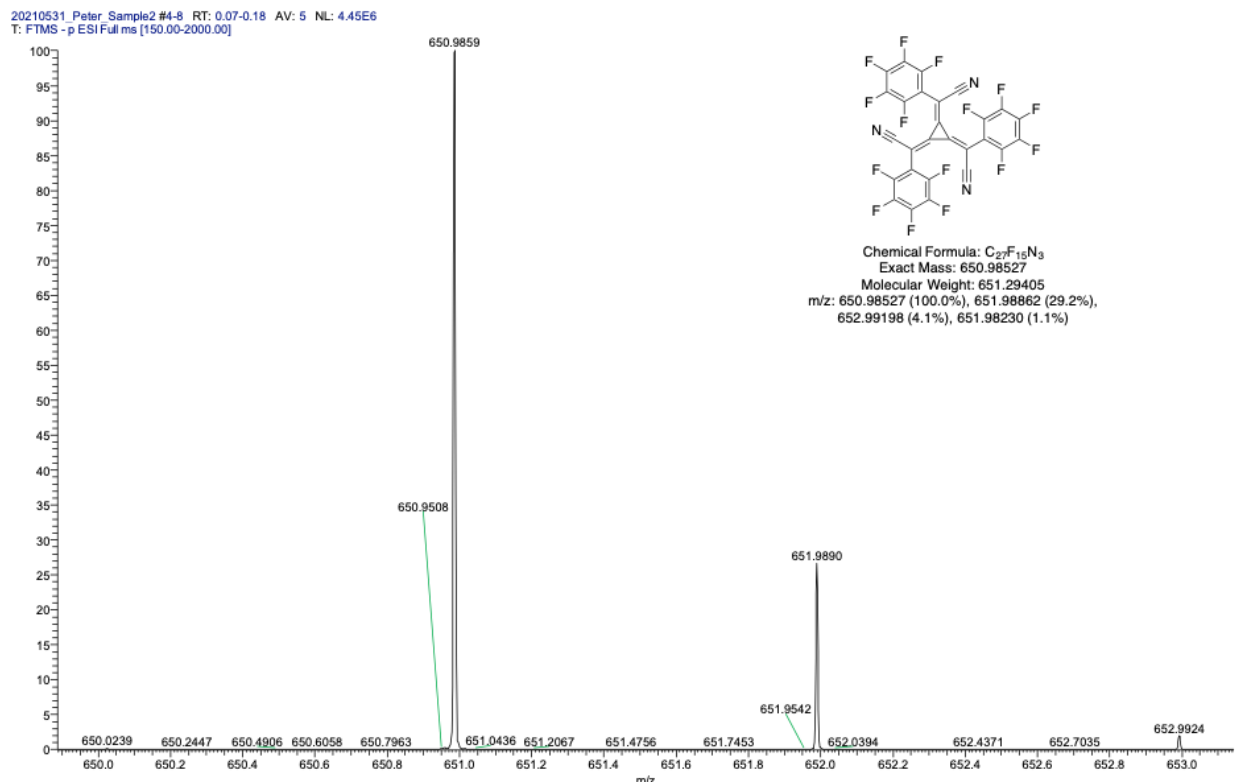


Figure B.8: High resolution mass spectra (HRMS) of *PFP3CN3-CP*.

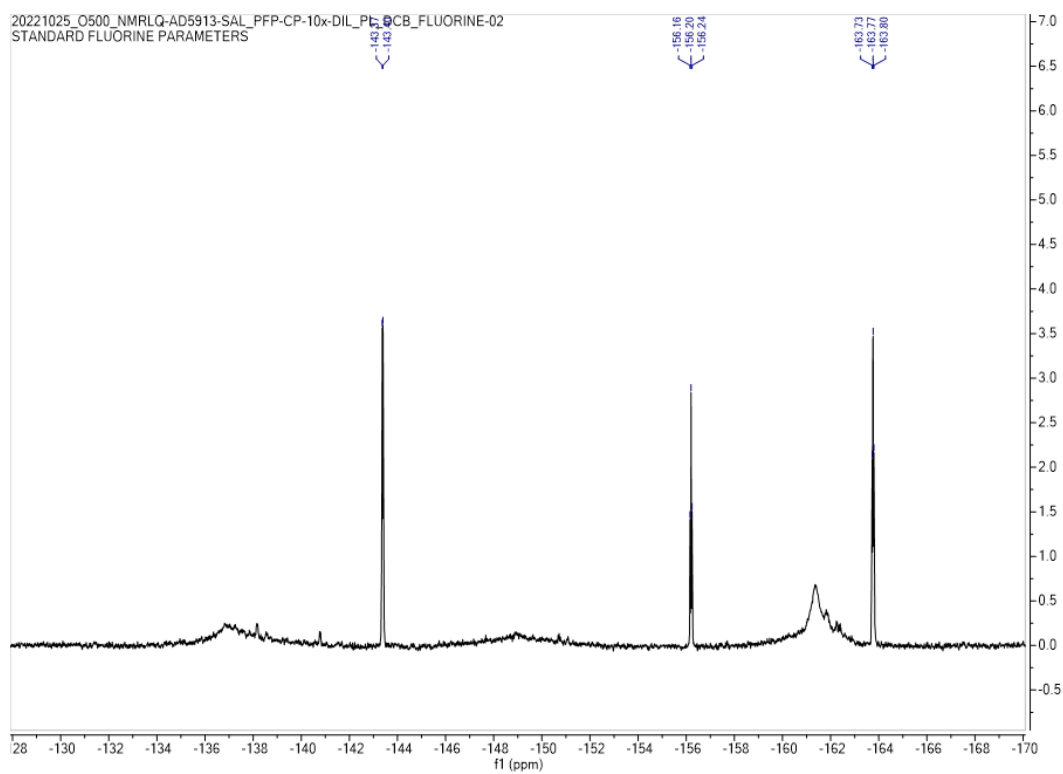


Figure B.9: ^{19}F NMR spectrum of *PFP3CN3 – CP*.

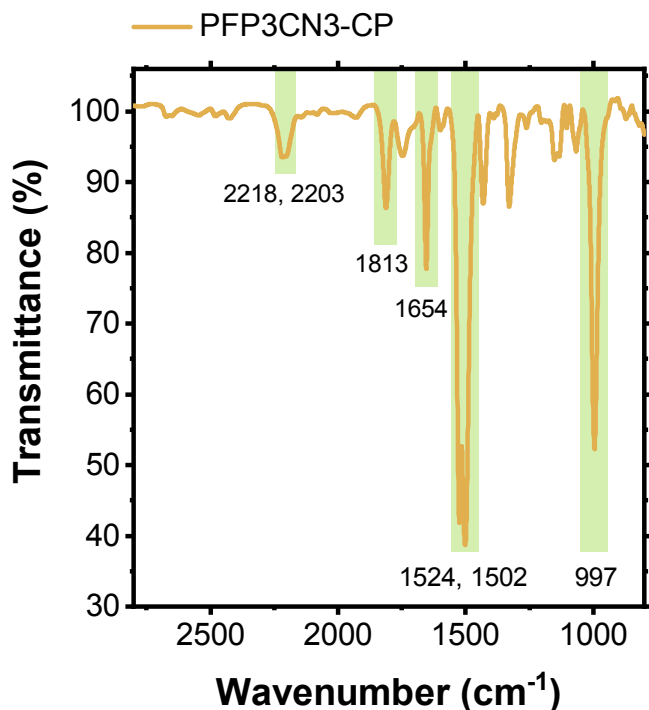


Figure B.10: Fourier-transform infrared spectroscopy of a dropcast *PFP3CN3-CP* film; peak assignment of the highlighted vibrations (based on DFT calculations): 2218 (w) cm^{-1} and 2203 (w) cm^{-1} : cyano stretch, 1813 (m) cm^{-1} symmetric cyclopropane ring stretch, 1654 (m) cm^{-1} : PFP ring stretch, 1524 (vs) cm^{-1} and 1502 (vs) cm^{-1} : pentafluoro phenyl ring twist, 997 (s) cm^{-1} : cyclopropane ring vibration.

B.4 Cyclic voltammetry

Voltammograms of $F_4\text{-TCNQ}$, $F_2\text{-TCNQ}$, and *PFP3CN3-CP* are shown in Figure B.11. We find one-electron reduction of *PFP3CN3-CP* occurs at -0.025 V (versus Fc/Fc^+), and the second one-electron reduction occurs at 0.874 V. Reduction potentials and derived LUMO energy levels of $F_4\text{-TCNQ}$, $F_2\text{-TCNQ}$, and *PFP3CN3-CP* are provided in Table B.3; the value used for the redox potential of ferrocene is -5.09 eV against vacuum. [82]

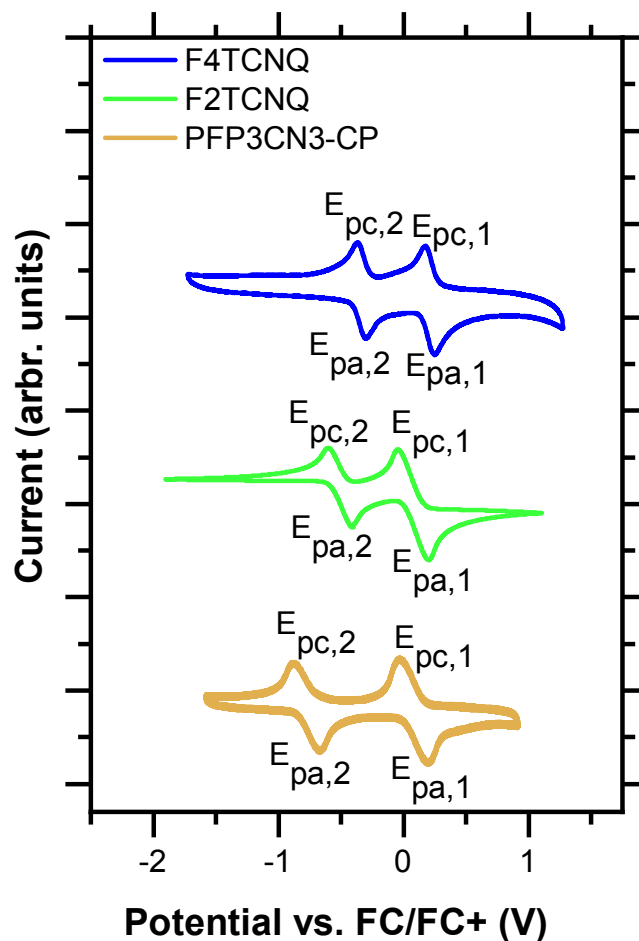


Figure B.11: Cyclic voltammograms of F_4 -TCNQ and F_2 -TCNQ in 0.1 M $n\text{-Bu}_4\text{NPF}_6$ acetonitrile solution using 50 mV/s scan rate referenced to ferrocene, and of $PFP3CN3-CP$ in 0.1 M $n\text{-Bu}_4\text{NPF}_6$ dichloromethane solution using 100 mV/s scan rate; $E_{pa,i}$ and $E_{pc,i}$ depict the anodic and cathodic peak potentials.

Dopant	$E_{red,1}$ (V)	$E_{LUMO,1}$ (eV)	$E_{red,2}$ (V)	$E_{LUMO,2}$ (eV)
F4TCNQ	0.21	-5.30	-0.34	-4.75
F2TCNQ	-0.04	-5.05	-0.61	-4.48
PFP3CN3-CP	-0.02	-5.07	-0.87	-4.22

Table B.3: Reduction potentials from cyclic voltammetry experiments and the derived LUMO energies of F_4 -TCNQ, F_2 -TCNQ and $PFP3CN3-CP$.

B.5 Supporting UV-vis/NIR absorption data

Absorption spectra of PFP3CN3-CP upon titration with KI

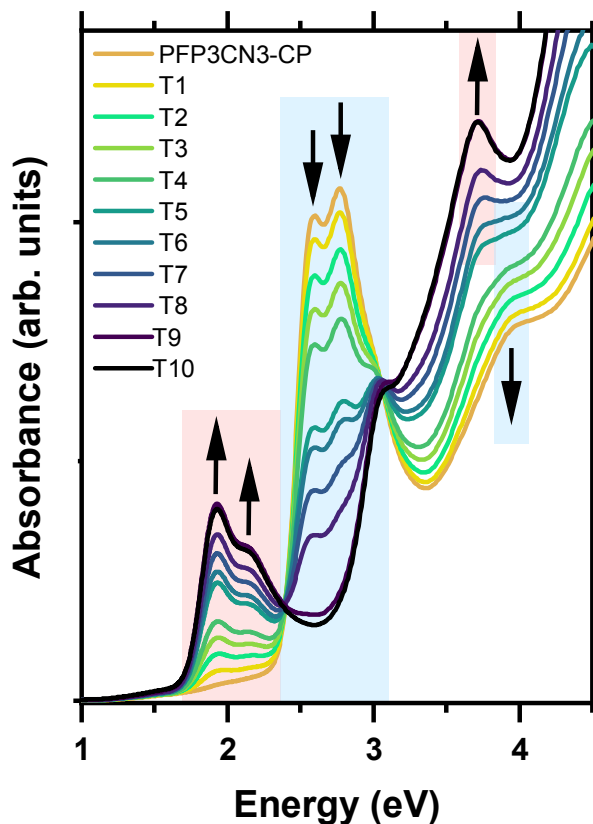


Figure B.12: Evolution of absorbance spectra of *PFP3CN3-CP* (0.8 g/L) upon increasing titration (T1 ... T10) with KI (0.35 g/L) in acetonitrile solution. Transitions assigned to the *PFP3CN3-CP* radical anion are highlighted in red, those of the neutral species in blue. Transitions assigned to the neutral *PFP3CN3-CP* are at 2.59, 2.77, and 3.95 eV, those of the dopant radical anion *PFP3CN3-CP*^{•-} arise at 1.93, 2.13 eV and at 3.71 eV.

Absorption spectra of spin-coated P3HT films doped with PFP3CN3-CP

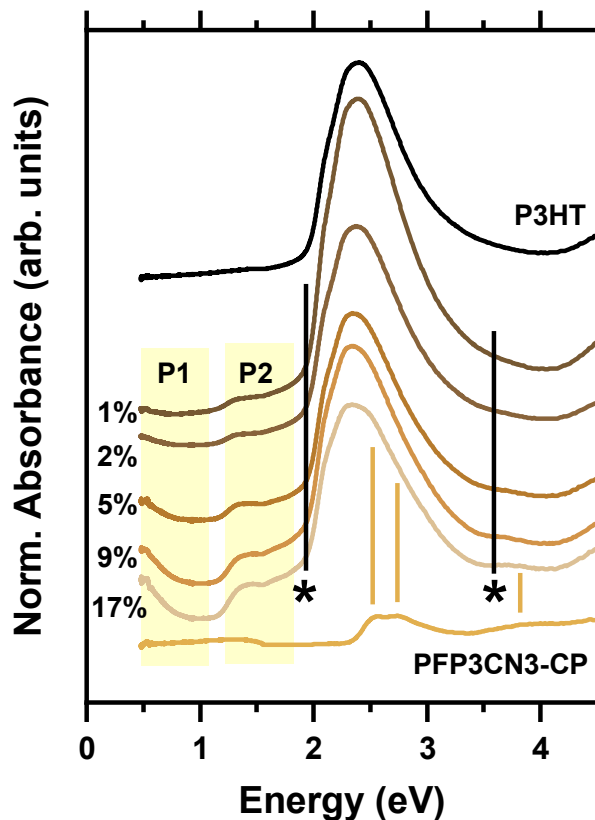


Figure B.13: UV-vis/NIR absorbance spectra of P3HT films doped with increasing molar ratios of and *PFP3CN3-CP*, spin-coated from common solution. Spectra are normalized to common thickness as individually determined by AFM; the results fully agree with the findings for dropcast films reported in the main text (Figure 4.3b).

Absorption spectra of h10T doped with F2TCNQ and PFP3CN3-CP

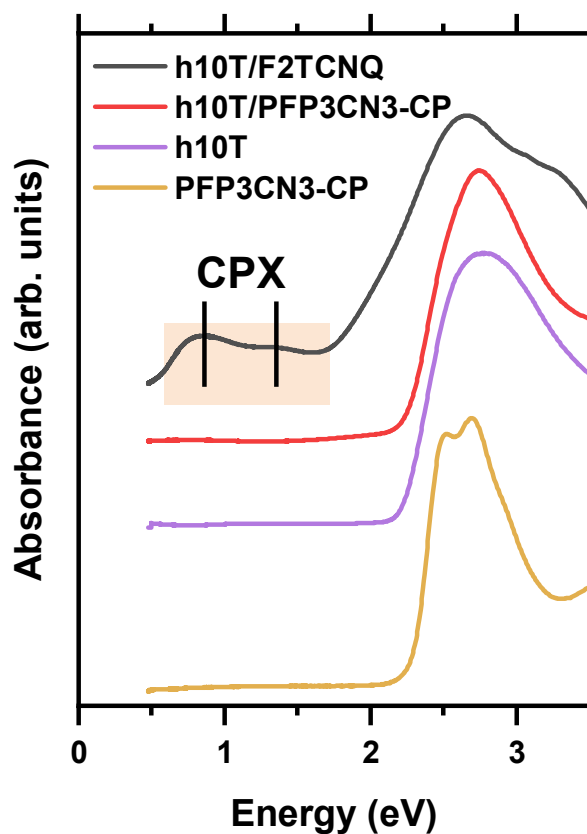


Figure B.14: UV-vis/NIR absorbance spectra of dropcast pure *PFP3CN3-CP*, pure h10T, and h10T films blended with *F₂-TCNQ* and *PFP3CN3-CP* at a molar ratio of 67%. For *F₂-TCNQ*, the characteristic transitions of the CPX are observed, while no sub-gap features are found for *PFP3CN3-CP*, indicating suppressed CPX formation for the latter.

B.6 Aging experiments

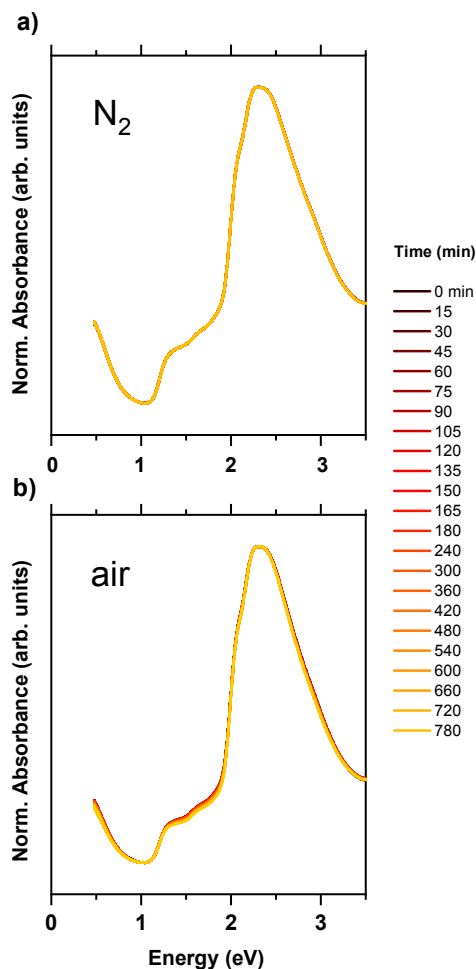


Figure B.15: UV-vis/NIR absorbance spectra of two dropcast P3HT films doped with *PFP3CN3-CP* (17%, nominally identical preparation parameters as for the sample depicted in Figure 3 of the main text) under (a) inert N_2 atmosphere (in a custom-built sealed box with quartz glass windows) and (b) in air (measured in the same box). In both cases, the box was kept in the same position within the spectrometer over the whole time of 780 min; all spectra are normalized to the pure P3HT absorbance maximum. Under N_2 , no changes are observed for the absorbance assigned to the low energy polaron at 0.62 eV (2000 nm). In air, after initial exposure to air, it remains stable for 1h to be then reduced by 2% after 3h, by 6% after 6h, and by 11% after 12h. For comparison, the same values for ECN5-CP (as given by Saska et al. in Ref. [12]) are: 2.5% (1h), 7% (3h), 12% (6h), and 17% (12h).

B.7 Supporting conductivity data

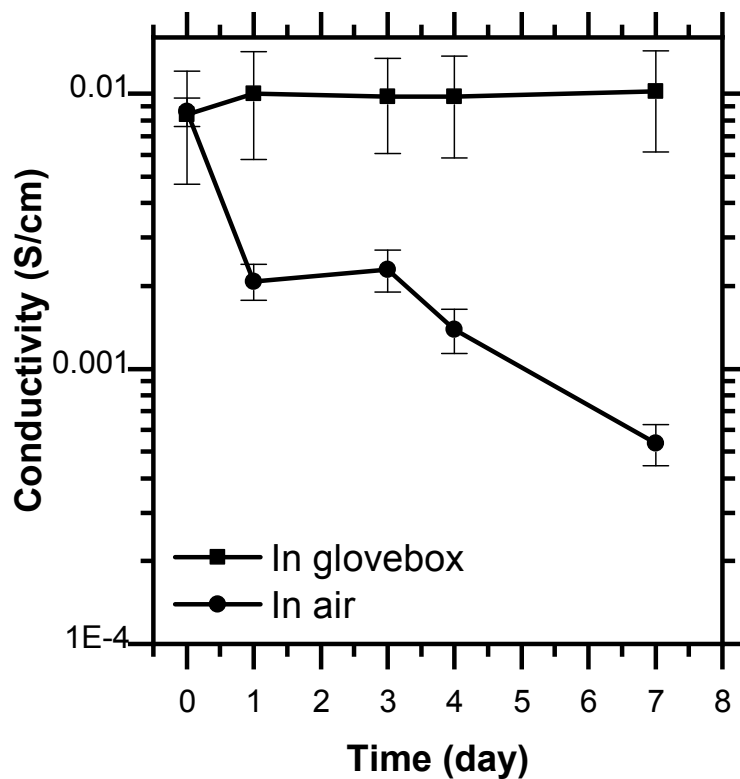


Figure B.16: Time-dependent room temperature conductivity of P3HT films doped with *PFP3CN3-CP* (17%) over seven days in two different environments: One film was kept in an inert atmosphere in an N_2 glovebox, the other film was kept in air for the whole time. While the conductivity is constant under N_2 , it is reduced by factors of 4, 6, and 16 for 1, 4, and 7 days, respectively. As a comparison, the conductivity of P3HT films doped with the similar species *TMCN3-CP* (as given by Saska et al. in Ref. [58]) drops by factors of 4, 7, and 9 in the glovebox and by 7, 45, and 100 in air over the same time.

B.8 Grazing-Incidence X-Ray Diffraction (GIXRD) data

We have studied the structural properties of P3HT films doped with *PP3CN3-CP* by GIXRD to assess potential changes in the thin film structure due to the dopant admixture. Figure B.17a shows the 2D GIXRD diffraction data of the pristine P3HT film in a reciprocal space map and reveals its preferential edge-on orientation, as is common for such films. The out-of-plane (h00) features correspond to lamellar stacking with a lattice spacing d_{100} of 16.53 Å, and the in-plane reflection is assigned to (020), representing the $\pi-\pi$ backbone stacking of P3HT with a lattice spacing of $d_{020} = 3.82$ Å; all values are in good agreement with published work on pristine P3HT [5, 47, 85, 149–151].

The diffraction patterns of P3HT doped at 1, 2, 5, 9, and 17% dopant molar ratio are shown in Figures B.17b-f. These data reveal that the main features for pristine P3HT are still observed for all doping ratios with only insignificant changes in intensity. Note that the pure *PP3CN3-CP* film does not show diffraction features, which is either because of too low diffraction intensity, e.g., of a non-textured, crystalline film, or because the pure dopant grows amorphous on the surface.

Upon doping P3HT, the lamellar d_{100} lattice spacing shows a gradual increase with increasing dopant ratio up to 17.54 Å for 17% *PP3CN3-CP* (see Figure B.18a for integrated line scans of the 2D GIXRD data), whereas d_{020} decreases with the dopant ratio (Figure B.18b) from initially 3.82 Å to 3.78 Å. This is indicative of the dopant being intercalated in the hexyl side-chain region of P3HT (which increases d_{100}), while a concomitantly reduced P3HT backbone tilt is deduced from the reduction in d_{020} ; the same has been reported before for *F4-TCNQ* doped P3HT for doping ratios where no CPX formation occurs [5, 152–155].

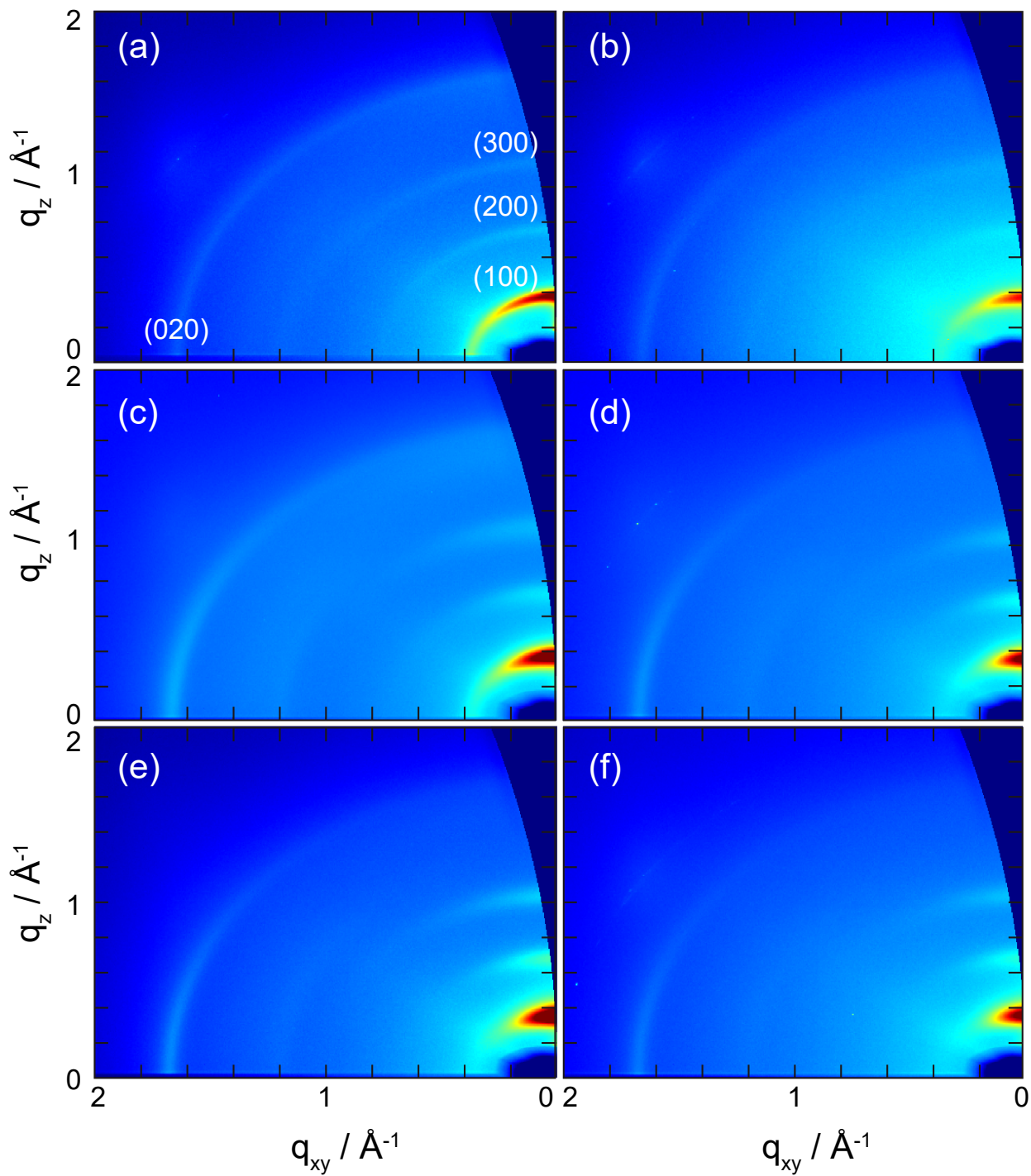


Figure B.17: GIXRD reciprocal space maps of dropcast films of pure P3HT (a) and films doped with *PFP3CN3-CP* at increasing dopant molar ratios of 1%, 2%, 5%, 9%, and 17% (b-f). q_z , q_{xy} are the out-of-plane and in-plane components of the scattering vector q , respectively; colors correspond to intensities on a logarithmic scale. (100), (200), and (300) indicate the lamellar spacing of the P3HT chains, while (020) stems from their $\pi-\pi$ backbone stacking.

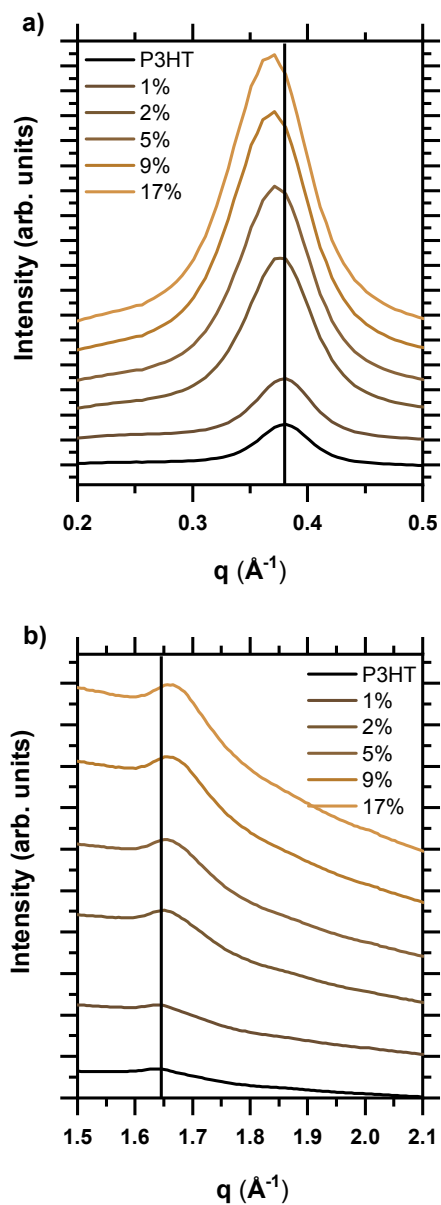


Figure B.18: GIXRD intensities radially integrated along constant values of the scattering vector $q = |q| = \sqrt{q_{xy}^2 + q_z^2}$ of the data shown in Figure B.17; data is shown in the range around (a) the peak corresponding to the (100) P3HT lamellar stacking and (b) that corresponding to the (020) $\pi - \pi$ stacking distance of P3HT; positions of the pristine P3HT film are marked by vertical lines. The PFP3CN3-CP percentages are mentioned in the figure.

B.9 Atomic Force Microscopy (AFM) data

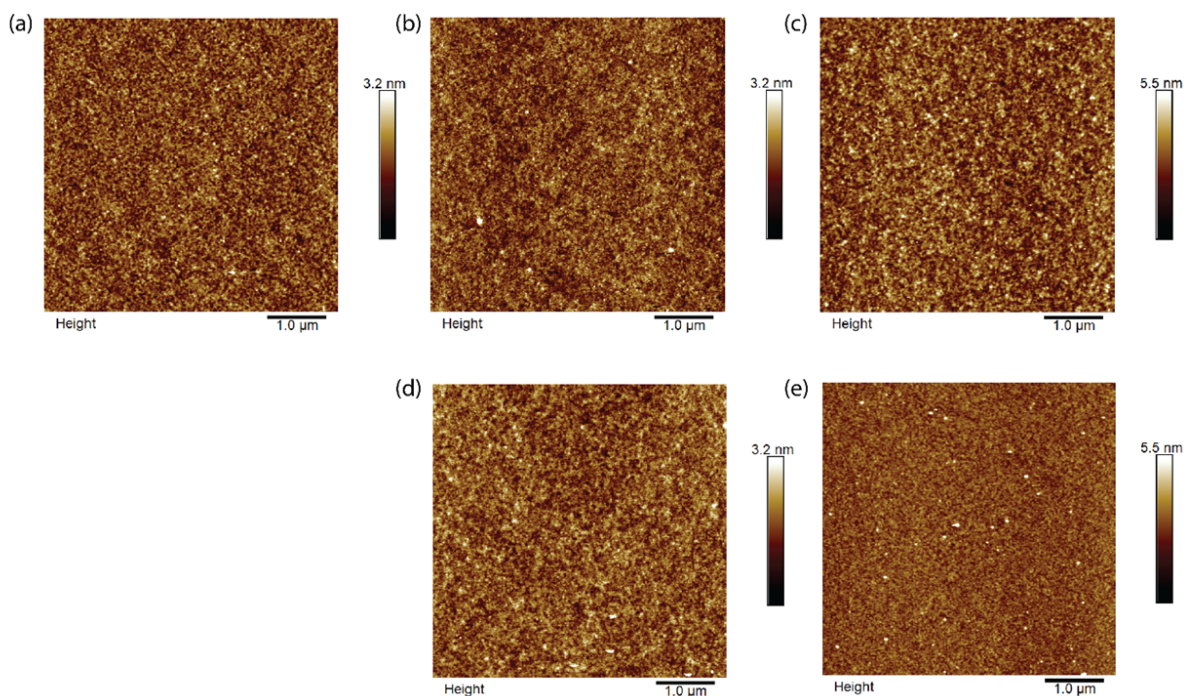


Figure B.19: Representative AFM micrographs of thin films spin-coated on silicon (native oxide layer), the corresponding RMS roughness values (determined for three $1 \times 1 \mu\text{m}$ areas in each image yielding 5% standard deviation) are given in brackets: P3HT [0.37 nm] (a), P3HT doped from common solution with 1% $F_2\text{-TCNQ}$ [0.37 nm] (b), 9% $F_2\text{-TCNQ}$ [0.65 nm] (c), 1% $PPF3CN3 - CP$ [0.35 nm] (d), and 9% $PPF3CN3 - CP$ [0.40 nm] (e). No apparent changes to the film morphology are observed by AFM, and the films show a smooth morphology of low roughness with no indication of dopant precipitation. However, for 9% $F_2\text{-TCNQ}$, the RMS roughness is significantly higher than in all other cases, which might be indicative of the formation of crystalline ground state charge transfer complexes, as reported in Ref. [5].

Appendix C

List of Abbreviations

- OSC:** organic semiconductors
COM: conjugated organic molecules
CP: conjugated polymers
HTM: hole transport material
TCNQ: Tetracyanoquinodimethane
FTCNQ: 2-fluoro-7,7,8,8-tetracyanoquinodimethane
F2TCNQ: 2,5-Difluoro-7,7,8,8-tetracyanoquinodimethane
F4TCNQ: 2,3,5,6-Tetrafluoro-7,7,8,8-tetracyanoquinodimethane
F6TCNNQ: 2,2'-(perfluoronaphthalene-2,6-diylidene)dimalononitrile
CN6-CP: hexacyano-trimethylene-cyclopropane
ECN5-CP: Ethyl 2-(2,3-bis(dicyanomethylene)cyclopropylidene)-2-cyanoacetate
DMCN4-CP: Dimethyl 2,20-(3(dicyanomethylene)cyclopropane-1,2-diylidene) (2Z,20E)-bis(2-cyanoacetate)
TMCN3-CP: trimethyl 2,20,200-(cyclopropane-1,2,3-triylidene)tris(cyanoacetate)
HAT-CN: 1,4,5,8,9,11-Hexaazatriphenylenehexacarbonitrile
PPF3CN3-CP: 2,2',2''-(cyclopropane-1,2,3-triylidene)tris(2-(perfluorophenyl)acetonitrile)
Mo(tfd)3: molybdenum tris(1,2-bis(trifluoromethyl)ethane-1,2-dithiolene)
P3HT: poly(3-hexylthiophene-2,5-diyl)